SENSING MECHANISMS IN CHEMIRESISITIVE SENSORS BASED METAL OXIDE THIN FILMS AND NANOSTRUCTURES

By

Niyanta Datta

(PHYS01201204014)

Bhabha Atomic Research Center, Mumbai

A thesis submitted to the
Board of Studies in Physical Sciences
In partial fulfillment of requirements
For the Degree of

DOCTOR OF PHILOSOPHY

of

HOMI BHABHA NATIONAL INSTITUTE

October, 2014

STATEMENT BY AUTHOR

This dissertation has been submitted in partial fulfillment of requirements for an advanced degree at Homi Bhabha National Institute (HBNI) and is deposited in the Library to be made available to borrowers under rules of the HBNI.

Brief quotations from this dissertation are allowable without special permission, provided that accurate acknowledgement of source is made. Requests for permission for extended quotation from or reproduction of this manuscript in whole or in part may be granted by the Competent Authority of HBNI when in his or her judgment the proposed use of the material is in the interests of scholarship. In all other instances, however, permission must be obtained from the author.

Niyanta Datta

DECLARATION

I, hereby declare that the investigation presented in the thesis has been carried out by me. The work is original and has not been submitted earlier as a whole or in part for a degree / diploma at this or any other Institution / University.

Niyanta Datta

List of Publications arising from the thesis

In Journals

1. “Kelvin probe and impedance measurements to investigate the role of various interfaces of CuO/ZnO random nanowires network in H_2S sensing”, **N. Datta**, N. Ramgir, S. Kumar, P. Veerender, M. Kaur, S. Kailasaganapathi, A.K. Debnath, D.K. Aswal, S.K. Gupta, , *Sens. Actuators B,* **2014**, *202*, 1270-1280.
2. “Effect of Fe modification on H_2S sensing properties of rheotaxially grown and thermally oxidized SnO_2 thin films”, N.S. Ramgir, **N. Datta**, S. Kumar, M. Kaur, S. Kailasaganapathi, A.K. Debnath, D.K. Aswal, S.K. Gupta, *J. Mat. Chem. Phys.*, 2014 (under review).
3. “Vacuum deposited WO_3 thin films based sub ppm H_2S sensor”, **N. Datta**, N.S. Ramgir, M. Kaur, M. Roy, R. Bhatt, S. Kailasaganapathi, A.K. Debnath, D.K. Aswal, S.K. Gupta, *Mater. Chem. Phys.,* **2012,** *134*, 851-857.
4. “Selective H_2S sensing characteristics of hydrothermally grown ZnO-nanowires network tailored by ultrathin CuO layers”, **N. Datta**, N.S. Ramgir, M. Kaur, S. Kailasaganapathi, A.K. Debnath, D.K. Aswal, S.K. Gupta, *Sens. Actuators B,* **2012,** *166– 167,* 394– 401.
5. “Metal oxide nanowires for chemiresistive gas sensors: Issues, challenges and prospects”, N.S. Ramgir, **N. Datta**, M. Kaur, S. Kailasaganapathi, A.K. Debnath, D.K. Aswal, S.K. Gupta, *Coll. Surf. A,* **2013,** *439*, 101-116.
6. “Selective H_2S sensing characteristics of CuO modified WO_3 thin films”, N. S. Ramgir, C.P. Goyal, P.K. Sharma, U.K. Goutam, S. Bhattacharya, **N. Datta**, M. Kaur, A.K. Debnath, D.K. Aswal, S.K. Gupta, *Sens. Actuators B,* **2013**, *188*, 525-532.

7. “Room temperature H_2S sensor based on Au modified ZnO nanowires”, N.S. Ramgir, P.K. Sharma, **N. Datta**, M. Kaur, A.K. Debnath, D.K. Aswal, S.K. Gupta, , *Sens. Actuators B,* **2013**, *186*, 718-726.
8. “Ethanol sensing properties of pure and Au modified ZnO nanowires”, N.S. Ramgir, M. Kaur, **N. Datta**, P.K. Sharma, S. Kailasaganapathi, S. Bhattacharya, A.K. Debnath, D.K. Aswal, S.K. Gupta, *Sens. Actuators B,* **2013**, *187*, 313–318.
9. “Growth and gas sensing characteristics of p- and n-type ZnO nanostructures”, N.S. Ramgir, M. Ghosh, P. Veerender, **N. Datta**, M. Kaur, D.K. Aswal, S.K. Gupta, *Sens. Actuators B,* **2011,** *156,* 875-880.
10. “H_2S detection by CuO nanowires at room temperature”, M. Kaur, S. Kailasaganapathi, **N. Datta**, K.P. Muthe and S.K. Gupta, *Int. J. Nanosci.,* **2011,** *10*, 733.
11. “Sub-ppm H_2S sensing at room temperature using CuO thin films”, N. S. Ramgir, S. Kailasa Ganapathi, M. Kaur, **N. Datta**, K. P. Muthe, D.K. Aswal, S. K. Gupta, and J.V. Yakhmi, *Sens. Actuators B,* **2010,** *151*, 90-96.

Book Chapter

1. ”Semiconductor nanowires and heterostructures based gas sensors”, N. S. Ramgir, **N. Datta**, M. Kaur, A.K. Debnath, D.K. Aswal, S.K. Gupta, Nova Science Publishers, **2011 (**USA ISBN 978-1-61470-287-0).

In conferences

1. ”Impedance Spectroscopy of Pure and CuO modified Random ZnO nanowires network”, **Niyanta Datta**, Niranjan Ramgir, Veerender Putta, Manmeet Kaur,

A.K. Debnath, D.K. Aswal, *International Conference on Electron Microscopy*, **2014**, Delhi University**.**

2. “Kelvin probe studies of H_2S exposed CuO:ZnO nanowires random networks”, **Niyanta Datta**, Niranjan Ramgir, Manmeet Kaur, Kailasa Ganpathi, A.K. Debnath, D.K. Aswal, and S.K. Gupta, *AIP Conf. Proc.*, **2013**, *1512*, 334.
3. “ZnO nanowires coated with CuO films as highly sensitive H_2S sensors”, **Niyanta Datta**, N.S. Ramgir, Manmeet Kaur, A.K. Debnath, D.K. Aswal et al. Citation: *AIP Conf. Proc*., **2012**, *1451*, 61.
4. “Ammonia Sensor Based On WO_3 Thin Films”, Niranjan Ramgir, Niyanta Datta, Manmeet Kaur, S. Kailasha Ganapati, A.K. Debnath, D.K. Aswal, S.K. Gupta, , *AIP Conf. Proc*, **2012**, *1451*, 185.
5. “Effect of CuO additive on H_2S sensing Properties of WO_3 thin films”, C. P. Goyal, Preetam K. Sharma, N. Ramgir, S. Bhattacharya, **N. Datta**, M. Kaur, A.K. Debnath, D.K. Aswal, S.K. Gupta, *National Seminar on Physics and Technology of Sensors (17th NSPTS),* **2013**, Jamia Milia Islamia, New Delhi.
6. “H_2S sensing properties of RF sputtered SnO_2 films”, Kailasa Ganpathi, Manmeet Kaur, Niranjan Ramgir, **Niyanta Datta**, Shovit Bhattacharya, A.K. Debnath, D.K. Aswal, and S.K. Gupta, *AIP Conf. Proc.* **2013**, *1512*, 780.
7. “Integrated Chemiresistive Gas Sensor for Monitoring Toxic Gases”, M. Kaur, S. Kailasa Ganapati, V. Chaware, V. Rane, V. Giramkar, G. Phatak, N. Ramgir, **N. Datta**, A.K. Debnath, D.K. Aswal, S.K. Gupta, *Theme meeting on Synergy in Physics and Industry (SPI-2013),* **2013**, Bhabha Atomic Research Centre, Mumbai, India.
8. “Technology of sensitive and selective H_2S sensors (5-50 ppm range)”, M. Kaur, S. Kailasa Ganapati, N.S. Ramgir, **N. Datta**, A.K. Debnath, D.K. Aswal, S.K.

Gupta, *Theme meeting on Synergy in Physics and Industry (SPI-2013)*, **2013**, Bhabha Atomic Research Centre, Mumbai, India.

9. "Growth and H_2S gas sensing properties of CuO functionalized ZnO Nanotetrapod", Manmeet Kaur, Kailasa Ganapathi, Niranjan S. Ramgir, **Niyanta Datta**, D.K. Aswal and S. K. Gupta, *IMCS 2012* **-** *The 14th International Meeting on Chemical Sensors*, **2012**, Nürnberg /Nuremberg, Germany.
10. "Ethanol Sensing Properties of Pure and Au Modified ZnO nanowires", Niranjan S. Ramgir, Manmeet Kaur, **Niyanta Datta**, Preetam K. Sharma, S. Kailasaganapathi, S. Bhattacharya, A.K. Debnath, D.K. Aswal, S. K. Gupta, *IMCS 2012* **-** *The 14th International Meeting on Chemical Sensors*, **2012**, Nürnberg /Nuremberg, Germany.
11. "Evaluation of compatibility of SnO_2:CuO thin-film based H_2S sensor on LTCC substrates", Manmeet Kaur, S. Kailasa Ganapathi, Varsha Chaware, Vivek Rane, Niranjan Ramgir, **Niyanta Datta**, Vijaya Giramkar, Girish Phatak, D.K. Aswal, S.K. Gupta, *International symposium on physics and technology of sensors*, **2012**, CMET, Pune.
12. "Enhanced H_2S sensing properties of Au modified WO_3 thin films", Niranjan S. Ramgir, S. Kailasaganapati, **N. Datta**, M. Kaur, A.K. Debnath, D.K. Aswal, S.K. Gupta, *International symposium on physics and technology of sensors*, **2012**, CMET, Pune.
13. "Opposite response of CO for WO_3 and Au: WO_3 Sensors", Niranjan S. Ramgir, S. Kailasa Ganapati, **N. Datta**, K. Kaur, A. K. Debnath, D. K. Aswal, S. K. Gupta, *56th DAE Solid State Physics Symposium*, **2011**, SRM University, Kattankulathur – 603 203, Tamilnadu.

Dedicated to my father

Acknowledgements

First of all, I would like to express my deepest appreciation to my guide **Prof. D.K. Aswal**, who has been a source of continual energy and inspiration during the course of this dissertation. The present thesis work would not have been possible without his endless support and astute guidance. His contagious enthusiasm and uninterrupted motivation has driven me to carry out timely submission of this dissertation. I would like to thank **Dr. S.K. Gupta**, Head Technical Physics Division, for encouragement, support and guidance.

I sincerely thank **Dr. A.K. Debnath** for valuable advices and support in the X ray photoelectron spectroscopy measurements and analyses. I would like to extend my warm gratitude and sincere appreciation to **Dr. Niranjan Ramgir** for consistent encouragement and support in each and every step of this dissertation work. I am thankful to large number of colleagues for extending help in different experiments: **Mr. Veerender** for impedance spectroscopy, **Dr. Vibha Saxena** and **Dr. Mainak Roy** for Raman measurements, **Dr. Debarathi Bhattacharya** and **Dr. Shashwati Sen** for X ray diffraction measurements and **Dr. Mohit Tyagi** for photoluminescence measurements.

I am exceptionally grateful to **Dr. Ranu Bhatt**, **Dr. Shovit Bhattacharya** and **Dr. Soumen Samanta** for their help, support, encouragement and most of all their affection that kept me in good spirits and enthusiastic while carrying out the dissertation work. I am thankful to **Dr. K.P. Muthe, Dr. Manmeet Kaur, Dr. Ajay Singh, Shri R. Prasad, Mrs. Ranita Basu, Dr. Anil Chauhan, Dr. Shankar Koiry, Dr. Purushottam Jha, Mr. Sajid Ahmad, Mrs K Ganapati, Shri K.N. Meshram,** for extending support and help at various stages of the thesis work.

Last but not the least, I would like to extend my heartiest gratitude to my mother **Mrs. Varsha Datta**, my brother **Anshul Datta** and my husband **Mr. B. Shreebhooshan**

for their unconditional support, love and patience during this dissertation work. I would also like to thank all my friends for their backing and encouragement during the dissertation work.

Niyanta Datta

CONTENTS

Page

No.

CHAPTER

4 p-n JUNCTIONS TYPE CHEMIRESISTIVE SENSORS

SYNOPSIS

Metal oxide semiconductors, both n-type (SnO_2, WO_3, ZnO etc) and p-type (Cr_2O_3, CuO etc) are well established class of functional materials for chemiresistive gas sensors. Metal oxides are intrinsically insulators but presence of natural defects during their synthesis give rise to significant conductivity (n-type or p-type depending upon the nature of defect). This makes metal-oxides suitable for gas sensing, as their electrical resistivity (or conductivity) change upon interaction with analyte gas molecules. The chemiresistive sensors have extensively been investigated in different forms such as bulk pellets, thick films, thin films and nanostructures. Thin films and nanostructures offer various advantages: (i) larger surface area to volume ratio, implying more active sites for oxygen adsorption, (ii) Debye length comparable to the grain size or structure size which enhances the sensitivity; and (iii) small size of the sensors implying low power consumption if the sensor is operated at higher temperatures. Nanostructure based sensors have additional advantages in terms of possibility of high integration densities, ease of incorporation into microelectronic devices and superior stability owing to high crystallinity.

A major issue with pure metal-oxides sensors is the lack of specificity i.e. same sensor detects many gases. In literature, attempts have been made to improve the specificity of the metal-oxides by following three strategies;

(i) *By changing the operating temperature*: The chemisorption or redox reaction with the analyte gas at the sensor surface is a function of temperature, therefore selectivity for a particular gas is obtained at a particular temperature. In general, higher operating temperature, yields faster response kinetics but it also affects the long term stability.

(ii) *Use of suitable additives*: The additives may improve the selectivity due to different effects. (a) Catalytic effect, wherein additives act as catalysts to favour a specific reaction; (b) spill over effect, wherein a particular additive molecule accelerates the reaction rate by dissociating particular test gas molecules and spilling over the reaction products onto the sensor surface; and (c) Fermi energy control, wherein the sensor signal is determined by the electronic contact between the semiconductor and the additive, which results in an alignment of Fermi energy of the metal oxide and the additive, leading to the formation of barrier potential. The additive particles becomes partially oxidised in the ambient gas atmosphere and its stoichiometry depends on the composition of the ambient air. The position of the Fermi level of this oxidised additive depends on its composition. So in a way, ambient oxygen is altering the additive and the additive is altering the electron density of the metal-oxides. If the concentration of the additive is high on the surface of metal-oxides as compared to other adsorbates and it is finely dispersed on the surface, the additive controls the barrier potential. The test gas reacts with the metal-oxides via additive and hence the chosen additive strongly changes the selectivity of the chemiresistive sensor.

(iii) *Use of appropriate filters*: In this case, an appropriate diffusion filter layer is deposited on the surface of the sensor. By choosing the material of diffusion layer with appropriate porosity, the sensor can be made specific towards test gases having small molecules. Only the filtered molecules are able to reach the surface of the sensing material. This approach suffers from a disadvantage of unavailability of suitable diffusion filters for all the gases.

Among above mentioned three strategies employed for selectivity improvement, use of additives has been employed widely. From the perspective of India, selective H_2S

sensors are needed for Heavy water plants to monitor its concentration in environment (in case of any leakage). In literature, several additives have been employed to make metal-oxides sensors selective to H_2S. However the mechanisms of enhancement of the H_2S specificity by additives are not fully understood. ***Therefore, this thesis aims at understanding the gas-sensing mechanisms in metal-oxides chemiresistive sensors with suitable additives that make them selective to H_2S gas.*** We have synthesized p-type (CuO) as well as n-type (ZnO, WO_3, SnO_2) metal-oxides thin films and nanostructures for H_2S sensors. In addition, these thin films and nanostructures are tailored using suitable additives so as to realize highly specific either p-n junctions (CuO:ZnO, CuO:WO_3, Fe_3O_4:SnO_2) or Schottky barriers (Au:ZnO, Au:WO_3) which enhances the specificity for H_2S. The gas sensing mechanisms were investigated using various techniques like X-ray photoelectron spectroscopy, impedance spectroscopy, Kelvin probe, photoluminescence, UV-Vis spectroscopy, X ray diffraction. The work done and the obtained results are organised in following six chapters.

Chapter 1: Introduction

In this chapter, we begin with introducing different types of sensors and discuss in detail about chemiresistive sensors based on metal-oxides semiconductors. Various sensor parameters, requirements and reported mechanisms of gas sensing are summarized. Depending upon the majority charge carriers and the role an additive plays, the chemiresistive sensor are classified into four categories: p-type, n-type, p-n junction type and Schottky barrier type. A literature on these types of sensors is reviewed. Finally the scope of present thesis is presented.

Chapter 2: Experimental details

This chapter describes the details of experimental methods used for fabrication of different types of sensors. Thin films of p-type CuO and n-type WO_3 were deposited by thermal evaporation and that of SnO_2 by sputtering. CuO nanowires were synthesized by thermal oxidation of Cu foil and isolated nanowires samples were prepared by dielectrophoresis method. ZnO nanowires were synthesized by hydrothermal method in which ZnO nanoparticles, prepared by chemical route, were used as a seed layer. CuO: ZnO and CuO: WO_3 p-n junctions were obtained in two steps. Firstly, Cu was thermally evaporated onto ZnO NWs and WO_3 thin films and secondly these samples were annealed in oxygen environment at 400°C to convert Cu to CuO. Fe_3O_4:SnO_2 sensors were fabricated bye-beam evaporation of Fe onto SnO_2 thin film followed by their oxidation. The method of preparing Schottky barrier type sensors by sputtering Au onto ZnO NWs and WO_3 thin films is also described in details. An overview of various characterization techniques, such as Scanning electron microscopy (SEM), X-ray photoelectron spectroscopy (XPS), UV-Vis spectroscopy (UV-Vis), Kelvin Probe microscopy (KPM), Photoluminescence (PL), Impedance spectroscopy (IS) etc are discussed. The details of gas sensing setup and Kelvin probe studies are presented.

Chapter 3: p-type and n-type chemiresistive sensors

This chapter deals with the detailed studies on the gas sensing properties of p-type CuO- thin films, NWs and n-type ZnO- nanoparticles, nanowires and SnO_2- thin films. The obtained results are:

1. The room temeprature sensing characteristics of CuO thin films for various gases was investigated. It was found that CuO thin films are highly sensitive towards H_2S. The H_2S response of CuO films could be divided in to three regions: (a)

low concentration (100–400 ppb), (b) intermediate concentration (500 ppb to 50 ppm), and (c) high concentration (>50 ppm) and gas sensing mechanism for each was proposed. Gas sensing properties of CuO NWs prepared by thermal oxidation was studied in 2 configurations (a) Isolated NW and (b) CuO NWs film. The isloated CuO NWs exhibited the better gas sensing properties.

2. The p-type ZnO nanoparticles and n-type nanowires were synthesized by simple chemical process. the response curves measured for nanoparticles-films and nanowires-films, respectively, exhibit a p- and n-type responses towards both reducing and oxidizing gases. Importantly, nanowires detected H_2S in ppm range with fast response and recovery times. The n-type behavior of nanowires-films is attributed to oxygen vacancies, whereas the p-type nature of nanoparticles-films is attributed to the zinc vacancy, surface acceptor levels created by the adsorbed oxygen and/or the unintentional carbon doping in ZnO.
3. H_2S sensing properties of SnO_2 films prepared by thermally evaporated and RF sputtering method were investigated and compared. A maximum response of 15 and 54 towards 10 ppm of H_2S were obtained for thermally evaporated and sputtered films at an operating temperature of 250 and 150°C, respectively. For thermally evaporated films the sensors response was found to saturate for concentrations above 100 ppm while sputtered films exhibited a linear response in the wide concentration range from 500 ppb to 500 ppm. Response kinetics for sputtered films improved which was attributed to the presence of bridging oxygen vacancies that facilitates the charge transfer between the sensor surface and the H_2S molecules.

Chapter 4: p-n junctions type chemiresistive sensors

This chapter describes the gas sensing properties of p-n junction type sensors.

1. The random ZnO nanowires networks were modified with ultrathin films of CuO. A nominal CuO thickness of 10 nm yield highly selective and sensitive H_2S sensors. The sensitivity of these sensors varied linearly in the concentration range of 0.5-10 ppm. The photoluminescence studies show that CuO aggregates form p-n junctions with ZnO-nanowires. A sensing mechanism based on the destruction of p-n junctions due to the formation of metallic CuS (product of chemical reaction between CuO and H_2S) has been proposed. The impedance studies were successfully employed to separate out the contribution of each element of a complex sensor device.
2. RF sputtered WO_3 thin films were altered by addition of a layer of CuO. CuO modified sample containing 2.25 at.% of Cu in the WO_3 host matrix exhibited a sensor response of 534 towards 10 ppm of H_2S at an operating temperature of 300◦C. The enhanced response and the high specificity are attributed to the formation of random nano p–n junction between p-type CuO and n-type WO_3
3. The faster response kinetics was achieved for SnO_2 films after putting Fe as an additive. SnO_2 films modified with 0.64 at.% Fe exhibited a sensor response of 14.5 at 225°C towards 10 ppm of H_2S with response and recovery time of 90 and 98s, respectively. An improved response has been attributed to the interaction of H_2S with adsorbed oxygen species and Fe (forming low band gap FeS). XPS studies were used to propose the sensing mechanism based on the interaction between p-type Fe_3O_4 and n-type SnO_2

Chapter 5: Schottky barrier type chemiresistive sensors

This chapter deals with the gas sensing properties of Schottky barrier type sensors.

1. ZnO nanowires grown on Si/SiO_2 using hydrothermal technique were modified by Au using RF sputtering. A room temperature H_2S sensing with a 16-fold increase in sensor response over pure ZnO nanowires towards 5 ppm H_2S was demonstrated. The room temperature sensing was achievable due to the formation of nano-Schottky type junction barriers at ZnO-Au interface. The gas sensing mechanism was corroborated with Kelvin probe studies of pure and modified ZnO nanowires before and after gas exposure. Both pure and Au modified sensor films detected ethanol with a maximum sensitivity at an operating temperature of 325°C. The sensor films exhibited a linear dependence of sensitivity between concentrations from 5 to 100 ppm. The Au modified sensor responded towards ethanol concentrations as low as 5 ppm with sensitivity of S = 1.33. Modification with Au resulted in the improved response kinetics: response and recovery times of 5 and 20 s towards 50 ppm of ethanol.
2. We deposited pure and Au incorporated WO_3 sensor thin films using a simple technique of vacuum deposition. Effect of operating temperature, gas concentration, and Au loading has been explored and correlated with the observed sensitivity values to determine the optimum condition for improved sensing performance. The sensor film containing 1 at. % of Au detected H_2S selectively and sensitively (S~16) at an operating temperature of 250^oC.

Chapter 6: Summary and Conclusions

In this chapter, we summarize the main conclusions of the thesis. The H_2S sensing mechanism of n-type, p-type, p-n junctions and Schottky barriers type sensors are summarized.

LIST OF FIGURES

Fig. 3.5. Schematics and band diagrams showing different stages before and after the CuO films were exposed to H_2S gas of different concentrations. (a) In air (before exposing to H_2S), the grains of CuO films absorb oxygen from air and form surface states. These surface states created by adsorbed oxygen species (O_2^-) allow electrons to be excited from valence band (VB) and induce holes in p-type CuO grains. (b) When low concentrated H_2S gas reaches CuO grains, it reacts with O_2^- and the released electrons recombine with the holes in the VB and, thereby causing an increase in the film resistance. (c) At high concentration, H_2S reacts with the CuO and forms CuS layers at the surface of CuO grains, which enhances the electrical connectivity between the adjacent CuO grains, and hence, decreases the film resistance.

Fig. 3.6. (a) Cu $2p_{3/2}$ and (b) S 2p XPS spectra recorded for CuO films before and after 400 ppm exposure to H_2S.

Fig. 3.7. SEM images of CuO nanowires grown by annealing Copper foils at temperatures of: (a) 650°C, (b) 675°C (c) 700°C and (d) 750 °C for 15 mins.

Fig. 3.8. (a) TEM image of branching in a single CuO nanowire (b) SAD pattern corresponding to the [101] zone axis.

Fig. 3.9. (a) XPS spectra of nanowires in Cu 2p region showing formation of CuO (b) Curve a shows optical absorption spectra of nanowires and curve b shows plot of $(\alpha E)^2$ versus energy for determination of band gap.

Fig. 3.10. (a) H_2S and (b) NO gas sensing characteristics at room temperature for CuO nanowire films.

Fig. 3.11. SEM of a sample with isolated CuO nanowires

Fig. 3.12. Room temperature gas sensing characteristics of isolated CuO nanowires on exposure to: (a) H_2S and (b) NO.

Fig. 3.23. (a) Response of a typical nanowire-film on exposure to 30 ppm of H_2S gas as a function of temperature and (b) the corresponding response and recovery times. (c) Response curves of ZnO- nanowire film towards different concentrations of H_2S at an optimum operating temperature of 350°C and (d) corresponding concentration dependence of sensor response.

Fig. 3.24. (a) Selectivity histogram of ZnO nanowire-film towards 30 ppm of different gases (except Cl_2 at 5 ppm) and (b) sensors response curve towards 5 ppm of Cl_2.

Fig. 3.25. Response curves of ZnO nanoparticles-film towards 10 ppm of H_2S and Cl_2 gases at an operating temperature of 350°C.

Fig. 3.26. 2-D work function map of ZnO (a) nanoparticles-films and (b) nanowires-films on indium tin oxide (ITO) substrate.

Fig. 4.1. (a) Measured Cu (at.%) in the CuO (d nm):ZnO- nanowires random networks as a function of the nominal thickness (d) of the CuO. SEM image of (b) ZnO- nanowires and (c) CuO (100 nm):ZnO- nanowires random networks.

Fig. 4.2. XRD patterns recorded for (a) ZnO-nanowires and (b) CuO (10nm): ZnO-nanowires random networks.

Fig. 4.3. XPS spectra recorded for pure ZnO nanowires network for (a) Zn 2p and (b) O 1s.

Fig. 4.4. XPS spectra recorded for CuO modified ZnO nanowires: (a) Zn 2p, (b) O1s and (c) Cu 2p.

Fig. 4.5. (a) Room temperature PL spectra recorded for ZnO-nanowires and CuO (10nm):ZnO-nanowires random networks. (b) Schematic representation of the formation of p-n junction between CuO and ZnO and quenching of near-band edge emission of ZnO due to dissociation of excitons.

Fig. 4.6. (a) UV-vis absorbtion spectra of pure and CuO modified ZnO nanowires network and (b) plot of $(\alpha E)^2$ vs. E for pure and CuO modified ZnO nanowires network.

Fig. 4.7. Variation of room temperature electrical resistance of CuO (d nm):ZnO-nanowires random networks as a function of the nominal thickness (d) of the CuO. The Y-axis variation shows the range of resistance measured for different samples of same nominal thickness of CuO

Fig. 4.8. Schematic representation of the equivalent electrical circuit of different CuO: ZnO-nanowires random networks.

Fig. 4.9. (a) Variation of the sensitivity (for 5 ppm H_2S) as a function of operating temperature for ZnO-nanowires, CuO (10nm): ZnO-nanowiresand CuO (100nm): ZnO-nanowires random networks. (b) The histogram showing the sensitivity (measured for 5 ppm at the optimum operating temperature) for different gases.

Fig. 4.10. Response curves as a function of H_2S concentration for (a) ZnO-nanowires (inset shows the magnified version of the response curve at 0.5 ppm) measured at 300°C, (b) CuO(10nm):ZnO-nanowires measured at 200°C and (c) CuO (100nm):ZnO-nanowires sensors measured at 350°C. (d) Variation of the sensitivity as a function of H_2S concentration. Inset shows enlarged view for CuO (100nm): ZnO-nanowires sensor.

Fig. 4.11. Schematic showing an energy band diagram, indicating a change in potential barrier n-ZnO/p-CuO/n-ZnO (in air) to n-ZnO/metallic CuS/n-ZnO (on exposing to H_2S) and vice versa.

Fig.4.12. (a) Schematic representation of the effective band bending between ZnO-nanowires network and, ZnO and Au electrode interface, (b) representation of the same in an equivalent circuit format.

Fig. 4.13. Room temperature Nyquist plot of pure and CuO (10 nm): ZnO nanowires films.

LIST OF TABLES

Chapter 1

Introduction

1.1 Introduction to gas sensors

1.1.1 Need of gas sensors

During the past few decades, tremendous industrialization has taken place all over the globe to improve the quality of human life. However, the darker side of the industrialization is the use and/or emission of toxic/flammable/erosive gases that keep the human life at risk, which demands detection and monitoring for these toxic during the indusial processes as well as in the environment. Some of these gases include hydrocarbons (for the exploration of oil fields), oxygen (for breathable atmospheres and combustion processes e.g. in boilers and internal combustion engines) and various other gaseous chemicals (for medical applications, manufacturing of different chemicals etc.). Wherever these gases are used, there exists a risk of their leakage and therefore a risk to the health of human beings working in the proximity. Thus it becomes essential to develop gas sensors that can detect and quantify the presence of toxic gases in the environment so that appropriate steps can be followed to control it. Thus there is a huge demand for the monitoring of useful as well as hazardous/toxic gases. Table-1.1 [1] shows exposure limit (short term and long term) data and the possible sources for some of the common toxic gases, such as, H_2S, NH_3, Cl_2 etc. The common sources for toxic gases include mines, industries, heavy water plants, automobiles, research labs etc. All these fields require human intervention and therefore safety of the environment and workers becomes a key issue. It may be seen that most of these gases must be detected at parts per million (ppm) levels in the ambient. A brief description of various common toxic gases is presented below.

Hydrogen disulphide (H_2S): It is highly toxic, heavier than air and flammable gas. It is very commonly dealt with in sewage treatment and petrochemical industries. It is considered as a broad spectrum poison i.e. affecting several systems in the body, nervous system being most affected. Since H_2S occurs naturally inside body, there exist enzymes which are able to detoxify small amounts. But beyond threshold values (Table 1.1), it hinders with cellular respiration. The immediate or short term exposure effects irritation, dizziness, headache, cough and shortness of breath. Long term exposures may lead to loss of appetite and memory loss. Short term, high level exposure may lead to death.

Table 1.1 Exposure limits and sources of various toxic gases.

Gas/ Vapor	**Long-Term Exposure Limit, 8 hr (ppm)**	**Short-Term Exposure Limit, 10 min(ppm)**	**Sources**
H_2S	10	15	Mines, Industries, Heavy Water Plants
CO	50	300	Household Appliances, Automobiles
NO_X	3	5	Automobiles, electric utilities
SO_2	2	5	Fossil Fuel Combustion, Volcano
CH_3OH	200	250	air
Cl_2	0.5	1	Industry, sewage treatment
NH_3	25	35	fertilizers

Carbon monoxide (CO): It is mainly produced by the incomplete oxidation of organic matter. The common sources of CO are gas stoves in homes, vehicle exhaust emissions, burning of fossil fuels and also burning of wood, trash, paraffin etc. It is fatal as it has a tendency to combine with hemoglobin to form carboxyhemoglobin, which fail to carry oxygen to other body tissues. A level of 50% carboxyhemoglobin may lead to coma, seizure, fatality. The common symptoms of CO exposure are headache, nausea, vomiting, and disorientation.

Nitrogen oxides (NO_x): NO_x are found in power plant emissions, nitrogen fixing plants and during combustion of natural gas and nitrogen. Nitrogen oxides damage forest ecosystem by direct impact on leaves, it speeds up the withering of monuments, acidifies surface water and hence affects aquatic biodiversity. NO_x forms fine particles (diameter < 2.5 μm) in the atmosphere which increases respiratory and cardiovascular problems in humans. Immediate effects of short term exposure include coughing, difficulty in breathing and chest pain.

Sulfur dioxide (SO_2): Sulfur dioxide is a product of combustion from coal and other fuel burning; therefore major sources of SO_2 include oil refineries, power plants and automobiles. Short term exposure leads to skin, throat and eye irritation and can also induce asthmatic attack. Long term exposure effects include airways dysfunction, testicular damage, and tumor. Chronic exposure of SO_2 may lead to death.

Methanol (CH_3OH): It is a toxic alcohol that is used industrially as a solvent, pesticide and alternate fuel source. It also occurs naturally in humans, animals and plants. Methanol is poisonous to the central nervous system and may cause blindness, coma and death.

Chlorine (Cl_2): Chlorine reacts with water, inside and out of body to form hydrochloric and hypochlorous acid, both of which are extremely poisonous. Short term exposures lead to breathing difficulty, throat swelling, abdominal pain, low blood pressure and necrosis. Long term exposure to Cl_2 leads to severe change in acid levels of blood, loss of vision, collapse and water filling lungs.

Ammonia (NH_3): The main sources of ammonia are natural: decaying of organic matter and excreta of humans and animals. Man made sources such as fertilizer and petrochemical industries are limited. Ammonia mainly effects the environment by leaching the water bodies if used in excess and affecting the aquatic organisms. It plays a role in transportation and enhanced deposition of acidic pollutants. Exposure to high concentrations can cause irritation of eye, nose, throat and burning of skin in humans.

1.1.2 Types of gas sensors

In order to monitor different gases, varieties of sensors have been developed and many of them are available commercially. In essence, a sensor converts the gas concentration into a measurable signal e.g. electrical, mass, optical etc., which is later amplified and measured. Table 1.2 [2,3,4,5,6,7] summarizes different types of sensors along with their detection principles. The sensors, depending upon the nature of signals, are broadly classified into three types: solid state sensors, mass sensitive sensors and optical sensors. Solid state sensors are further classified into chemiresisitive, chemiresistive field effect transistors (chemFET), calorimetric, potentiometric and amperometric in which properties respectively, conductance, current, temperature, potential difference and diffusion limited current changes are measured as a function of gas concentration. In general, gas sensor should be able to fulfill certain requirements like high sensitivity, selectivity, accuracy of measurement, reproducibility over a period of time, possibility of integration and miniaturization, fast response/recovery times and economic.

Table 1.2 Types of gas sensors and their detecting principles.

Sensor type	**Gas Sensor**	**Detection Principle**
Solid State Sensors	Chemiresistive	A change in conductivity of semiconductor is measured when it interacts with the analyzing gas.
	Chemical field effect transistors (ChemFET)	Current –Voltage (I-V) curves of a field effect transistor (FET) are sensitive to a gas when it interacts with gate.
	Calorimetric	The concentration of combustible gas is measured by detecting the temperature rise resulting from the oxidation process on a catalytic element.
	Potentiometric	The signal is measured as the potential difference (voltage) between the working electrode and the reference electrode. The working electrode's potential must depend on the concentration of the analyte in the gas phase.
	Amperometric	Diffusion limited current of an ionic conductor is proportional to the gas concentration.
Mass Sensitive Sensors	Acoustic	Change in frequency of surface-acoustic waves (SAW) excited on a quartz or piezoelectric substrate upon ad- or absorption of gas in a suitable sorption layer (e.g. metals, polymers).
	Microelectromechanical systems (MEMs) based sensors	Change in mechanical bending of micro- or nanocantilevers upon adsorption of gas.
Optical Sensors	Surface Plasmon Resonance (SPR)	Change in SPR signals is proportional to the refractive index close to the sensor surface and, is therefore, related to the amount of bound gas molecules.
	Optodes	The change of optical properties measured can base on absorbance, reflectance, luminescence, light polarization, Raman and others.

Among various gas sensors, semiconductor-based chemiresistor sensors are most investigated and widely used for detection of combustible and toxic gases owing to their low cost, high sensitivity to a range of gases, operating speeds, small sizes and relative simplicity. Historically, chemiresistive sensors based onsemiconducting metal-oxides (ZnO thin films)were demonstrated for the first time in 1962 when it was shown that their conductivity is sensitive to the traces of reactive gases present in the air [8]. In the same year, similar properties were reported for SnO_2, with an additional advantage of a greater stability [9]. Subsequently, various oxides, such as, semiconducting oxides (SnO_2, ZnO, WO_3, In_2O_3), catalytic oxides (V_2O_5, MoO_3, CuO, NiO) and mixed oxides ($LaFeO_3$, $ZnFe_2O_4$, $BaTiO_3$ and $Cd_2Sb_2O_{6.8}$) have been studied for gas sensing properties and, many more new oxides are currently being explored. However, most of the gas-sensing studies are based on empirical methods, though there have been some good scientific publications dedicated to the understanding of the gas sensing mechanisms. Nevertheless, metal-oxides based gas sensors are a commercial success and, for a host of gases, are easily available in the market for last 25 years.

1.2 Chemiresistive gas sensors

1.2.1 Basic characteristics

In principle, gas sensors are constructed by combining two key functions, i.e., a function to recognize gas molecules (receptor) and another to transduce the recognition into signal output. Therefore the factors governing the gas sensing parameters are:

a. *Receptor function* concerns the ability of the oxide surface to interact with the target gas. Chemical properties of the surface oxygen of the oxide itself is responsible for this function in a neat oxide device, but this function can be largely modified to induce a large change in sensitivity when an additive (noble metals, acidic or basic oxides) is loaded on the oxide surface.

b. *Transducer function* concerns the ability to convert the signal caused by chemical interaction of the oxide surface (work function change) into electrical signal. Metal-oxides often have granular morphology. Therefore, the transducer function is played by each boundary between grains, to which a double-Schottky barrier model can be applied. The resistance depends on the barrier height as well as on the concentration of the target gas. This situation is essentially unchanged with a change in the grain size (diameter, D) of the oxide unless D is kept above a critical value (D_c) which is just equal to twice the thickness of surface space charge layer (L_s) of the oxide. For D smaller than D_c, sensitivity increases sharply with decreasing D. Since usually L_s is a function of the concentration of electron donors in the bulk oxide, D_c can be changed by doping the base oxide with foreign additives. When the oxide is loaded with a foreign additive, the additive can modify L_s and barrier height if it interacts electronically with the oxide. In fact sucha change in L_s or barrier height explains marked sensitizing effects of certain noble metals like Pd or Pt [10] for the sensors of this type.

c. *Utility factor* concerns the accessibility of inner oxide grains to the target gas. The importance of this factor is made obvious when one considers that the target gas (reducing gas) reacts with the oxide surface on the way of diffusing into the balk of device. If the rate of reaction is too large compared with that of diffusion, the gas molecules cannot access the grains located at inner sites, leaving them un-utilized for gas sensing and thus resulting in a loss in sensor response. So, utility factor can be described as the ratio of actual sensor response to the hypothetical sensor response when all the grains are assumed to be accessible to the test gas molecules.

The electrical resistance of a chemiresistive sensor changes drastically (increase or decrease) as a result of chemical reactions occurring at their surface with the molecules of test gas. Increase or decrease in resistance depends on the nature of sensor material (n-type or p-type) and the gas (reducing or oxidizing). A typical response curve, that is, variation of resistance of sensor with time on exposure and withdrawal of test gas, is schematically depicted in Fig. 1.1. The response curve of a sensor is characterized by five parameters: (i) Sensitivity, (ii) Response time, (iii) Recovery time, (iv) Selectivity and (v) Long term stability. These parameters are discussed below.

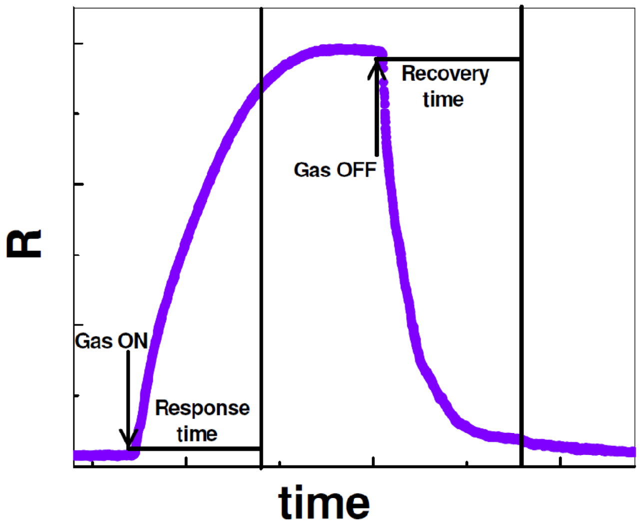

Fig.1.1. Schematic representation of a typical response curve of a chemiresistive sensor.

Sensitivity: The sensitivity (S) of a sensor can be defined by many ways. The often used definitions of S are the following.

(a) A ratio of resistance in ambient air to that in test gases i.e. $S = \frac{R_{air}}{R_{gas}}$, and $S = \frac{R_{gas}}{R_{air}}$ for reducing and oxidizing gas respectively, higher the values of S, better is the material as a gas sensor.

(b) $S(\%) = 100 \times (\frac{R_{air} - R_{gas}}{R_{air}})$. A positive value of S implies film resistance decreases on gas exposure and vice versa.

Response time: The response time is the time interval over which resistance attains a fixed percentage (usually 90%) of final value when the sensor is exposed to full-scale concentration of the gas. It is represented as T90, T80, T50 etc. A T90 of 50 s implies that the sensor exhibits 90% of the saturation value of resistance in 50 s. As the sensor should sense the toxic gas in minimum time, therefore smaller response times are a characteristic of a good sensor.

Recovery time: This is the time interval, usually referred as T10, over which sensor resistance reduces to 10% of the saturation value when the sensor is exposed to full-scale concentration of the gas and then placed in the ambient air. A good sensor should have a small recovery time so that sensor can be used over and over again.

Selectivity: Usually most chemiresistive sensors sense many gases under similar operating conditions. Thus the selectivity or specificity of a sensor towards an analyzing gas is expressed in terms of dimension that compares the concentration of the corresponding interfering gas that produces the same sensor signal. The selectivity can be quantified as:

$$Selectivity = \frac{Sensitivity\ of\ the\ sensor\ for\ interfering\ gas}{Sensitivity\ towards\ the\ target\ gas} \tag{1.1}$$

An ideal sensor should sense only one target gas under particular operating conditions and its sensitivity towards other gases should be negligible.

Long term stability: This is the ability of the sensor to maintain its properties when operated continuously for long durations in hostile environment. The sensor should be such that its basic properties as well as change in those properties on reaction with gas molecules should remain unchanged over a long period of time.

All the above parameters depend on the sensing material, the interaction between the gas and the sensor, the sensor operating conditions etc.

1.2.2 Sensor materials

A vast literature on chemiresistive sensors how that both metal-oxides and non-oxides have been employed as sensing element, which are in the form of bulk pellet, thick films and/or thin films [11]. Here we present an overview of various sensing materials.

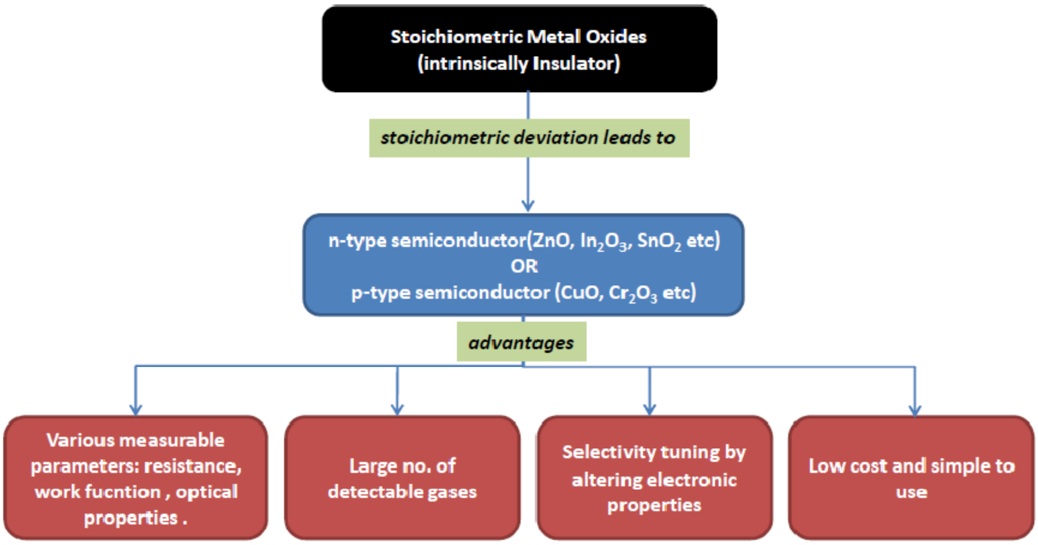

Fig.1.2.Schematic showing the advantages of metal-oxides for use in chemiresistive gas sensors.

(a) Metal oxides

In Fig. 1.2 we schematically show various characteristics’ of metal-oxides that make them suitable for use in chemiresistive gas sensors. The stoichiometric metal-oxides are intrinsically insulators with wide band gaps (~ 2-3 eV) but are very prone to deviation in stoichiometry, leading to the formation of defects [12]. Depending upon the nature of defects, the metal-oxides turn either n-type or p-type semiconductors. The defects introduced in their matrix often vary with the synthesis technique, and therefore, becomes a useful tool for controlling the electronic properties of metal-oxides to tune their selectivity for various gases. The electronic properties of metal-oxides can also be altered by adding suitable additives, and hence making them selective for a particular gas. Another advantage of metal-oxide sensors is that apart from resistance, other parameters, such as, work function (to measure the change in Fermi levels of metal-oxide with additive modifications and/or with gas exposures), optical properties (to measure the energy gap) can be measured, which can assist in making a particular metal-oxide as selective sensor. Also metal-oxides based sensors are low cost, easy to fabricate and simple to use.

As summarized in Table 1.3, metal-oxides can be divided into p-type and n-type semiconductors. It is also seen that sensitive layers are often mixed with additives to make the senor selective to a particular gas. The initial sets of experiments of using the metal-oxide as sensing material were largely based on empirical methods. However, as the interactions between gas molecules and metal-oxide surfaces were investigated and understood [13, 14, 15, 16, 17], the material design for a specific gas became scientific. For practical applications, a gas sensor should fulfill many requirements, which depend on the purposes, locations and conditions of sensor operation [18, 19]. Among the requirements, primarily important would be sensing performance-related (e.g., sensitivity, selectivity and rate of response) and reliability-related (e.g., drift, stability and interfering gases). The key properties, determining the choice of a gas sensor, include: adsorption ability, electronic, electro-physical and chemical properties, catalytic activity, thermodynamic stability, crystallographic structure, interface state, compatibility with materials and technologies to be used in gas sensors fabrication, reliability [20, 21, 22, 23, 24, 25, 26, 27]. In the following we briefly review the sensing characteristics of various metal-oxides.

Table 1.3. Literature review of various metal-oxides used for gas sensors.

Metal oxides	**Additives**	**Analyzing gas**	**Ref.**
p-type semiconductor			
Cr_2O_3	Fe_2O_3	NH_3, H_2S, Cl_2	[28, 29]
Co_3O_4	Fe_3O_4 , SiO_2	Acetone, Toluene, NH_3, CO, CH_4, C_3H_8, H_2, NO_2, Cl_2, H_2S	[30, 31, 32, 33, 34]
CuO	MoO_3, ZnO, SnO_2	NO_2, Glucose, CO, ethanol, H_2S	[35, 36, 37, 38]
n-type semicondutor			
Al_2O_3	Er, Al, SiO_2/Si, ZnO, CeO_2	Aerosol, Humidity, CH_4, NH_3	[39, 40, 41, 42]
Bi_2O_3	Sb_2O_3, WO_3	Smoke, CO, NO	[43, 44, 45]
Fe_2O_3	Au, Zn (Pt, Pd, RuO_2)	Methane, propane, Benzene, Toluene, CO, NO_2, Methanol, Acetone, H_2S	[46, 47, 48, 49]
In_2O_3	Au, Al, SnO_2	O_3, NO_2, H_2, CO, C_3H_8, H_2S, Cl_2, CO_2, SO_2, NH_3, Ethanol, acetone, VOCs	[50, 51, 52]
NiO	ZnO, Li, TiO_x	Triethylamine, H_2, HCHO, CH_4, CH_3COOH, CO, NO_2	[53, 54, 55, 56, 57, 58]
Ta_2O_5	Au	H_2, Humidity	[59, 60]
SnO_2	Pt, Ag, Pd, Os, Fe, Au, In, Ru, Bi_2O_3, CeO_2, CuO	Toluene, Humidity, CO, CH_4, SO_2, N_2O, CO_2, NO_2, CH_3OH, C_2H_5OH, C_3H_8, H_2, LPG, H_2S, NH_3, C_nH_{2n+2}	[61, 62, 63, 64, 65, 66, 67, 68, 69, 70, 71, 72, 73, 74]
WO_3	Mg, Zn, Mo, Re, Au, Pt, C	Acetone, NO_2, NH_3, H_2S	[75, 76, 77, 78, 79, 80]
ZnO	Al, Sn, Cu, Pd, Au, graphene	NH_3, H_2, NO_2, LPG,H_2S, Cl_2, CH_4, CO, H_2S acetone, formaldehyde	[81, 82, 83, 84, 85, 86, 87, 88, 89, 90, 91, 92]

(i) p-type metal-oxide semiconductors

- **Chromium oxide (Cr_2O_3):** Cr_2O_3 adopts the corundum structure, consisting of a hexagonal close packed array of oxide anions with 2/3 of the octahedral holes occupied by chromium. Cr_2O_3 is a p type semiconductor with a band gap of 3.4 eV. Cr_2O_3 is found to be sensitive to H_2S and Cl_2. TiO_2-doped Cr_2O_3 is reported to be sensitive to NO_2, O_2 and humidity. Recently, sensors based on $Cr_{2-x}Ti_xO_3$ (x = 0.05–0.4) has been commercialized by Capteur Sensors.
- **Cobalt Oxide:** Cobalt oxide occurs in two different forms i.e. CoO and Co_3O_4. Both have a cubic lattice. Co_3O_4 is a spinel with Co^{2+} and Co^{3+} ions being simultaneously present but at different lattice sites in the crystal. Co_3O_4 is antiferromagnetic. CoO has an energy band gap of 2.2–2.8 eV, whereas Co_3O_4 has 1.4–1.8 eV. Both cobalt oxides are normally non-stoichiometric with an excess of oxygen, which makes them p-type semiconductors. Co_3O_4 has been found to be sensitive to a range of gases NH_3, CO, CH_4, C_3H_8, NO_2 and Cl_2. Co_3O_4 thin films sense NH_3 even at room temperature.
- **Copper oxide (CuO):** CuO is a p type semiconductor (band gap ~ 1.2-1.8 eV) having monoclinic crystal structure. It has a crystallographic point group of 2/m or C_{2h} and the space group of its unit cell is C2/c with lattice parameters a = 4.6837, b = 3.4226, c = 5.1288. The copper atom is coordinated by 4 oxygen atoms in an approximately square planar configuration. CuO has potential applications in many fields such as high critical- temperature superconductors, photovoltaic materials, field emission, and catalysis. It is known that gas-sensing materials can have either n-,or p-type of conductivity. Semiconductors of n and p-type have inverse direction of conductivity's change at interaction with the same gases, which is very important fact for their application. For materials with p-type

the conductivity rises with oxygen pressure's growth, whereas for n-type oxides it drops. Previous research has shown that, in general, all n-oxides are thermally stable and have possibility to work at lower oxygen partial pressure in comparison with well known p-type oxides. It is known that many p type oxides are relatively unstable because of the tendency to exchange lattice oxygen easily with air. Besides, the interaction with reducing gas decreases the resistance of n-type oxides. This is the preferred direction for sensor's resistance change during detection of reducing gases, contributing to simpler compatibility with peripheral measuring devices, and better reproducibility of output signal. A few studies on gas sensing characteristics of CuO nanopowders, nanoribbons, and nanorods have been reported. In addition, CuO has been widely used in thin-film based H_2S sensors. CuO is mainly used as additives in n-type metal-oxides, which either form a composite or a random network of heterojunctions.

(ii) n-type metal-oxide semiconductors

- **Aluminum Oxide (Al_2O_3):** Aluminium oxide is an electrical insulator with trigonal crystal structure and octahedral coordination geometry. It commonly occurs in its polymorphic phase α-Al_2O_3. It is an excellent sensing material for humidity, apart from other gases, such as, CH_4, NH_3. Humidity sensors are usually made of porous Al_2O_3, which is prepared by electrochemical anodization of aluminium thin films. These humidity sensors, however, were found to saturate on exposure to a very high humidity level as well as after a prolonged exposure. These sensors, however, can be easily regenerated by heating them above 100°C. In addition, nanoporus alumina has been found to be a good room temperature operating ammonia sensors.

- **Bismuth-oxide (Bi_2O_3):** Bi_2O_3 has five crystallographic polymorphs. The room temperature phase α- Bi_2O_3 has a monoclinic crystal structure. The α-phase exhibits p type conductivity at room temperature which transforms to n type between 550°C to 650°C. Bi_2O_3 has been found sensitive to many gases, such as, H_2, CO_2, NO and O_2. Bi_2O_3 is being used as a smoke sensor as smoke mainly consists of CO and CO_2. The negative point of this sensor is that the operating temperature is very high (450°C). It has been observed that by adding Sb_2O_3, the operating temperature of Bi_2O_3 sensor drops down to 200°C. Recently, it has been demonstrated that addition of Fe and Ag lead to stabilization of α-Bi_2O_3 phase, Cu addition leads to α-Bi_2O_3 phase and, In and Ni addition stabilize $Bi_2O_{2.33}$ structure. Among these, $Bi_2O_{2.33}$ structure was found to be highly selective for NO.
- **Cadmium oxide (CdO):** CdO crystallizes into cubic rocksalt lattice like sodium chloride with octahedral cation and anion centers. It is an n type semiconductor with a band gap of 2.18 eV at room temperature. Sensor based on pure CdO has not been reported so far. However, the ethanol sensing properties of $ZnFe_2O_4$ has been found to be drastically improved by adding CdO. This is because, addition of CdO stabilizes $Zn_{0.8}Cd_{0.2}Fe_2O_4$, which adsorbs more oxygen compared to the $ZnFe_2O_4$. The improved characteristics include: (i) High ethanol sensitivity with a linear behavior in the concentration range from 100 to 1000 ppm; (ii) excellent selectivity to ethanol against other common gases which may co-exist with ethanol, such as petrol, H_2, CO, LPG and other hydrocarbon gases; (iii) good stability and durability of the performance; and (iv) almost instant response and recovery behavior.
- **Ceria (CeO_2):** Cerium oxide or Ceria has a fluorite structure containing 8 coordinate Ce^{4+} and 4 coordinate O^{2-}. At high temperatures it can be reduced to a

non-stoichiometric, anion deficient form that retains the fluorite lattice, CeO_{2-x} where $0 < x < 0.28$. In the most stable fluorite phase of ceria, it exhibits several defects depending on partial pressure of oxygen or stress state of the material. The primary defects of concern are oxygen vacancies. CeO_2 has been found to be a good sensor for the oxygen because of its chemical stability and high diffusion coefficient of oxygen vacancies. It has been observed that CeO_2 can be easily reduced into a non-stoichiometric compound. Therefore adding CeO_2 (particularly in the form of nanoparticles) with TiO_2 acts as an effective catalyst for the oxygen sensitivity of TiO_2. Doping SnO_2 by CeO_2 was found to be sensitive to H_2S at room temperature.

- **Iron oxide:** In Fe-O system, three different polymorphic forms, FeO, Fe_3O_4, and Fe_2O_3 exist. Also, Fe_2O_3 has two typical modifications: α-Fe_2O_3 (hematite, corundum-type hexagonal lattice, a = 5.035Å and c = 13.750 Å) and γ-Fe_2O_3 (maghaemite). α-Fe_2O_3 has a complex defect structure in which three type's defects species, namely, oxygen vacancies, Fe^{3+}interstitials and Fe^{2+}interstitials are present. The presence of theses defects give rise to semiconducting properties. Loss of oxygen leaves behind extra electrons and produces an n-type semiconductor; while extra oxygen (entering the lattice as O_2) creates a deficit of electrons (i.e. introduces electronic holes), which produces p-type behavior. Thus, in α-Fe_2O_3 a transition from n- to p-type response or vice versa can be induced by the change in the gas concentration, by appropriate dopant and/or by the operating temperature. Nanocrystalline Fe_2O_3 thin films exhibit n type response towards H_2S at 250°C.$Fe_2O_3$is known to show high sensitivity towards organic gases. Various metal oxides have been doped into Fe_2O_3 to make it selective for a particular gas. It has been demonstrated that ZnO doped Fe_2O_3 works as a selective NH_3 sensor working at room temperature. When doped with Pt, Pd or RuO_2, Fe_2O_3 sensor detects acetone, which finds utility in medical diagnostics. Au or Zn doped Fe_2O_3 is reported to sense CO and NO_2 [56]. γ -Fe_2O_3 is known to be a good sensing element for H_2.

- **Indium Oxide (In_2O_3):** The crystalline form of In_2O_3 (n type semiconductor) exist in two phases, the cubic (bixbyite type) and rhombohedral (corundum type). Both phases have a band gap of about 3 eV. In_2O_3 is found to be very suitable for detection of low concentrations of oxidizing gases like O_3 and NO_2. It has been observed that MoO_3 doping significantly enhances selectivity of In_2O_3 for NO_2. However, there are reports of gas sensing to other toxic gases, such as, H_2S, Cl_2, NH_3.
- **Nickel oxide (NiO):** NiO is a p-type semiconductor with a wide band gap of 4.2 eV. NiO finds a wide range of applications due to its good chemical stability as well as excellent optical and electrical properties. NiO is being considered as one of the promising potential electrode materials for super capacitors as well as for many other applications such as catalyst, electrochromic films, p-type transparent film and fuel cell electrodes. Recent works have shown that NiO is also an attractive functional gas-sensing layer for application both in thermoelectric and chemiresistive-type gas sensors. A novel thermoelectric hydrogen gas sensor using NiO film as a thermoelectric material and Pt film as a catalyst have been proposed in the literature.
- **Tantalum oxide (Ta_2O_5):** Ta_2O_5 is known to exist in two forms, low temperature form, known as L- or β-Ta_2O_5, and the high temperature form known as H- or α-Ta_2O_5. The transition between these two forms is slow and reversible; taking place between 1000-1360°C, with a mixture of structures existing at intermediate

temperatures. The overall crystal structure is orthorhombic in both the cases. Ta_2O_5 is an insulator and its band gap has variously been reported as being between 3.8 to 5.3 eV. Ta_2O_5 is not a popular material for gas sensors. However, Ta_2O_5 is reported to be a good humidity sensor. Interestingly it has been observed that by using an overlayer of Ta_2O_5 improves significantly the sensitivity and response time of $In_xO_yN_z$ films to CO, H_2, and CH_4. Thus there is a need to investigate the role of Ta_2O_5 as a promoter in gas sensors.

- **Tin dioxide (SnO_2):** SnO_2 crystallizes with the rutile structure (space group $P4_2/mnm$) with lattice parameters $a = 4.737$ Å, $c = 3.185$ Å, wherein the tin atoms are six coordinate and the oxygen atoms three coordinate. There are two formula units per primitive unit cell with the threefold-coordinated oxygen atoms forming distorted octahedral configurations around the Sn atoms. SnO_2, an n-type wide band semiconductor ($E_g = 3.6$ eV at 300 K), is favorably used due to its superior stability, sensitivity, and low cost. SnO_2 is the most widely used materials for detection of various gases. The unique conductance property and the ability to tailor the stoichiometry have been used effectively to realize sensors. The characteristics of SnO_2 containing cations with mixed valences and adjustable oxygen deficiency enables tuning of its structure and properties. Besides, it can be easily synthesized into conventional (pellets, thick and thin films) as well as novel nano forms (nanoparticles and nanowires). Gas sensors made from SnO_2 have the desirable property that their resistance depends strongly on the adsorption of certain gases. However, SnO_2 responds to reducing species, e.g. H_2S, H_2, CO, Hydrocarbons etc, as well as to oxidizing gases like NO_x and O_3, making it a highly non-selective material. An interaction with reducing gases leads to decrease in its electrical resistance; while oxidizing gases cause an increase in the resistance. Thus, from the response curve of a SnO_2 sensor it is difficult to distinguish between different gases with the same sign of electrochemical potential. In general, the poor selectivity of metal-oxide gas sensors is a major concern. SnO_2 has been widely modified with additives to improve its selectivity.

- **Tungsten oxide (WO_3):** WO_3 is an n-type semiconductor and shows good response to both NH_3 and NO. These two gases are characterized by opposite resistance changes in the film which makes it possible to detect NH_3 and NO selectively, if only one of the two gases is present in the ambient. Unlike SnO_2, the surface of WO_3 is not sufficiently covered with adsorbed O_2 and requires catalyst or promoters to obtain adequate sensitivity. In the past, several workers have reported WO_3 films doped with different elements including Au, Mo, Mg, Re etc., to selectively detect different toxic gases. Doping of WO_3 thick films with Cu has been shown to enhance NH_3 sensitivity. Surface modifications of WO_3 films with Au and Pt were also found to enhance sensitivity towards NH_3. Thin films of tungsten oxide covered by Pt over layer have been studied for NH_3 detection.
- **Zinc oxide (ZnO):** ZnO is a key technological material. ZnO is a direct wide bandgap (3.4 eV) semiconductor of II-IV semiconductor group that is suitable for short wavelength optoelectronic applications. ZnO crystallizes into two main forms, hexagonal wurtzite and cubic zinc blende. The wurtzite structure is most stable at ambient conditions and hence most common. The high exciton binding energy (60 meV) on ZnO crystal ensures efficient excitonic emission at room temperature and room temperature ultraviolet (UV) luminescence has been reported in disordered nanoparticles and thin films. ZnO is transparent to visible light and can be made highly conductive by doping. The high electron mobility,

high thermal conductivity, wide and direct band gap and large exciton binding energy make ZnO suitable for a wide range of devices, including transparent thin-film transistors, photodetectors, light-emitting diodes and laser diodes that operate in the blue and ultraviolet region of the spectrum ZnO is a versatile functional material that has a diverse group of growth morphologies, such as nanocombs, nanorings, nanohelixes/nanosprings,nanobelts, nanowires and nanocages. Nonstoichiometry is typically the origin of n-type character in ZnO. Out of various native defects (Zn vacancy, O vacancy, Zn interstitial etc) oxygen vacancies have the least formation energy and act as donor states responsible for n-type ZnO. Wurtzite zinc oxide has a hexagonal structure (space group *C*6*mc*) with lattice parameters $a = 0.3296$ and $c = 0.520\ 65$ nm. The structure of ZnO can be simply described as a number of alternating planes composed of tetrahedrally coordinated $O^{2-}$and Zn^{2+} ions, stacked alternately along the *c*-axis. The tetrahedral coordination in ZnO results in noncentral symmetric structure and consequently piezoelectricity and pyroelectricity. ZnO is a remarkable material with a wide variety of optical, electrical and piezoelectric applications. As discussed in the Introduction, ZnO is the first metal-oxide gas sensing material, and has been investigated widely. It is sensitive to many gases, such as, trimethylamine, hydrogen, oxygen, ethanol and NH_3 at moderate temperature, with good stability. A NH_3 selective sensor working at room temperature is reported when Fe_2O_3 is doped in ZnO. In recent studies, nanostructured ZnO in the form of wires, tapes, particles, etc. have been found to exhibit improved sensitivity to different gases owing to a larger surface to volume ratio.

(b) Non-oxides

Apart from several metal-oxides, several non-oxides, as listed in Table 1.4, have been used as chemiresistive sensors. These are semiconductors (e.g. Te, CuBr), porous-silicon, carbon nanotubes, and polymers, and a brief overview on these materials is discussed below.

- **Tellurium**: Tellurium (Te) is an elemental semiconductor and shows p-type conduction. The use of tellurium thin films for room temperature detection of NO_2**.** Recently, the gas sensing characteristics of Te films for various gases, such as, H_2S, NH_3, CO and NO_2 have been extensively studied. Te film resistance increases reversibly on exposure to reducing gases like NH_3, H_2S, etc., while the resistance decreases on exposure to NO_2. The main advantages of Te films based sensors are that they operate at room temperature, show considerably short response times, and have a good relative sensitivity in the ppm concentrations range.

Table 1.4 Literature reviews of various non-oxides used as chemiresistive gas sensors.

Non Oxides	**Analyzing gas**	**References**
Te	H_2S, NH_3, NO_2	[93, 94, 95]
Porous- Si	Humidity, NO_2	[96, 97]
CuBr	NH_3	[98, 99]
Carbon nanotubes	Alcohol, NH_3, CO_2	[100, 101, 102]
Polypyrrole	NH_3	[103]
CoPc	Cl_2	[104, 105]

- **Porous Si:** Recently porous silicon has been explored for chemiresistive sensors. It has been found that porous silicon sensor with Pd nano-structures is suitable for hydrogen sensing in the range of 0–1.5%, and operates at room temperature. The room temperature operable porous-silicon-based NO_2 sensors have also been reported.
- **Copper bromide:** In aqueous solution chemistry, an interactions between copper ions and ammonia molecules is well established, where they lead to the formation of amine complexes, such as $[Cu(NH_3)_2]^+$. Assuming that similar interactions exist at the interface between ammonia molecules and a solid ionic or mixed conductor with mobile Cu+ ions, such as CuBr; then ammonia can have a selective adsorption on CuBr. The specificity of this process has been implemented to develop an ammonia gas sensor operating at room temperature with an improved selectivity in comparison to oxide-based sensors. These sensors also have a fast response owing to the high ionic conductivity.
- **Carbon nanotubes**: Since the discovery by Iijima in 1993 [106], carbon nanotubes (CNT), both single and multi-walled, have become a promising material for a variety of potential applications. Recently, the CNT-based gas sensors have received considerable attention because of their outstanding properties, such as faster response, higher sensitivity, lower operating temperature and a wider variety of detectable gases in comparison with the other types of gas sensors. To date, the CNT-based gas sensors have been employed to detect a variety gases, such as N_2, H_2, NH_3, NO_x, etc. CNT are promising materials for gas sensing because of their high surface areas, provided by their central hollow cores and the outside walls, for gas adsorption as well as their tendency to change their electrical properties at room temperature in the presence of different gases.

However, one limitation of the sensors is slow and deficient recovery. There have been some efforts devoting to overcome this weakness but the results have not been satisfactory. In order to improve the recovery of CNT–based sensors, a detailed understanding of the mechanism of gas adsorption and desorption of the CNT is needed.

- **Polymers*:*** Organic semiconductors, such as, conducting polymers are also being investigated for gas sensing applications. Organic semiconductors have the advantages of easy processing, low cost and room temperature operation. Since the chemical and physical properties of conducting polymers can be tailored at ease for a particular need, they are gaining importance in the fabrication of gas sensors. Conducting polymers have alternate single and double bonds and the structure is stabilized through the resonances that result in the delocalization of electronic states. Polymers can be doped to be n-type (reduced) or p-type (oxidized). The dopant ions are generally introduced into the polymer system during chemical or electrochemical polymerization. The dopant ion influences the distribution of positive charge on the polymer backbone and, can cause formation of electronic states within the band gap. The small lattice distortions, which occur locally, induce charge inequalities in the polymer backbone. The net effect is that the oxidation state changes and the equivalent of free radicals are formed. A charged site interacting with a free radical forms a polaron, which is normally highly unstable, but can be stabilized by further oxidation of the polymer to form a bipolaron. Polarons can be cationic or anionic but oxidation removes an electron from the system, forming a dication, which is a spin less defect in the polymer. It is these defects that make conducting polymers interesting for chemical sensing. The first polymer gas sensor reported was polyacetylene. Exposure of this polymer to iodine vapor resulted in 11 orders of magnitude change in conductivity [107]. It may be noted that all polymer based sensors work at room temperature. However, similar to their inorganic counterparts they, too, suffer from specificity. In addition, their response and recovery times are very sluggish. Since the studies and development of polymer-based sensor is an emerging field, improvement in the sensing properties are expected in the near future. Recently flexible polypyrrole nanosheets (thickness 150 nm) have been investigated for NH_3 gas sensing. These sensors exhibited a reversible response towards NH_3 at room temperature with sensitivity of 12% for 50 ppm. Also cobalt phthalocyanine ultrathin (20 nm) films deposited on sapphire substrate acted as selective Cl_2 sensors in ppb range (5-2000 ppb).

1.2.3 Limitations of metal-oxides and strategies to overcome them

In Fig. 1.3, we schematically summarize the rating of different sensing properties as excellent, good and poor, for metal-oxide chemiresistive sensors, which clearly show that in sensitivity and response/recovery time are excellent. However, the selectivity of metal-oxide sensors is poor, and is major issue for investigation. This is also evident from the Table1.3 where metal-oxides sense more than one gases. The issue of selectivity could not be resolved for a particular metal-oxide as the gas sensing mechanism is not fully understood. The sensing mechanism is quite complex as it involves gas-surface interactions, reduction/oxidation of surface, electron transfer of delocalized conduction electrons to localized surface states and vice versa, etc. Another issue with meatl-oxide based chemiresistive sensors is their high operating temperatures for certain gases, which affects their long term stability.

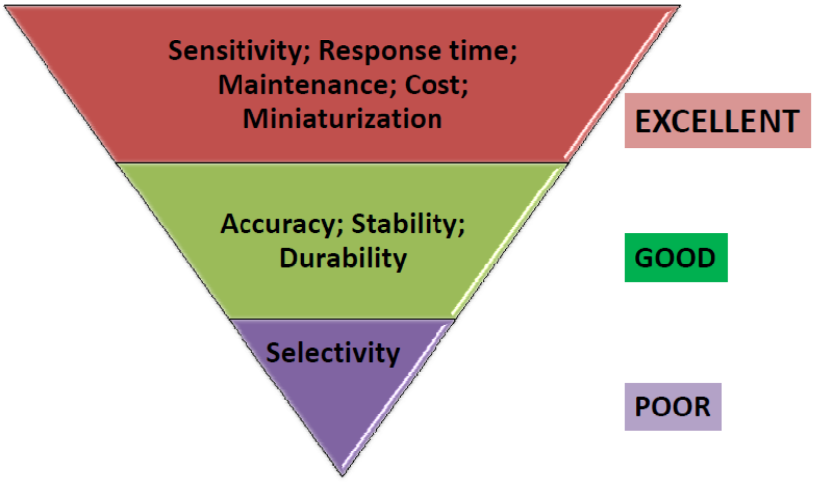

Fig. 1.3. Schematic showing rating of different sensing parameters for metal-oxides based gas sensors.

In literature attempts have been made to improve the selectivity of the metal-oxides by following three strategies:

(i) *By changing the operating temperature*: The chemisorption or redox reaction with the analyte gas at the sensor surface is a function of temperature, therefore selectivity for a particular gas is obtained at a particular temperature. In general, higher operating temperature, yields faster response kinetics but it also affects the long term stability.

(ii) *Use of suitable additives*: The additives such as, Pd, Cu, Au, etc. may improve the selectivity due to different effects, as shown in Fig.1.4.In the *catalytic effect*, demonstrated as Process-I in Fig. 1.4, the metal clusters present at the surface of SnO_2 facilitates the reaction between the reactive gas (R) and the atmospheric oxygen. Therefore, this process has no effect on the resistance of the semiconductor. In *spillover effect* (Process-II), the metallic clusters catalyze reactions and reaction products subsequently spill-over from the clusters onto the metal-oxide support. Catalyst particles on the surface are able to activate certain gas molecules, e.g. dissociation of oxygen or hydrogen. The spill-over effect can accelerate the reaction, resulting in shorter response times and higher sensitivities. A well known example of this effect is the spill-over of hydrogen and oxygen from metal catalyst (Pt) onto the semiconductor support. Since the bonding energy of Pt atoms to the hydrogen or oxygen atoms is not so different from the bonding energy one hydrogen or oxygen atom to the other, only little energy is needed to dissociate hydrogen or oxygen molecules. Consequently, the catalyst reduces the energy normally needed for dissociation to a great extent. The subsequent spill-over onto tin oxide is possible after breaking the rather weak bond between hydrogen and/or oxygen and Pt. In this way catalyst lowers the activation energy needed for the dissociation process and increases the probability of a reaction. In *Fermi energy control* (Process-III**)** the sensor signal is determined by the electronic contact between the semiconductor and the additive, which results in an alignment of Fermi energy of the metal oxide and the additive, leading to the formation of barrier potential. The additive particles becomes partially oxidised in the ambient gas atmosphere and its stoichiometry depends on the composition of the ambient air. The position of the Fermi level of this oxidised additive depends on its composition. So in a way, ambient oxygen is altering the additive and the additive is altering the electron density of the metal-oxide. If the concentration of the additive is high on the surface of metal-oxides as compared to other adsorbates and it is finely dispersed on the surface, the additive controls the barrier potential. The test gas reacts with the metal-oxide via additive and hence the chosen additive strongly changes the selectivity of the chemiresistive sensors.

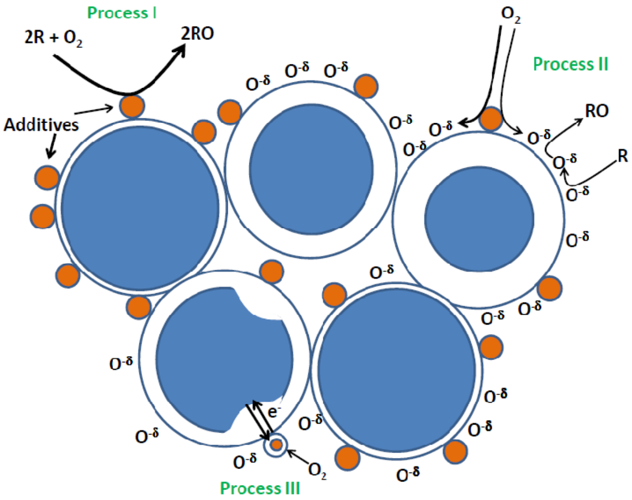

Fig. 1.4. Schematic of three processes occurring at the surface of metal-oxide loaded with additives.

(iii) *Use of appropriate filters*: In this case, an appropriate diffusion filter layer is deposited on the surface of the sensor. By choosing the material of diffusion layer with appropriate porosity, the sensor can be made specific towards test gases having small molecules. Only the filtered molecules are able to reach the surface of the sensing material. This approach suffers from a disadvantage of unavailability of suitable diffusion filters for all the gases.

1.3 Sensing mechanisms of metal-oxide sensors

Gas sensing is predominantly a surface phenomenon wherein gas molecules react with the surface of the metal-oxide sensing layer. The surface of metal-oxide is characterised by the presence of surface states due to deviation in stoichiometry and/or breaking of the translation symmetry at the surface. The ambient oxygen gets chemisorbed through one of these surface states and test gas molecules interact with metal-oxides through these chemisorbed oxygen molecules. All these steps are explained in details in the following sections.

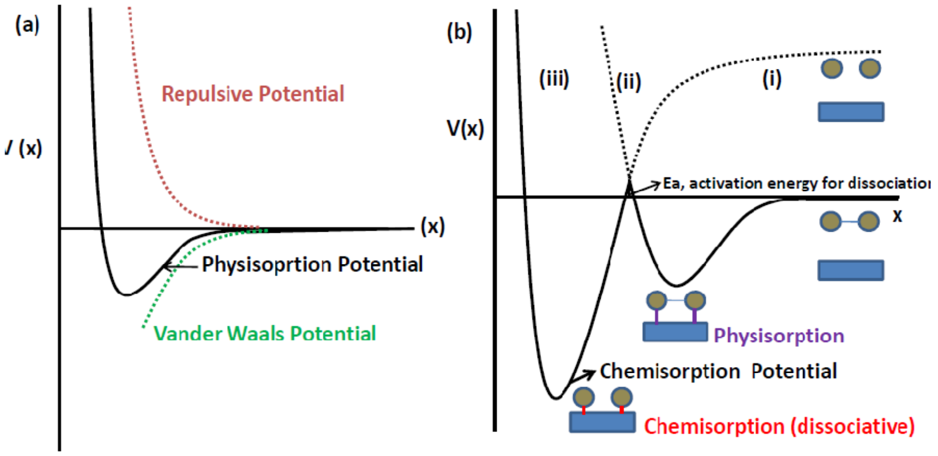

Fig.1.5. Schematic representation of the potential energy curves for: (a) Physisorption and (b) Chemisorption

1.3.1 Adsorption

Adsorption is adhesion of atomic and/or molecular species onto a surface of a solid, which results in creation of a layer of the adsorbate. Adsorption is a surface phenomenon and significantly from the absorption process in which the atomic/molecular species diffuse deep inside the bulk of the solid. Adsorption can be of the following two types:

Physisorption: Physical adsorption generally occurs when the bond energy is less than 10 kcal/mol and Vander Waals forces are responsible for the bonding. Van der Waals forces originate from the interactions between induced, permanent or transient electric dipoles, and therefore, it affects the electron affinity of a semiconductor. Physisorption requires no activation energy and takes place at low temperature (thermal energy at room temperature ~ 26 meV).A physisorbed state is attained by the balance between the above attractive and repulsive forces. A physisorption potential is represented by the sum of the repulsive and attractive Van der Waals contributions as shown in Fig. 1.5 (a).

Chemisorption: Chemisorption is a kind of adsorption which involves a chemical reaction between the surface and the adsorbate. New chemical bonds are generated at the adsorbant surface. Examples include macroscopic phenomena that can be very obvious, like corrosion, and subtler effects associated with heterogeneous catalysis. The strong interaction between the adsorbate and the substrate surface creates new types of electronic bonds. In this case the bond energy is more than 10 kcal/mol and the reaction is specific unlike physisorption and also requires activation energy for occurrence. It affects the surface charge region of the semiconductor. Fig. 1.5 (b) shows the schematic of chemisorption. The total potential energy curve (iii) is the combination of (i) chemisorption potential of two dissociated atoms and (ii) physisorption potential. The potential energy for adsorption is only dependent on distance between molecule and surface. Potential energy is assumed to be independent of angular orientation of molecule, changes in internal bond angles and bond length and position of the molecule along the surface.

1.3.2 Surface state (ss) formation

The periodic pattern of chemical bonds in the crystal is interrupted at the surface, resulting in unsaturated (dangling) bonds, which can rearrange themselves (surface reconstruction) and/or which might be saturated by a (mono) layer of adatoms (sometimes oxygen). This results in a change of both the surface crystal structure and the allowed energies that depend sensitively on the materials and bulk crystal structures involved. Often, the electronic surface structure has little to do with the bulk structure. Also in normal semiconductors there are ~10^{-7}-10^{-8} impurity levels for each atom of the crystal.

The impurity levels, which are intermediate in energy between the filled band and conduction band, represent states in which the electron is localized around a foreign atom or other defect in the crystal lattice. The presence of surface states can affect the adsorption process in several ways. Firstly, there would usually be a band bending before chemisorption starts. The adsorbate may change the surface-state structure by shifting the energy levels of the states and changing their density. Lastly, one has to consider charge exchange between the adsorbate and both the space-charge region and the surface states. There are two types of surface states: (a) Donors that are neutral when occupied and positively charged when unoccupied. (b) Acceptors that are neutral when unoccupied and negatively charged when occupied. The concept of charge transfer at the surface provides simple explanation to the surface dynamic occurring due to the adsorption. The effect of adsorption is reflected in the change of barrier heights at the interface of two species, change in surface conductance and change in work function (Φ). The change in electron affinity (χ) will also come into picture if adsorbed molecules have dipole moments aligned perpendicular to the surface. The schematic, as shown in Fig. 1.6, shows the flat band conditions when there is no net charge transfer from surface state to the host matrix and the equilibrium condition where Fermi level aligns with the surface states (ss) to give rise to band bending due to charge transfer. The band bending can be quantified with the help of Poisson's equation. Let x_d denote the extent of depletion region into the bulk starting from the surface x=0 and N_d is the dopant density (per m^3). All donors are ionized in the depletion region giving a space charge density of $\rho = eN_d$. The Poisson equation for the x-dependence of the potential V (x) within the depletion region $0 \leq x \leq x_d$ is:

$$\frac{d^2V}{dx^2} = \frac{e^2N_d}{\epsilon\epsilon_o} \Rightarrow V(x) = -\frac{e^2N_d}{2\epsilon\epsilon_o}(x - x_d)^2 \tag{1.2}$$

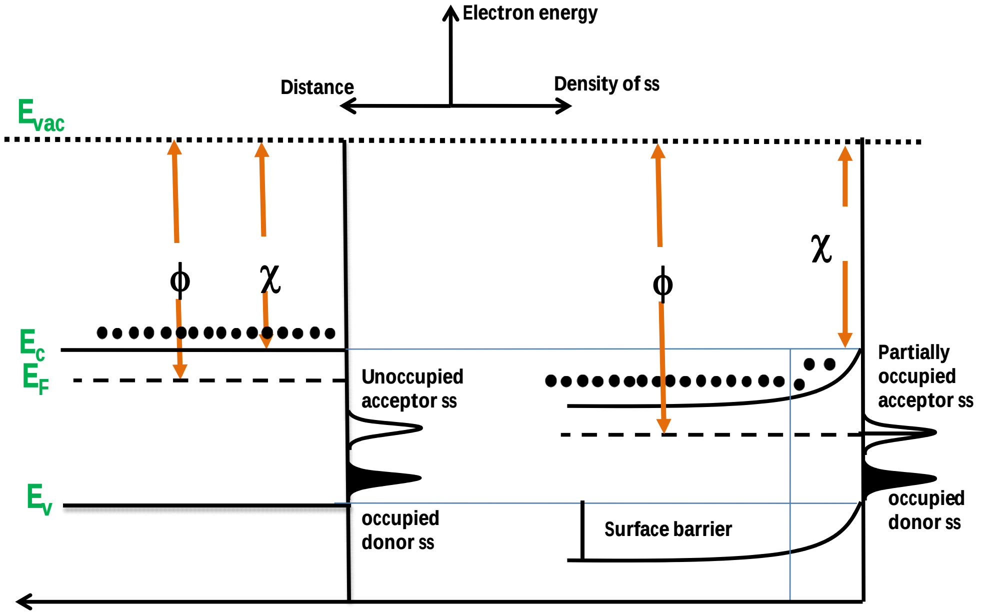

Fig.1.6 Schematic showing the band energy diagram for flat band and equilibrium conditions between surface states (ss) and metal-oxide surface.

where the normalization of V was chosen as V = 0 in the bulk ($x > x_d$) and the constant of integration was chosen to match $V(x_d) = 0$ accordingly. As clear from the equation, the bands bend quadratically, with a total shift of $V(x \rightarrow 0^+) = -\frac{e^2 N_d x_d^2}{2\epsilon\epsilon_o}$. More generally, the local curvature of the band is proportional to the local space charge density.

1.3.3 Oxygen adsorption – n type and p type semiconductor

The atmospheric oxygen gets chemisorbed on the surface of a semiconductor. Due to the electron affinity of oxygen, the electron can be transferred to the chemisorbed oxygen and consequently there will be oxygen ions on the surface and not oxygen atoms. And depending upon the operating temperature, oxygen is adsorbed on the sensor surface in different forms, usually from physisorption to chemisorption as shown below

$$\tfrac{1}{2} O_{2(gas)} \rightarrow \tfrac{1}{2} O_{2(phys)} \rightarrow \tfrac{1}{2} O_2{}^{-}{}_{(chem)} \rightarrow O^{-}{}_{(chem)} \rightarrow O^{2-}{}_{(chem)} \qquad (1.3)$$

The species, ½ $O_{2(phys)}$, ½ $O_2^-{}_{(chem)}$, $O^-{}_{(chem)}$ and $O^{2-}{}_{(chem)}$ exist at temperatures < 200 K, from room temperature (298 K) to around 150°C (423 K), from 150°C (423 K) to 400°C (673 K) and above 400°C (673 K), respectively [12]. These ions are formed due to trapping of electrons by molecular oxygen from the conduction band of the semiconductor. These can be regarded as free oxygen ions which are electro statically stabilised in the vicinity of the surface.

n-type semiconductor: The electrical conductivity and work function is collective physical properties of semiconductors that are changed by an ionosorption process and are accessible to measurement. The simplified picture showing adsorption influence on surface conductivity and work function is as follows. An oxygen molecule is physisorbed at the surface.

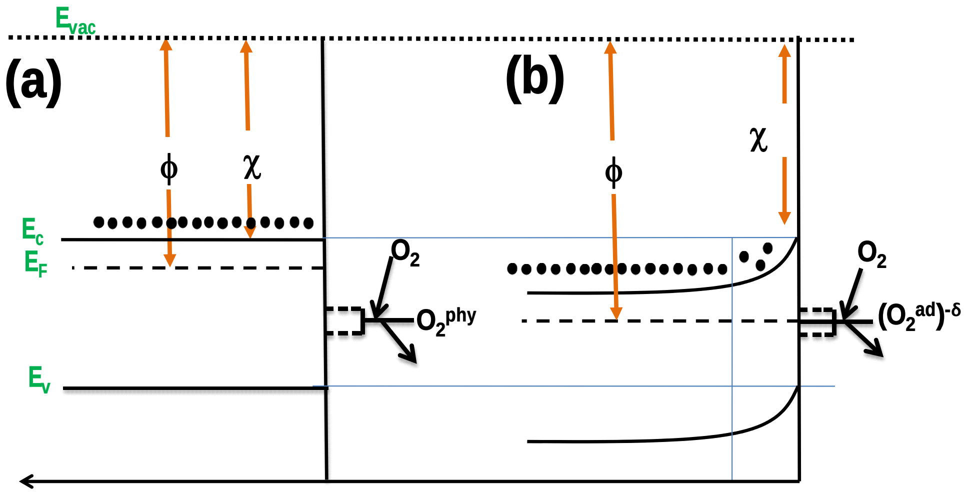

Fig.1.7. Schematic showing the oxygen adsorption process at the n-type metal-oxide semiconductor surface.

In the next step, an electron from the oxide’s conduction band is trapped at the adsorbed oxygen molecule. The adsorbed oxygen molecule and the surface itself become negatively charged. The flow of electrons from the semiconductor into the chemisorbed layer, without any diffusion of ionic species at the same time, induces a space charge between the interior of the semiconductor and its surface. The negative surface charge is compensated by a positive charge in a space-charge layer that forms below it. This positive space-charge layer has a reduced electron density, compared to the bulk, and is called an "electron-depleted layer". The energy band at the surface bends upwards with respect to the Fermi level. This causes the creation of barriers on the surface ($q\Delta Vs > 0$), where q is the elementary charge and V_S is the surface potential by this increasing work function ($\Delta\varphi = q\Delta Vs > 0$) and decreasing surface conductance ($G = G_o \exp(-\frac{q\Delta Vs}{kT})$. The process of charge transfer continues until equilibrium is reached and a steady state is achieved. Fig. 1.7 depicts oxygen adsorption in case of n type metal-oxides.Here we introduce the concept of Debye length, L_D which is defined as the distance over which a local electric field affects the distribution of free charge carriers.

$$L_D = \sqrt{\frac{\in kT}{q^2 N_d}} \tag{1.4}$$

where, ε is the dielectric constant and N_d is the donor concentration. Also it is related to the width of depletion layer as

$$w = L_D \sqrt{\frac{qV_s}{kT}} \tag{1.5}$$

Typical values of depletion layer *w*, are usually 1-100 nm. If the dimension of the crystallites, taking part in the gas sensing, are smaller than the space charge region, a strong change in the conductance is expected.

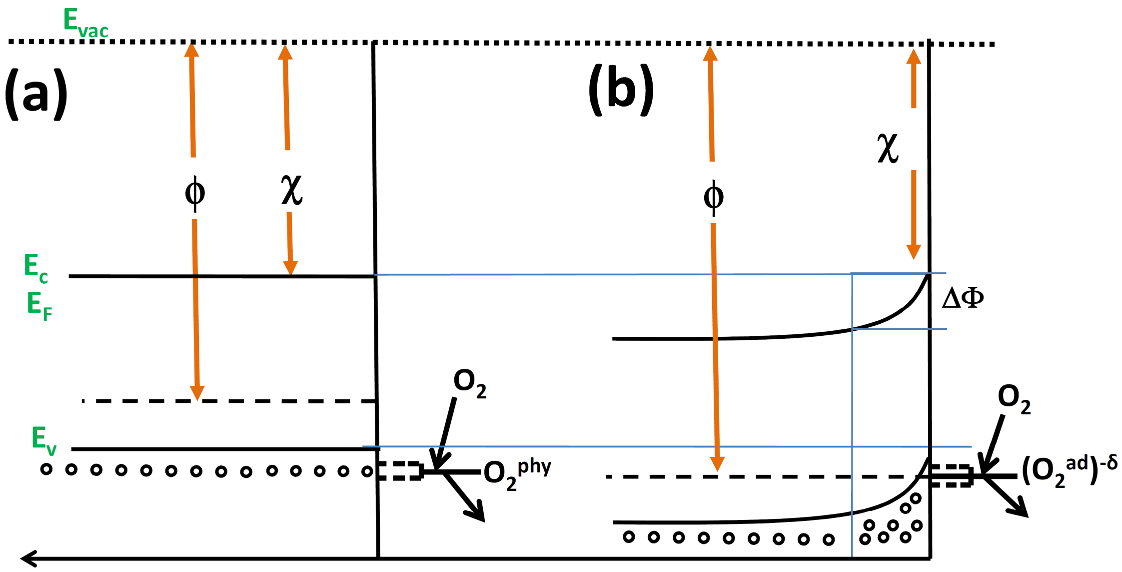

Fig.1.8. Schematic showing the oxygen adsorption process at the p-type metal-oxide semiconductor surface.

p- type semiconductor: If there are no oxygen ions adsorbed at the surface of p-type semiconductor then there are no surface states (assuming the absence of intrinsic surface states), and therefore, the energy bands can be represented as flat bands. Oxygen is chemisorbed at the surface of the films by capturing the electrons from the valence band of p-type metal-oxides. The surface traps that are associated with the adsorption of oxygen result in an increase of the concentration of holes in the vicinity of the surface, i.e. build-up of an accumulation layer as against a depletion layer in n type metal-oxides. As a consequence the conductance of the film increases in comparison with the flat bands situation. This process, as shown in Fig. 1.8 is described in the energy bands representation as an upward band bending. The thickness of accumulation layer is also related to the Debye length.

1.3.4 Role of nanostructures in gas sensing

The resistance of a chemiresistive sensor depends on the grain size. Three different cases can be distinguished according to the relationship between the grain size (*D*) and the width of the depletion layer (*L*) that is produced around the surface of the grains due to chemisorbed oxygen ions.

(i) ***D>>2L***: In this case most of the volume of the grains is unaffected by the surface interactions with the gas phase, as depicted in Fig. 1.9 (a). Here, the predominant effect of the ambient gas on the sensor's conductivity is introduced via the GB barriers for inter-grain charge transport from one grain (agglomerate) to another. The electrical resistance depends exponentially on the barrier height. Thus, for a sample with large grains (D>2L) the gas sensing mechanism is controlled by the GB barriers. Since GB barriers are independent of the grain size; the sensitivity is independent of D.

(ii) **D≥2L**As the grain size decreases the depletion region extends deeper into the grains and, consequently, the core region (which is relatively conductive with respect to the depletion region) becomes smaller. When D approaches 2L but is still larger than $2L$, i.e., when D>$2L$, the depletion region that surrounds each neck forms a constricted conduction channel within each aggregate, as depicted in Fig. 1.9 (b). Consequently, the conductivity depends not only on the GB barriers but also on the cross section area of these channels. The current constriction effect adds up to the effect of the GB barriers, and therefore the gas sensitivity is enhanced with respect to the case of D>>$2L$. Sensitivity to gases increases when D decreases.

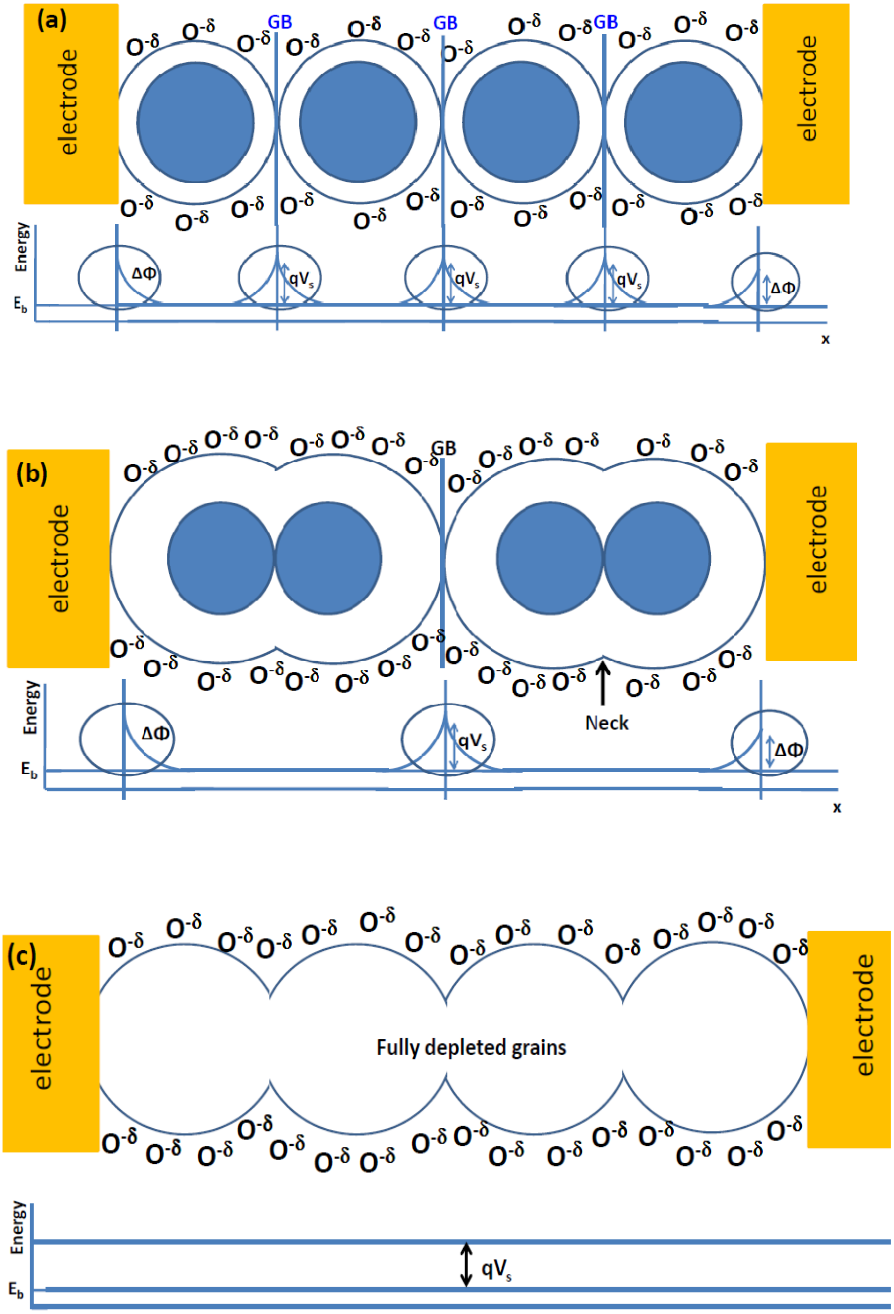

Fig.1.9. Schematic showing a model describing the effect of grain size on sensitivity (a) D>>2L: Grain boundary control (b) D≥2L: Neck control (c) D<2L: Grain control. E_b is the potential value for the bulk.

(iii) ***D*<2*L*:** In this case the depletion region extends throughout the entire grain and the crystallites are almost fully depleted of mobile charge carriers, as shown in Fig. 1.9 (c). As a result, the conductivity decreases steeply since the conduction channels between the grains have vanished. The energy bands are nearly flat throughout the whole structure of the interconnected grains, and since there are no significant barriers for intercrystallite charge transport the conductivity is essentially controlled by the intracrystallite conductivity i.e. grain controlled.

As gas sensing is a surface phenomenon, the grain size of the films play a predominant role. The nanostructures, such as, nanowires and nanoparticles, due to high surface-to-volume ratio and possibility of a case of $\boldsymbol{D}<\boldsymbol{2L}$ (as discussed above) make them potential candidate for the chemiresistive sensors with faster response and recovery times. Other advantages associated with nanostructures can be low power consumption and possibility of high integration densities. However, nanoparticles, in particular, can suffer from poor stability and degradation due to grain coalescence when operated for longer time and/or at high operating temperatures. In this regard, nanowires have advantages as they can have high degree of crystallinity across their length. Nanowires however suffer from non uniform growth, poor control over density and distribution and reproducibility. In addition, preparing ohmic electrical contacts on nanostructures is still a key issue.

1.4 Scope of thesis

The motivation of present thesis work is to develop highly selective H_2S sensors, which are needed for Heavy water plants to monitor its concentration at the plant as well as in the local environment (in case of any leakage). In a heavy water plant, heavy water (D_2O) is produced employing H_2S-H_2O bithermal isotopic exchange process i.e., Girdler-Sulfide process ($HDS_{gas} + H_2O_{liq} \leftrightarrow H_2S_{gas} + HDO_{liq}$). The bi-thermal process operates in a pair of cold and hot columns maintained at 30°C and 130°C at 20 kg/cm^2 pressure and permits extraction of about 20% of the deuterium contained in the feed water (0.015% deuterium). This process enriches the feed water 1000 fold yielding 15% concentration in cold tower of third stage, which is further enriched to nuclear grade in Distillation Unit.

As discussed earlier, H_2S is highly toxic and flammable gas and its exposure to high concentrations can cause de-functioning of lungs and could be fatal. In literature, several additives have been employed to make metal-oxide sensors selective to H_2S. However the mechanisms of enhancement of the H_2S specificity by additives are not fully understood. ***Therefore, this thesis aims at understanding the gas-sensing mechanisms in metal-oxide chemiresistive sensors with suitable additives that make them selective to H_2S gas.*** We have synthesized p-type (CuO) as well as n-type (ZnO, WO_3, SnO_2) metal-oxide thin films and nanostructures for H_2S sensors. In addition, these thin films and nanostructures are tailored using suitable additives so as to realize highly specific either p-n junctions (CuO:ZnO, CuO:WO_3, Fe_3O_4:SnO_2) or Schottky barriers (Au:ZnO, Au:WO_3) which enhances the specificity for H_2S. The gas sensing mechanisms were investigated using various techniques like X-ray photoelectron spectroscopy, impedance spectroscopy, Kelvin probe, photoluminescence, UV-Vis spectroscopy, X ray diffraction. The thesis encompasses the following chapters. In ***Chapter 2***, we describe the details of experimental methods used for fabrication of different types of sensors based on thin films, nanoparticles, nanowires, p-n junctions and Schottky-barriers. Details of various techniques used during the thesis work, such as, scanning electron microscopy (SEM), x-ray photoelectron spectroscopy (XPS), UV-Vis spectroscopy (UV-Vis), Kelvin probe microscopy (KPM), photoluminescence (PL), impedance spectroscopy (IS) and gas sensing setup are presented. In ***Chapter 3,*** we present the results on the gas sensing properties of thin films and nanowires of p-type (CuO) as well as n-type (ZnO nanowires and SnO_2 thin films). In Chapter 4, we describe the gas sensing properties of p-n junction type sensors i.e. ZnO: CuO, WO_3: CuO and SnO_2: Fe_3O_4. In ***Chapter 5***, we discuss the gas sensing properties of Schottky barrier type sensors e.g. ZnO-nanowires/Au and WO_3/Au. The main conclusions of the thesis and H_2S sensing mechanisms of n-type, p-type, p-n junctions and Schottky-barrier sensors are summarized in ***Chapter 6***.

Chapter 2

Experimental Techniques

2.1 Introduction

This chapter describes the fabrication processes of various types of sensors, i.e. n-type and p-type thin films/nanostructure based chemiresistive sensors, p-n junction and Schottky–barrier sensors. The details of the techniques employed for the characterization of active layer of sensors has been discussed. In addition, the details of experimental sensing setup to evaluate the response curves of the chemiresistive sensors as a function of sensor temperature and gas concentration are discussed.

2.2 Steps in sensor fabrication

The various steps involved in the fabrication of chemiresistive sensors are depicted in the flowchart shown in Fig. 2.1. These steps are discussed in the following sections.

2.2.1 Substrate preparation

In this research work we have used polycrystalline Al_2O_3substrate for the deposition the thin film based chemiresistive sensors. Polycrystalline Al_2O_3 substrates are chosen because of their granular morphology, excellent heat resistance, high mechanical strength, abrasion resistance and small dielectric loss. Moreover, these substrates are quite economical and therefore suitable for sensor fabrication at low-cost [108]. For the fabrication of ZnO and CuO nanowires based chemiresistive sensors, we have employed n-type (100) Si substrate having 120 nm SiO_2 layer and for Cu foils, respectively.

The cleanliness of the substrates is of crucial importance for the subsequent growth of thin films and nanowires. Thus substrate preparation is very important step before growth studies. Prior to the growth, substrates are thoroughly cleaned in different organic solvents. In the first step, the substrates were ultrasonicated in trichloroethylene bath for 10 minutes to remove oil, grease etc. Thereafter the substrates were sonicated in acetone and methanol separately to remove polar and non polar organic, inorganic impurities and dust particles. To remove the solvent, the substrates were dried under the jet flow of dry high purity Ar gas. Finally these substrates were used for thin film deposition and nanowires growth.

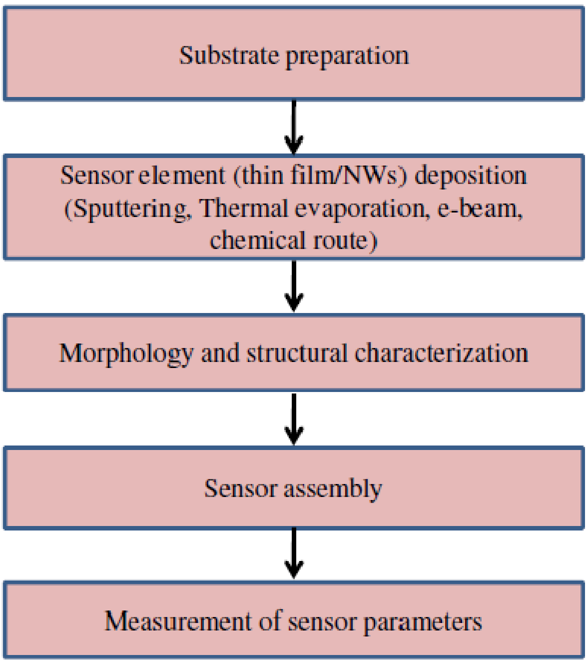

Fig.2.1. Flowchart depicting the steps involved in the fabrication of a sensor.

2.2.2 Preparation of sensing layer

(a) Preparation of thin films

For the preparation of CuO, $WO_3$and SnO_2sensing layers without and/or with different additives (like Fe, Au and Cu), we have employed thermal evaporation, electron-beam evaporation and/or DC/RF sputtering. The details of the preparation of thin films using different techniques are presented below.

(i) Rheotaxially grown thermal evaporation technique (RGTO): The RGTO technique of making metal oxide thin films consists of two steps: In the first step, metallic thin films (W or Sn) are deposited by thermal evaporation on a substrate, which is kept at a temperature higher than the metal melting point of the metal. This step is known as rheotaxial growth (i.e. deposition of melted metal) as the metal forms microspheres at the surface of the substrates due to the liquid-phase surface tension. In the second step, the metallic films are oxidized by high temperature thermal oxidation process. RGTO method of preparing metal-oxide thin films is simple, robust and therefore widely used.

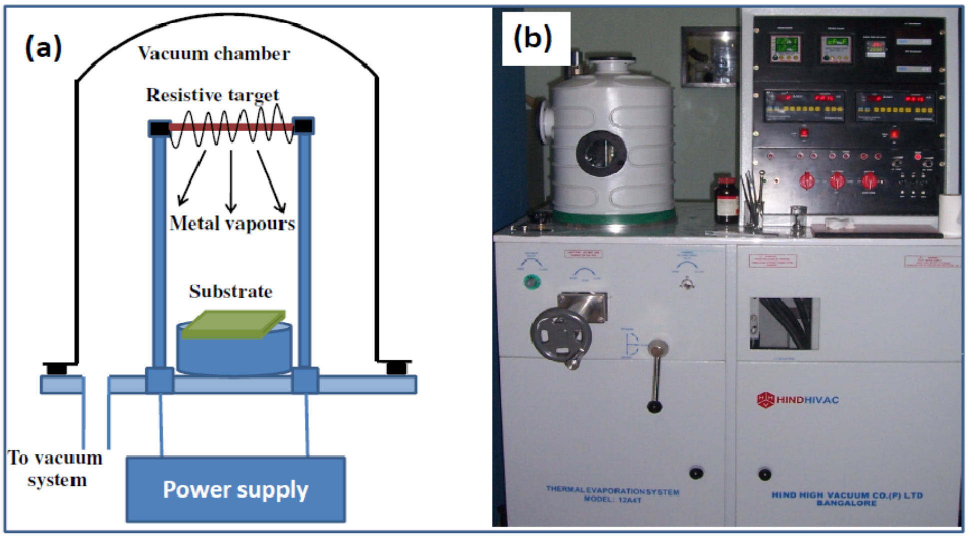

Fig.2.2. (a) Schematic of thermal evaporation technique (b) A photograph of the thermal evaporation system used for thin film deposition.

Fig. 2.2 shows the schematic (a) and the photograph (b) of thermal evaporation system used in the present work. This involves resistive heating of the material to be deposited to the point of evaporation. The temperatures achieved using this techniques can go upto 1800°C. The various filaments used to heat the evaporation sources are W (Melting point- 3380°C), Ta (3000°C) or Mo (2620°C). The process is performed at a vacuum of 10^{-5} Torr to increase the mean free path and to decrease the impurities in the film. The common evaporant materials deposited using this technique is Au, Ag, Al, Sn, Cr, Sb, Ge, In, Mg or Ga. The typical filament current is of the order of 200-300 A and typical deposition rates are 1-20 Å/s.

SnO_2 thin films prepared by RGTO included the following two steps: (i) Sn was evaporated onto Al_2O_3 substrate which was kept at a 250°C that is well above its melting point (232°C). The Sn grows in the form of small metallic Sn microspheres. (ii) Sn film was annealed at ~800°C under the oxygen flow in which metallic Sn microspheres convert into SnO_2, which also accounts for the increase in its volume by ~30-35% [109]. The oxidation kinetics is limited by the diffusion of oxygen through the growing surface of SnO_2 layer towards the interior metallic Sn [110]. The oxidation of Sn is a critical step as partial or incomplete oxidation may result in the drift in sensor properties especially for the sensors working at elevated temperatures. This is due to the fact that the stable (drift free) operation demands bulk lattice oxygen in the SnO_2 grains to be effectively frozen. We have annealed Sn films were at 800°C (for 1 h) which assured a complete oxidation of the films.

Using RGTO method WO_3 films were deposited in the following manner. First, W films (~600 nm thick) were deposited onto Al_2O_3 substrates (having pre-deposited Au electrodes) using W-foil (purity: 99.99%) under application of a very high current ~80 A. The W films were then subjected to a post deposition annealing at 600°C to form WO_3 phase.

(ii) Electron beam evaporation: Thermal evaporation technique, as described above, has a limitation for making thin films materials having melting point >1500°C, such as, transition elements, refractory materials etc. Thin films of such materials can be easily prepared by electron beam (e-beam) evaporation, in which the evaporant is heated directly using a focused beam of high energy electrons. The schematic of e-beam evaporation process is shown in the Fig. 2.3 along with the photograph of a system used for deposition of sensor films in the present thesis work. The evaporant is kept in a heavy, water-cooled copper hearth and a beam of electrons is emitted from a filament, usually set below the hearth, is accelerated through an extraction grid and bent through 270°C before striking the evaporant. Magnetic field is used to focus as well as sweeping the e-beam to allow larger evaporant surface area to be exposed for higher deposition rates. This method provides an advantage of sequential deposition of different layer in single pump down if multiple hearths are used. This method is more complex but extremely versatile and can achieve temperatures in excess of 3000°C. The typical emission voltage is 8-10 kV and deposition rates achieved are in the range of 10-100 Å/s.

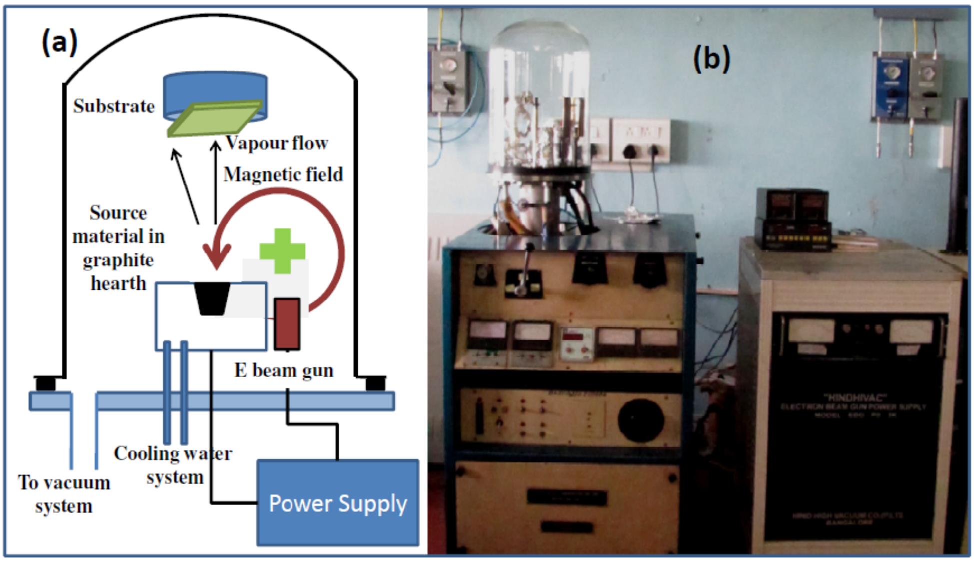

Fig.2.3 (a) Schematic of e beam evaporation technique (b) A photograph of the system

In this thesis work, we have employed e-beam evaporation for the deposition of Fe layer onto RGTO grown SnO_2 films, which improves the selectivity of the sensors. We have deposited Fe films having different thicknesses (5, 8, 12 and 18 nm as measured using QCM) using high purity Fe (99.99%) target. The films were then subjected to a post deposition annealing at 400°C for 1 h under oxygen environment to uniformly disperse the iron oxide into SnO_2 matrix.

(iii) RF/DC Sputtering: Fig. 2.4 shows the schematic of sputtering technique along with the photograph of the system (Milman DC-RF sputter system MM-114) used in present thesis work. Within the sputtering process gas ions out of plasma are accelerated towards a target consisting of the material to be deposited. Atoms/ions are sputtered from the target and get deposited onto a substrate. The process is realized in a chamber, which is pumped down to a vacuum base pressure (~10^{-7} Torr) before deposition starts. To enable the ignition of plasma, argon is fed into the chamber up to a pressure between ~10^{-2} Torr. In the dc-sputtering a negative potential (U) up to some hundred volts is applied to the target. As a result, the Ar-ions are accelerated towards the target and set material free; on the other hand they produce secondary electrons. These electrons cause a further ionization of the gas. The gas pressure (p) and the electrode distance (d) determine a break-through voltage (U_d) — from which a self sustaining glow discharge starts — following the equation: $U_d = \frac{A \times p \times d}{(\ln(p \times d)) + B}$, with materials constants A and B.

The bombardment of a non-conducting target with positive ions would lead to a charging of the surface and subsequently to a shielding of the electrical field. The ion current would die off. Therefore, dc-sputtering is restricted to conducting materials like metals or doped semiconductors. There are now two ways to produce dielectric films: In rf-sputtering (radio frequency) an ac-voltage is applied to the target. In one phase ions are accelerated towards the target surface and sputter material. In the other phase charge neutrality is achieved. Hereby also sputtering of non-conducting materials is possible.

Alternatively, for reactive sputtering other gases like oxygen or nitrogen are fed into the sputter chamber additionally to the argon, to produce oxidic or nitridic films.

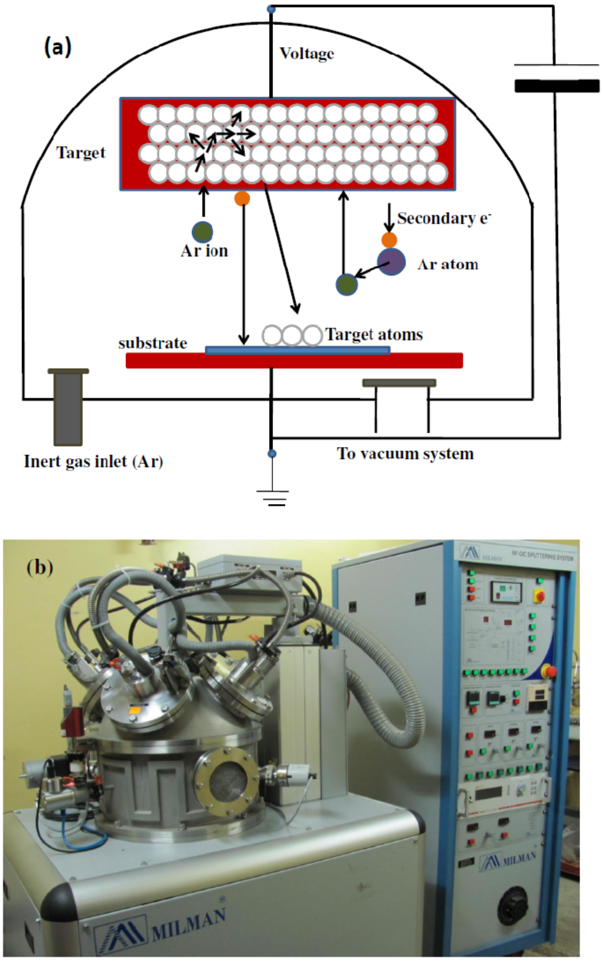

Fig.2.4. (a) Schematic of sputtering process, (b) Photograph of the sputtering system used.

We have deposited SnO_2 films of ~400 nm (measured using Ellipsometer) at room temperature onto alumina substrates using RF sputtering. The base pressure of the sputtering chamber was 4×10^{-6} mbar. The deposition was carried out using SnO_2 target (55 mm diameter and 99.99 % pure) at 3×10^{-3} mbar of Ar and 60 W power. Similarly WO_3 thin films were deposited using reactive RF sputtering. In this case, sputtering was performed using W target. The other sputtering parameters were: substrate temperature:

350°C; power: 100 W, deposition time: 2 h, deposition pressure: 3×10^{-3} mbar and Ar to O_2 ratio of 4:1. After sputtering, the films were subjected to a post deposition annealing at 400°C for 1 h under O_2.

In some of experiments, the surface modification of WO_3 thin films was carried out using CuO. For this, first Cu films of different thicknesses were deposited at room temperature using Cu target (at 30 watt) by varying the deposition time. All the samples were then subjected to thermal oxidation at 400°C for 1 h thereby allowing conversion of Cu into p-type CuO. It is well established that thermal oxidation of Cu at temperatures >270°C leads to the formation of pure CuO phase [111].

(b) Synthesis of nanostructures

We have synthesized several nanostructures, such as ZnO nanoparticles, ZnO nanowires and CuO nanowires for chemiresistive sensors. The details of the methods used for synthesis of these nanostructures include, chemical route, hydrothermal process and thermal oxidation, which are described below.

(i) Chemical route: We have grown ZnO nanostructures i.e. unintentionally doped p-type ZnO NPs having size between 5 and 15 nm by chemical method. ZnO NPs were synthesized by chemical process using zinc acetate dihydrate as precursor. The NaOH solution in ethanol (5–15 mM concentration) was slowly added (over a period of 15 min) to the solution of zinc acetate dihydrate in ethanol (30–45 nM concentration) kept at a temperature of 60–75 °C (the volume ratio of the two solutions was maintained at 2:1). Growth was carried out for few hours under constant stirring. Growth at temperatures above 60 °C ensures that the precipitation of hydroxides does not take place. NPs with different sizes were obtained by controlling the precursor concentration and the growth temperatures. For gas sensing measurements, NPs were spin casted on oxidized silicon wafers to result in a continuous film.

(ii) Hydrothermal method: The random networks of ZnO-nanowires were grown on the native oxide of the Si substrates (size 10×10 mm^2) by hydrothermal method using ZnO nanoparticles (synthesized by chemical route) as seed. The seed layer was prepared by spin-casting the dispersed ZnO-nanoparticle (prepared in de-ionized water) onto the native oxide surface of Si (100) substrates. The thickness of the seed layer was ~100nm. The ZnO-nanowires growth was carried out on the seed layer by suspending the wafer upside-down in an open beaker filled with an aqueous equimolar (0.025 M) solution of zinc nitrate hexahydrate, $Zn(NO_3)_2.6H_2O$, and hexamethylenetetramine (HMTA), $(CH_2)_6N_4$, at 90°C for 6 h. After the growth of random ZnO-nanowires networks, the substrates were rinsed using de-ionized water and dried under Ar flow.

(iii) CuO nanowires by thermal oxidation: Synthesis of CuO nanowires was carried out by thermal oxidation of high-purity Cu sheets of 1mm thickness. Copper sheet of 10×10mm^2 size was first cleaned in dilute nitric acid to remove the native oxide layer and adsorbed impurities. The foil was then throughly rinsed with deionized water followed by ultrasonication in acetone for 5 min. Thermal oxidation of Cu sheet was carried out in a resistively heated furnace at different temperatures (between 400 to 800 °C) and times under flowing oxygen atmosphere. The sample temperature was monitored by placing a thermocouple in vicinity of the sample. In all the experiments, the rate of heating of copper sheet was maintained at 6°C/min and after oxidation samples were quenched by removing from furnace. A constant oxygen flow rate was maintained during the complete cycle of heating, oxidation and quenching of the samples.

2.2.3 Morphology and structural characterization

(a) Scanning electron microscopy equipped with EDX: We have used scanning electron microscope (TESCAN VEGA) to investigate the surface morphology of the sensor films and nanostructure. The scanning electron microscope (SEM) provides information relating to topographical features, morphology and phase distribution [112]. A photograph of SEM used for morphological characterization in the present study is shown in Fig. 2.5. Briefly, SEM is the focused probe of electrons accelerated to a moderately high energy and positioned on to the sample by electromagnetic fields. These beam electrons interact with atoms of the specimen by inelastic (energy is transferred to the sample leads to secondary electron (SE) emission) and elastic (energy is not transferred to the sample leads back scattered electrons (BSE) emission) collisions. The most widely utilized signal, produced by the inelastic interaction of the primary electron beam with sample is the secondary electron signal. Secondary electrons are emitted from the outer shell of the specimen atom upon impact of the incident beam. It is the most useful signal for examining surface structure and gives the best resolution image of 10 nm or better. Since the secondary electron intensity is a function of the surface orientation with respect to the beam and the secondary electron detector and thus, produces an image of the specimen morphology. The secondary electron intensity is also influenced by the chemical bonding, charging effects and back scattered electron intensity, since the back scattered electron generated secondary electrons are significant part of the secondary electric signal.

The compositional analysis has been carried out using energy dispersive x-ray analysis system (OXFORD INCA) equipped with SEM. The minimum detection limit (MDL) of the EDX is about 0.1 wt%. X-rays are produced as a result of ionization of an atom by high-energy radiation wherein an inner shell electron is removed. To return the ionized atom to its ground state, an electron from a higher energy outer shell fills the vacant inner shell and, in the process, releases an amount of energy equal to the potential energy difference between the two shells. This excess energy, which is unique for every atomic transition, will be emitted by the atom either as an X-ray photon or will be self-absorbed and emitted as an Auger electron. For example, if the K shell is ionized and the ejected K-shell electron is replaced by an electron from the L shell, the emitted X-ray is labeled as characteristic Kα X-ray. The hole that exists in L shell will be filled by an electron from a higher shell, say the M shell, if one exists. This M-L transition may result in the emission of another X-ray, labelled in turn according to one of the many M-L transitions possible. The cascade of transitions will continue until the last shell is reached. Thus, in an atom with many shells, many emissions can result from a single primary ionization.

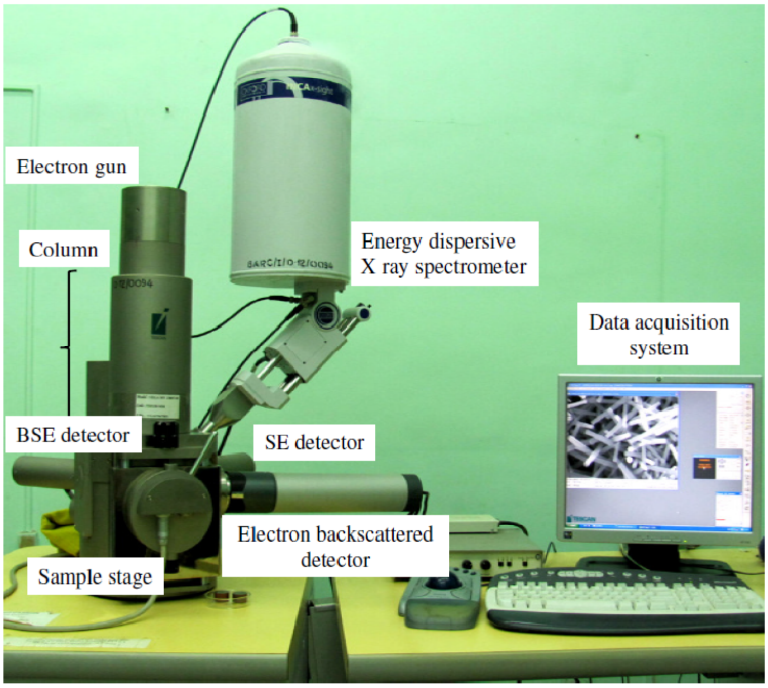

Fig.2.5. A photograph of the scanning electron microscope used in the present work.

(b) X-ray Diffraction: For determination of the structure and morphology of the deposited films and nanostructures, x-ray diffraction measurements were carried out. We used powder X-ray diffractometer (Seifert XRD 3003TT) in θ-2θ scan mode to characterize the orientation and structure of the samples. The X-ray source used was Cu K_α having wavelength of 1.54Å. For mounting thin films, specially designed Perspex holder (having a groove of dimension 10mm × 10mm × 1mm) was employed. The films were mounted on this groove using red wax in such a way that X-rays fall on the film plane. Since the wavelength (λ) of X-rays coincides with the atomic spacing (d) in the solids, it diffracts in those orientations of 2θ, where the Bragg condition of diffraction [113] i.e. $2d \sin\theta = n\lambda$ (θ being the angle which incident beam makes with the plane of the sample) is satisfied. The recorded diffraction patterns were least square fitted using software to determine the lattice parameters.

(c) UV- visible spectroscopy: UV- visible spectroscopy is generally used to study the electronic transition in molecule. The absorption of ultraviolet or visible radiation generally results from excitation of bonding electrons (π, σ or even non bonding electrons); as a consequence, the wavelength of absorption peaks can be correlated with the type of bonds in the spices [114]. The absorption may sometime occur due to the *d* and *f* electron and also due to charge transfer electrons. So this absorption study is very important tool to indentify the molecule or functional group in the molecule. For our experiment we have use JASCO B430 spectrometer. In this spectrometer the intensity (I) of the beam passing through the sample is compared with a reference beam (I_0) and in output we get absorbance ($A = log_{10}I/I_0$) vs wavelength.

(d) X-ray photoelectron spectroscopy: XPS uses a soft X-ray source (Al-K$_\alpha$ or Mg-K$_\alpha$) to ionize electrons (by knocking out the core-level electron) from the surface of a solid sample (top few atomic layers). The binding energies of these electrons are measured, which are characteristics of the elements and associated with chemical bonds (chemical state). The advantages of XPS technique are (*i*) quantitative analysis of elements and chemical states of all elements except hydrogen and helium, (*ii*) typical element detection limits are 0.1 atomic percentages from the top few nm, and (*iii*) samples can be conductors, semiconductors or insulators [115, 116]. In this work, we have used XPS system (RIBER system model: FCX 700) consisting of Al-K$_\alpha$ (1486.6eV) and Mg-K$_\alpha$ (1253.6eV) X-ray sources and MAC-2 electron analyzer. The binding energy scale was calibrated to Au-4f$_{7/2}$ line of 83.95eV. For charge referencing adventitious C-1s peak set at 285eV was used. Each data set was first corrected for the non-linear emission background. The data was then fitted with Gaussian function to find the peak positions.

(e) Kelvin Probe: The work function of the sample was measured using ambient scanning Kelvin Probe Force Microscopy (SKP 5050). In brief, Kelvin Probe (KP) is a versatile technique that measures contact potential difference (CPD) between two surfaces brought in close proximity [117]. When electrically connected, electrons flow from the semiconductor with the smaller work function to the metal with the larger work function (Fig.2.6 (b)). The surfaces (not in physical contact) develop equal and opposite charges and act like a parallel plate capacitor. The voltage developed across capacitor is the CPD. The Kelvin apparatus consists of a probe surface and a sample surface acting together as a parallel plate capacitor. The work function of the probe is known by calibrating against a standard Au coated clean surface, so the work function of the sample can be determined. Backing voltage V_b is adjusted such that voltage across the circuit disappears, at which point V_b is equal to V_{CPD} (Fig.2.6c).

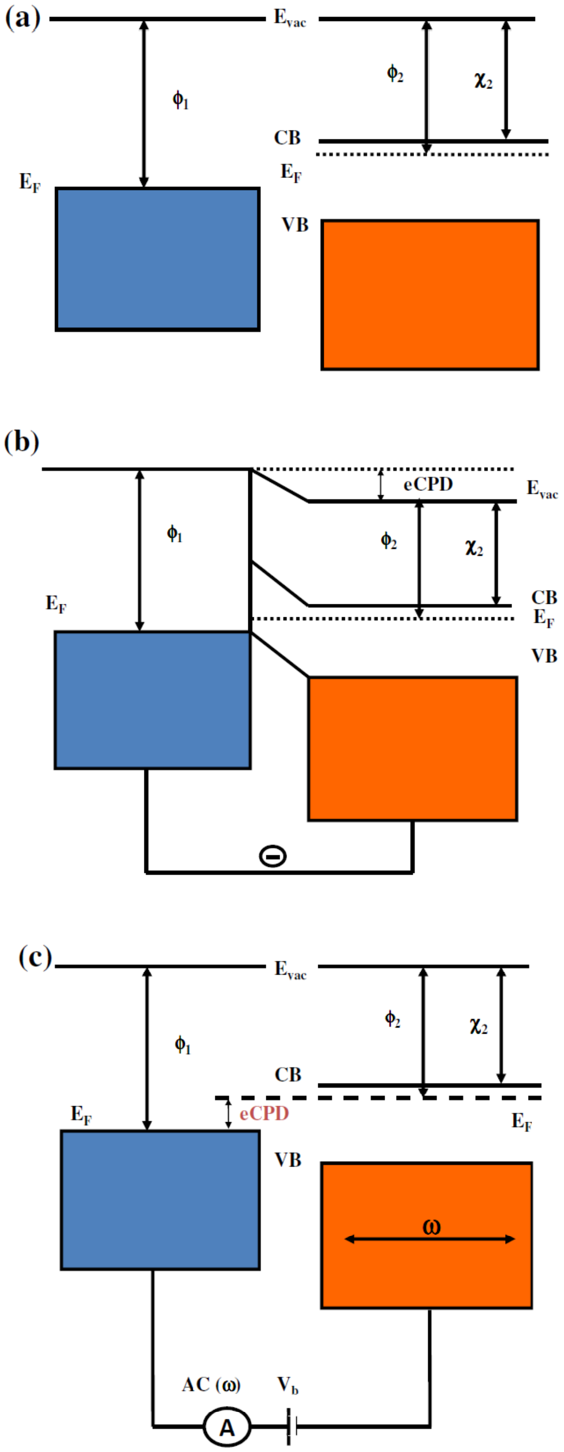

Fig.2.6. Block diagrams depicting Kelvin Probe process. (a) Flat band condition (b) band bending between metal and sample after electrical contact (c) Equilibrium condition after application of backing voltage.

To ensure more than one measurement, entire charge from previous measurement should dissipate, therefore the probe is vibrated (ω = 27 kHz) to produce varying capacitance. The output voltage as a result of oscillation: $V_o = (V_{CPD} - V_b)RC_o \in \sin(\omega t + f)$, where, R is current-voltage converter feedback resistance, $\in$ is a ratio of average distance between probe and sample to the amplitude of oscillation called as modulation index, and C_o is the capacitance. Lock in amplifier which is a phase sensitive detector is appropriate to detect null output condition when signal to noise ratio is very low. It multiplies the input signal with a reference signal and integrates over a span of ms to s. The resulting signal is a DC signal, where the contribution from any signal that is not at the same frequency as reference is attenuated to zero. It also attenuates the out of phase signal of same frequency. A photograph of the system for present work is shown in Fig. 2.7.

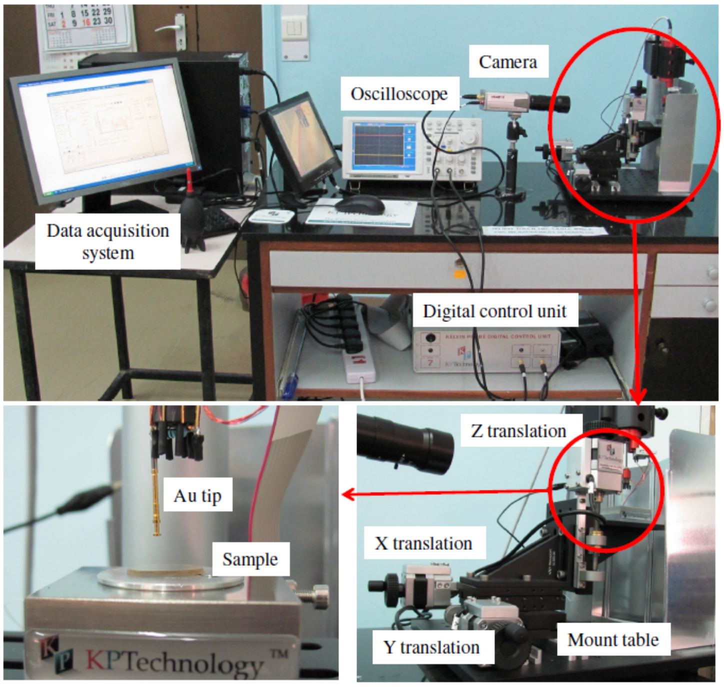

Fig.2.7 A photograph of Kelvin Probe system.

(f) Photoluminescence: Photoluminescence (PL) studies were carried out using Edinburgh Fluorescence Spectrometer FLP 920 in reflection geometry. Xenon lamp was used for excitation (280 nm). Luminescence is the phenomenon in which absorption of light of a given wavelength by a molecule is followed by the emission of light at longer wavelengths [118]. Different type of transitions that can occur between ground and excited states are shown in Fig. 2.8. Emission spectrum is the distribution of wavelength-dependent intensity of emitted energy. The electronic structure and dynamics of an excited state of a molecule may be elucidated from luminescence as it is a property related to the difference between two electronic states, viz. the emitting state and the ground state. Based on practical observations of persistence of two types PL was historically called fluorescence for life times shorter than 100μs and much longer lasting up to a few hours and even days is called phosphorescence.

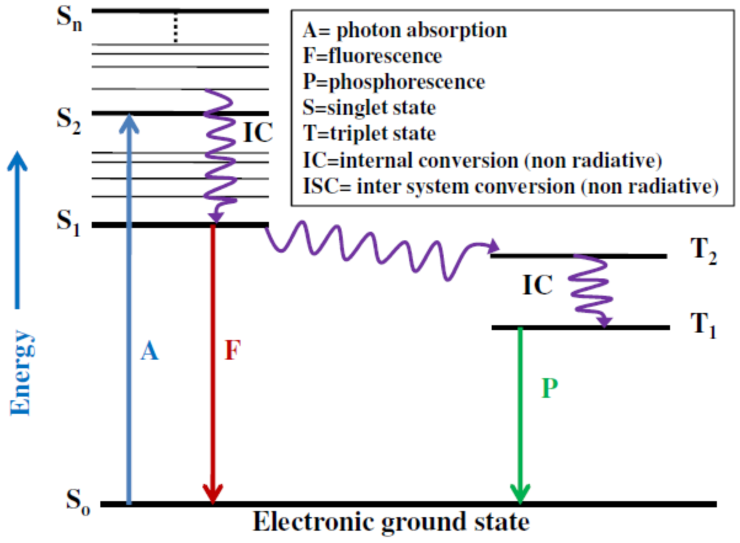

Fig.2.8. Schematic of a Photoluminescence process

(g) Impedance Spectroscopy: Impedance spectroscopy studies in the frequency range of 1 Hz to 1 MHz were carried out using a frequency response analyzer (FRA) attached with a potentiostat (PG-STAT20, Echo Chemie, The Netherlands). The peak to peak amplitude of ac signal and dc signal was maintained at 20 mV and 500 mV, respectively. Impedance spectroscopy (IS) technique is employed to study the various electron transfer processes occurring at the interfaces of a sensor assembly and hence for the identification of different elements of a complex sensor device. The measured data were fitted using ZSimpwin software.

(h) Raman Spectroscopy: Raman measurements were performed in order to obtain the fingerprints of the different sensor materials synthesized for this thesis work. The Raman spectroscopy was carried out using LabRAM HR800, Jobin Yvon Horiba, France using green wavelength (513 nm) at room temperature and also in the presence of test gas to elucidate the nature of interaction with the sensor film.

2.2.4 Sensor assembly

After the morphological and structural characterization of sensor element, samples are masked to deposit gold pads (1 mm spacing, 120 nm thickness) using thermal evaporation technique. This step is followed by fixation of Ag wires to connect the sensors with the data acquisition system. The metal-oxide based chemiresistive sensors generally have low sensitivity at room temperatures so they need to be maintained at their respective operating temperature. In order to achieve that Pt-100 heater, 2 Nos., were fixed to the substrate on the back side of the sensor element using commercially available alumina paste and silver paste. One of the Pt-100 was used to heat the films and the other one was used as a reader to monitor the temperature of the sensor.

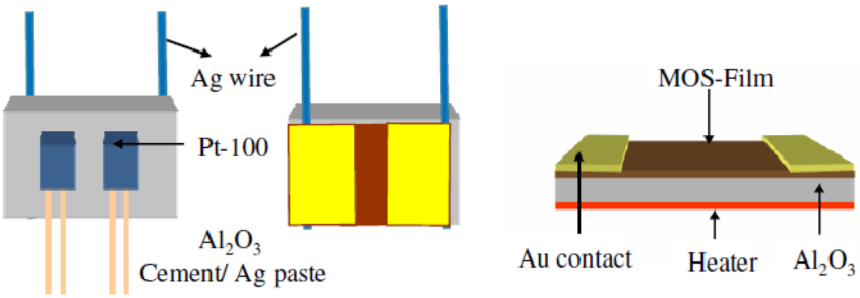

Fig.2.9. Schematic of backside, front side and side view, respectively of the sensor.

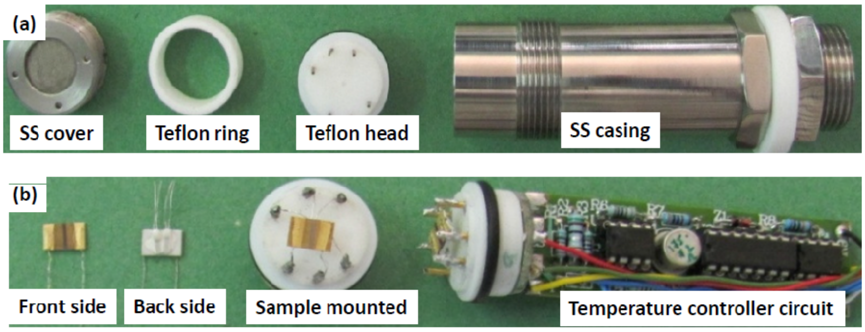

Fig.2.10. (a) Photograph of all the components of a stainless steel sensor casing (b) photograph of a sensor film showing its front side, backside, and temperature controller circuit.

Fig. 2.9 shows the layout of the sensor assembly. Fig. 2.10 shows the photograph of typical sensor assembly components. Fig. 2.10 (a) shows the various components of a SS sensor casing which consists of a SS cover with a net to allow the path of gas molecules to the sensor film, teflon head with an O-ring and teflon ring to ensure leak proof environment for efficient interaction of gas molecules with the sensor film. Fig. 2.10 (b) shows the photograph of a sensor film. It clearly shows the gold electrode with Pt wire on the front side and Pt-100 (2 No's) on the backside of the sensor film. Fig. 2.10 (b) also illustrates the mounting of sensor film onto the teflon head which is then soldered onto the temperature controller circuit. Finally the temperature controller circuit with sensor film attached to it is enclosed within the SS casing shown in Fig. 2.10 (a).

2.2.5 Measurement of sensor parameters

We used two-probe method for resistance measurement as it is the simplest and a straightforward method. It is capable of giving accurate measurements above 100 kΩeasily as for lower resistances; interconnecting cables add significant resistance which affects the measurement. Most of the metal-oxide based sensors fall well within the range of resistances, suitable for 2 probe measurement. We monitored resistance as a function of time for most of the sensor films but in some of the sensor films having high resistance (~ 10 MΩ) aconstant voltage was applied to the sensor element, and the resulting current was measured as a function of time on exposure to the desired gas.

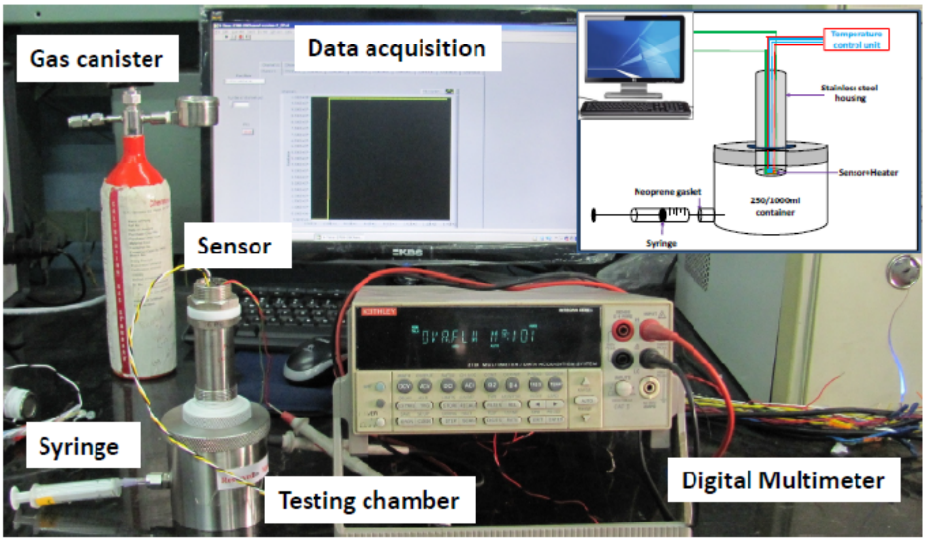

Fig. 2.11 Gas sensing set up used in the present work and schematic in the inset.

The gas sensitivity of the films was measured using a home-made gas sensitivity measurement setup, as shown in Fig. 2.11. The sensor films are mounted on a heater surface. The temperature of the heater was controlled by an external power supply and temperature controller. The sensor assembly was mounted in a leak tight 1000 ml stainless steel container, and the known amount of gas (to be sensed) was injected into the chamber using a micro-syringe. To measure the response of the sensor films for a particular gas, current at a particular bias as a function of time was measured by interfacing Keithley make 6487 picoammeter/voltage source with a personal computer having Labview based data acquisition software. For the recovery of the sensor, the chamber was exposed to the ambient atmosphere.

Chapter 3

p-Type and n-Type Chemiresistive Sensors

3.1 Introduction

In this chapter we discuss the sensing characteristics of p-type as well as n-type chemiresistive gas sensors. The p-type chemiresistive sensors investigated in the present work include thin films of CuO, drop-cast films of CuO nanowires and isolated CuO nanowires. n-type chemiresistive sensors are investigated based on SnO_2 thin films. In the case of ZnO, it has been demonstrated that in the form of nanoparticles ZnO exhibit p-type behaviour; while in the form of nanowires it exhibits n-type behaviour.

3.2 p-type CuO chemiresistive sensors

3.2.1 Thin films based sensors

The preparation of CuO thin films by thermal oxidation of evaporated metallic Cu films on alumina substrate is discussed in section 2.2.2 (b) (iii). We have optimized the film thickness and found that 200 nm thick CuO films yield best gas sensing properties.

(a) Structural and morphological characterization

The SEM image and XRD pattern of the grown CuO film is shown in Fig. 3.1(a) and (b) respectively. It is seen that CuO films consist of well facetted grains having average grain size of ~8 µm. CuO films do not show any microcracks. The XRD pattern of the grown film indicated formation of the pure monoclinic structure of CuO with lattice constants: a = 4.682 Å, b= 3.431 Å, c = 5.178 Å and β = 99.54°, which are in agreement with reported literature values [119]. No peaks corresponding to the formation of either Cu_2O or Cu_3O_4 were observed. It is well established that thermal oxidation of Cu at temperatures >270°C leads to formation of pure CuO phase [111]. However, sub oxides (Cu_2O and Cu_3O_2) are formed if the oxidation is carried out at temperatures below

270°C. In the present case, since the oxidation of Cu films were carried out at 500°C under oxygen flow, which assured formation of pure CuO phase films.

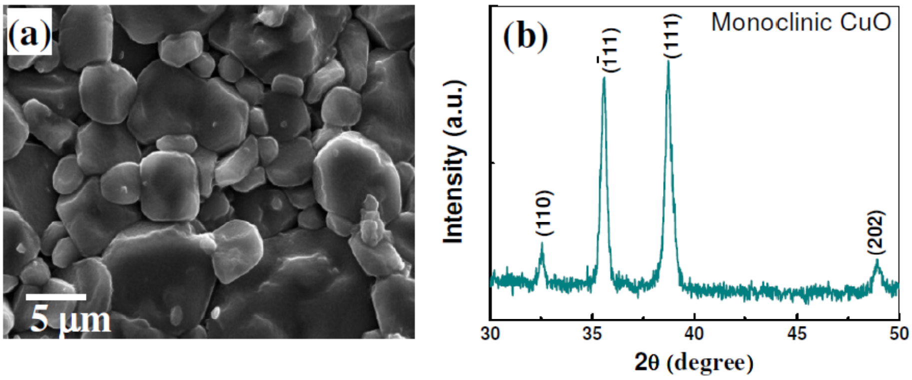

Fig. 3.1. (a) SEM image and (b) XRD pattern of the grown CuO thin film.

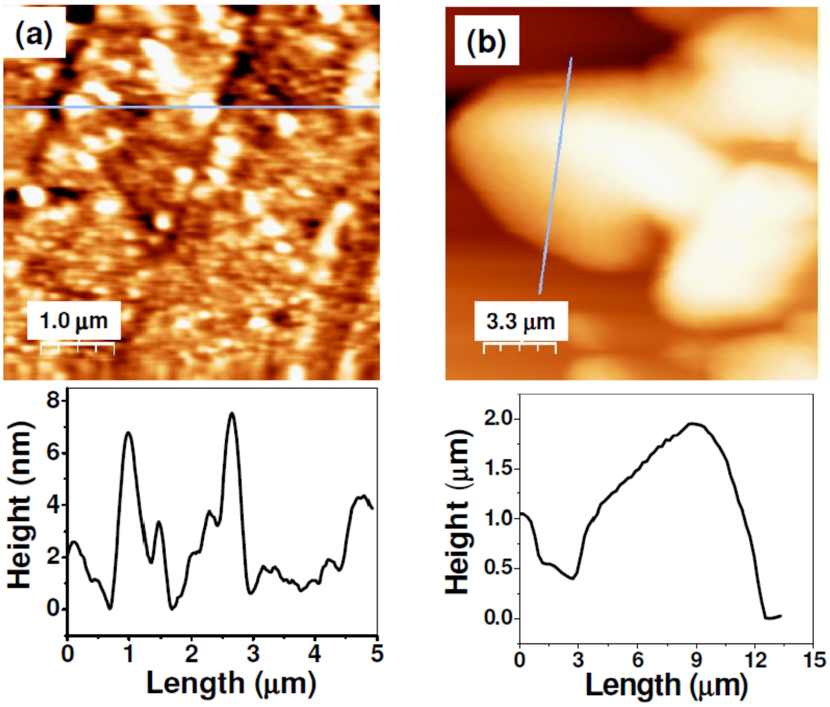

Fig. 3.2. AFM images and the height profiles across the lines drawn in AFM images for (a) as-deposited Cu film and (b) CuO film obtained after oxidation of Cu film.

Typical AFM images obtained for as-deposited Cu films and CuO films (obtained after annealing of Cu films at 500 °C for 1 h) are shown in Fig. 3.2. It is seen that Cu film is very smooth with surface roughness of 8 nm. The average grain size of Cu films was found to be ~0.3 µm. On the other hand, CuO film exhibited large size grains (~8 µm), which is consistent with SEM image. Interestingly, the height of the CuO grains was found to be ~2 µm. This indicates that in the presence of oxygen, during annealing Cu grains undergo a grain growth mechanism to form CuO. Formation of CuO by oxidation of Cu is known to take place through a diffusion-controlled oxidation mechanism known as Wagner's "parabolic rate law", in which Cu atoms are assumed to migrate from the metal domain through the oxide layer to the oxide-oxygen interface [120]. This process is mainly driven by the Cu ions concentration gradient between the metal domain and the oxygen-oxide interface.

(b) Gas sensing

Typical response curves recorded at room temperature for H_2S concentrations ranging from 100 ppb and 400 ppm are shown in Fig. 3.3. Depending upon the nature of response curve, data are divided in to three regions: (a) low concentrations: 100–400 ppb range, (b) intermediate concentrations: 500 ppb–50 ppm range and (c) high concentrations: >50 ppm.

From these data following inferences are made

(i) For low H_2S concentrations (100–400 ppb), the response curve is highly reversible. The base line resistance stability was found to be better than 5 % over a period of 60 days even after repeated exposure to H_2S. The sensitivity is found to vary linearly with H_2S concentration. However, the response (~60 s) and recovery (~90 s) times are very small, and interestingly, are independent of H_2S concentration.

(ii) For intermediate H_2S concentrations (500 ppb - 50 ppm), though sensitivity varies linearly with concentration, the base resistance drifts continuously to lower values, as marked by the dotted line in Fig. 3.3 (b) and 3.3 (b1). In addition, both response and recovery times increase with H_2S concentration.

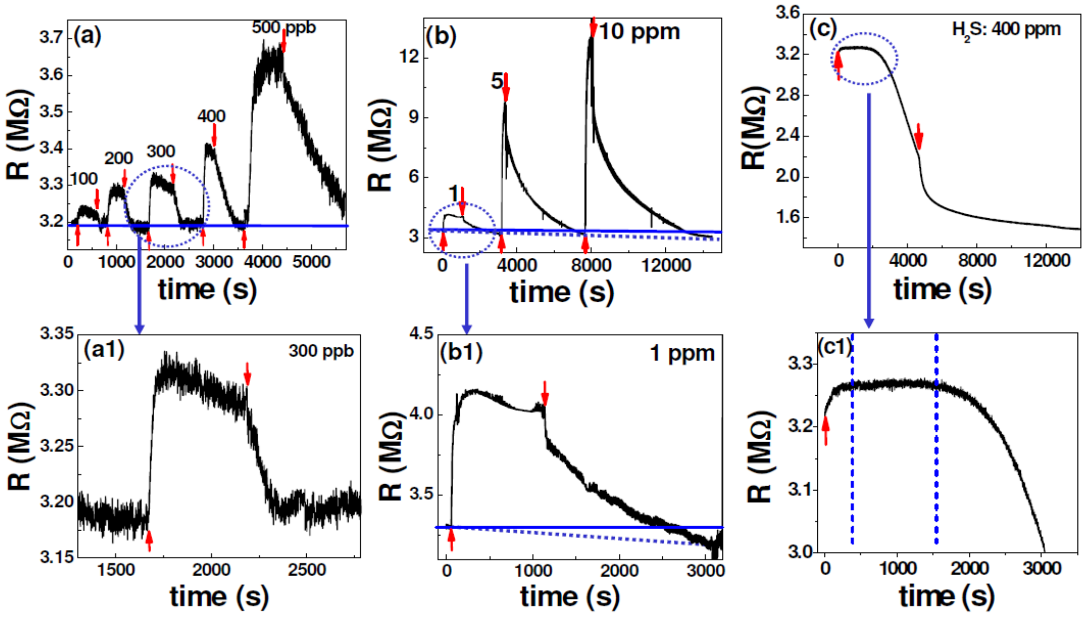

Fig. 3.3. Typical H_2S response of CuO films recorded in three different concentration range: (a) low concentrations: 100–400 ppb, (b) intermediate concentrations 500 ppb – 50 ppm (Note: the dotted line shows a drift in the base line resistance to lower values) and (c) high concentrations (recorded at 400 ppm). (a1), (b1) and (c1) are the magnified plots of the marked region (dotted circles) in (a), (b) and (c), respectively. The time at which the H_2S pulse of desired concentration was injected in the gas-testing chamber is marked by ↑ and the time at which air was inlet in the chamber is marked by↓. In (c1) on H_2S exposure, the resistance increases initially followed by a time independent region (between the two dotted lines) before it decreases.

(iii) For high H_2S concentrations (>50 ppm), the response curve shows a unique feature. Initially the resistance increases marginally, followed by a time independent region (Fig.3.3 c1), and finally the resistance decreases. Even after removal of H_2S, the resistance keeps decreasing.

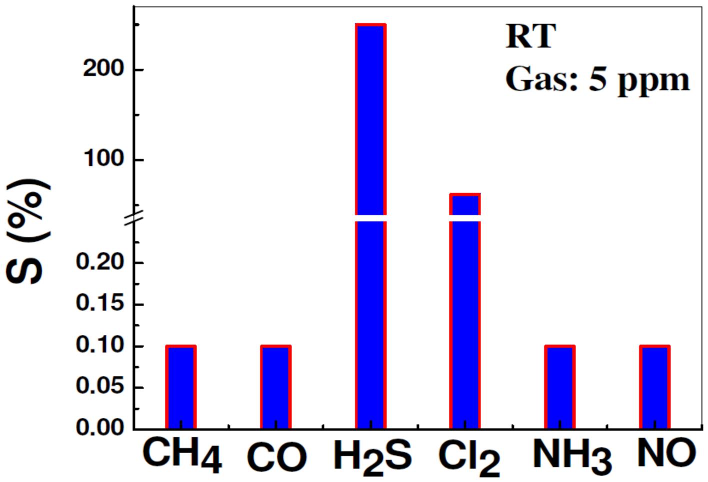

Fig. 3.4. Selectivity histogram of CuO thin films towards 5 ppm of different gases at room temperature.

It is evident from the above results that CuO films are very good room temperature operating sensors for H_2S in the concentration region of 100-400 ppb. In addition, the CuO films show very good selectivity for H_2S. The histogram showing the sensitivity for 5 ppm of different gases i.e. Cl_2, NH_3, CH_4, CO or NO is presented in Fig. 3.4. It may be noted that the sensitivity for Cl_2 is ~60 %, no full recovery was observed for 3 hr. For all other gases, the sensitivity was < 0.1 %. It may be noted that the room temperature behavior for vertically aligned CuO nanowire arrays assembled in a sandwich structure at H_2S concentration ≥10 ppm is similar to that observed by us [146]. These sensors could not detect ppb level H_2S and a possible reason for this could be the poor diffusion of gas owing to their sandwich structure. On the other hand, sensors based on single CuO nanowires exhibited response to NO_2 and NH_3 gases [121]. However, these authors have not reported the sensing behavior for H_2S gas. Thus, our work demonstrates the first ever ppb level H_2S sensors using CuO films.

(c) Sensing mechanism

The response curve is reversible at low H_2S concentration (<500 ppb), whereas irreversible at high concentrations (>50 ppm). From above inferences it is apparent that two different sensing mechanisms, as schematically shown in Fig. 3.5, are operating in the present case. It is well established that CuO is p-type semiconductor owing to Cu vacancies [122].Under ambient conditions, CuO surface absorbs oxygen from air and creates surface states. These surface states allow electrons to be excited from valence band (VB) and, as a result, holes are induced in the p-type CuO grains, see Fig. 3.5 (a). When low concentrated H_2S (<500 ppb) arrives at the surface of CuO grains, H_2S reacts with the oxygen adatoms (O_2^-) via reaction: $2H_2S_{(g)} + 3O_2^-{}_{(ads)} \rightarrow 2H_2O_{(g)} + 2SO_{2(g)} + 3e^-$

The released electrons from the surface states recombine with the holes in VB (Fig. 3.5 (b)), which results in an increased resistance. This process is recovered if H_2S is removed and CuO film is exposed to the ambient conditions. In other words, the adsorbed oxygen on the surface causes the oxidation of H_2S. During recovery, the adsorption of oxygen species easily rejuvenates the CuO surface. The processes for response (oxidation of H_2S by adsorbed oxygen) and recovery (adsorption of oxygen species at CuO surface) are spontaneous in nature. Thus for H_2S concentration range 100-400 ppb, the response and recovery time are not only very small but also independent of concentration. Moreover, since there is no irreversible chemical reaction involved, the baseline resistance does not change.

The linearity in sensitivity is expected as the number of $O_2^-{}_{(ads)}$ consumed depends on the number of H_2S molecules arriving at the surface of CuO grains [123,124]. To support the fact that at lower concentrations CuS formation is negligible we have carried out additional experiments in which CuO sample has been exposed to low concentration H_2S gas (100- 500 ppb) for an hour. In this case resistance initially increases and saturates to a certain value. In these graphs, there is no sign of decrease in resistance indicating formation of CuS. After an hour sample is exposed to air and resistance decreases rather slowly. Gas in and Gas out denotes the time for which sample was exposed to gas and air respectively.

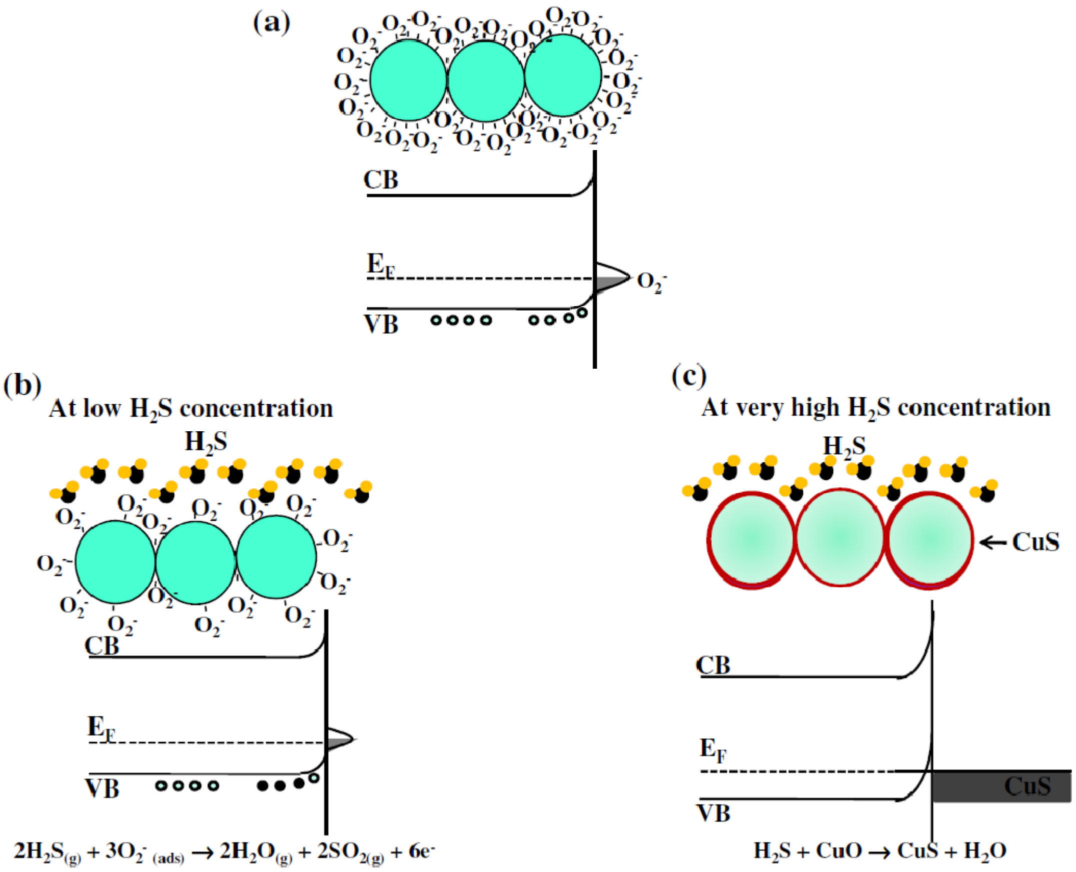

Fig. 3.5. Schematics and band diagrams showing different stages before and after the CuO films were exposed to H_2S gas of different concentrations. (a) In air (before exposing to H_2S), the grains of CuO films absorb oxygen from air and form surface states. These surface states created by adsorbed oxygen species (O_2^-) allow electrons to be excited from valence band (VB) and induce holes in p-type CuO grains. (b) When low concentrated H_2S gas reaches CuO grains, it reacts with O_2^- and the released electrons recombine with the holes in the VB and, thereby causing an increase in the film resistance. (c) At high concentration, H_2S reacts with the CuO and forms CuS layers at the surface of CuO grains, which enhances the electrical connectivity between the adjacent CuO grains, and hence, decreases the film resistance.

On the other hand, when a very high concentration of H_2S (>50 ppm) reaches at the CuO surface, in addition to the H_2S oxidation (as described above), following chemical reaction might take place: $H_2S_{(g)} + CuO_{(s)} \rightarrow CuS_{(s)} + H_2O_{(g)}$. This reaction causes formation of CuS layer, which covers the surface of CuO grains. CuS being metallic enhances the connectivity between the neighboring CuO grains, which results in a decrease of film resistance. In order to confirm the formation of CuS, we have carried out XPS studies on pure and 400 ppm H_2S exposed CuO films. Recorded Cu $2p_{3/2}$ and S 2p spectra are shown in Fig. 3.6. For pure CuO films, Cu $2p_{3/2}$ spectrum shows presence of a peak at 932.5 eV along with a satellite, which confirms the formation of CuO [125]. In the case of H_2S exposed film, Cu $2p_{3/2}$ spectrum shows that main peak has two components at 932.6 and 930.8 eV, corresponding to CuO and CuS, respectively. Confirmation of CuS formation also comes from the appearance of a peak at 164 eV in the S 2p spectrum of the H_2S exposed CuO film.

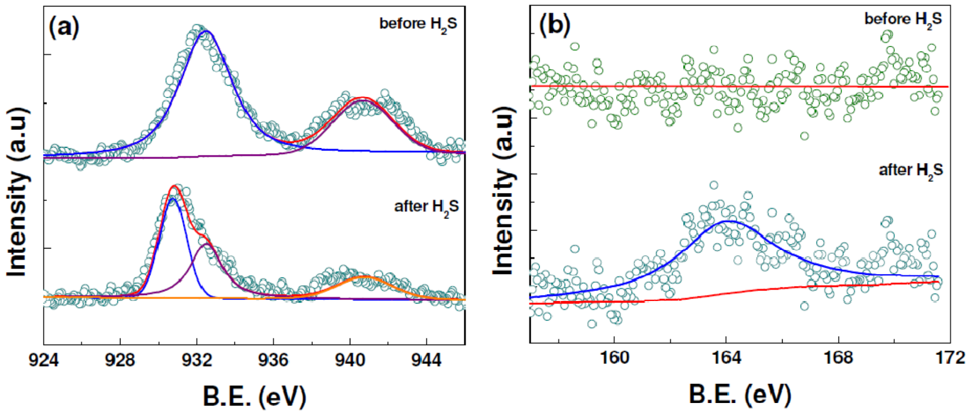

Fig. 3.6. (a) Cu $2p_{3/2}$ and (b) S 2p XPS spectra recorded for CuO films before and after 400 ppm exposure to H_2S.

Using the two mechanisms, that is, H_2S oxidation and CuS formation, the response curve of CuO films exposed to 400 ppm H_2S can be understood. As seen in Fig.

3.3 (c and c1), the initial rise in the resistance is due to the domination of the H_2S oxidation mechanism. The other mechanism i.e. CuS formation will cause a decrease in the resistance of the sensor film. These two mechanisms competes each other and when the contributions of both mechanism equalizes, a time independent region is achieved (as shown in Fig.3.3 (c1). For longer period, CuS formation mechanism dominates, which leads to formation of metallic CuS layer around the CuO grains. The improved intergrain connectivity results in a sharp decrease in the resistance. In order to have a recovery, CuS formed at the grain surface need to be converted back in CuO, which takes place via the reaction: $CuS + \frac{3}{2}O_2 \rightarrow CuO + SO_2$. This reaction is very sluggish at room temperature, and therefore, no recovery takes place even after several hours.

In the case of intermediate H_2S concentrations (500 ppb - 50 ppm), the response curve is governed by both H_2S oxidation and CuS formation mechanisms. In this region the sensitivity increases with H_2S concentration because of more $O_2^-{}_{(ads)}$ are consumed. However, the response time is increased as the formation of metallic CuS also takes place, which lowers down the resistance. Formation of CuS also explains the longer recovery time and drifting of the base resistance to lower values.

We have further investigated that if the CuS formed at the surface of CuO grains on exposure to high concentration of H_2S can be converted back to CuO. For this purpose, we have annealed the 400 ppm H_2S exposed CuO film at 350°C for 1 h under flowing oxygen. As expected the CuS indeed was found to convert into CuO without any changes in film morphology, as confirmed by SEM and XPS analysis. Moreover, the base resistance of the CuO films was regained and the response curves for the low concentrations of H_2S were reproduced.

3.2.2 Nanowires based sensors

As discussed in Section 2.2.2 (b), CuO nanowires were grown by thermal oxidation of Cu foils. In this section we discuss growth mechanisms of CuO nanowires. The gas sensing properties of CuO nanowires has been investigated using two different configurations: (i) films of CuO nanowires and (ii) isolated nanowires aligned between two gold contacts.

(a) Growth mechanisms of CuO nanowires

SEM micrographs of nanowires grown by oxidation of Cu sheets for a period of 4 h at different temperatures between 650 and 750°C are shown in Fig. 3.7. The optimum growth of CuO nanowires was found to be at temperature of 675°C. The length of nanowires at 675ºC was found to increase with time and nanowires having length of ~50 μm and diameter in the range of 50 –200 nm could be reproducibly grown in 24 h. It may be noted that at lower growth temperature (i.e. 650°C), the density of grown CuO nanowires is lower. On the other hand, at higher temperatures the diameter of nanowires increases while the length saturates. Almost similar results have been reported by Chen et al and Li et al who used the same method for nanowires synthesis [126, 127].

A typical TEM image of grown single CuO nanowire is shown in Fig. 3.8 (a), which clearly exhibit branching and this phenomenon has been observed in several nanowires. The structure of nanowires studied using transmitted selected area electron diffraction (SAD), as shown in Fig. 3.8 (b), corresponds to the $[10\bar{1}]$ zone axis. Curiously, some extra reflections, encircled by broken circles, at (0 1 0) and (1 0 1) positions are also observed in this diffraction pattern. Stereographic analysis of several nanowires and branches showed that the wire always grew along the [0 1 0] direction while the branching occurred along the [2 1 0] direction. XPS spectrum, as shown in Fig.

3.9 (a), exhibit well-defined shake-up satellite structures on the high binding energy side of the Cu $2p_{3/2}$ core line (centered at 932 eV). These satellites are typical of Cu_2^+ species and confirm that the grown nanowires are CuO and not Cu_2O in which satellites are absent [125].

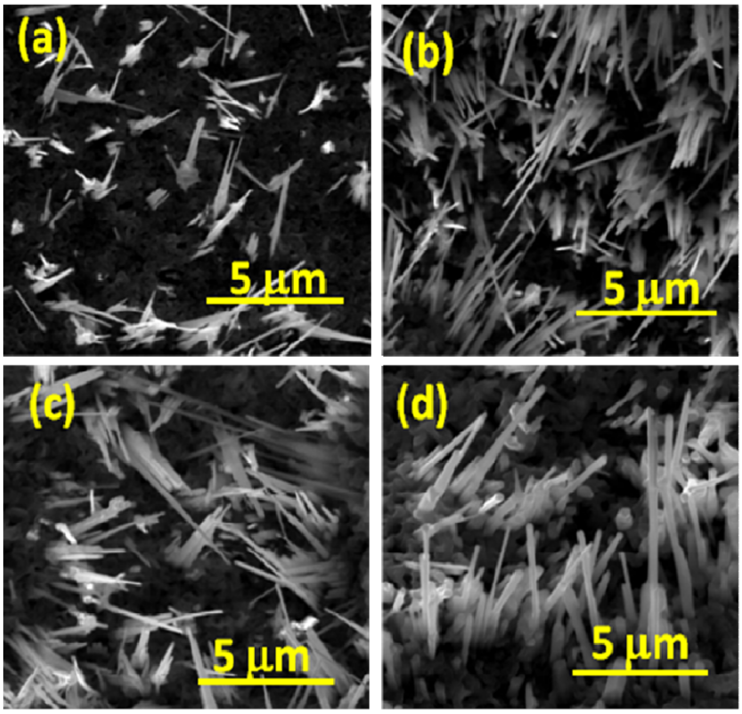

Fig. 3.7. SEM images of CuO nanowires grown by annealing Copper foils at temperatures of: (a) 650°C, (b) 675°C (c) 700°C and (d) 750 °C for 15 mins.

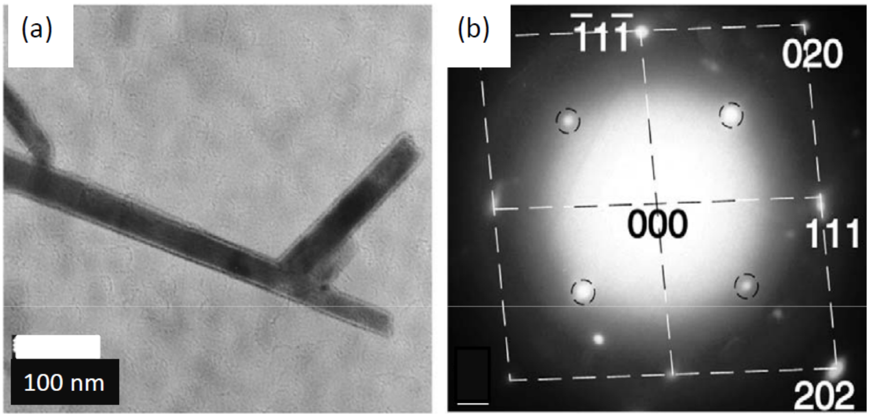

Fig. 3.8. (a) TEM image of branching in a single nanowire (b) SAD pattern corresponding to the [101] zone axis.

We have further determined the energy band gap of the grown CuO nanowires using UV–visible spectroscopy. For this purpose, the CuO nanowires were dispersed in methanol and the UV/vis spectra of the solution was recorded. Typically obtained plot is shown in Fig. 3.9 (b). Frequency dependence of absorption coefficient of semiconductors is given by: $\alpha(\nu)h\nu = A(h\nu - E_g)^{m/2}$, where α is the absorption coefficient, ν is the frequency of photons, A is a proportionality constant and m = 1 for direct transitions. To determine the band gap we have plotted $(\alpha h\nu)^2$ as function of $(h\nu\text{-}E_g)$ in Fig. 3.9 (b). The band gap of CuO nanowires obtained was 2.03 eV, which is slightly higher than that reported for bulk CuO (1.85 eV) [128]. The difference from bulk values is observed because band gap in present study is measured for grown nanowires including the branches.

Now we discuss the growth mechanism of CuO nanowires. The oxidation of Cu metal leads to the formation of two types of cationic deficit p type oxide phases of Cu i.e. Cu_2O (> 270ºC) and CuO (< 270ºC). The formation of CuO nanowires is related to the CuO/Cu_2O interface reaction [129]. In literature, nanowire growth is described using two different mechanisms i.e vapor–solid (VS) or vapor–liquid–solid (VLS). In the case of CuO nanowires, oxidation of Cu occurs at temperatures which are far lower than the melting points of both Cu and its oxides, leading to negligibly small equilibrium vapor pressures. Therefore both VS and VLS mechanisms cannot explain the formation of CuO nanowires. The most accepted mechanism of CuO nanowire formation is based on compressive stresses in the CuO layers. The lattice mismatch at CuO/Cu_2O interface, leads to the stresses which drives outward diffusion of Cu cations, resulting in the growth of CuO nanowires [130].

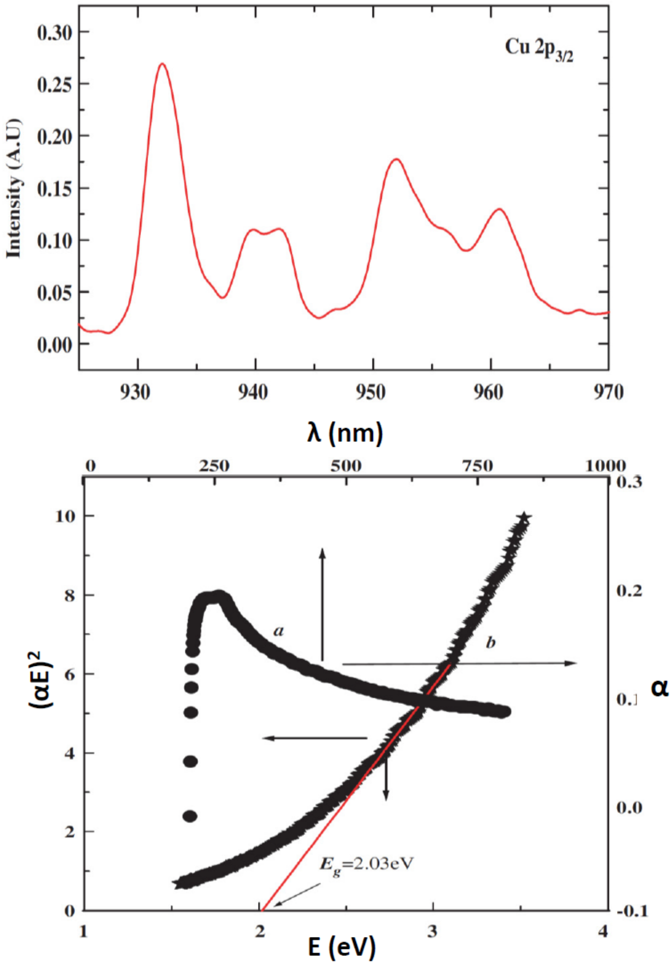

Fig. 3.9 (a) XPS spectra of nanowires in Cu 2p region showing formation of CuO (b) Curve a shows optical absorption spectra of nanowires and curve b shows plot of $(\alpha E)^2$ versus energy for determination of band gap.

(b) Sensing properties of films of CuO nanowires

Films of CuO nanowires were prepared by dispersing the CuO nanowires in methanol and spreading this solution between the two gold electrodes prefabricated on alumina substrate. The response of nanowire films on exposure to H_2S and NO at room temperature are shown in Fig. 3.10. The increase in resistance on exposure to the reducing H_2S (Fig. 3.10 (a)) and decrease on oxidizing NO (Fig. 3.10 (b)) gas indicates the p-type behavior of the NWs films and the mechanism is similar to as the one discussed for CuO thin films (section 3.2.1 (c)). The response and recovery times of sensor films, for 10 ppm H_2S is ~4 and 16 minutes, respectively. In addition the recovery for higher concentrations of H_2S is very slow. These results demonstrate that nanowire CuO films exhibit inferior sensing properties as compared to the CuO thin films prepared by oxidation of thermally deposited Cu films (see Fig. 3.3). This may be attributed to the lack of proper interconnections among CuO nanowires, as can also be seen from the SEM image, Fig. 3.7 (b). However, the sensitivity of CuO nanowire based films, as shown in Fig. 3.10 (b), for NO is very low, making them selective towards H_2S. In literature, CuO nanowire films have also been shown to be sensitive to CO and NO_2 [131].

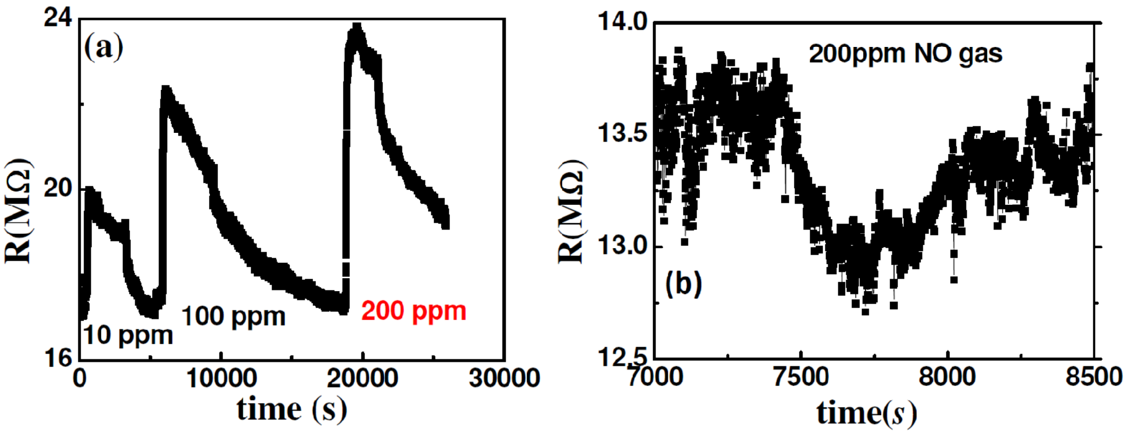

Fig.3.10. (a) H_2S and (b) NO gas sensing characteristics at room temperature for CuO nanowire films.

(c) Sensing properties of isolated nanowires aligned between two electrodes

Dielectrophoresis technique i.e. electric field assisted assembly of nanowires onto pre-fabricated electrodes, has been employed to fabricate isolated CuO nanowire based sensors. The grown CuO nanowires were dispersed in methanol and ultrasonicated for 10 min. A droplet of this nanowires suspension was applied between the pre-fabricated Au electrodes onto alumina substrates. A potential of15 V at 100 kHz was applied acoors the two electrodes. This signal generated an alternating electrostatic force on the CuO nanowires in the solution. Under the electrical polarization force, the CuO nanowires get aligned across the electrodes. By controlling the concentration of the nanowires in the solution, a sample with 3-4 CuO nanowires across the two electrodes was made. Fig.3.11 shows the typical SEM image of an isolated CuO nanowires aligned between two gold electrodes.

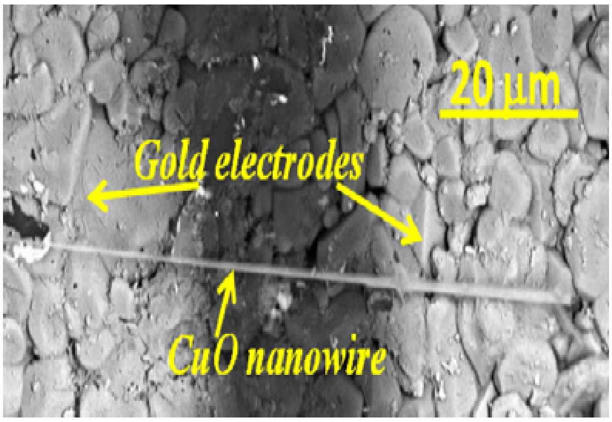

Fig.3.11. SEM of a sample with isolated CuO nanowires

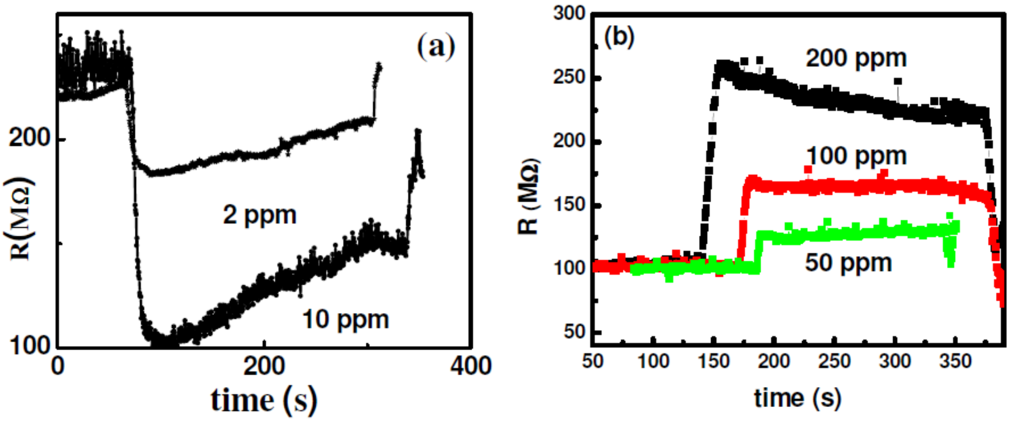

Fig. 3.12. Room temperature gas sensing characteristics of isolated CuO nanowires on exposure to: (a) H_2S and (b) NO.

Gas sensing properties of isolated CuO nanowires were investigated for oxidizing (Cl_2, NO and CO_2) as well as reducing (H_2S, CO) gases. On exposure to H_2S

and NO, the change in resistance is that of n-type, which is in contrast to that expected for p-type semiconductor. This anomalous behavior observed in case of isolated nanowires could be attributed to the contribution from their reactive surfaces due to high surface-to-volume ratio. Any unintentional doping (e.g. Hf, Zr) [132] may lead to the formation of defects giving rise to n-type character which shows dominant effect in case of isolated wires as opposed to nanowires films and thin films.

However, isolated CuO nanowires exhibit good sensitivity for H_2S (~200% for 10 ppm of H_2S gas) with very fast response (30 s) and recovery times (60 s). In addition, CuO nanowires also exhibit reasonably high sensitivity for NO (e.g. for 200% for 200 ppm). These features are far superior as compared to that observed for CuO thin films, and is attributed owing to higher surface-to-volume ratio of nanowires. The flip side of the isolated nanowire sensors is the long term stability, as due to very reactive surfaces the chemisorptions of atmospheric gases modify the surface states and a drift in the base resistance occurs with time.

3.3 n type SnO_2chemiresistive sensors

SnO_2 thin films of identical thickness (400 nm), as discussed in Section 2.2.2 (a), have been deposited using two methods namely, RGTO and sputtering. Here we discuss the morphology and sensing characteristics of these films.

3.3.1 Structure and morphology

Fig.3.13 shows the XRD spectra recorded for RGTO and sputtered SnO_2 films. The spectra matches well with the SnO_2 reference crystal structure assigned to tetragonal rutile structure (space group: D_{4k}^{14}, $P42/mnm$). The peaks marked with asterisk are from the alumina substrate. It is clearly evident from the figure that sputtered SnO_2 are highly oriented along (002) direction, while RGTO films are polycrystalline in nature. Crystallite size calculated using the Scherrer formula for (002) oriented peaks was found to be approximately 76 and 85 nm for RGTO and sputtered films, respectively. The SEM image shown in Fig. 3.14 shows that sputtered films are relatively smoother as compared to that of RGTO films.

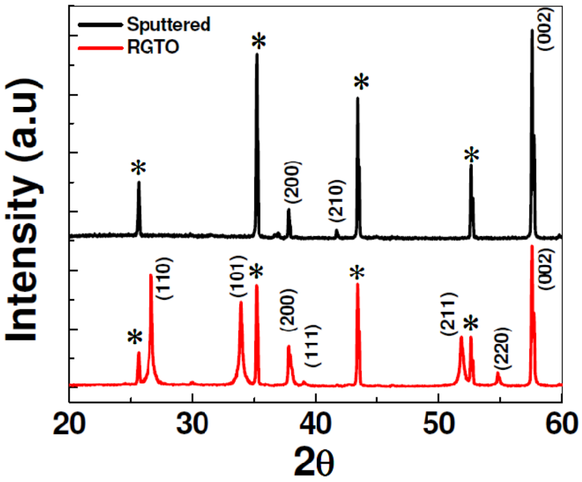

Fig. 3.13 XRD pattern of sputtered and RGTO grown SnO_2 films, the peaks marked with "*" are from alumina substrate.

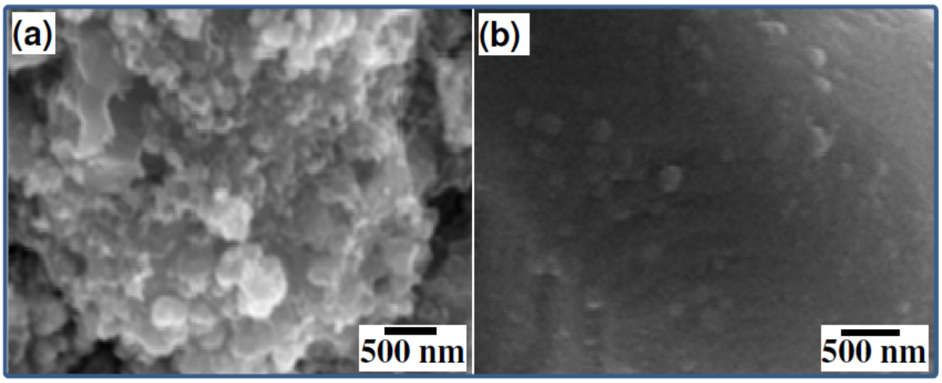

Fig. 3.14. SEM images of (a) RGTO grown and (b) sputtered SnO_2 thin films.

The Sn 3d and O 1s XPS spectra recorded for RGTO and sputtered SnO_2 films are shown in Fig. 3.15. In all spectra the solid squares denotes the experimental data while solid lines represent both the fitted curve and the deconvoluted individual peaks of different species. The residual fit of the spectra is also shown along with the results for comparison. As shown in Fig.3.15 (a) and (c), both the films exhibited two prominent peaks corresponding to the binding energies of $Sn3d_{5/2}$ and $Sn3d_{3/2}$, respectively [133]. The peak to peak separation of Sn 3d peaks for both the sensor films is found to be 8.46 eV. Fig.3.15 (b) and (d) shows a comparison of O1s peak for both the sensor films. The O 1s spectra can be de-convoluted into two different peaks: (i) a major peak at 529.8 eV corresponding to the lattice oxygen peak of $SnO_2$and (ii) a minor peak at 531.2 eV attributed to the chemisorbed oxygen species [134, 135, 136]. From the XPS data, the surface composition (Ci) can be quantified using the relation: $C_i = \frac{n_x}{\sum n_i} = \frac{\frac{I_x}{S_x}}{\sum \frac{I_i}{S_i}}$; where $x; i$ = Sn or O.

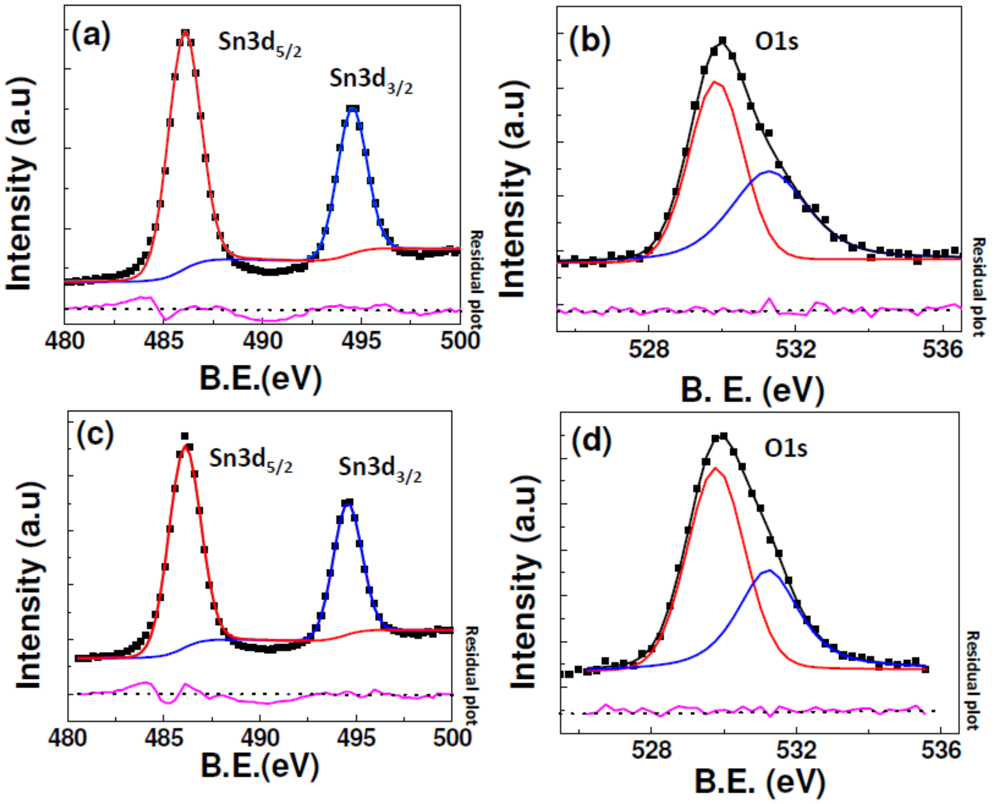

Fig. 3.15. De-convoluted Sn $3d_{5/2}$ [(a) and (c)] and O 1s [(b) and (d)] XPS spectra for RGTO and sputtered SnO_2 films, respectively.

Here I_x represents the intensity of the Sn or O and is determined by finding the total area under the core level peak using the least-squares fitting of Gaussian line shape [137]. S_x is the atomic sensitivity factor and has values of 4.095 and 0.711for Sn $3d_{5/2}$ and O 1s, respectively. The O/Sn ratio thus calculated using equation 4 was found to be 1.66 and 1.33 for RF sputtered and RGTO grown films, respectively. It is clearly evident that the RGTO films are comparatively much more sub-stoichometric or more oxygen deficient than RF sputtered SnO_2 films.

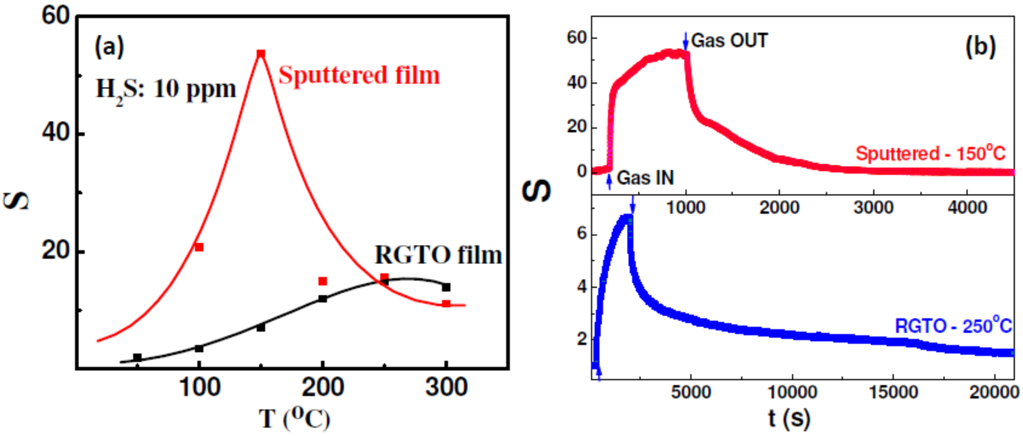

Fig.3.16. (a) Variation of sensor response as a function of operating temperature recorded for both RGTO and sputtered films towards 10 ppm of H_2S (b) Response curves for RGTO film and sputtered film recorded towards 10 ppm of H_2S at an operating temperature of 250 and 150°C, respectively.

3.3.2 Gas sensing characteristics and mechanism

Fig. 3.16 (a) shows the plot of sensor response as a function of an operating temperature towards 10 ppm of H_2S measured for both the sensor films. RGTO films exhibited a maximum response of S= 15 at a temperature of 250°C where as sputtered films exhibited an enhanced response of S = 54 at a lower operating temperature of 150°C. This result clearly indicates that sputtered film exhibited better response towards H_2S in comparison to that of RGTO films. All the further measurements were performed at respective optimum working temperatures which being 150°C for sputtered films and 250°C for RGTO films. Besides lower operating temperature and sensor response values, sputtered films exhibited better response kinetics towards H_2S in comparison to that of RGTO films as also shown in Fig. 3.16 (b). At best optimum temperature, sputtered films exhibited a response and recovery time of 8 and 17 minutes while RGTO films exhibited 5 and 120 minutes, respectively.

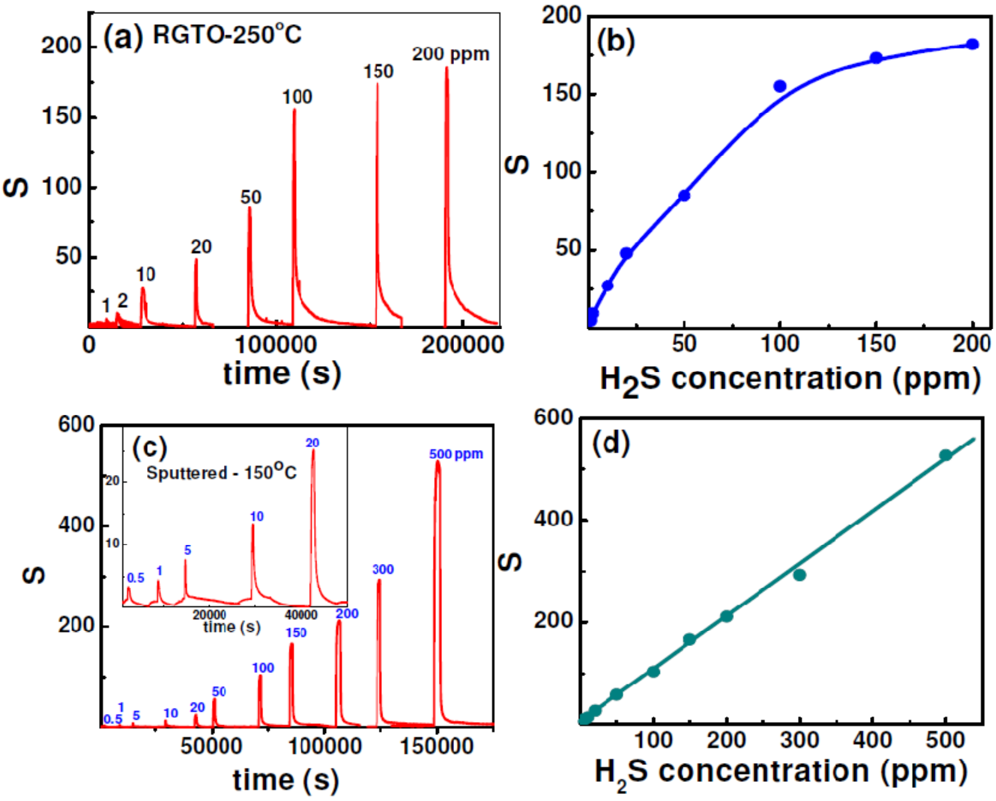

Fig. 3.17 (a) Response curves recorded as a function of H_2S concentration for RGTO films and (b) corresponding plot of sensor response vs. H_2S concentration. (c) Response curves recorded as a function of H_2S concentration for sputtered films and (d) corresponding plot of sensor response vs. H_2S concentration.

Further, a systematic investigation of change in sensor response as a function of gas concentration was carried out and is shown in Fig. 3.17. The response curves indicated that both the sensor films recovered completely and the response was observed to increase with gas concentration (Fig. 3.17 (a) and (b)). For RGTO films the sensors response was found to saturate for concentrations above 100 ppm. For sputtered film, response curves are found to be reversible and repeatable in the wide concentration range from 500 ppb to 500 ppm (Fig. 3.17 (c)). Moreover, the sensor response varies linearly with concentration from 500 ppb to 500 ppm Fig. 3.17 (d). A linear dependence of “S” over such a wide concentration range suggests that RF sputtered films are right candidate for fabrication of gas sensors.

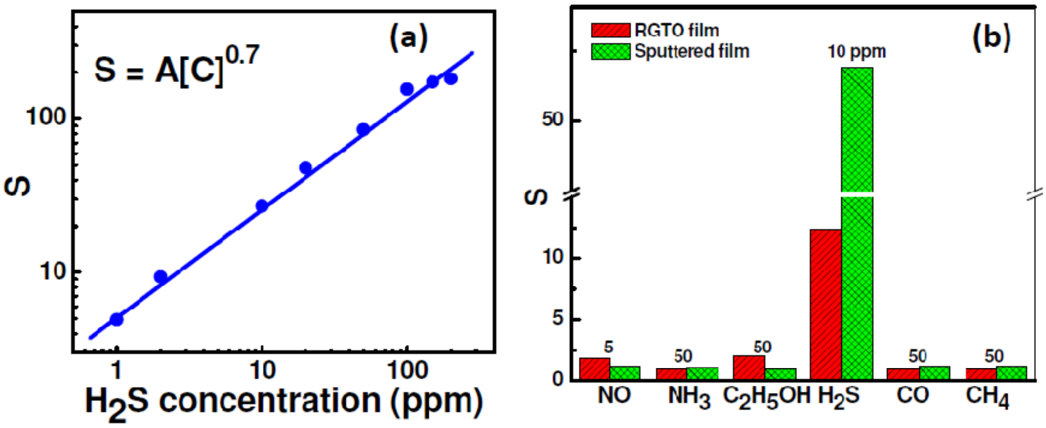

Fig. 3.18 (a) Log-Log plot of response versus concentration for RGTO film showing value of exponent “n” to be 0.7. (b) Selectivity histogram of RGTO and sputter SnO_2 films towards different gases at an operating temperature of maximum sensitivity i.e., 250 and 150°C, respectively. Concentration of the gases tested is mentioned in the histogram.

For metal-oxide sensor, dependence of the sensor response on the H_2S partial pressure at constant temperature has a power-law character: $S = A[C]^n$, where, Sis sensor response, C is concentration and n is a constant. In a recent report Liu et. al. [124] have shown that the value of “n” changes from 1 to 0.5 to 0.25 depending on the species of the chemisorbed oxygen (O_2^- or O^- or O^{2-}). Indirectly, since the chemisorbed species depend on temperature, value of “n” indirectly depends on operating temperature. In the case of RF sputtered films a linear dependence of “*S*” over a wide concentration range suggests the value of exponent to be “1”. The exponent has a value of “0.7” in the case of RGTO film as calculated from slope of log–log plot of response as a function of gas concentrations as shown in Fig.3.18 (a). Different values of exponent in the two cases are justified as the sensor films are operating at two different temperatures. In case of sputtered films at 150°C the chemisorbed oxygen species is mainly O_2^-while in the case of RGTO films both the chemisorbed species namely O_2^- and $O^-$are present due to the higher operating temperature of 250°C. Fig.3.18 (b) showed the selectivity histogram measured for the two types of sensor films towards different gases namely CO, NO, NH_3, H_2S, CH_4 and C_2H_5OH at their optimum operating temperatures.It is observed that both the films are highly selective and sensitive towards H_2S.

At working temperature in air, SnO_2 surface is saturated with chemisorbed oxygen species and the resistance of SnO_2 is at highest level. Upon exposure, chemisorbed oxygen species interacts with H_2S as shown in equations 3.1 (for 150°C) and also as depicted below (for 250°C) [138]: $2H_2S_{(g)} + 4O^-_{(ads)} \rightarrow 2H_2O_{(g)} + 2SO_{2(g)} + 4e^-$, This causes the release of large number of electrons into the conduction band of SnO_2 evident as a sharp decrease in the resistance of the sensor film. As stated above the interaction with the test gas is primarily governed by the nature of the adsorbed oxygen species/oxygen vacancies. XPS analysis indicated that the RGTO grown films are comparatively more oxygen deficient than sputtered films. It has been shown that the increase in the oxygen-vacancy-related defects leads to the enhancement of sensors response and vice-a versa [139, 140]. This has been attributed to the role of oxygen vacancies acting as a preferential adsorption sites for the gas molecules. It is interesting to note that the increase in oxygen vacancy defects also leads to an increase in the charge carrier density. Now as the depletion width is inversely proportional to the square root of the free-carrier concentration, an increase in the electron density results in the corresponding decrease in the modulation of the depletion width and thereby lower sensor response. Thus, oxygen related defects plays the dual role i.e., provides preferential adsorption site and modulates the charge carrier density. The response towards a test gas is governed by the oxygen defects and its interaction with the test gas.

The type of oxygen vacancies present in the sensing material is strongly influenced by the deposition method and thermal treatments namely temperature and time duration of annealing. XRD studies indicated that the sputtered SnO_2 films are highly oriented along (002) direction while RGTO films are polycrystalline in nature. Sputtered SnO_2 films were deposited at room temperature using SnO_2 target without any post deposition oxidation. The films grown by sputtering are known to be well adherent and have composition close to that of the source material. On the other hand RGTO thin films are oxidized at a high temperature of 800°C (1073K). Defect electronic states appearing due to SnO_2 annealing at temperatures less than or above 800 K has been found to result in "bridging-type" and "in-plane-type" oxygen vacancies, respectively [141]. Thus it is expected that for sputtered films the oxygen vacancies present is bridging type.

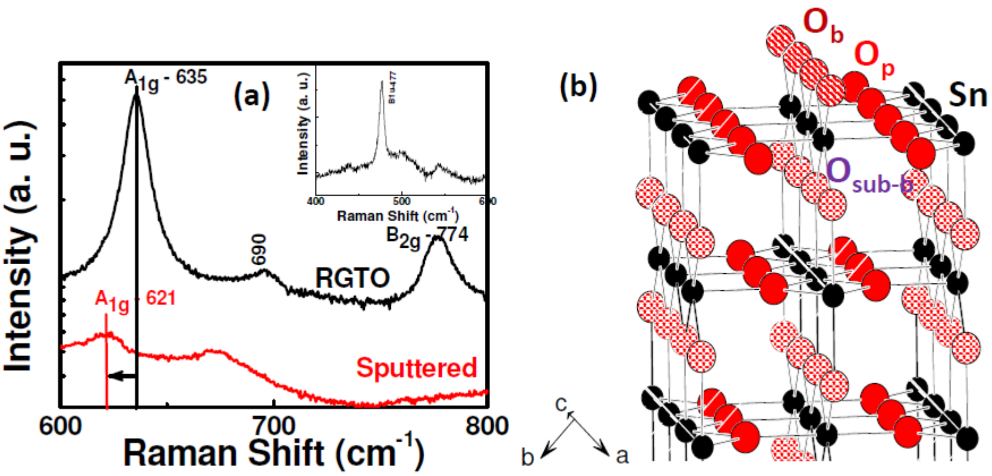

Fig. 3.19 (a) Raman spectra of RGTO and sputtered SnO_2 films. (b) Schematic representation of the different types of oxygen vacancies in SnO_2.

In order to further support the observation Raman measurements were performed as it is a fingerprint technique used to identify the types of oxygen vacancies [142, 143]. Fig.3.19 (a) shows the corresponding Raman spectra recorded for the two sensor films. RGTO films exhibited peaks at 635, 690 and 774 cm^{-1} attributed to the A_{1g}, A_{2u} LO (IR active) and B_{2g} vibrational modes, respectively. The presence of IR modes could be attributed to the nanoscale crystal size or the degree of disorder. Additionally, RGTO films exhibited a peak at 477 cm^{-1} attributed to B_{1u} mode and a broad shoulder type band beginning at ~440 cm^{-1} arising from the deeper oxygen vacancies. Sputtered films exhibited peaks at 621 and 675 cm^{-1} corresponding to A_{1g} and A_{2u} LO (IR active) vibrational modes, respectively. Careful investigations revealed that for sputtered films the peak corresponding to A_{1g} is found to downshift to 621 $cm^{-1}$and could be attributed to the presence of “bridging” oxygen vacancies [[141]]. Hence it can be concluded that though both the films are oxygen deficient, the kind of oxygen deficiency is different in the two cases. In sputtered films oxygen deficiency is attributed mainly to the “bridging” oxygen vacancies and in RGTO film it is attributed to the deeper oxygen vacancies such as "in-plane/sub-bridging" type.

The two type of oxygen vacancies are depicted clearly in Fig. 3.19 (b). SnO_2 crystallizes in a tetragonal rutile structure with $P4_2/mnm$ space group [144]. There are two formula units per primitive unit cell with the threefold-coordinated oxygen atoms forming distorted octahedral configurations around the Sn atoms. An outermost plane of oxygen atoms appearing in rows along c-axis (hatched red symbol with lines - O_b) is composed of “bridging” oxygen atoms. In the second atomic layer, there are five fold-coordinated (Sn_{5c}), six fold-coordinated (Sn_{6c}) Sn atoms and “in-plane” oxygen atoms (red colored - O_p). A third and fourth plane of oxygen atoms located below are “sub-bridging” oxygen atoms (hatched red symbol with squares – $O_{sub\text{-}b}$). During the sputtering process the growing film experiences an intense bombardment of energetic plasma particles namely electrons and negative ions. Bombardment of such energetic particles promotes oxygen desorption and could possibly result in the formation of “bridging” oxygen vacancies. The formation of bridging oxygen vacancies lowers the coordination number of the surface tin cations from an initial value of six to four, which in turn, reduces their charge state from Sn^{4+} to Sn^{2+}. The four- coordinated Sn^{2+} ions are more acidic compared to Sn^{4+} cations and accordingly promotes a higher chemisorptions. Epifani et al. have studied chemisorption properties of these vacancies, by DFT modeling of the NO_2/SnO_2 interaction and suggested that the in-plane vacancies facilitate the NO_2 adsorption at low operating temperatures, while the bridging vacancies, enhance the charge transfer from the surface to the adsorbate [145]. Thus, the better sensing properties exhibited by sputtered SnO_2 films could be attributed to the existence of bridging type oxygen vacancies. The bridging type oxygen vacancies serve as a preferential adsorption site for gas molecules. These vacancies further enhances the charge transfer processes between the sensor surface and the H_2S gas molecules and results in a better response as well as faster response kinetics.

3.4 ZnO nanoparticles and nanowires chemiresistive sensors

In this section, we discuss the results obtained on ZnO nanoparticles, which were synthesized using chemical route, as described in section 2.2.2 (b). These ZnO nanoparticles were also used as a seed layer for the growth of random ZnO nanowire networks.

3.4.1 TEM, SEM and XRD studies

Chemical route for the synthesis of nanoparticles provides an advantage of precise control over the particle size. In present case particles of size 5, 10 and 15 nm were obtained using 5, 10 and 15 mM solution of zinc acetate dihydrate along with 30, 30 and 45 mM solution of NaOH at growth temperatures of 60, 65 and 75°C, respectively. Fig. 3.20 shows the corresponding TEM micrographs of typical nanoparticles.

The results of ZnO nanowires grown on Si substrates without seed particles and with seed ZnO nanoparticles for different growth time are shown in Fig. 3.21. It is seen that the ZnO nanowires grown on substrates with seed ZnO nanoparticles are more uniform and have lower diameter of 50-100 nm compared to ~500 nm for those grown on substrates without seed. Length of ZnO nanowires was found to increase with increase in growth time. ZnO nanowires grown on substrates with seed particles were used for further studies.

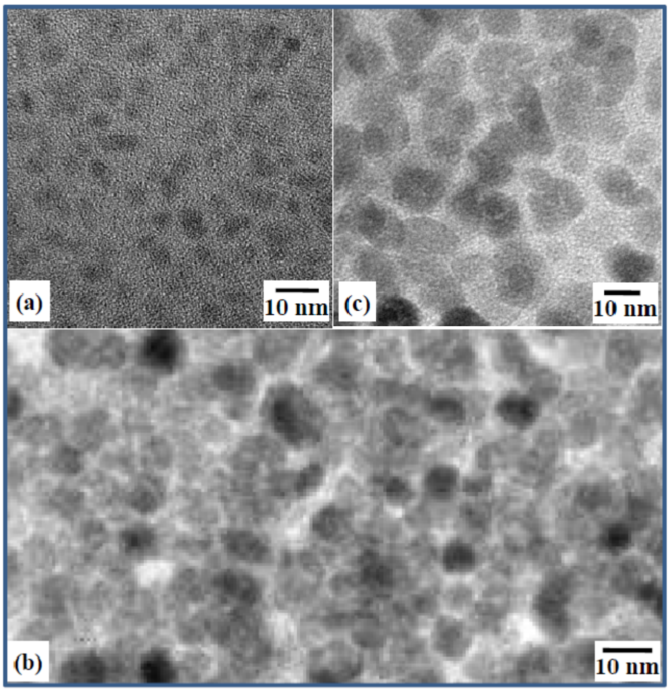

Fig. 3.20. TEM micrograph of ZnO nanoparticles of sizes (a) 5, (b) 10 and (c) 15 nm, respectively.

Fig. 3.22 shows the XRD patterns recorded for ZnO nanoparticles and random oriented ZnO nanowires films. Both the XRD patterns could be indexed to the pure hexagonal wurtzite structure of ZnO. ZnO nanoparticle films are found to be polycrystalline in nature with broadening of the peaks as compared to ZnO nanowires.

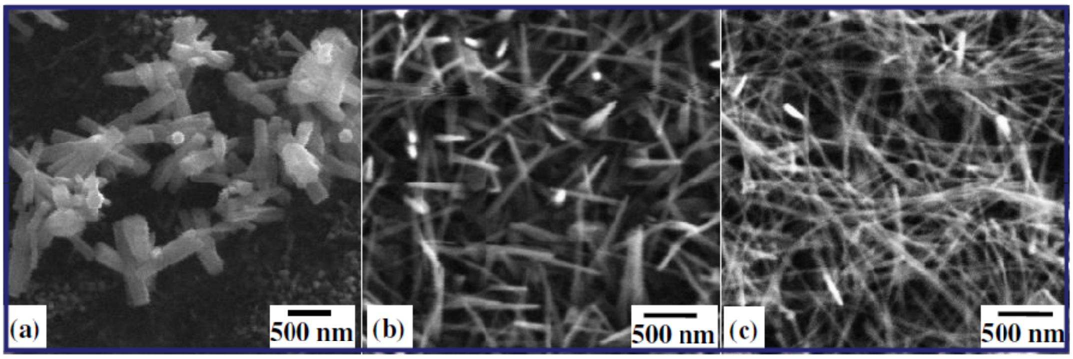

Fig. 3.21. SEM images of nanowires grown on silicon substrates: (a) without seed particles and with seed ZnO nanoparticles for (b) 6 h and (c) 21 h growth times.

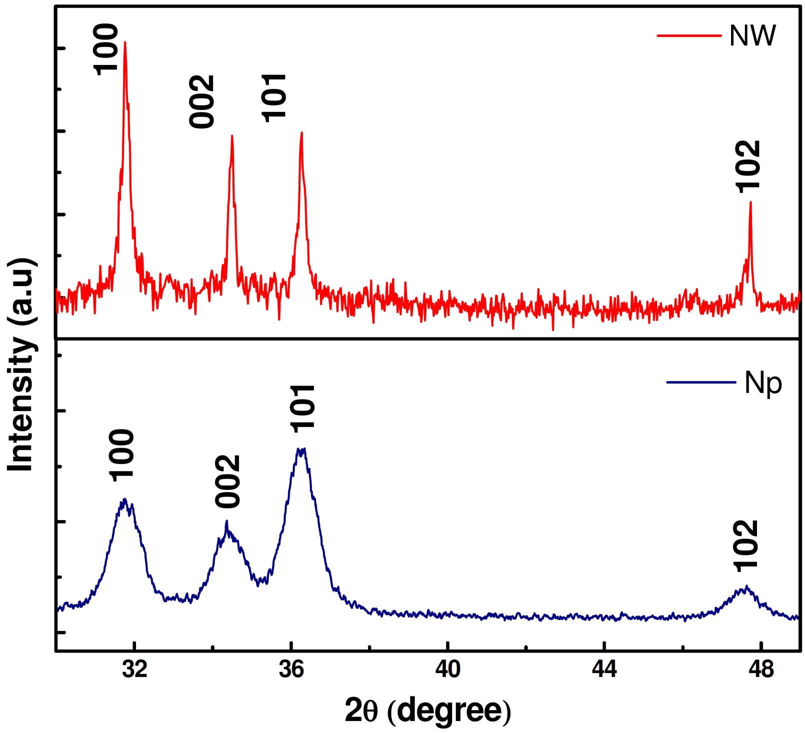

Fig. 3.22. XRD patterns recorded for ZnO nanparticle and nanowires films.

3.4.2 Gas sensing studies and sensing mechanism

Response of ZnO nanowire films was investigated on exposure to 30 ppm of H_2S as a function of temperature and the results for a typical sensor are shown in Fig. 3.23 (a), along with the corresponding response and recovery times (Fig. 3.23(b)). Sensor response is found to increase with temperature with maximum at 350°C. As expected both the response and recovery times were found to decrease with increase in the temperature. For optimum temperature of 350°C, the response and recovery times were 11 and 65 s, respectively. Annealing the films upto 900°C for 1 h did not have any significant effect on the sensing characteristics. Response curves of nanowire films towards different concentrations of H_2S and at optimum operating temperature of 350°C are shown in Fig. 3.23 (c) and concentration dependence of response is shown in Fig. 3.23(d). These characteristics were obtained at fixed applied voltage of 1 V. It is seen that the nanowire films can reliably detect H_2S at 1 ppm concentration. Sensor response is also observed to increase with concentration saturating at around 15 ppm according to equation 3.4 and the value of n was found to be 0.7. The power law dependence arises from receptor and transducer functions i.e., the adsorption or interaction of H_2S with the sensor surface and the change of surface potential, respectively.

The sensor response was also compared with that on other test gases and the results on exposure to 30 ppm of different gases are depicted in Fig. 3.24(a). It is seen that the NW-films have negligible response to other oxidizing and reducing gases except chlorine indicating partial selectivity. For comparison a typical response curve on exposure to Cl_2 at 5 ppm concentration is shown in Fig. 3.24 (b). Exposure to high concentrations of Cl_2 (>20 ppm) was observed to deteriorate the sensor film resulting in incomplete recovery.

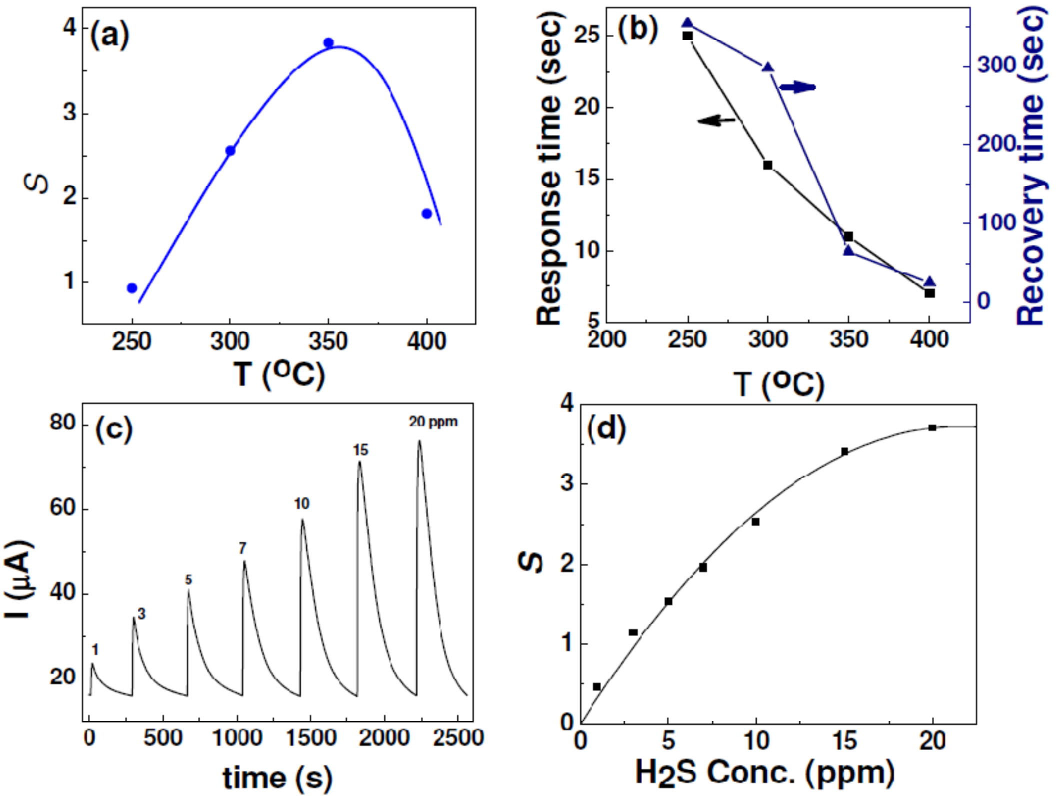

Fig. 3.23 (a) Response of typical nanowires-film on exposure to 30 ppm of H_2S gas as a function of temperature and (b) the corresponding response and recovery times. (c) Response curves of ZnO nanowires-film towards different concentrations of H_2S at an optimum operating temperature of 350°C and (d) corresponding concentration dependence of sensor response.

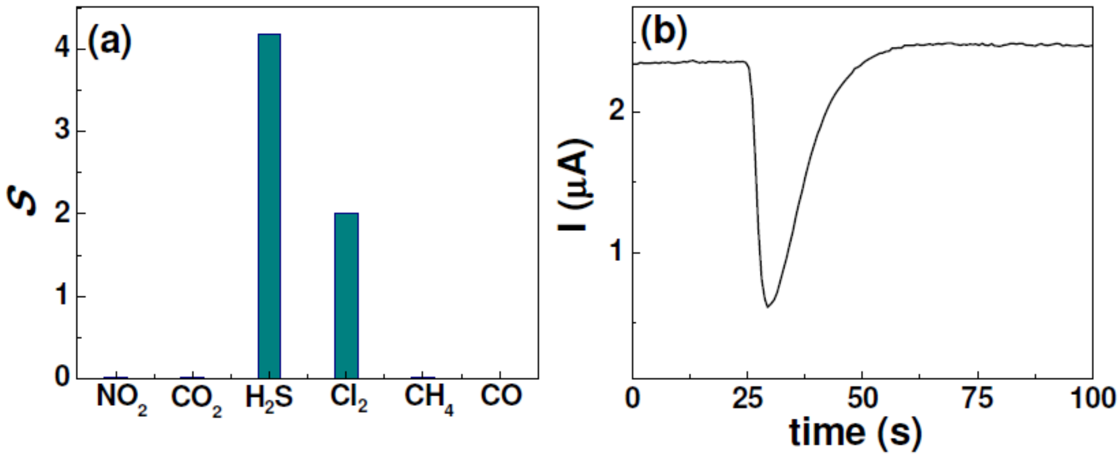

Fig. 3.24. (a) Selectivity histogram of ZnO nanowires-film towards 30 ppm of different gases (except Cl_2 at 5 ppm) and (b) sensors response curve towards 5 ppm of Cl_2.

Response of nanoparticles-films (size:10 nm) was also studied on exposure to H_2S and Cl_2 gases at 350°C and response on exposure to 10 ppm of these gases is shown in Fig. 3.25. Nanoparticles are found to have lower response to the gases and interestingly the change in resistance is in opposite direction to that of nanowires indicating p-type conduction in nanoparticles. We may add that nanoparticles also showed p-type behavior at room temperature though response and recovery times were significantly higher which were 2 s and 12 s respectively for Cl_2 and 10 s and 40 s respectively for H_2S.

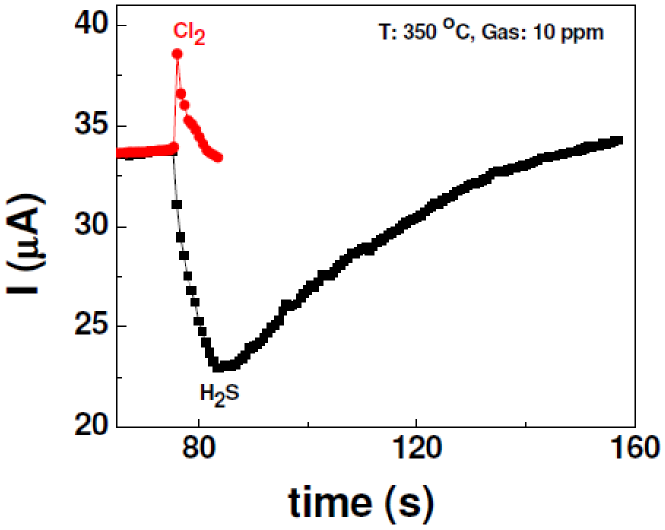

Fig. 3.25. Response curves of ZnO nanoparticles-film towards 10 ppm of H_2S and Cl_2 gases at an operating temperature of 350°C.

To understand the opposite response of nanowires and nanoparticles to H_2S and Cl_2, we note that oxygen is mainly adsorbed on the sensor surface in ionic forms. The adsorbed oxygen traps electrons from bulk of oxide and causes increase in resistance of n-type materials and decrease in resistance of p-type material. On exposure to H_2S gas at an operating temperature of 350°C, O^{2-} species interacts with H_2S resulting in release of electrons as per the reaction [146]: H_2S (g) + O^{2-} (ads) → $SO_2 + H_2 + 2e^-$. This causes release of the trapped electrons resulting in decrease in resistance for n-type and increase in resistance for p-type material. An opposite response on interaction with Cl_2arises due to reactions: $\frac{1}{2}Cl_2 + e^- \rightarrow Cl^-_{(ad)}$ and $\frac{1}{2}Cl_2 + e^- + V_O \rightarrow Cl^-_O$; where subscripts (ad) and (o) indicate species adsorbed on the surface and occupying oxygen lattice site and V_O indicates vacancy at oxygen site, respectively. As, on exposure to Cl_2, additional electrons are trapped from the oxide lattice, it has opposite effect on resistance to that of H_2S. Our data in Fig. 3.24 and 3.25, therefore indicates that the nanowires are n-type and nanoparticles are p-type.

The formation of n-type nanowires and p-type nanoparticles were independently confirmed by hot probe and Kelvin probe CPD measurements, respectively. For hot probe measurements, thin films of required nanomaterial (with two Au electrode contacts) were heated from one end and the developed thermo-e.m.f was measured. With the hot and cold probes connected to positive and negative terminal of the voltmeter respectively, a negative voltage for nanoparticles-films and positive voltage for nanowires-films were obtained confirming the p-type and n-type nature of nanoparticles and nanowires, respectively.

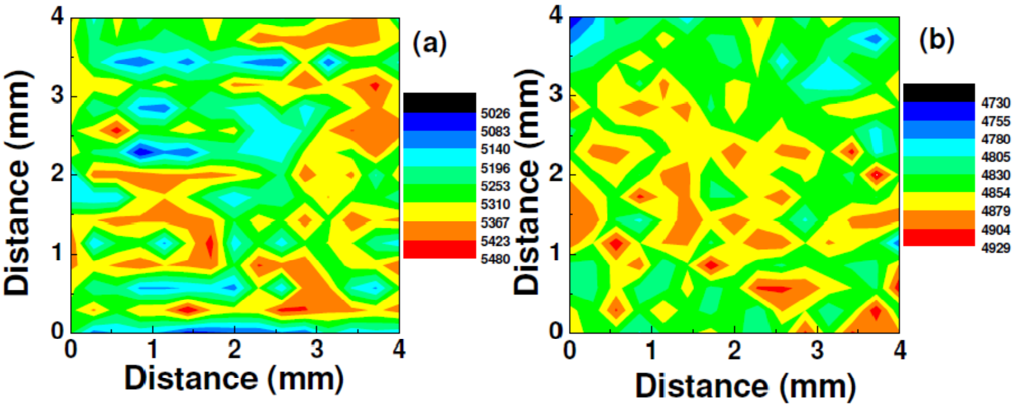

Fig. 3.26. 2-D work function map of ZnO (a) nanoparticles-films and (b) nanowires-films on indium tin oxide (ITO) substrate.

Fermi level of a semiconductor is close to conduction band for n-type and to valence band for p-type materials. Therefore, it is expected that the work function of a material should increase when the nature of conductivity changes from n to p-type. To confirm difference in nature of conduction for nanoparticles and nanowires, thin films of both materials were deposited on indium tin oxide (ITO) coated glass substrates and work function was scanned across the substrates (4 x 4 mm^2 size) by Kelvin probe. The results shown in Fig. 3.26 give average work functions of 4.8 and 5.3 eV for nanowires- and nanoparticles-films respectively, which is in accordance with the change in nature of conductivity from n to p-type.

The origin of p-type as well as n-type character of ZnO is a current matter of debate. The n-type behavior is usually attributed to oxygen vacancies and/or native defects like H [147,148]. Whereas, the p-type nature of ZnO is attributed to the zinc vacancy, surface acceptor levels created by the adsorbed oxygen and/or the unintentional carbon doping in ZnO [149,150,151]. In the case of carbon doping, carbon immobilizes the oxygen in the interstitial site forming a carbon-oxygen cluster defect that acts as a shallow acceptor [152]. In the present work, nanoparticles were prepared by using zinc acetate dihydrate as the starting material, which is known to induce Zn vacancies in ZnO, and hence a p-type conductivity [153]. On the other hand, nanowires were grown from zinc nitrate hexahydrate, which possibly incorporates the oxygen vacancies in ZnO, and therefore, produces n-type conductivity.

3.5 Conclusions

In this Chapter we have investigated room temperature sensing characteristics of p-type CuO in three different forms i.e. thin films, nanowire thin films and isolated nanowires. The isolated nanowires exhibited n-type behavior owing to the surface states created by unintentional doping. These isolated CuO nanowire sensors exhibited fastest response and recovery times, as expected owing to large surface-to-volume ratio. Unfortunately these sensors exhibit poor long term stability, as due to very reactive surfaces the chemisorptions of atmospheric gases modify the surface states and a drift in the base resistance occurs with time. Moreover, making electrical contacts to isolated nanowires is a key issue. In terms of long term stability and facile fabrication, CuO thin film based sensors are the best. These sensors exhibited a base line resistance drift of <5%. Also these sensors were capable of detecting the H_2S at ppb levels, as CuO chemically reacts with H_2S. However, for very high H_2S concentrations (>50 ppm), CuO nanowires based sensors exhibited better response/recovery as compared to CuO thin films.

n-type SnO_2 thin films have been prepared by RGTO and sputtering techniques. Sputtering method yielded films of uniformly distributed grains of relatively smaller in size, and hence, exhibited better sensitivity and response/recovery kinetics for H_2S as compared to RGTO films. Moreover, the optimum operating temperature of sputtered films was found to be quite lower (150°C) as compared to that of RGTO films (250°C). The improved response of sputtered films has been attributed to the oxygen deficiency (in particular the presence of bridging type oxygen vacancies) on the surface of sputtered SnO_2 films that facilitated the charge transfer between the sensor surface and the H_2S molecules. Unlike, p-type CuO thin films, SnO_2 thin films could not detect ppb level H_2S. However, thin films of n-type SnO_2 exhibited better long term stability as compared to p-type CuO films.

n-type ZnO sensors was investigated in two configurations, i.e. nanoparticles and nanowires. The response curves measured for nanoparticle films and nanowire films, exhibited respectively p- and n-type responses towards both reducing and oxidizing gases.

The n-type behavior of nanowires films is attributed to oxygen vacancies, whereas the p-type nature of nanoparticle films is attributed to the zinc vacancy. Nanowire films detected H_2S in ppm range with fast response and recovery times. Nanoparticles based sensors were not found stable for periods > 2 weeks as nanoparticles got agglomerated with time.

Chapter 4

p- n Junctions Type Chemiresistive Sensors

4.1 Introduction

In this chapter, we discuss the mechanisms involved in governing the gas sensing properties of p-n junction type chemiresistive gas sensors. The p-n junctions investigated are: (i) n- ZnO nanowires: p-CuO, n-WO_3: p-CuO and n- SnO_2: p- Fe_3O_4. It has been demonstrated that in all the cases, p-n junction's based sensors gas yield improved sensing properties as compared to the individual layer. The gas sensing mechanism has been probed using photoluminescence, work function and Raman studies.

4.2 CuO: ZnO nanowires chemiresistive sensors

In this section, we present gas sensing characteristics of random p-n junction networks consisting of n- ZnO-nanowires and p-type CuO and investigate the involved mechanisms. ZnO-nanowires: CuO random networks were prepared in two steps: (i) growth of ZnO-nanowire random networks on the native-oxide surface of Si by hydrothermal process (as discussed in Section 2.2.2 (b) (ii)) and (ii) deposition of CuO films of varying thickness between 5 and 100 nm onto ZnO-nanowires networks. The deposition of CuO films is described in Section 2.2.2 (a) (i).The optimization of gas sensing characteristics revealed that ZnO-nanowire: CuO (10 nm) random networks are highly sensitive and selective to H_2S.

4.2.1 Structural, morphological and compositional analysis

Fig. 4.1 (a) shows the results of EDX analyses of ZnO-nanowires: CuO networks with varying thickness (d) of CuO layer. The plot between measured Cu (at.%) as a function of nominal thickness (d) of the deposited CuO layer indicates a linear dependence. Fig. 4.1(b) shows the SEM image of the as grown ZnO-nanowires network.

It is evident that randomly grown ZnO-nanowires (diameter: 50-200nm and length 1-2 μm) form a dense network. The quasi-hexagonal ends of the ZnO-nanowires indicate that their main axis is preferentially oriented along the [0001] direction, which is in accordance with the growth habit of wurtzite crystals. The variation in the diameter of the ZnO-nanowires and their alignments with respect to the substrate surface is attributed to the random distribution of different sizes of seed ZnO nanoparticles (5-10 nm).

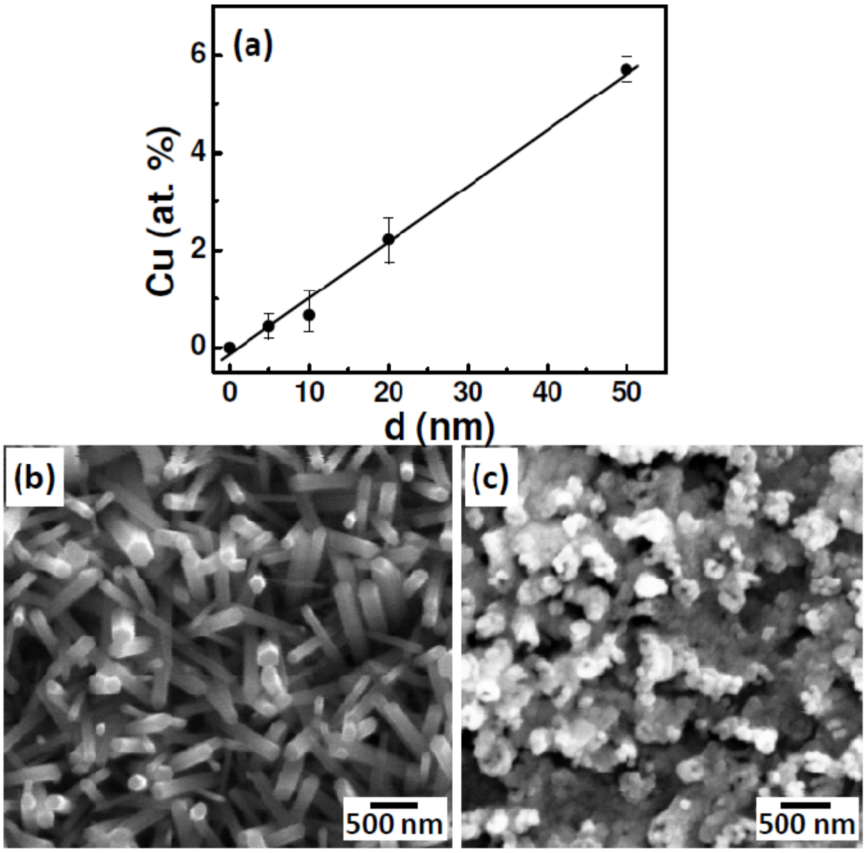

Fig. 4.1 (a) Measured Cu (at.%) in the CuO (d nm):ZnO- nanowires random networks as a function of the nominal thickness (d) of the CuO. SEM image of (b) ZnO- nanowires and (c) CuO (100 nm):ZnO- nanowires random networks.

The surface morphology of CuO: ZnO-nanowires network did not change upon deposition of CuO layers upto a nominal thickness of 10 nm. This is expected as at very low thicknesses ≤10 nm), CuO does not make a full coverage on ZnO-nanowires network. It can reside on the surface of ZnO-NW in the form of small aggregates and occupy the gaps between ZnO-nanowires facilitating the formation of random p-n junctions, which is confirmed by electrical resistance and photoluminescence studies (as discussed later). However, at very high nominal thickness, CuO makes a full coverage over ZnO-nanowires network, which is evident from the SEM image shown in Fig. 4.1 (c).

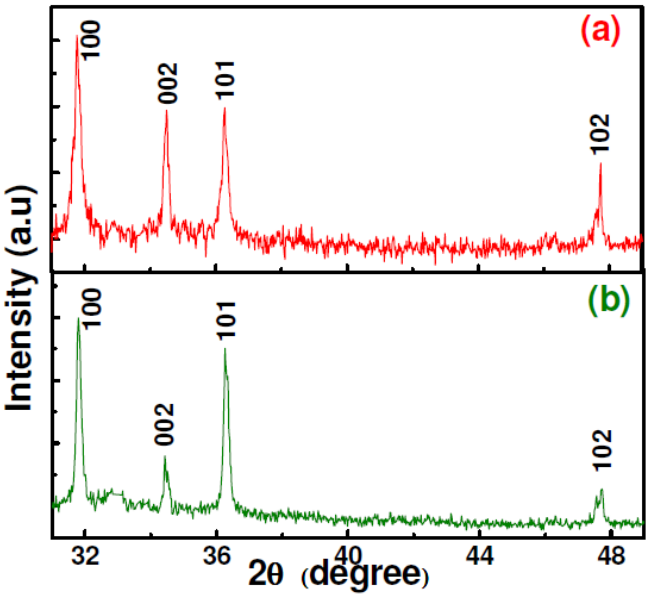

Fig. 4.2. XRD patterns recorded for (a) ZnO-nanowires and (b) CuO (10nm):ZnO-nanowires random networks.

Fig. 4.2 (a) and (b) shows the XRD pattern of random ZnO-nanowires and CuO (10nm):ZnO-nanowires networks, respectively. No characteristics peaks of the impurities corresponding to the precursors zinc nitrate and HMTA were observed in the XRD patterns. Presence of (100), (002), (101) and (102) peaks clear indicates that ZnO-nanowires are randomly oriented, which is in accordance with the SEM image. Interestingly, for low nominal thickness of CuO neither any shift in the XRD peak positions (indicating no chemical reaction between ZnO and CuO) nor presence of peaks corresponding to CuO (due to the quantity being less than the detection limit of XRD, 5 at%) was observed.

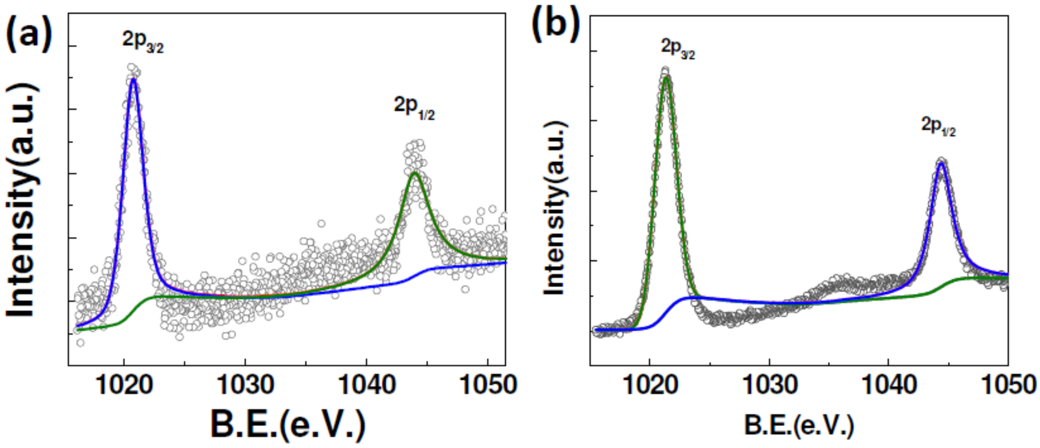

Fig. 4.3 Zn 2p spectra recorded for (a) pure ZnO and (b) CuO/ZnO nanowire network.

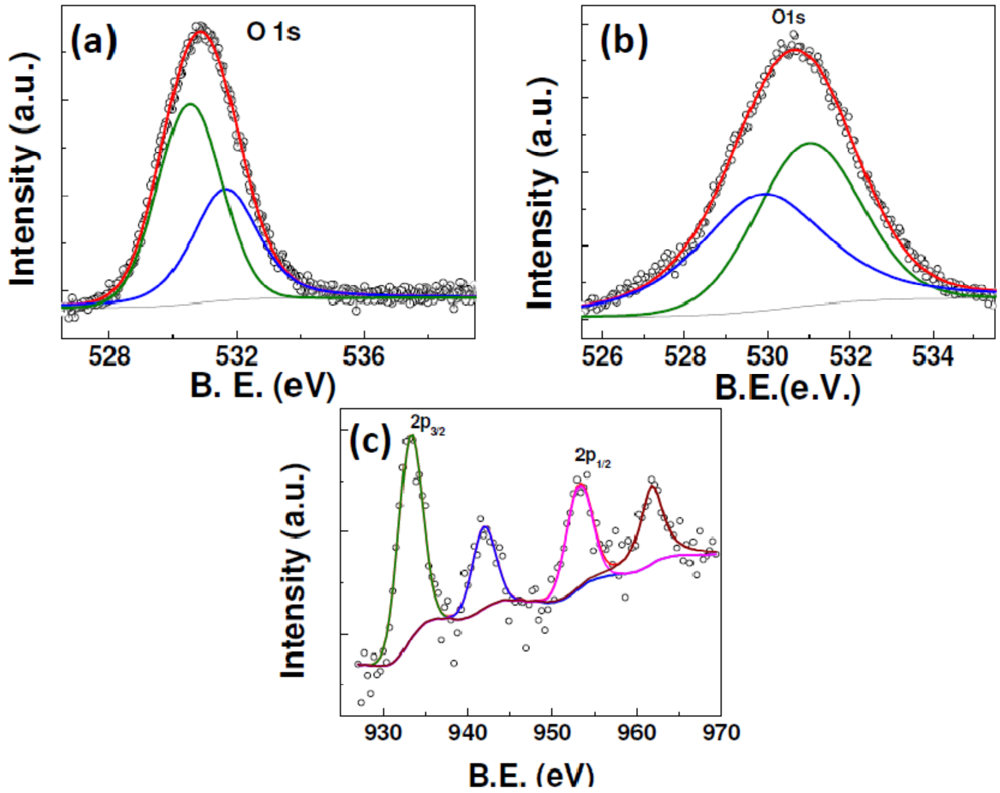

Fig. 4.4 O 1s spectra recorded for (a) pure ZnO and (b) CuO/ZnO nanowire network (c) Cu 2p spectra recorded for CuO/ZnO nanowire network.

The thickness of 10 nm corresponding to the 0.66 at.% as measured using EDX analysis was chosen as this composition gave the best response towards H_2S. In order to confirm the formation of CuO, XPS measurements were performed. Fig. 4.3 shows the deconvoluted Zn 2p spectra recorded for both pure and CuO-modified ZnO NWs. In all the spectra, the hollow circles represent the original data, while the solid lines represent both the fitted curves and the deconvoluted individual peaks of different species. For pure ZnO, two peaks at BE values of 1020.8 and 1043.9 eV corresponding to Zn 2p3/2 and 2p1/2, respectively, were observed. While for CuO-modified samples, the peaks were observed at BE values of 1021.3 and 1044.3 eV, respectively. Fig. 4.4 shows the O 1s spectra for both the samples. For pure ZnO, oxygen peak can be deconvoluted into two individual peaks at BE values of 530.5 and 531.6 eV corresponding to O 1s and adsorbed oxygen species, respectively. Interestingly, for CuO-modified samples, the oxygen peak can be deconvoluted into two individual peaks at BE values of 529.9 and 531 eV. The low-intensity peak at 529.9 eV could be attributed to the O 1s corresponding to CuO. Interestingly, for CuO modified samples the original data can be fitted and deconvoluted into individual four peaks at binding energies of 933.2, 941.9, 953.2 and 961.7 eV, respectively. The two peaks located at 933.2 and 953.2 eV correspond to the Cu $2p_{3/2}$ and $2p_{1/2}$ core levels, respectively [154]. Shake up features at 941.9 and 961.7 eV for the Cu $2p_{3/2}$ and $2p_{1/2}$ core levels are evident and diagnostic of an open $3d^9$ shell corresponding to Cu^{2+} state [155]. The presence of satellite peaks confirms the formation of CuO phase. The relative intensities of the shakeup lines to the main core level of both the Cu $2p_{3/2}$ and $2p_{1/2}$ is a function of Cu concentration [125]. For the case of Cu_2O formation, the core level Cu $2p_{3/2}$ peak appears at 932.5 eV [156]. Thus, XPS studies clearly indicate that Cu exists in Cu^{2+} state in the form of CuO over ZnO-nanowires random network.

4.2.2 Optical properties

(a) Photoluminescence studies

In order to investigate the nature of interaction between ZnO-nanowires and CuO we have carried out PL studies. Typical room temperature PL spectra recorded for ZnO-NW and CuO(10nm):ZnO-nanowires random networks are shown in Fig. 4.5 (a). The inferences drawn from this figure are:

(i) Both the spectra have a peak at 384 nm corresponding to a near band edge emission (NBE) of ZnO [157].

(ii) In the case of CuO(10nm):ZnO-nanowires random network, no NBE of CuO (~285 nm) appears, as CuO does not luminesce in the measured spectral range. The absence of luminescence in the 520 nm region indicates that the sample does not contain Cu_2O and the deposited Cu on annealing has been oxidized to CuO [158].

(iii) For ZnO-nanowires network, the broad band peak at 595 nm could be attributed to oxygen vacancies [159]. However, for CuO(10nm):ZnO-nanowires network, this band not only broadens and intensifies but its peak position also shifts to higher wavelength (i.e. 627 nm). The origin of such a peak has been attributed to the plasma resonances of oxidized copper aggregates.

Another interesting feature of PL spectra is the quenching of ZnO NBE by ~42% on CuO deposition. This phenomenon can be explained based upon the formation of p-n junction between p-type CuO and n-type ZnO, as schematically shown in Fig. 4.5(b). When a photon is incident on the sample, electron gets excited into the conduction band leading to the formation of an exciton. The p-n junction enhances the dissociation of excitons as ZnO transports electrons away and CuO transports the holes. Dissociation of excitons greatly suppresses the electron-hole recombination necessary for PL emissions [160].

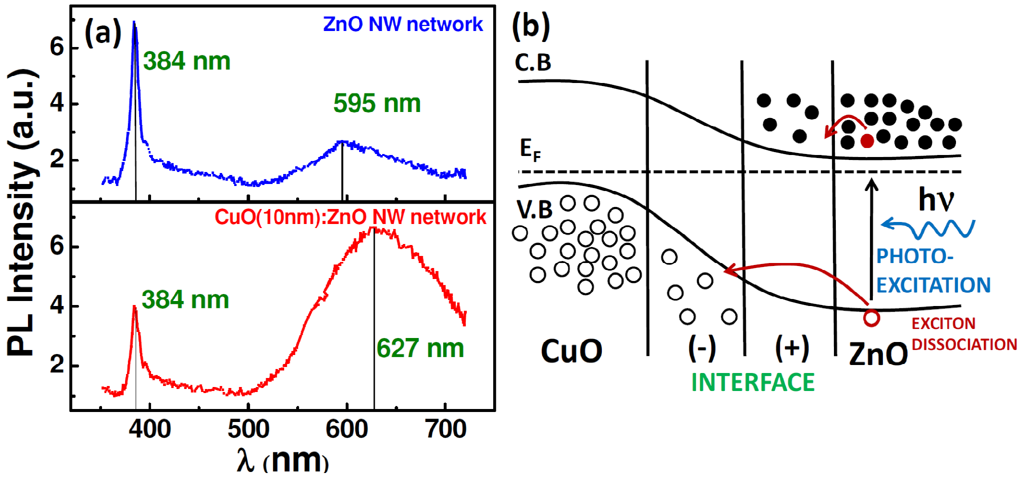

Fig. 4.5 (a) Room temperature PL spectra recorded for ZnO-nanowires and CuO (10nm):ZnO-nanowires random networks. (b) Schematic representation of the formation of p-n junction between CuO and ZnO and quenching of near-band edge emission of ZnO due to dissociation of excitons.

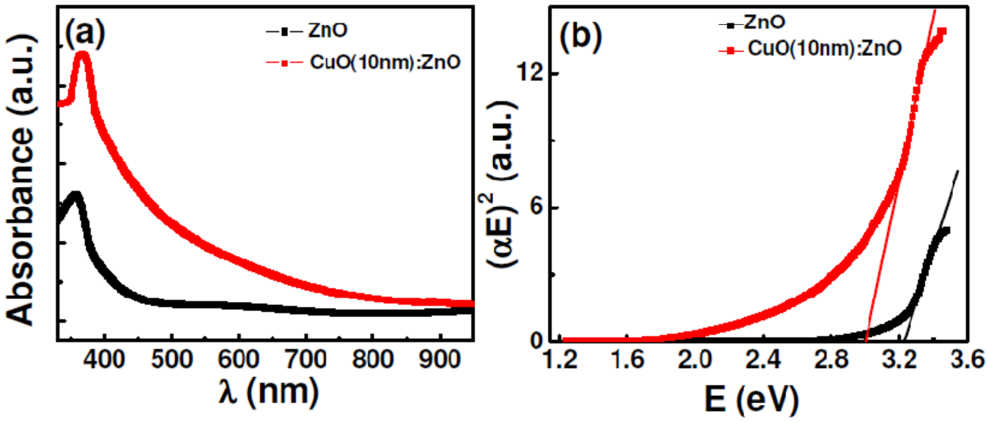

Fig. 4.6 (a) UV-vis absorbtion spectra of pure and CuO modified ZnO nanowires network and (b) plot of $(\alpha E)^2$ vs. E for pure and CuO modified ZnO nanowires network.

(b) UV-visible spectroscopy

Fig. 4.6 shows the Uv-visible spectra of pure and CuO modified ZnO-nanowires. As seen in the Fig.4.6 (b), pure ZnO exhibits UV band extending from 3.6 to 2.75 eV, while CuO modified ZnO-nanowires show broader UV band with considerable absorption in visible range extending from 3.56 to 1.42 eV. Also, the band edge absorption is red shifted in case of CuO modified ZnO-nanowires from 3.2 eV (consistent with exciton absorption of ZnO) [161] to 3.0 eV. The band edge absorption of CuO is at ~1.7 eV which triggers the absorption in CuO modifiedZnO-nanowires over a wide range. This may also be attributed to the formation of an excess defects at the interface of ZnO-nanowires and CuO, which is of particular importance for gas sensing applications [162].

4.2.3 Electrical properties

In order to further investigate the effect of p-n junction formed between CuO and ZnO-nanowires on the electrical properties of networks, we have measured the room temperature electrical resistance as a function of CuO layer thickness, and the results are presented in Fig. 4.7. In order to generate better statistics, we have measured at least 3 samples for each nominal thickness of CuO. The results unambiguously show that the resistance increases sharply upto a nominal thickness of 10 nm and then decreases monotonically.

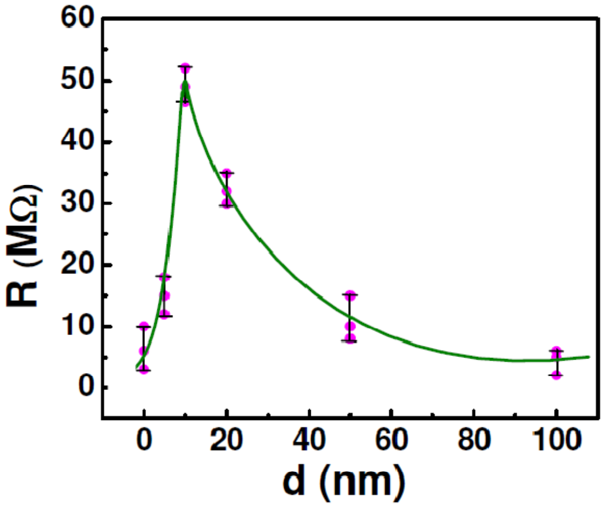

Fig. 4.7 Variation of room temperature electrical resistance of CuO (d nm): ZnO-nanowires random networks as a function of the nominal thickness (d) of the CuO. The Y-axis variation shows the range of resistance measured for different samples of same nominal thickness of CuO.

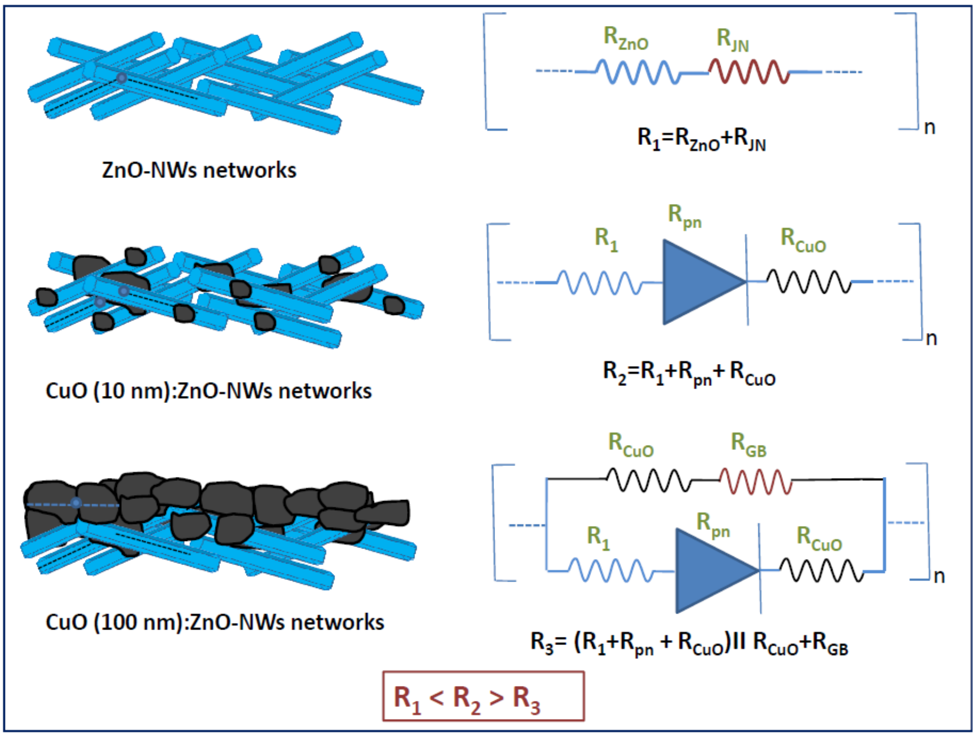

Fig. 4.8 Schematic representation of the equivalent electrical circuit of different CuO:ZnO-nanowires random networks.

This result can be explained on the basis of equivalent electrical circuits of the different samples, as schematically depicted in Fig. 4.8. The electrical resistance (R_1) of bare ZnO-nanowires network can be represented as the series resistance of the ZnO-nanowires (R_{ZnO}) and the junction resistance formed between the ZnO-nanowires (R_{JN}). The resistance (R_2) of ZnO-nanowires network modified with a CuO layer upto a nominal thickness of 10 nm can be represented as a series equivalent to that of R_{ZnO}, R_{JN}, p-n junction and CuO aggregates. Due to the presence of p-n junction the value of R_2 is expected to be very high. However, at very high nominal thickness, CuO fully covers the ZnO-nanowires network (as also seen in SEM image). Thus a continuous CuO layer acts as a parallel resistance, which reduces the total resistance (R_3) of the sample. Herein the CuO layer contributes two resistances one corresponding to CuO layer (R_{CuO}) and the other corresponding to the grain boundary (R_{GB}) resistance between CuO grains. Thus $R_1<R_2>R_3$ is in accordance with experimental results.

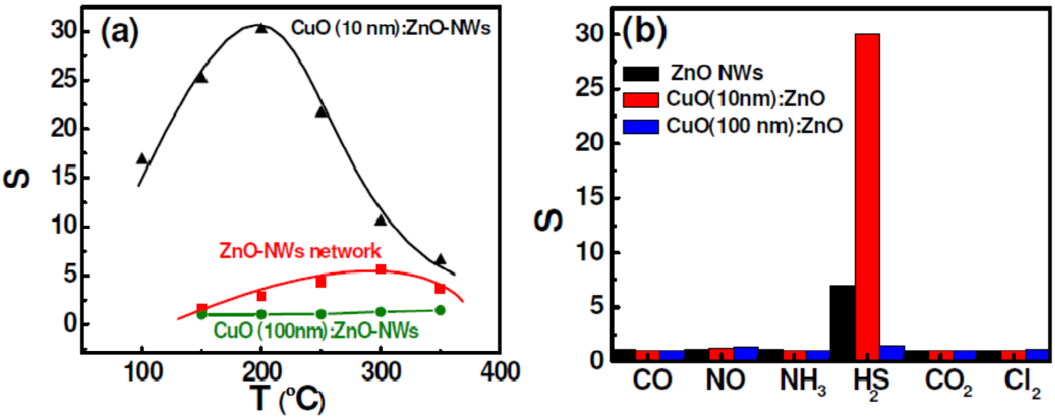

Fig. 4.9 (a) Variation of the sensitivity (for 5 ppm H_2S) as a function of operating temperature for ZnO-nanowires, CuO (10nm):ZnO-nanowires and CuO (100nm):ZnO-nanowires random networks. (b) The histogram showing the sensitivity (measured for 5 ppm at the optimum operating temperature) for different gases.

4.2.4 Gas sensing studies and proposed mechanism

We investigated gas sensing characteristics of three samples namely, ZnO-nanowires, CuO (10nm):ZnO-nanowires, and CuO (100nm):ZnO-nanowires random networks. Fig.4.9 (a) shows the response recorded for the three sensors as a function of operating temperature towards 5 ppm of H_2S. It is clearly evident that at all operating temperature CuO (10nm):ZnO-nanowires network exhibited better sensitivity towards H_2S in comparison to that of other samples. For CuO (100 nm): ZnO-nanowires network films the sensitivity is found to increase with temperature upto 350°C. Pure ZnO nanowires network exhibited better sensing characteristics as compared to that of CuO (100 nm): ZnO-nanowires network with maximum sensitivity at an operating temperature of 300°C. CuO (10 nm):ZnO-nanowires network detected H_2S with maximum at 200°C. The selectivity histogram recorded upon exposure to 5 ppm of different gases for pure

ZnO-nanowires network and the ZnO-nanowires network modified with 10 and 100 nm CuO layer at an operating temperature of 300, 200 and 350°C, respectively is shown in Fig. 4.9 (b). It is evident that CuO (10nm):ZnO-nanowires sensors are highly selective towards H_2S, as they have negligible response to other test gases namely CO, NO, NH_3, CO_2, Cl_2.

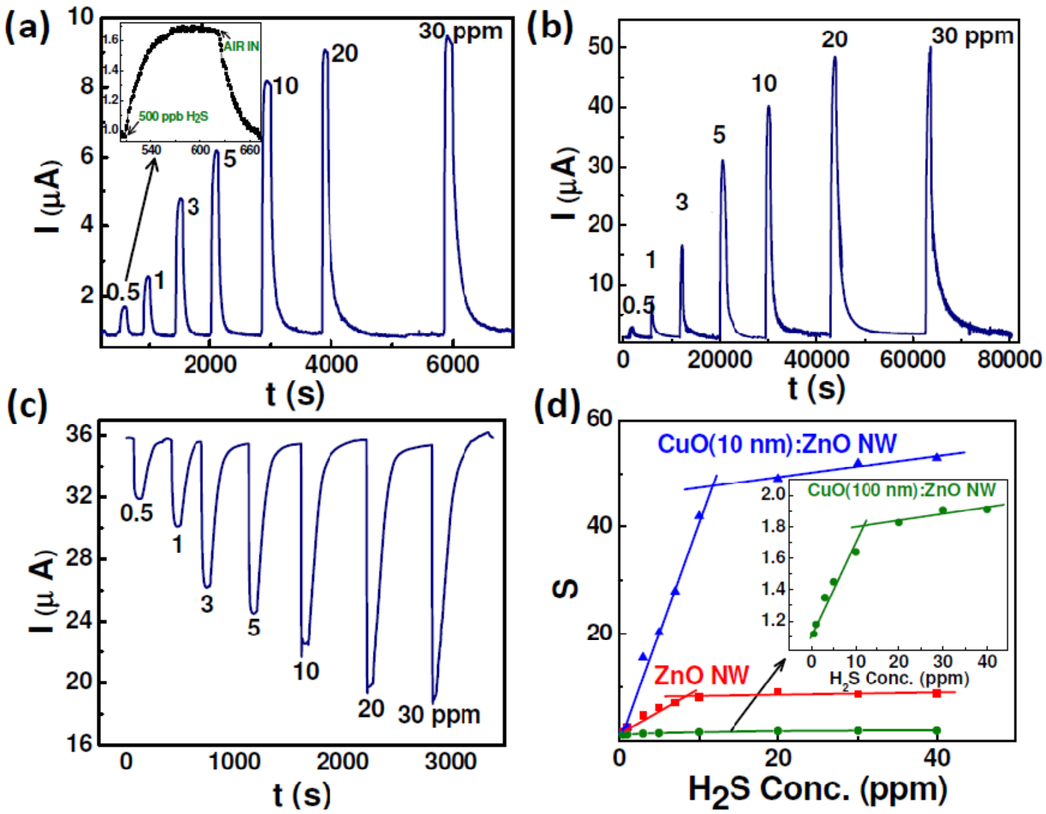

Fig. 4.10 Response curves as a function of H_2S concentration for (a) ZnO-nanowires (inset shows the magnified version of the response curve at 0.5 ppm) measured at 300°C, (b) CuO(10nm):ZnO-nanowires measured at 200°C and (c) CuO (100nm):ZnO-nanowires sensors measured at 350°C. (d) Variation of the sensitivity as a function of H_2S concentration. Inset shows enlarged view for CuO (100nm):ZnO-nanowires sensor.

Fig. 4.10 (a-c) shows the response curves of all the three sensors measured as a function of H_2S concentration. Response of CuO (100nm):ZnO-nanowires (decreasing current or increasing resistance) is opposite to that of ZnO-nanowires and CuO

(10nm):ZnO-nanowires sensors, i.e., (increasing current or decreasing resistance). The sensitivity as a function of H_2S concentration is plotted in Fig. 4.10 (d). It is clearly evident that the sensor film with 10 nm of CuO layer exhibited enhanced sensitivity towards H_2S as compared to that of pure and 100 nm films. For all the samples sensitivity increases linearly with concentration upto 10 ppm, and saturates for concentrations >10 ppm. Typical response and recovery times measured for CuO (10nm): ZnO-nanowires sensors upon exposure to 5 ppm of H_2S were 6 and 30 min, respectively. These results clearly suggest that modification of ZnO-nanowires with 10 nm of CuO layer resulted in an enhanced sensing performance towards H_2S.

The gas sensing mechanisms for ZnO-nanowires and CuO (100nm):ZnO-nanowires sensors are pretty straightforward. In the case of CuO (100nm):ZnO-nanowires sensors, the sensing action comes from the top CuO layer. Under atmospheric conditions, oxygen gets adsorbed at the ZnO or CuO surface in the form of O^{2-} by picking up electrons from the host matrix. Upon exposure to reducing H_2S gas, it reacts with the adsorbed O^{2-} species (eqn. 3.7) and trapped electrons are released into the host matrix. In the case of n-type ZnO the released electrons leads to increase in current or decrease in resistance. Exactly opposite is expected for p-type CuO i.e. decrease in current or increase in resistance, which is in accordance to the response curves shown in Fig. 4.10(c).

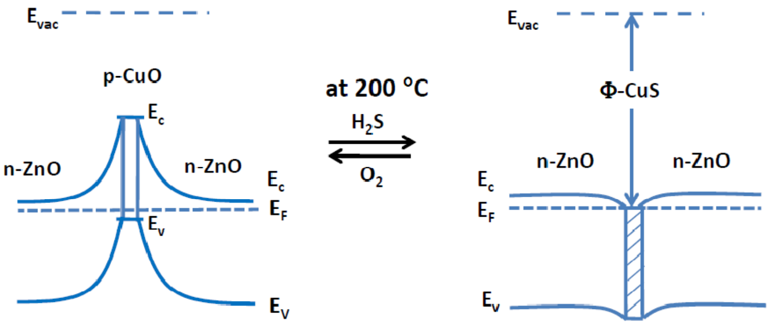

Fig. 4.11 Schematic showing an energy band diagram, indicating a change in potential barrier n-ZnO/p-CuO/n-ZnO (in air) to n-ZnO/metallic CuS/n-ZnO (on exposing to H_2S) and vice versa.

A very high sensitivity of CuO (10nm):ZnO-nanowires sensors for H_2S indicates that the sensing mechanism in this case is quite different. The sensing mechanism can be explained on the basis of the response of the p-n junction formed between CuO and ZnO-nanowires towards H_2S. Since CuO is a p-type and ZnO is n-type semiconductor, modification of ZnO nanowires network with CuO (10nm) results in the formation of random n-p-n type junctions. The potential barrier formed at the ZnO/CuO/ZnO heterojunction results in a very high resistance of the film as shown schematically in Fig. 4.11. Exposure to H_2S causes the potential barrier to disappear due to formation of CuS. CuS being metallic will destroy the n/p/n junction as well as the potential barrier, and a new type of n-ZnO/metallic-CuS/n-ZnO heterojunction will be formed. The destruction of potential barrier results in a sharp decrease in the electrical resistance. During recovery,CuS reacts with oxygen forming once again CuO. Since CuS converts back to CuO, potential barrier reappears due to the formation of n-ZnO/p-CuO/n-ZnO heterojunctions, and original high resistance is regained. This model explains well the H_2S sensing mechanism CuO(10nm):ZnO-nanowires random networks. The unique chemical reaction between CuO and H_2S also explains why CuO(10nm):ZnO-nanowires random networks are very specific towards H_2S.

4.2.5 Impedance spectroscopy

(a) Model proposed for sensing elements

The sensing layer consists of interconnected random nanowires network. Nanowires, in particular are depleted of charge carriers due to adsorption of ambient oxygen. The depletion layer thickness and height depends on the ambient. As shown in Fig. 4.12 (a), the sensor films comprises of nanowires, nanowires junction (nanowires-CuO-nanowires) and the metal- nanowires contact resistance. In order to find out the exact contributions of the sensing elements in the governing sensing mechanism a systematic impedance studies were performed as a function of temperature and the detection gas for both pure and CuO modified sensor films. The different contributions of the sensor films distinguished using impedance spectroscopy were fitted to a model ($R_b(R_jQ_j)(R_cQ_c)$) as shown in Fig. 4.12 (b).

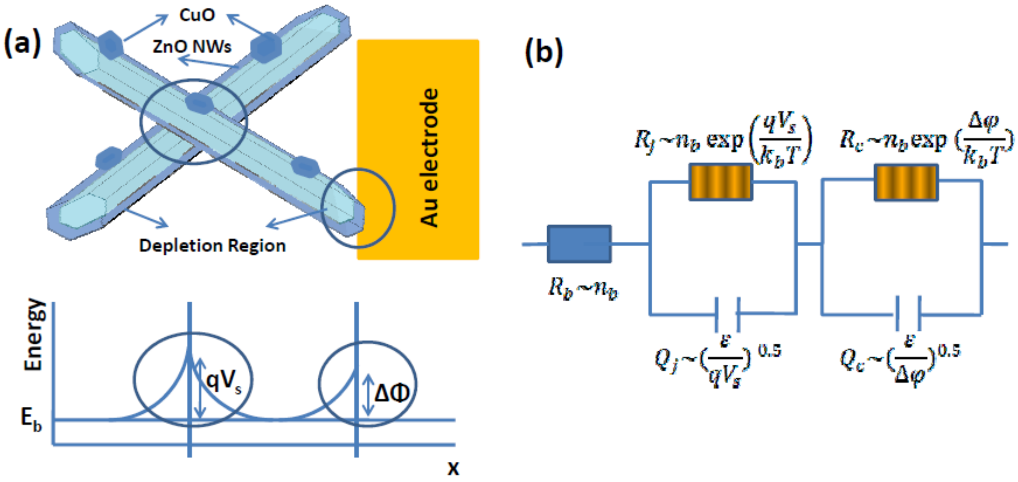

Fig.4.12 (a) Schematic representation of the effective band bending between ZnO-nanowires network and, ZnO and Au electrode interface, (b) representation of the same in an equivalent circuit format.

R_b: resistor representing the bulk of nanowires; R_j and Q_j: junction resistor and capacitor due to sandwiching of high resistive depletion layers between two conductive plates of bulk material (ZnO-CuO-ZnO); Rc and Q_c: junction resistor and capacitor representing nanowires-electrode contact. Here,

$$R_j \sim n_b \exp\left(\frac{qV_s}{k_bT}\right) \tag{4.1}$$

$$Q_j \sim \left(\frac{\varepsilon}{qV_s}\right)^{0.5} \tag{4.2}$$

$$R_c \sim n_b \exp\left(\frac{\Delta\varphi}{k_bT}\right) \tag{4.3}$$

$Q_c \sim (\frac{\varepsilon}{\Delta\varphi})^{0.5}$ (4.4)

and

$R_b \sim n_b$ (4.5)

where, ε is the dielectric constant, k_b is the Boltzmann constant.[163]

(b) Room temperature Nyquist diagram for pure ZnO and CuO (10 nm):ZnO nanowires sensors

The relationship between the real and imaginary part of the complex impedance i.e., Nyquist diagram, at room temperature is shown in Fig. 4.13 for pure and CuO modified ZnO nanowires films. The symbols represent the original data and the continuous line represents the modelling curve. Both the samples exhibited a single capacitive semicircle pattern with centre near the x-axis. A single semicircle implies that the time constant associated with these components must be identical i.e.

$S = R_bC_b = R_jC_j = R_cC_c$ (4.6)

The total impedance of the sensor can be given as

$Z = Z_b + Z_j + Z_c$ (4.7)

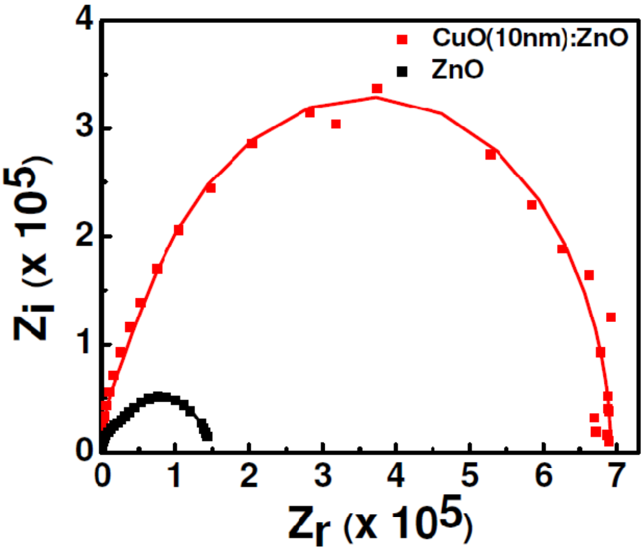

Fig. 4.13 Room temperature Nyquist plot of pure and CuO (10 nm): ZnO nanowires films.

where, Z_b, Z_j and Z_c represent the individual complex impedance contributions. The bulk resistance of the nanowires can be estimated from the interception of the semicircle at high frequency with the real axis [164]. The intercept of Nyquist semicircle with real axis Z_r at low frequency gives the junction resistance. It is clearly evident from the figure that the modification with CuO resulted in an increase in the resistance contribution. The increase in the resistance is attributed mainly to the formation of p-n junction between the CuO island type film and ZnO nanowires. It is interesting to note that the value of junction capacitance resulting from the sandwiching of high resistive depletion layers of nanowires has reduced down to one order of magnitude after the modification with CuO. This gives a better insight into the geometry of the sensor and is attributed to the presence of CuO islands in between the nanowires networks, reducing the effective dielectric constant and hence the capacitance.

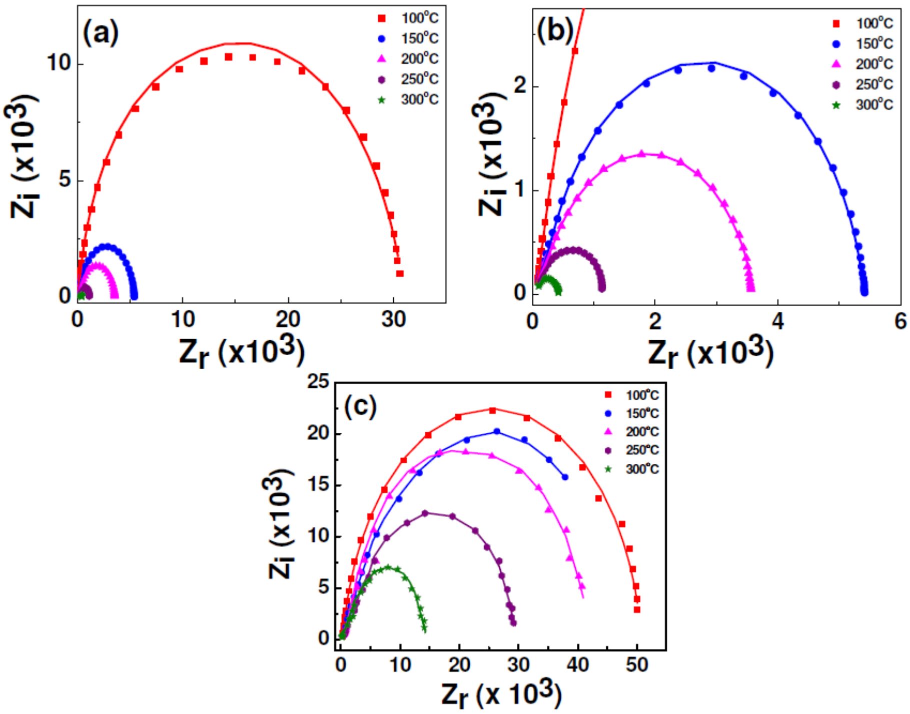

Fig. 4.14. Nyquist plot of pure [(a) and (b)] and CuO (10 nm):ZnO nanowires samples (c) recorded as a function of operating temperatures from 100 to 300°C.

(c) Nyquist plots as a function of temperature for pure ZnO and CuO(10 nm):ZnO nanowiress sensors

Fig. 4.14 shows the Nyquist plot of pure [(a) and (b)] and CuO modified ZnO nanowires samples (c) recorded as a function of operating temperatures between 100 and 300°C. For both pure and CuO modified ZnO samples the diameter of the semicircle was found to decrease with increase in the temperature. The variations in R_j and R_c with temperature were in accordance to the relations (1) and (3) (not shown here). Both the samples exhibited a significant change in the resistance values than the capacitance values implying that the temperature change mainly alters the surface layer of the sensor. This is attributed mainly to the type of oxygen species (reactive) adsorbed on the sensor surface which is dependent on the operating temperature.

(d) Nyquist plots as a function of H_2S concentration for pure ZnO and CuO (10 nm): ZnO nanowires sensors

Fig. 4.15 shows the Nyquist plot recorded as a function of H_2S concentrations (5-50 ppm) for pure and CuO modified ZnO nanowires at their respective operating temperatures. For both the cases, the diameter of the semi-circle reduced as the concentration of H_2S increased inside the test chamber. For all the H_2S concentrations the plot varies in a similar manner suggesting an identical sensing mechanism. R_c and Q_c were independent of the ambient gas atmosphere, as expected. The variations in the value of R_j and Q_j with H_2S concentration are shown in Fig.4.15 (c) and (d). H_2S concentration has a strong effect on the Rj as evident from Fig. 4.15 (c). The variation of Qj with gas concentration can be explained in terms of changes in dielectric constant ε and the band bending V_s (equation 4.2). The change in ε is dominating the capacitive behaviour when there is presence of large number of OH groups (surface dipole) on the surface of host matrix. When such a host matrix is exposed to the gas environment, surface dipoles are removed from the surface and electrons are released resulting in the reduction of ε and hence capacitance. But as seen in Fig.4.15 (d) Q_j increases from 1.2 to 1.8 × 10^{-8} and 3.1 to 3.4×10^{-9} F in case of pure and CuO modified ZnO nanowires, respectively. Hence, it is clear that the dominating factor in governing the variation of capacitance is the decrease in band bending and not increase in ε. Accordingly the resistance is decreased and the capacitance is increased. Further, a relatively small variation in the capacitance implies that the H_2S affected mainly the surface charge region of the ZnO nanowires.

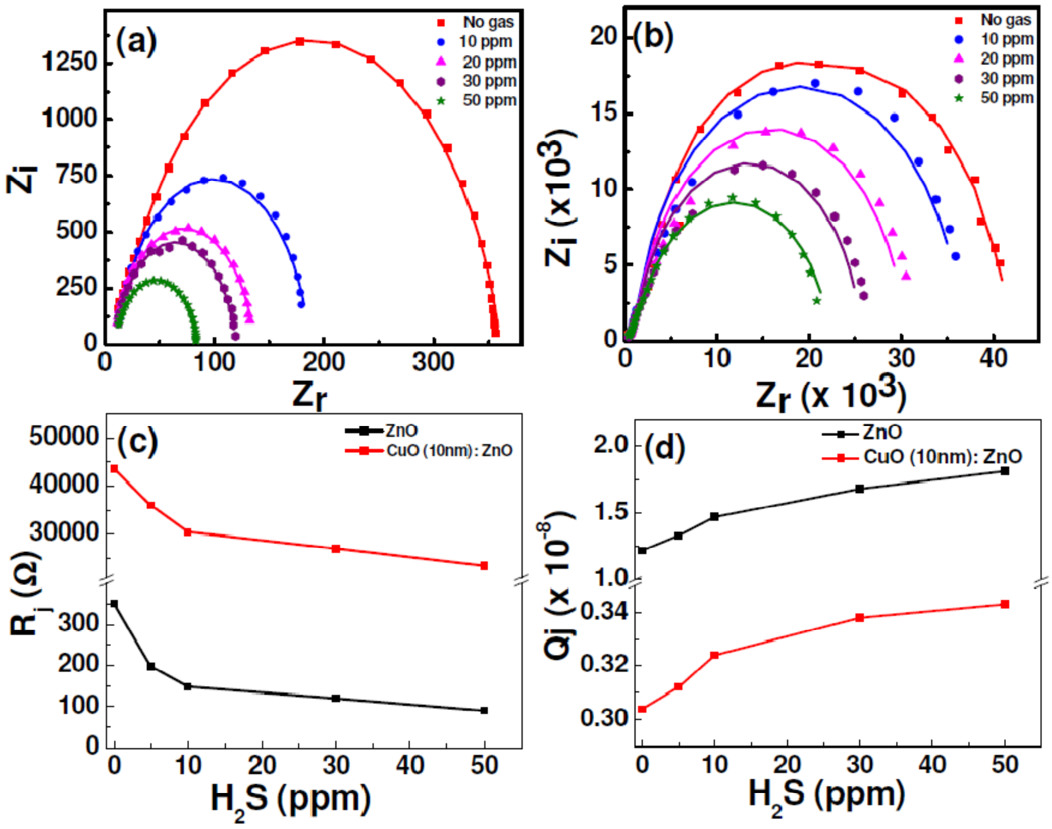

Fig. 4.15. Nyquist plot recorded as a function of H_2S concentrations (5-50 ppm) at an optimum operating temperature of 300 and 250°C for (a) pure and (b) CuO modified sensor films, respectively. Corresponding variation of (c) Rj and (d) Qj as a function of H_2S concentration.

(e) Frequency distribution of charge carrier relaxation process

The peak frequencies associated with the relaxation process can be estimated from the plot of imaginary part of impedance (Z_i) against the logarithm of the frequency. Fig. 4.16 and 4.17 shows the plot of Z_i vs logarithm of frequency for both pure and CuO modified ZnO nanowires as a function of operating temperature and H_2S concentration.

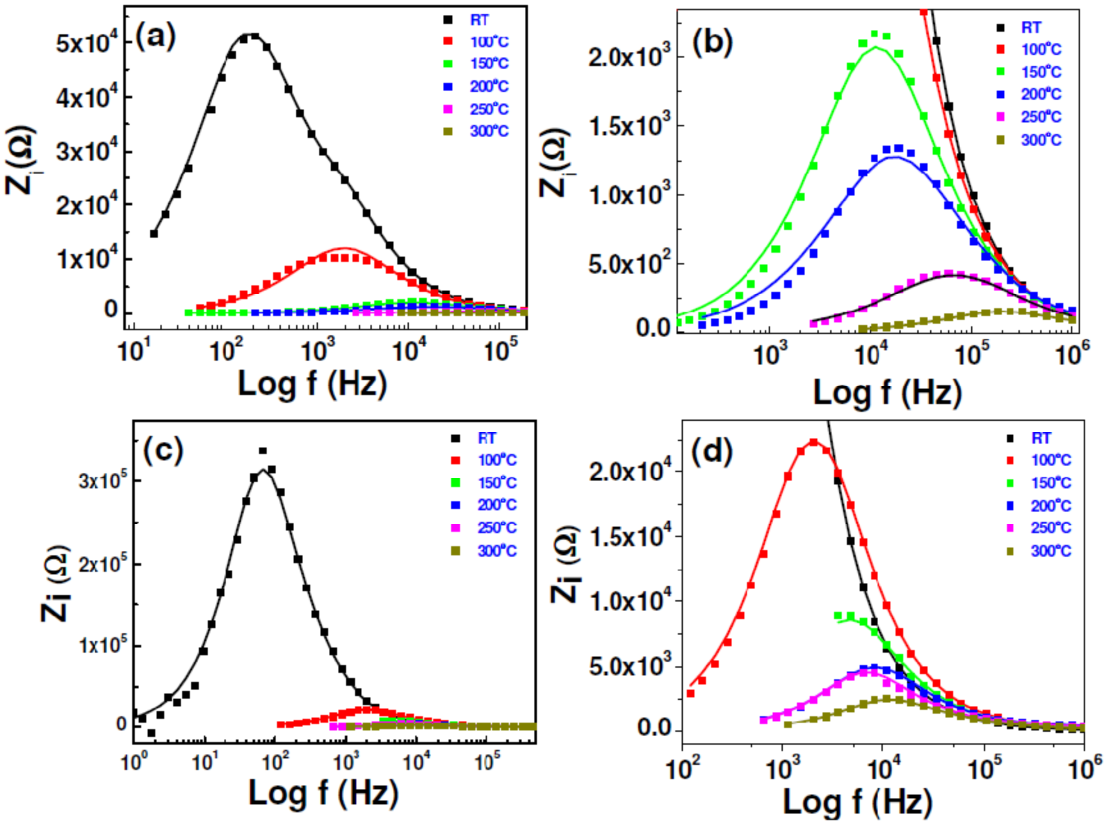

Fig. 4.16. Impedance vs. Log (F) plot recorded as a function of operating temperature for pure (a) and (c), and CuO modified ZnO (c) and (d) nanowires network films.

It is evident from the figures that the peak frequency shifts towards higher frequencies, and the peak height decreases with the increase in operating temperature as well as H_2S concentrations. The observed peak broadening could be attributed to the dependence of the relaxation process on the temperature and the gas concentrations [165].

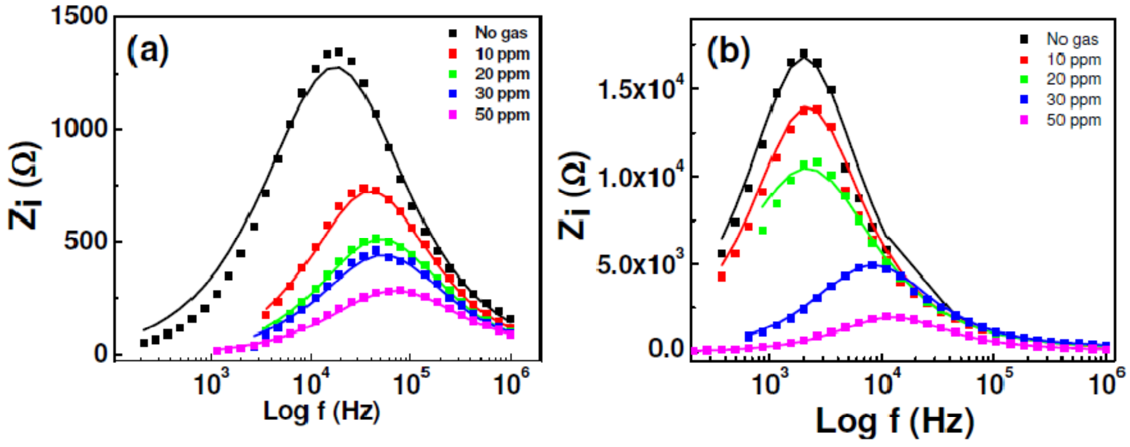

Fig. 4.17. Impedance vs. Log (F) plot recorded as a function of H_2S concentrations pure (a) and (b), and CuO modified ZnO nanowires network films.

4.2.6 Work function measurements

The work function of the material has two components that can be influenced by surface reactions (relation (4.8)):

$$\phi = qVs + \chi \tag{4.8}$$

$$\Delta\phi = \pm\, q\Delta Vs \pm \Delta\chi \tag{4.9}$$

where, qVs is the surface band bending and χ represents the electron affinity which is the measure of surface dipole moment. The $q\Delta Vs$ can be directly calculated for n-type semiconductors using:

$$q\Delta Vs = -kT\ln\left(\frac{G_{gas}}{G_{air}}\right) \tag{4.10}$$

where, G_{gas} and G_{air} are the values of conductance in the presence of gas and ambient air, respectively, which are experimentally determined. Fig. 4.18 shows the work function area map recorded for both pure and CuO modified sensor films. The average work function values were found to be 5.06 and 5.36 eV for pure and CuO modified ZnO, respectively. This increase in work function by ~0.2 eV further supports the formation of p–n junctions over the surface of the sensor films thereby leading to the upward band bending. Fig. 4.18 shows the change in work function upon exposure to reducing (H_2S) and oxidising gases (Cl_2) for pure (Fig. 4.18 (b)) and CuO modified ZnO sensor films, (Fig. 4.18 (c)) respectively. The average work function values before and after the exposures have been tabulated in Table 4.1. As expected, exposure to H_2S and Cl_2 causes the work function to decrease and increase, respectively. In case of H_2S exposure, the change in work function value is attributed mainly to the unique interaction of CuO with H_2S leading to CuS formation further corroborating the results of impedance studies.

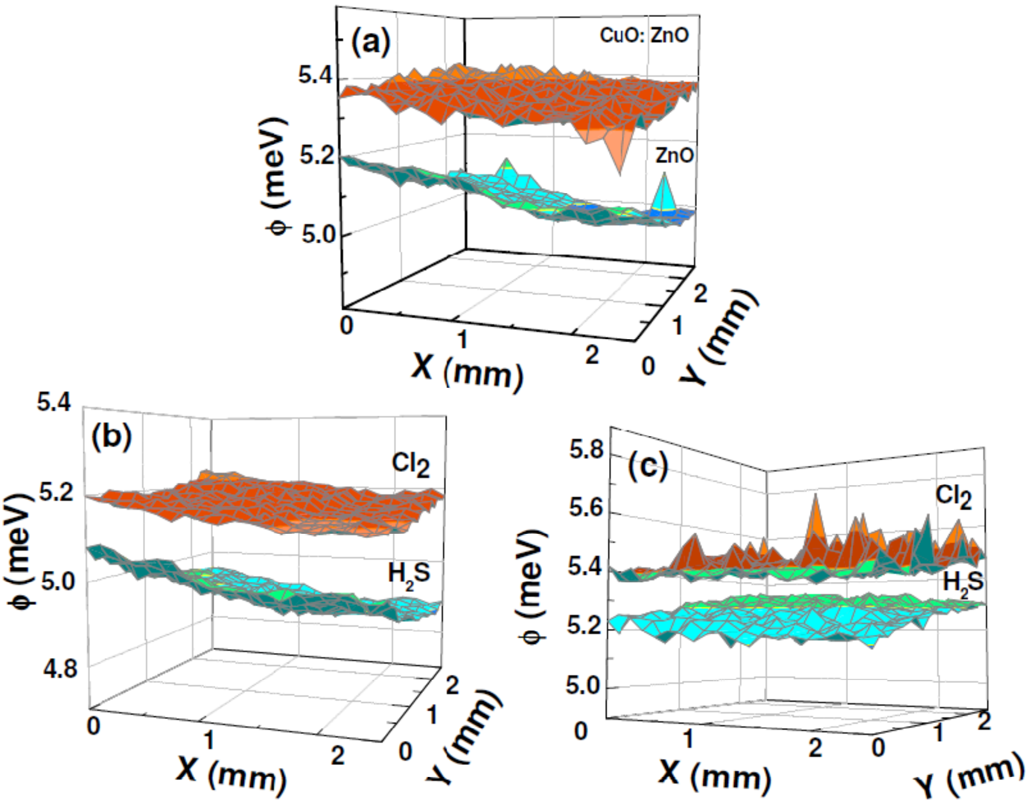

Fig.4.18. Work function area scan recorded for (a) pure and CuO modified ZnO nanowire network. Effect of reducing (H_2S) and oxidising (Cl_2) on the work function values of (b) pure and (c) CuO modified ZnO nanowire network.

Band bending contribution to the work function calculated using equation 4.10 is -75 and -135 meV (for 20 ppm H_2S) for pure and CuO modified sensor films, respectively. The negative sign indicates the decrease in upward band bending after H_2S exposure.

After subtracting the band bending (equation 4.9) we arrive at a dipole induced increase in work function of 195 meV and 225 meV respectively. This indicates a surface dipole layer with positive side towards the vacuum. The possible factors affecting the surface dipole layer are charge transfer across the interface, rearrangement of electron cloud at the semiconductor surface in presence of adsorbate and also existence of interface state serving as a buffer of charge carriers [166]. ZnS formation on ZnO nanostructures on reaction with H_2S has been reported,[167] which might result in charge transfer from ZnS to ZnO due to varying electronegativities of O and S and hence increasing the dipole contribution to the work function. The larger increase in work function in CuO-modified sensor films (compared to pure ZnO nanowires films) may be attributed to the formation CuS after H_2S exposure. CuS being metallic in nature leads to further charge transfer to ZnO, enhancing the above effect.

Table 4.1. Work function values for pure and CuO modified ZnO nanowires network before and after exposure to H_2S.

	ZnO (eV)	**CuO(10nm): ZnO (eV)**
Without gas	5.06	5.36
H_2S	4.94	5.27
Cl_2	5.23	5.45

4.3 CuO: WO_3 chemiresistive sensors

In this section we list the H_2S gas sensing properties of randomly distributed nanop-n junction between CuO and WO_3 prepared by RF sputtering technique as explained in section 2.2.2 (a), (iii). The CuO modification led to the better gas sensing characteristics as compared to pure WO_3 thin films.

4.3.1 Sensor characterization

The deposition time of 2 h resulted in the WO_3 film with thickness of ~ 70 nm as measured using ellipsometry studies. Fig. 4.19 shows the SEM images of the pure and CuO modified WO_3 thin films. Both pure and CuO modified WO_3 films exhibited large number of faceted microparticles having grain sizes < 2 μm. These microparticles were found to get deformed with CuO modification as is clearly evident in Fig. 4.19 (f).

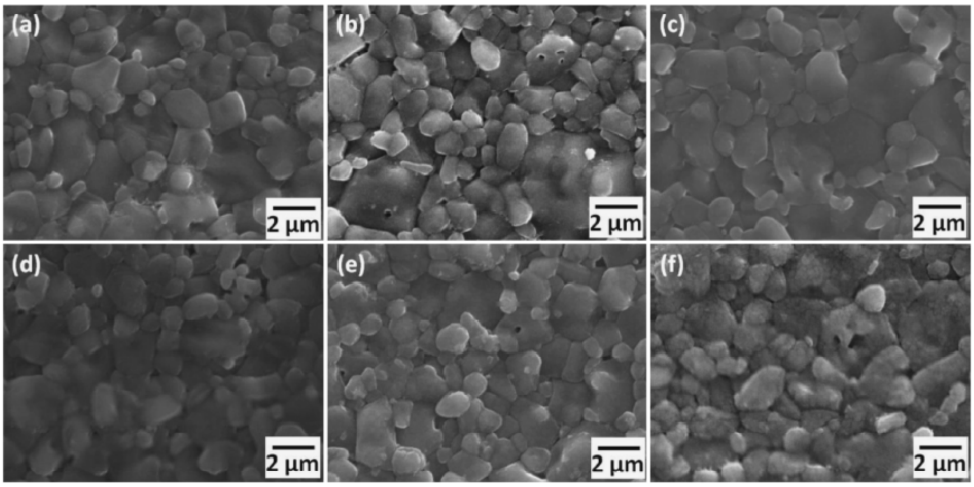

Fig. 4.19. SEM images of pure (a) and CuO modified WO_3 thin films corresponding to (b) 1.86, (c) 2.11, (d) 2.25, (e) 2.47 and (f) 2.64 at.% of Cu, respectively.

Elemental x-ray mapping of the CuO modified WO_3 thin film was performed to check the distribution of Cu over the surface. Fig. 4.20 shows the area mapping of Cu, O and W over the WO_3 surface. It is clearly evident that both W and Cu are uniformly distributed over the surface with higher percentage of O. As CuO and WO_3 are intrinsically p-type and n-type in nature, surface modification resulted in a randomly distributed nano p-n junctions.

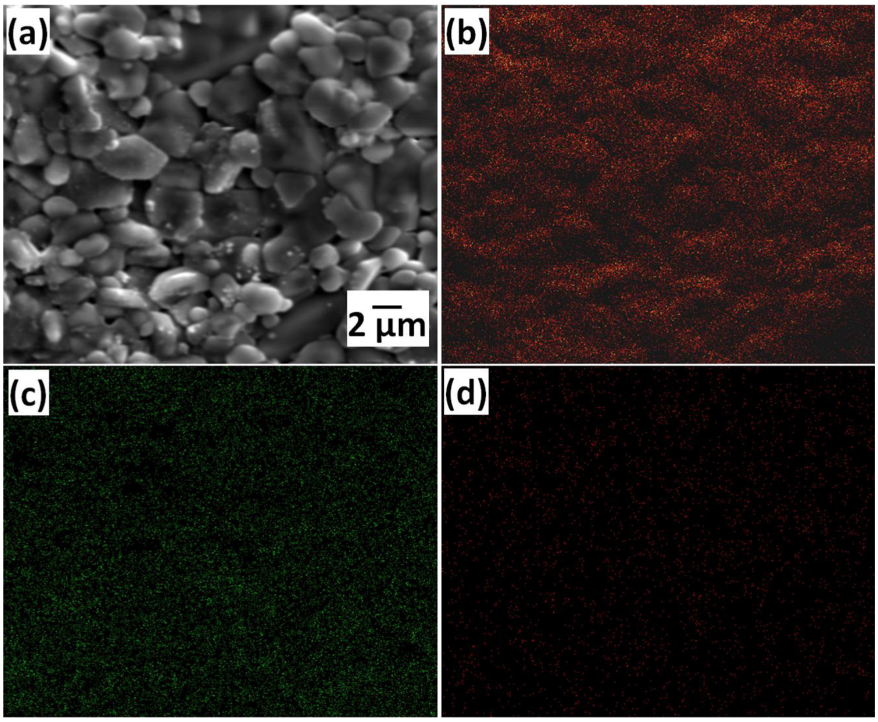

Fig. 4.20. Elemental x-ray mapping performed for CuO (Cu: 2.25 at.%) modified WO_3 thin films (a) SEM image and (b) O, (c) W and (d) Cu elemental distribution over the surface of the sensor films.

Fig. 4.21 shows the GIXRD plots recorded for pure and CuO modified WO_3 thin films. Both the spectra match well with the monoclinic phase of WO_3 with space group $P2_{1/}c$. The lattice parameters were found to be a = 5.269, b = 5.158 and c = 7.602, β = 92.072 for pure WO_3 and a = 5.225, b = 5.089 and c = 7.476, β = 92.527 for CuO modified WO_3 thin films. No peaks corresponding to the presence of CuO were observed attributed to the smaller percentage of Cu. It has been shown that thermal oxidation of Cu at temperatures > 270°C leads to the formation of pure CuO phase.

In order to confirm the CuO formation an XPS measurements were performed over the Cu modified WO_3 sensor films. The experimental data was fitted and deconvoluted into individual four peaks at binding energies of 933.8, 945, 953.5 and 963.4 eV, respectively (similar to Fig. 4.4 (c)). The two peaks located at 933.8 and 953.5

eV correspond to the Cu $2p_{3/2}$. And the two peaks at 945and 963.4 eV for the Cu $2p_{3/2}$and $2p_{1/2}$core levels are evident and diagnostic of an open 3d9 shell corresponding to Cu^{2+}state.The presence of satellite peaks confirms the formation of CuO.

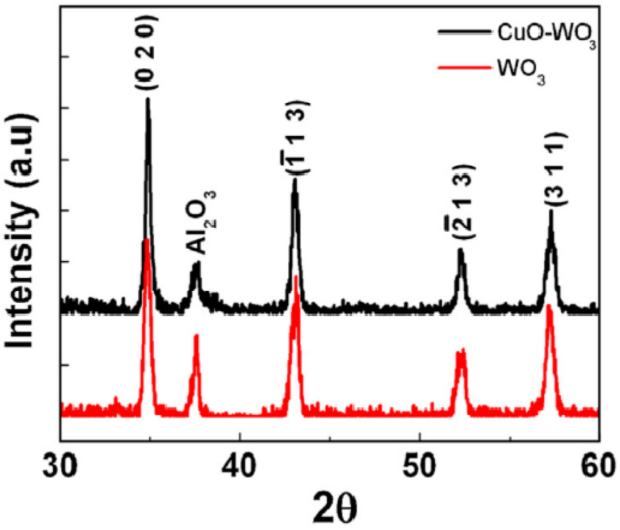

Fig. 4.21. GIXRD pattern recorded for pure and CuO modified WO_3 thin films.

4.3.2 Sensing characteristics and mechanism

In order to determine the optimum conditions for the H_2S detection, a systematic investigation of operating temperature effects on gas sensing properties of pure and CuO modified WO_3 were performed. At all the operating temperature CuO modified sample exhibited a maximum sensor response. The sensor response was found to increase with temperature up to 300°C. Gas sensing measurements were not performed at temperatures above 300°C as the catalytic decomposition of H_2S is well known to occur between 300°C and 400°C [168]. For all the further measurements 300°C was chosen as the optimum temperature. Fig.4.22 shows the typical response curve recorded for pure and CuO modified WO_3 films towards 10 ppm of H_2S at 300°C. CuO modified sample exhibited an enhanced response of 534 as compared to that of 21 exhibited by pure WO_3

thin films. Both pure and CuO modified samples exhibited a response with fast reaction kinetics. For examples for pure WO_3 the response and recovery times were 7 s and 31 min, while for CuO modified sample they were 5 s and 24 min, respectively. It is clearly evident from the figure that modification with CuO resulted in an increase in the base line resistance of the sensor film attributed to the formation of random p-n junction distributed over the surface of the sensor film.

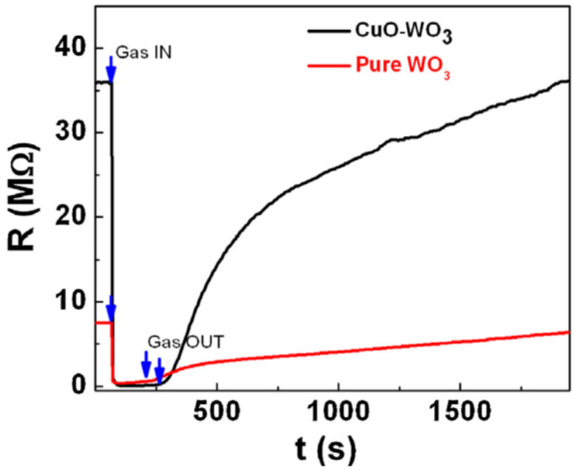

Fig. 4.22. Response curves recorded for pure and CuO modified (2.25 at. %) WO_3 thin films towards 10 ppm of H_2S at an operating temperature of 300ºC.

The sensor responses were also measured as a function of CuO concentration in order to find the optimum concentration over the WO_3 sensor. The maximum response was observed for sensor containing 2.25 at%(as measured using EDX analysis) of Cu corresponding to the deposition time of 90 s. Fig. 4.23 shows the response curves recorded for sensors with different Cu loading. Additionally, Fig. 4.23(f) shows the calculated recovery times for different Cu loading. All the sensor films exhibited a faster response time <10 s towards 10 ppm of H_2S at 300ºC. The recovery time was found to decrease upon CuO modification with minimum (6 min) obtained for sensor film with 2.11 at% of Cu. With further increase in Cu the recovery time is increased. The amount and distribution of the CuO over the WO_3 surface plays a crucial role in determining the sensing properties.

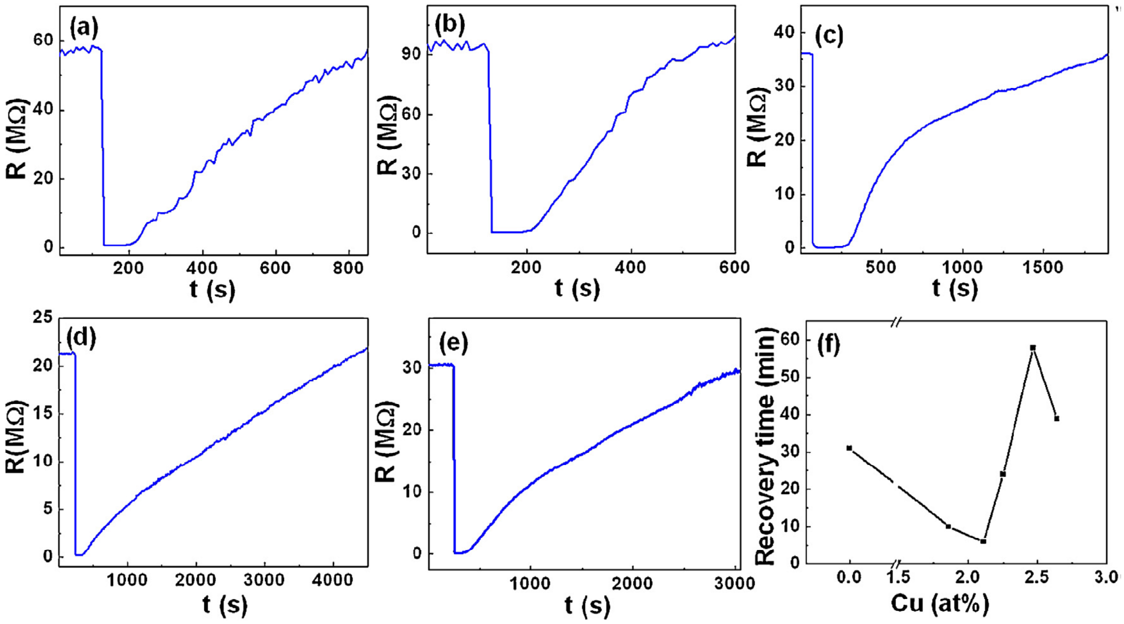

Fig. 4.23. Response curves recorded for different Cu (at%) in WO_3 (a) 1.86, (b) 2.11, (c) 2.25, (d) 2.47, (e) 2.64 at% and (f) variation in sensors recovery time as a function of Cu%.

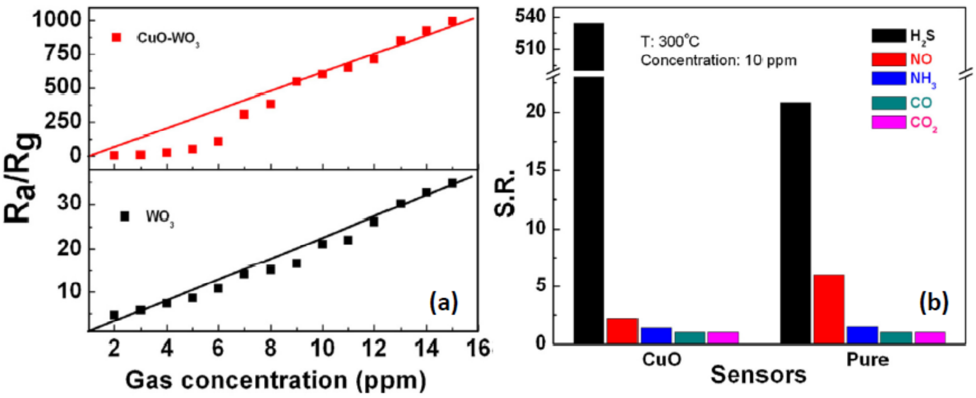

Fig.4.24 (a) Variation in sensor response as a function of H_2S concentration recorded for both pure and CuO modified (2.25 at%) sensor films at 300°C.(b) Selectivity histogram of pure and CuO modified sensor (Cu: 2.25 at%) films towards 10 ppm of different gases at an operating temperature of 300°C.

Gas sensing is governed by the three processes namely adsorption, desorption and Langmuir Hinshelwood (LH) bimolecular interaction between adsorbed species [169,170]. Surface modification with sensitizers results in the alteration of the kinetic characteristics of the response to gas. Degree of change is determined by the amount and distribution of sensitizers. Presence of CuO modifies the reaction rates (LH) and the parameters of the chemisorptions sites (density, sticking co-efficient and sticking probability). Lower CuO concentration causes discontinuity in the distribution while for higher concentrations better connectivity between adjacent CuO grains implies that the response is predominantly governed by CuO and hence a reduction in response is obtained. Additionally, higher concentration leads to the generation of defects that exerts a stronger negative influence on the response. Usually, the surface disorder is accompanied by the increase of the surface state density which could lead to the pinning of surface Fermi level and decrease of sensor response [23,171]. At optimum distribution in this case for 2.25 at% of Cu, the free electrons released as a result of interaction with H_2S are transferred to WO_3 host matrix causing a drastic change in its resistance values. At 2.25 at% of Cu, it is anticipated that the processes namely adsorption and desorption are at equilibrium and the LH reaction rate is at its maximum thereby resulting in maximum response.

Fig. 4.24 (a) shows the variation in sensor response as a function of H_2S concentration. Both pure and CuO modified sensor films exhibited a linear response towards H_2S up to 15 ppm. CuO modified sensors exhibited an enhanced response as compared to that of pure WO_3 sensors films. The sensor films were also highly selective towards H_2S as is evident from the selectivity histogram shown in Fig. 4.24 (b). Sensor films exhibited a negligible response towards other interfering gases like NO, NH_3, CO and CO_2. Stability of the sensor is also one of the important criteria and accordingly, we have investigated the sensor response towards 10 ppm of H_2S at an operating temperature of 300°C measured over a period of 30 days. As shown in Fig. 4.25 (a), the base resistance of the sensor is found to increase with time (26 to 37 MΩ in 30 days) and resulted in a corresponding increase in the sensor response. Even after 30 days the sensor exhibited a selective response towards H_2S thereby implying its stability. Also, throughout the measurement period the sensor exhibited a fast response towards H_2S. Fig. 4.25 (b) shows the response curve recorded for the samples on 6th and 31st day, respectively. The response and recovery time on 6th day of measurements were 5 s and 17 min while they were 5 s and 50 min, respectively on 31st day. The similar response time is attributed to the unique interaction of CuO with H_2S while the slow recovery is attributed to the surface poisoning, fluctuations of temperatures in the surrounding atmosphere and humidity related effects [23,172].

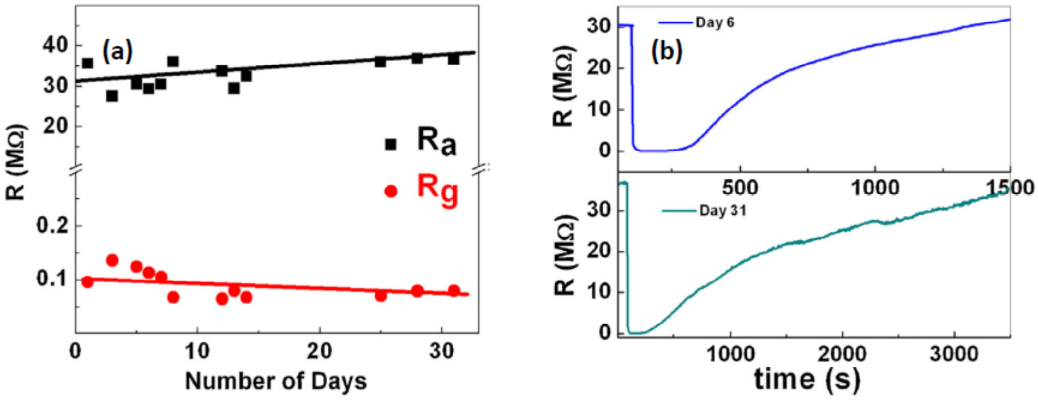

Fig.4.25 (a) Long term stability measurements for the CuO modified (Cu: 2.25 at %) WO_3 sensor films towards 10 ppm of H_2S at an operating temperature of 300°C. (b) Response curve recorded for CuO modified (Cu: 2.25 at %) WO_3 sensor films towards 10 ppm of H_2S at an operating temperature of 300°C on 6th and 31st day, respectively.

WO_3 is an n-type wide band gap material and its surface is characterized by the presence of adsorbed oxygen species that play the crucial role in gas sensing. Both pure and CuO modified sensor films exhibited a maximum response towards H_2S at an operating temperature of 300°C. At this temperature the sensor surface is mainly characterized by the presence of adsorbed oxygen species namely O^-. Modification with CuO causes an increase in the adsorbed oxygen species abstracting electrons from the host matrix. This is reflected as an increase in the resistance of the sensor films. The nano p-n junctions formed at the grain boundaries between CuO and WO_3 resulted in a potential barrier. Upon exposure, H_2S reacts with O^- as per the reaction depicted in equation 3.6 releasing large number of electrons into the host matrix. However, at the interface between WO_3 and CuO and elevated temperature of 300°C, H_2S predominantly interacts with CuO forming CuS resulting in the collapse of the barrier leading to a release of large number of electrons in the WO_3 matrix. This is evident as a drastic change/decrease in the resistance of the sensor film.

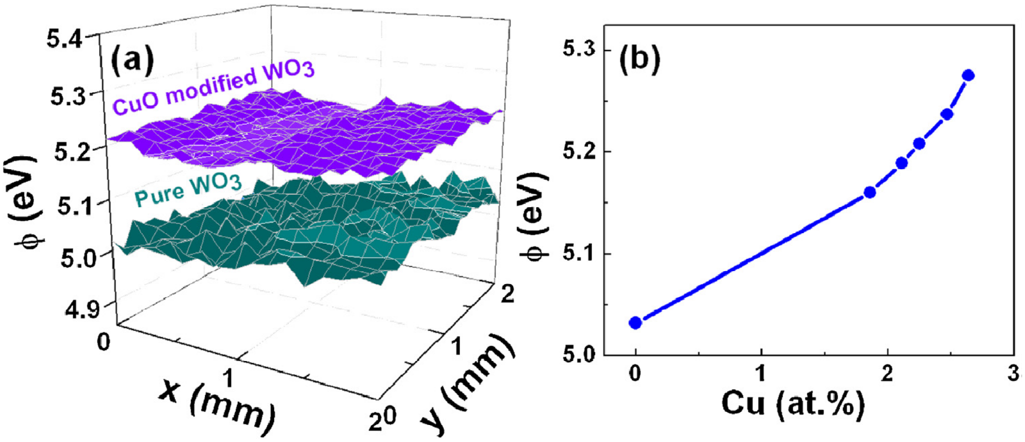

Fig. 4.26. (a) Work function area map (2x2) mm^2 recorded for both pure and CuO modified WO_3 thin films and (b) change in average work function as a function of Cu (at.%) as measured using EDAX analysis.

In order to further support the observation, work function measurements were performed. Fig. 4.26 shows the work function area map recorded for both pure and CuO modified sensor films (Cu: 2.25at.%). The average work function values were found to be

5.032 and 5.208 eV for pure and CuO modified WO_3 films, respectively. The value of work function was found to increase with increase in CuO contents as shown in Fig.4.26 (b). This increase in work function further supports the formation of p-n junctions over the surface of the sensor films. Fig.4.27 shows the change in work function upon exposure to H_2S for CuO modified WO_3 thin film. Exposure to H_2S causes the work function to decrease by ~0.2 eV. This large change in work function value is attributed to the unique interaction of CuO with H_2S leading to CuS formation further corroborating the results.

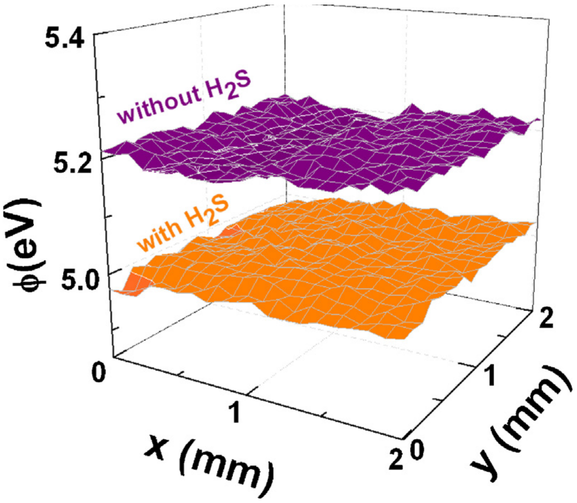

Fig.4.27 Change in work function of CuO modified WO_3 films upon exposure to 50 ppm H_2S.

4.4 Fe_3O_4:SnO_2chemiresistive sensors

The SnO_2 thin films prepared by RGTO method were modified by Fe. The modification was carried out in two steps, firstly Fe ultra-thin films were deposited using e gun and secondly annealed under oxygen environment to form oxides of Fe, as explained in section 2.2.2 (a) (ii). Modification with Fe resulted in an improved and selective response towards H_2S and the results are shown in the following sections.

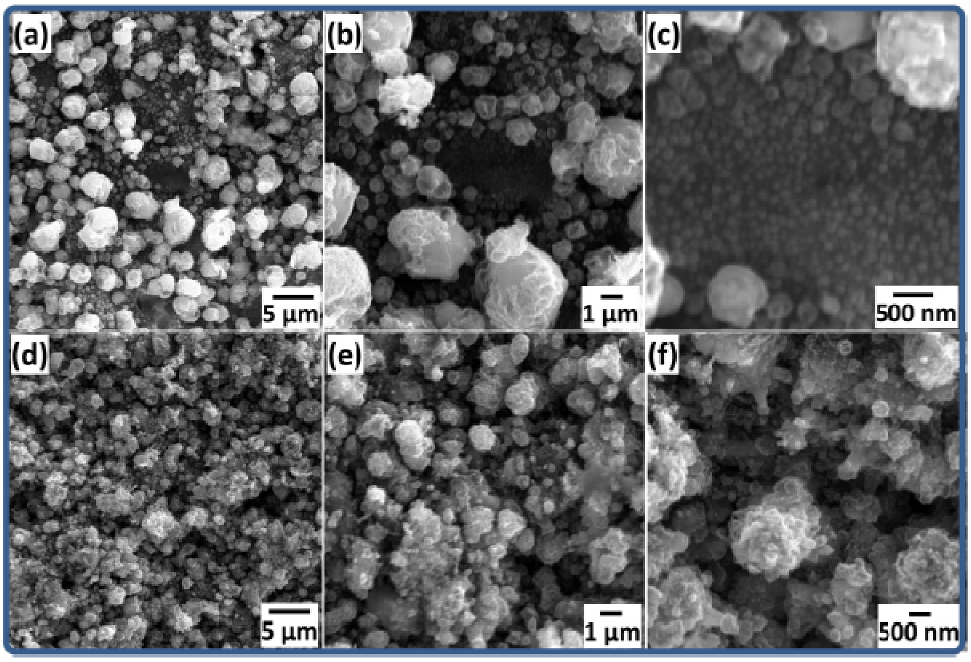

Fig.4.28. SEM images taken at different magnification for pure (a, b, c) and Fe modified (d, e, f) SnO_2 thin films after thermal oxidation at 800°C for 1 h.

4.4.1 Morphological and structural characterization

Fig.4.28 shows the SEM images taken at different magnification for pure and Fe modified SnO_2 thin films after oxidation. The morphology of the SnO_2 films is governed by different process parameters including type of substrate, deposition temperature and rate, vacuum and partial pressure of oxygen [173]. Pure SnO_2 showed large number of polydisperse ‘spongy agglomerates’ with sizes < 2 µm. The spongy agglomerates are the typical of RGTO method having a very large specific surface characterized by cavities and a three dimensional random network of interconnected grains. Some of the spongy agglomerates indicated a uniform morphology towards the base. In between the agglomerates large number of smaller individual spherical nanocrystallites with sizes between 20 and 200 nm were also observed (Fig.4.28 (b and c)). Being well separated from each other they are not expected to contribute to the sensing response. Fe modified samples also exhibited similar morphology of polydisperse spongy agglomerates but with lesser individual spherical agglomerates (Fig. 4.28 (d, e and f)) and hence are expected to result in improved sensing response.

The uniform distribution of Fe over SnO_2 films was confirmed by elemental mapping of the modified sensor films. Fig. 4.29 shows the elemental mapping performed on 0.64 at. % Fe modified samples, which was found to be an optimized Fe loading for best sensor performance for H_2S. As is clearly evident all the elements namely Sn, O and Fe show a uniform distribution throughout the measured area.

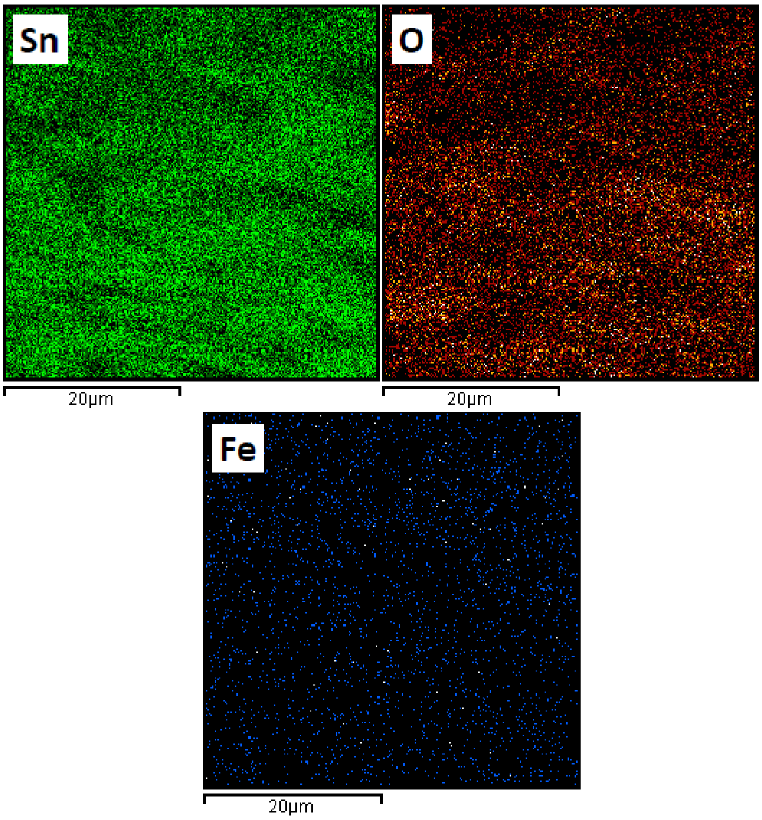

Fig. 4.29. Elemental mapping of Sn, O and Fe for 0.64 at.% Fe modified sensor films.

In order to confirm the phase and oxidation state of Fe an XPS measurements were performed over the sensor films. Fig.4.30 shows the deconvoluted Sn 3d and O 1s spectra recorded for pure SnO_2 films. In all the spectra the hollow circles represents the original data while the solid lines with different colours represents both the fitted curves (red) and the deconvoluted individual peaks (other colours) of different species. All the elements and the corresponding BE values have been tabulated in Table 4.2. For pure SnO_2, two peaks located at BE values of 486.2 and 494.7 eV corresponding to Sn $3d_{5/2}$ and $3d_{3/2}$, respectively were observed. The peak to peak separation of Sn 3d peaks is 8.5 eV and is in accordance with the bulk SnO_2. The presence of Sn^{2+} cannot be ruled out because the binding energy of Sn $3d_{5/2}$ for SnO is very close to that for SnO_2 ($\Delta E \sim 0.7$ eV) and is also beyond the spectral resolution of our spectrometer (overall resolution ~1 eV) [174]. Oxygen O1s peak can be deconvoluted into two peaks located at 530.5 and 532.4 eV corresponding to the lattice oxygen in the SnO_2 crystal and the adsorbed oxygen species, respectively [175, 176].

Upon modification with Fe, the Sn 3d peaks (Fig.4.31) were found slightly shifted to the lower binding energy values of 485.8 and 494.3 eV. Oxygen O1s peaks can be deconvoluted into two peaks at 529.2 and 530.9 eV corresponding to the lattice oxygen of Fe_2O_3 and SnO_2 lattice crystal, respectively [177]. Additionally, the Fe modified SnO_2 exhibited Fe 2p peaks that were deconvoluted into two peaks at BE values of 709.3 and 723.3 eV corresponding to Fe $2p_{3/2}$ and $2p_{1/2}$ peak, respectively.

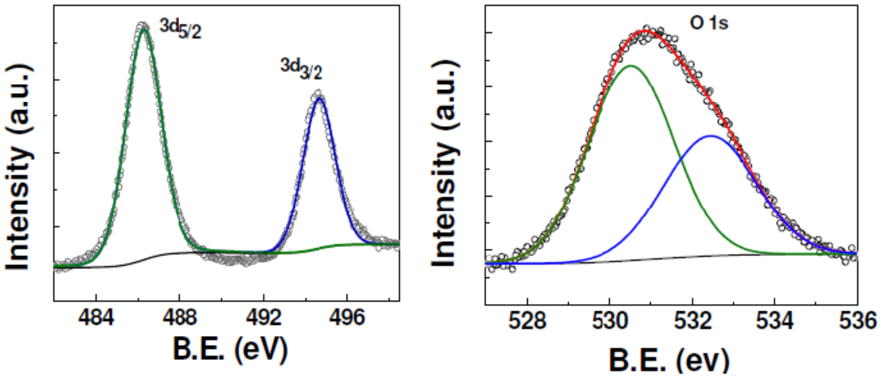

Fig.4.30. Deconvoluted (a) Sn 3d and (b) O1s spectra recorded for pure SnO_2 sensor films.

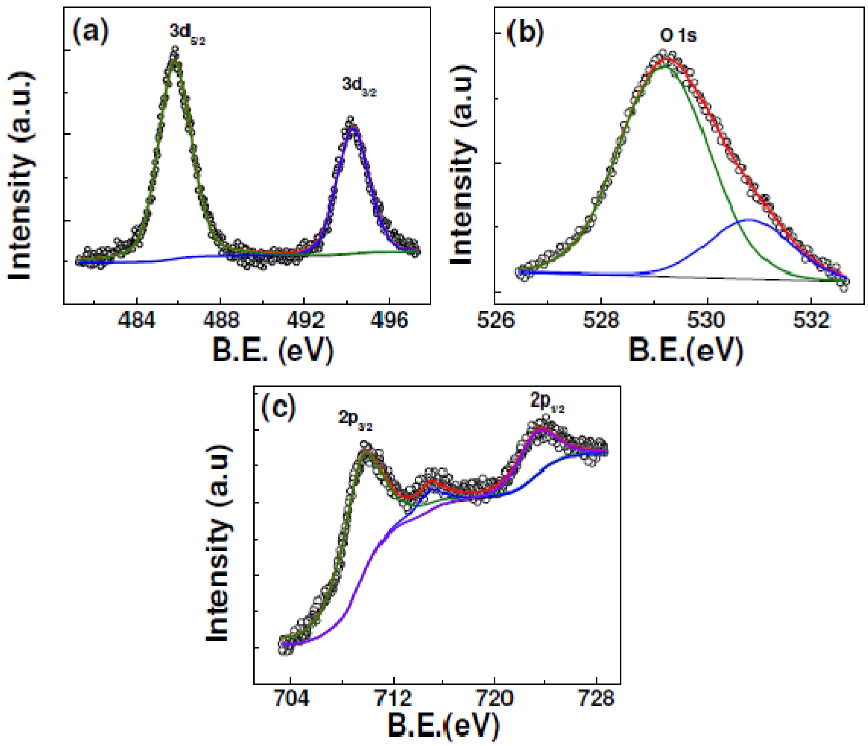

Fig.4.31. Deconvoluted (a) Sn 3d, (b) O1s and (c) Fe 2p spectra recorded for Fe modified SnO_2 sensor films.

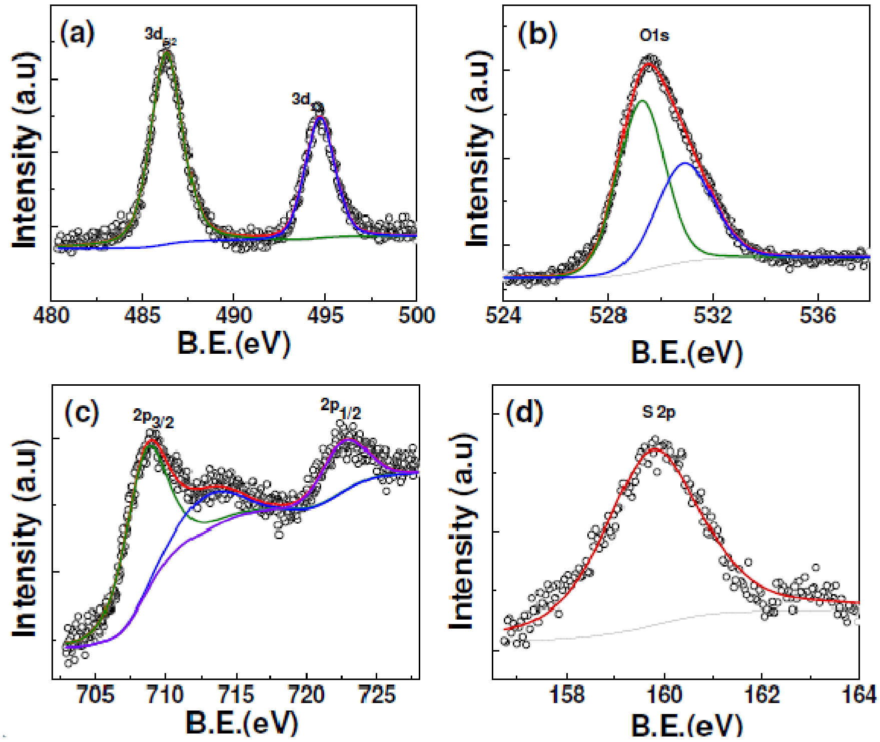

Fig.4.32. Deconvoluted (a) Sn 3d, (b) O1s, (c) Fe 2p and (d) S 2p spectra recorded for Fe modified SnO_2 sensor films after exposure to H_2S.

The peak at 715 eV is attributed to the satellite peak of Fe^{3+} [178]. The relative position of Fe 3d peaks confirms that the Fe exists as Fe_3O_4 phase [179]. The Fe $2p_{3/2}$ is stronger and has more area than $2p_{1/2}$ peak attributed to the spin-orbit (j-j) coupling; Fe $2p_{3/2}$ has degeneracy of four states while $2p_{1/2}$ has only two. Thus, XPS studies clearly indicate that Fe exists in the form of Fe_3O_4 over SnO_2 sensor films.

Upon exposure to H_2S (Fig.4.32) the Sn 3d peaks were observed at 486.3 and 494.7 eV, while oxygen O 1s peaks were located at 529.3 and 530.9 eV, respectively. Interestingly, the Fe 2p peaks were found to be shifted towards lower BE values of 708.5 and 722.5 eV. This clearly indicates that H_2S interacts strongly with the Fe present on the sensor surface. Fig.4.36 (d) shows the S 2p spectrum recorded for Fe modified sample upon exposure to H_2S. A single peak located at BE value of 159.8 eV can be attributed to the presence of sulfide species [180].

Table 4.2. Binding energy values for different element as measured using XPS analysis

Element		**SnO_2** **BE (eV)**	**Fe: SnO_2** **BE (eV)**	**Fe: SnO_2** **After H_2S**
Sn	$3d_{5/2}$	486.2	485.8	486.3
	$3d_{3/2}$	494.7	494.3	494.7
O	1s/FeO lattice	530.5	529.2	529.3
	Adsorbed/SnO_2lattice	532.4	530.8	530.9
Fe	$2p_{3/2}$	-	709.3	708.5
	Satellite 1	-	715	713
	$2p_{1/2}$	-	723.3	722.5
S	2 p	-	-	159.8

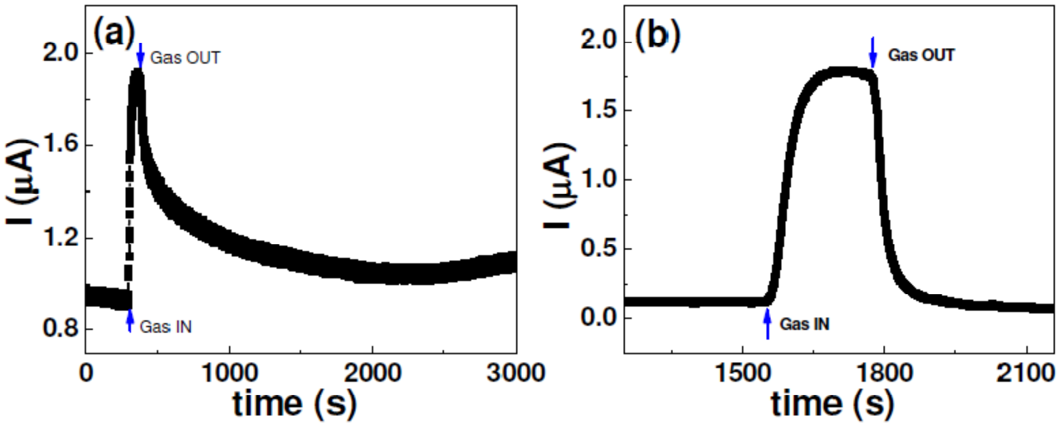

Fig.4.33. A typical response curve recorded for (a) pure and (b) Fe modified SnO_2 sensor films towards 10 ppm of H_2S at an operating temperature of 225°C.

4.4.2 Gas sensing studies and sensing mechanism

A typical response curves of pure and Fe modified SnO_2 films at an operating temperature of 225°C towards 10 ppm of H_2S are shown in Fig.4.33. Compared to pure SnO_2 that exhibited a sensor response of S = 1.98, Fe-modified (0.64 at.%) SnO_2 films exhibited an enhanced response of 14.5 with improved response kinetics. For example, the response and the recovery times towards 10 ppm of H_2S were 90 and 98 s, respectively. Additionally, Fe modified samples exhibited a complete reversible curve as compared to pure SnO_2 that showed only a partial recovery. Modification with Fe resulted in an increase in the base line resistance of the sensor film attributed to the increase in the oxygen coverage. The sensor responses were also measured as a function of Fe concentration in order to find the optimum concentration over the SnO_2 sensor. As shown in Fig.4.34 (a), maximum response was observed for sensor containing 0.64 at% (as measured using EDX analysis) of Fe. At optimum distribution in this case for 0.64 at% of Fe, the free electrons released as a result of interaction with H_2S are transferred to SnO_2 host matrix causing a drastic change in its resistance values.

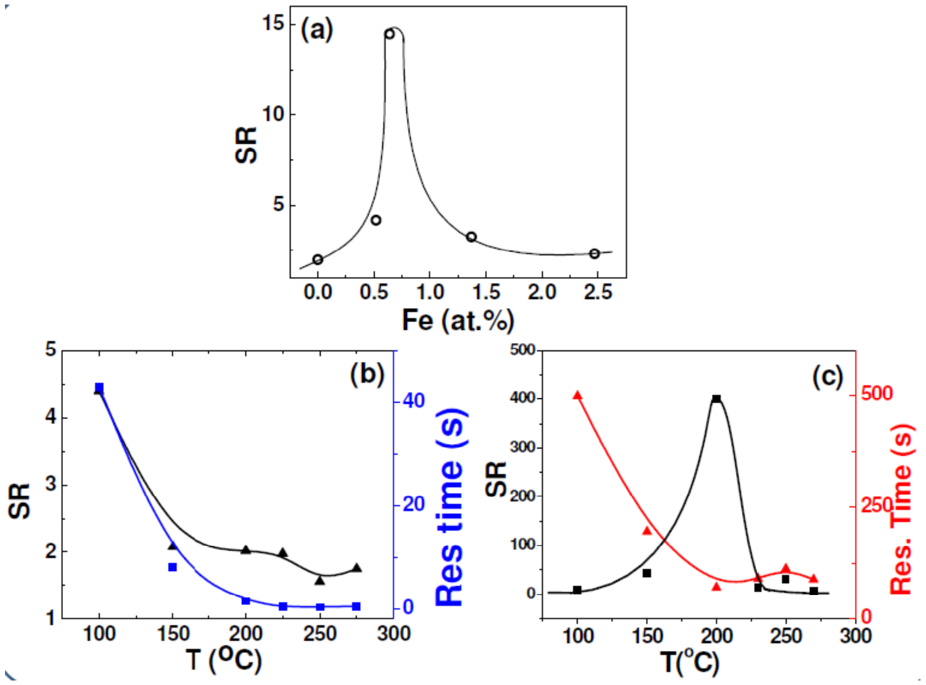

Fig.4.34. (a) Sensor response as a function of Fe concentration (as measured using EDAX analysis) towards 10 ppm of H_2S at 200°C. Effect of operating temperature on sensor response and response time recorded for (b) pure and (c) Fe modified SnO_2 sensor films towards 10 ppm of H_2S.

In order to further determine the optimum conditions for the H_2S detection, a systematic investigation of operating temperature effects on the gas sensing properties of pure and Fe modified SnO_2 films have been performed. Fig.4.34 (b) and (c) shows the plot of sensor response and response time as a function of operating temperature towards 10 ppm of H_2S. At all the operating temperature Fe modified (0.64 at.%) sample exhibited a maximum sensor response. For Fe modified sample the sensor response was found to increase with temperature upto 200°C. Although, the sensor exhibited a maximum response at 200°C the recovery time exhibited was 12 min which is larger than that of the sensor working at 225°C that exhibited a recovery time of 98 s. Because of this faster response kinetics, the operating temperature of 225°C was chosen for all the future experiments.

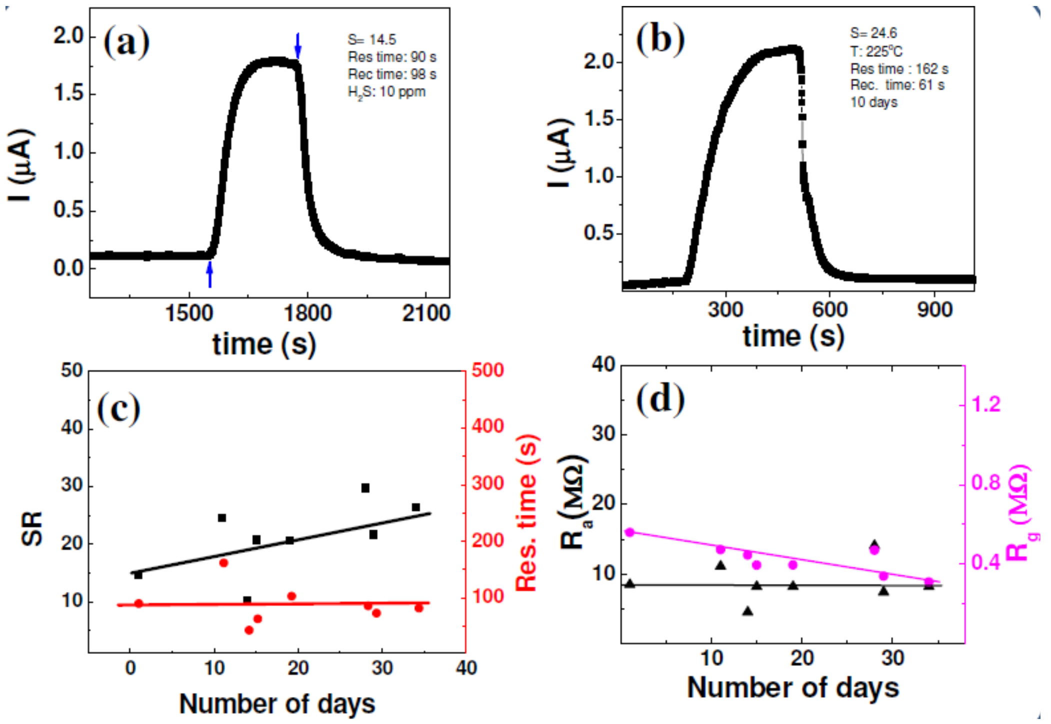

Fig.4.35. Response curves towards 10 ppm of H_2S at an operating temperature of 225°C recorded for sample with 0.64 at.% Fe-modified SnO_2 sensor films on (a) 1st day and (b) 10th day. Variation in (c) sensor response and response time, and (d) resistance in air and gas (10 ppm H_2S) of Fe-modified SnO_2 sensor films recorded over a period of 35 days.

Fig. 4.35 shows the stability measurements performed over a period of 35 days. Fig. 4.35 (a) and (b) shows the response curves recorded after first and 10th day. As is clearly evident the sensor exhibited faster response kinetics towards H_2S. Fig. 4.35 (c) shows the variation in sensor response and response time as a function of number of days. The **S** was found to increase with nearly identical response time. This could be attributed to the changes associated with the value of R_g as shown in Fig. 4.35 (d). Over the complete measurement period of 35 days the baseline resistance did not exhibited more than 10% drift from its resistance at first day. This clearly implies that the sensor has a reasonable stability towards H_2S.

Fig. 4.36 shows the selectivity histogram for pure and Fe modified sensor films towards 10 ppm of various gases. Fe modified sensor films exhibited a highly sensitive and selective response towards H_2S. It exhibited a negligible response toward all the other interfering gases.

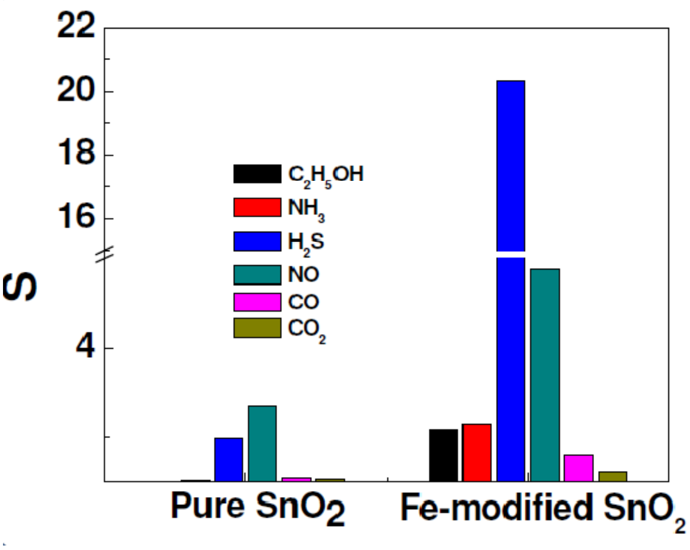

Fig.4.36. Selectivity histogram for pure and Fe modified SnO_2 films towards 10 ppm of different gases at an operating temperature of 225°C.

At an operating temperature of 225°C, the sensor surface is mainly characterized by the presence of adsorbed oxygen species namely O^-. Fe is present on the sensor surface as Fe_3O_4 that causes an increase in the adsorbed oxygen species abstracting electrons from the host matrix. This is reflected as an increase in the resistance of the sensor films. Additionally, the interconnected mesoscale spongy structures (as shown in Fig.4.28) further helps in improving the response by providing the percolation path. The space charge layer as a result of oxygen adsorption over the surface of SnO_2 films is expected to be close to the Debye length of SnO_2 (~6 nm) and could possibly help in improving the sensor response.

Apart from O^-, H_2S also interact with the Fe_3O_4 present on the sensor films as per the equation [181]; $Fe_3O_4 + 4H_2S \rightarrow 3FeS + S + 4H_2O$, Here, FeS is a low band gap material and hence causes a drastic decrease in the resistance of the sensor film. During recovery, FeS interacts with the atmospheric oxygen to regain the original state and the adsorption of oxygen species further helps to rejuvenate the sensor surface.

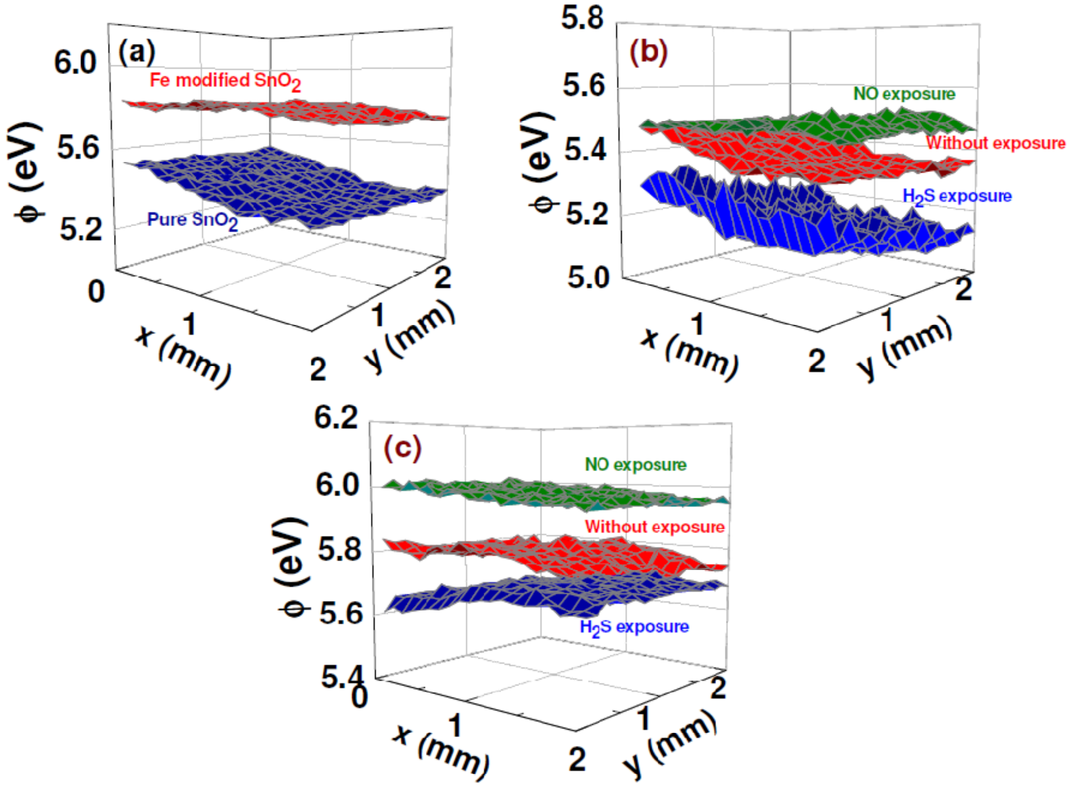

Fig.4.37. Work function area map (2 x 2 mm^2) recorded for both (a) pure and Fe modified sensor films (Fe: 0.64 at.%), and change in work function area map for (b) pure SnO_2 and (c) 0.64 at.% Fe modified films upon exposure to reducing (H_2S) and oxidizing gases (NO), respectively.

In order to further support the observation, work function measurements were performed. Fig.4.37 shows the work function area map recorded for both pure and Fe modified sensor films (Fe: 0.64 at. %). The average work function values before and after exposure to reducing and oxidizing gases have been tabulate in table in Fig. 4.37.

The average work function values were found to be 5.416 and 5.791 eV for pure and Fe-modified SnO_2 sensor films, respectively. An increase of work function by ~0.38 eV upon Fe modification was observed. Presence of Fe causes an increase in the concentration of adsorbed oxygen species abstracting electron from the host SnO_2 matrix and accordingly is responsible for the increased value of work function. This further corroborates the findings of increase in base line resistance upon Fe modification. Fig.4.37 shows the change in work function upon exposure to oxidizing (NO) and reducing (H_2S) gases for both pure (Fig.4.37 (b)) and Fe modified SnO_2 (Fig.4.37 (c)) thin films, respectively. As expected exposure to NO and H_2S causes the work function to increase and decrease, respectively.

Table 4.3: Average work function values recorded for pure and FeO modified SnO_2 films before and after exposure to reducing (H_2S) and oxidizing (NO) gases, respectively.

Sample	**Work function (eV)**	
	SnO_2	**SnO_2-Fe**
Without exposure	5.416	5.791
H_2S	5.195	5.681
NO	5.488	5.980

4.5 Conclusions

We have demonstrated chemiresistive sensors that work on the principle of p-n junctions. In these sensors, the host matrix was n-type semiconductor that was modified by a p-type additive. The investigated sensors are: CuO:ZnO nanowires; CuO: WO_3 thin films and Fe_3O_4: SnO_2 thin films. The optimized content of the p-type additive in these cases were respectively, 0.85%, 2.25, and 0.64 at. %. The p –type additive gets randomly distributed in the host matrix, leading to the formation of randomly distributed p-n junctions. The formation of p-n junctions was confirmed by resistivity, photoluminescence, and work function measurements.

The p-n junction based chemiresistive sensors exhibited improved gas sensing characteristics as compared to their individual counterparts. This was attributed to the destruction of p-n junctions in presence of H_2S. On reacting with H_2S, CuO and Fe_3O_4 converts to CuS and FeS respectively, which are metallic in nature. This lead to the destruction of p-n junctions and sharp reduction in resistance values, which enhanced the sensitivity of modified sensors towards H_2S. The gas sensing mechanism was further corroborated with impedance, Raman and XPS measurements.

Among three sensors, CuO: ZnO, CuO: WO_3 and Fe_3O_4:SnO_2, the best sensitivity towards H_2S is exhibited by CuO: WO_3 which is 534 times for 10 ppm. But the operating temperature of these sensors is higher, 300°C, than CuO: ZnO (200°C) and Fe_3O_4:SnO_2 (225°C) sensors. The fastest response kinetics is obtained in case of Fe_3O_4:SnO_2 based sensors which was 90 and 98 s respectively. The utility of these sensors can be decided according to the priority of the sensing parameters. All three sensors are able to sense H_2S selectively with fairly high sensitivities, therefore choice can be made according to the requirement of technique of fabrication at hand, low operating temperature or high sensitivity.

Chapter 5

Schottky-barriers Type Chemiresistive Sensors

5.1 Introduction

In this chapter we discuss the gas sensing properties of Schottky barrier type Au: ZnO nanowires and Au: WO_3 chemiresistive gas sensors. We also discuss the mechanisms guiding these sensing properties. The modification with Au resulted in improvement in gas sensing characteristics due to two effects namely, Schottky barrier formation and catalytic activity of Au.

5.2 Au: ZnO chemiresistive sensors

ZnO nanowires grown by hydrothermal method (details in section 2.2.2 (b) (iii)) were modified with gold (Au) that resulted in the formation of nano-Schottky barriers like junctions on the surface of ZnO. The formation of nano-Schottky barriers was corroborated using charge transport and work function measurements. Ultrathin films of gold of varying thickness were sputtered onto ZnO random nanowire network based sensors by varying the deposition time from 0 and 210 s. The Au modified samples were annealed at 400°C for 1 h to ensure uniform distribution throughout ZnO nanowires matrix. We were able to achieve room temperature H_2S sensing as a result of Au modification.

5.2.1 Au loading effect on ZnO random nanowires network

The Au loading was quantified as atomic weight % using EDX analysis as shown in Fig. 5.1 (a), where at.% of Au is plotted with varied deposition times.To determine the optimum Au concentration a systematic investigation of Au loading and its effect on response towards H_2S have been carried out. Fig.5.1 (b) shows the plot of variation in sensor response as a function of Au concentration (at %). Maximum response is obtained for 1.2 at% Au corresponding to a deposition time of 30 s and could be attributed to the formation of Au islands ~5 nm size. The deposition time could not be reduced further as ensuring the constancy of sputtering parameters was not possible for such small deposition times.

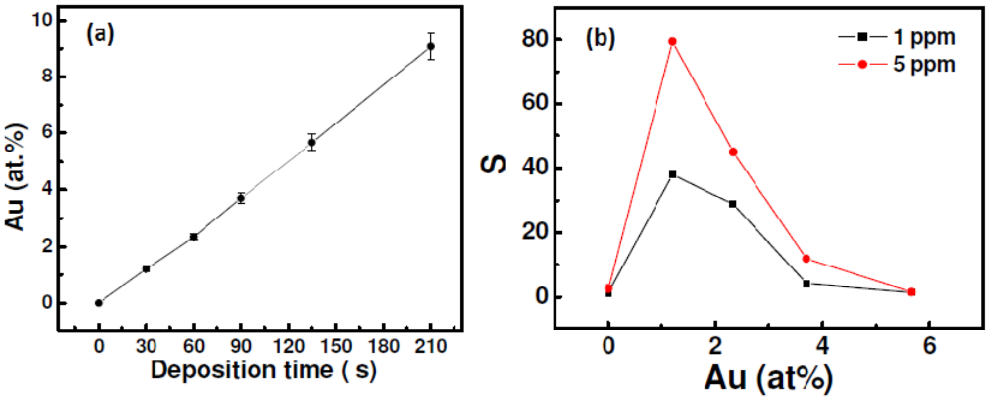

Fig.5.1. (a) Variation of Au (at.%) as measured using EDX with sputter deposition time of Au on ZnO NWs (b) Variation of room temperature sensor response as a function of Au (at%).

In order to further support the findings of EDX analysis Raman measurements were also performed. Fig. 5.2 shows the Raman spectra of pure and Au modified ZnO NWs. Both pure and Au modified ZnO NWs sample exhibited peaks at 437, 519, 580 and 660 cm^{-1}. The peaks at 437 and 660 cm^{-1} corresponds to E_2 (high) and A_1 modes, respectively. The broad peak at 519 cm^{-1} is a substrate peak (Si/SiO_2). The peak at 580 cm^{-1} could be assigned to a quasi-LO mode which is a mixed of A_1 (LO) occurring at 577 cm-1 and E_1 (LO) occurring at 588 cm^{-1} symmetry. This has been further attributed to ZnO crystallites with random orientation [182,183]. No shift in peak position was observed upon Au modification. However, an increase in Au loading results in the weakening and broadening of peak at 437 cm^{-1} and could be assigned to the deterioration of the host ZnO lattice by the distortion of the local atomic arrangement around the deposited Au. Additionally, two peaks at 580 and 660 cm^{-1} appears whose intensity is found to increase gradually with Au loading and is probably arising from disorder induced Raman scattering [184, 185]. As ZnO retain its lattice properties till Au loading of 1.2 at. %, we chose it as an optimized value for further gas sensing studies.

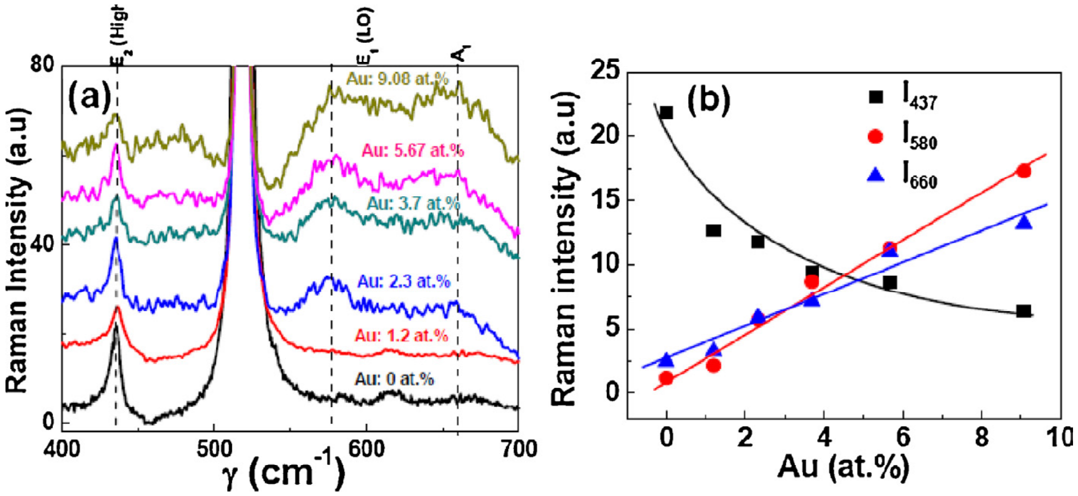

Fig.5.2. (a) Raman spectra of pure and Au modified ZnO NWs samples and (b)Relative variation in intensity of peaks at 437, 580 and 660 cm^{-1} as a function of Au modification.

To better understand the effect of Au modification (1.2 at. %) on NWs and the charge transport mechanism temperature dependant DC conductivity studies were performed. The charge transport measurements were carried out using two probe configurations with in-plane electrode geometry. The low temperatures measurements (300-50K) were carried out using closed cycle cryostat (in a helium gas environment), Keithley 6487 picoammeter/voltage source and Labview based data acquisition system. All measurements were performed in dark to avoid the problem of photoconductivity. Fig.5.3 (a) shows the logarithmic plot of resistivity as a function of temperature for both pure and Au modified samples. A typical semiconductor type behavior with resistivity increasing monotonically with decrease in temperature, over the whole measurement range is observed. Au modified samples exhibited a higher resistivity compared to that of pure ZnO NWs. This could be attributed to the formation of nano-Schottky type barrier junctions at the ZnO-Au interface. At lower temperatures the charge transport is in the presence of defect states [186] and modification with Au results in an additional defect states. The charge transport properties in disordered systems have been explained using various conduction mechanisms, including the thermal activation conduction, the nearest neighbor hopping conduction, the Mott variable-range hopping (VRH) conduction and the Efros-Shklovskii VRH conduction processes [187].

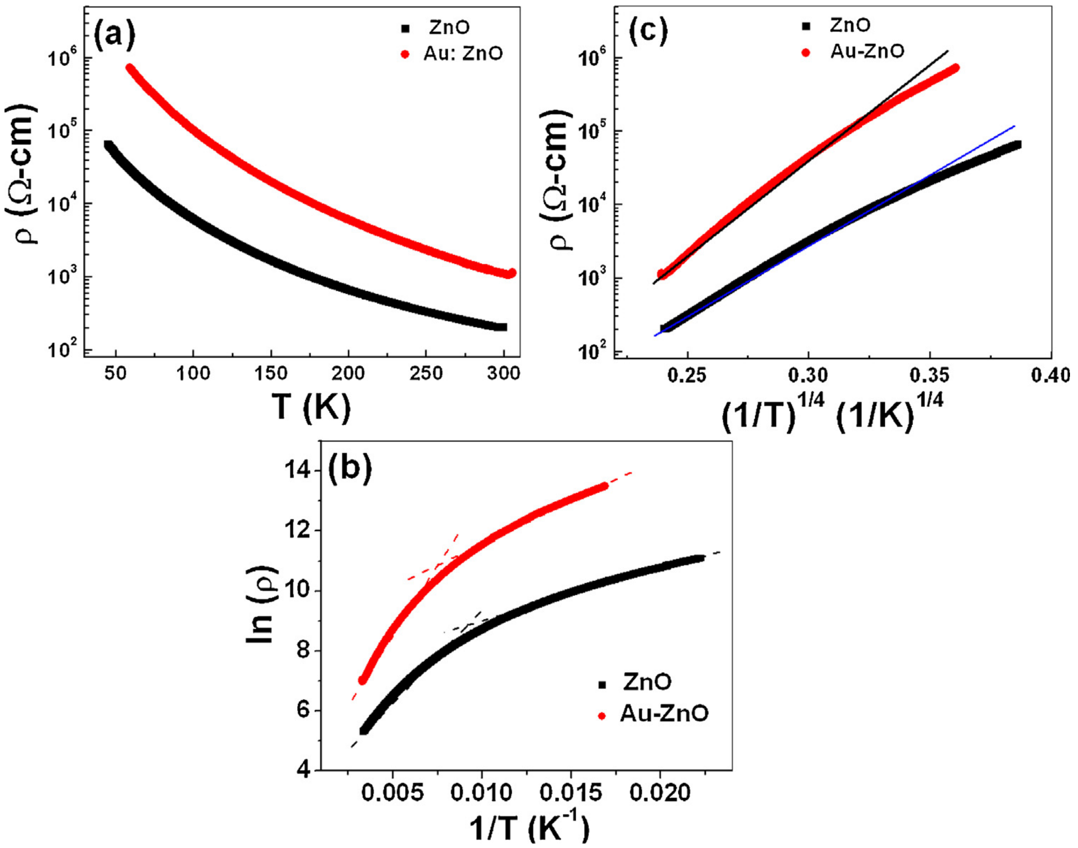

Fig. 5.3. (a) Variation in logarithm of resistivity with temperature for pure and Au modified ZnO NWs and (b) Variation in logarithm (to the base e) of resistivity with (1/T) for pure and Au modified ZnO NWs film. The dotted lines indicates the fit in the two temperature zones, 300–150 K and <110 K, respectively and (c) Variation in logarithm of resistivity with $(1/T)^{1/4}$ for pure and Au modified ZnO NWs film. The straight solid lines indicate the linear fit to the curve according to Eq. 5.3.

To determine the conduction principle involved in the present case a careful investigation of the temperature dependent resistivity measurement was performed. As shown in Fig.5.3 (a and b) at temperatures between 70 and 300 K, ρ smoothly increases with decreasing temperature. This implies that there is no visible straight regime in any temperature interval. Here, the measured $\rho(T)$ can be quantitatively described by the equation;

$$\rho(T)^{-1} = \rho_1^{-1}e^{-E_1/k_BT} + \rho_2^{-1}e^{-E_2/k_BT} \qquad (5.1)$$

where k_B is the Boltzmann constant, ρ_1 andρ_2 are temperature insensitive resistivity prefactors, and E_1 and E_2 are the relevant activation energy associated with the two types of thermal activation conduction process with the convention $E_1 > E_2$. Table 1 indicates the corresponding fitted values for both the sensor films.

Table 5.1. Calculated values of activation energies and resistivity prefactors from ln ρ vs 1/T plots.

Sample	**ρ (300K) (Ω cm)**	**ρ_1 (Ω cm)**	**E_1 (meV)**	**ρ_2 (Ω cm)**	**E_2 (meV)**
ZnO	205	34.6	48.8	1.6×10^3	14.4
Au-ZnO	1100	73.9	73.3	6.7×10^3	8.8

These results illustrates that there exist a group of shallow/intermediately deep donors with E_1 activation energy that are responsible for the charge transport between 300-150 K. And as the temperature decreases below ~ 110 K, the charge transport is governed by the electrons that hop from an occupied state to an unoccupied nearest-neighbor state in the impurity band. This nearest-neighbor hopping process is phonon assisted and requires a small amount of energy i.e, E_2 activation energy. The shallow donor concentration (n_D) can be estimated using the relation $n_D = (\rho e \mu_e)^{-1}$, where e is the elementary charge and μ_e is the electron mobility which takes the value of 10 cm^2/Vs for the measured temperature range. Using the values of ρ_1 from table 5.1 the n_D values were found to be ~1.8 and 0.8 $x10^{16}$ cm^{-3} for ZnO and Au modified ZnO NWs, respectively.

At temperatures below 110 K, the charge transport is has been found to be governed by Mott VRH mechanism. According to the Mott [188] the temperature dependence of the VRH resistivity, ρ, (also referred to as phonon-assisted quantum-mechanical tunneling process) is given as:

$$\rho = \rho_0 e^{(T_0/T)^{1/4}} \quad (5.2)$$

$$ln\rho \propto (T_0/T)^{1/4} \quad (5.3)$$

where, $\rho_{o,}$ is the pre-exponential resistivity factor and $T_{0,}$ is a characteristic temperature related to the disorder in the system and given as

$$T_0 = \lambda\alpha^3/ k_B N(E_F) \quad (5.4)$$

where $N(E_F)$ is the localized state density at the Fermi level, α is a parameter such that $\xi = 1/\alpha$ is the localization length of the wave function for localized states, $\lambda = 16$ is related to the hopping probability [189, 190]. A hopping electron will always try to find the lowest activation energy ΔE and the shortest hopping distance r. A good curve fitting as evident from figure 10 (c) indicates that the conductivity of pure and Au modified ZnO obey the $ln\rho \propto (1/T)^{1/4}$. In order to confirm the validity of the Mott VRH mechanism the most probable hopping distance ($R_{hop} = 3/8\ \xi\ (T_o/T)^{1/4}$) was determined using the Mott characteristic temperature. The characteristic temperature for pure and Au modified ZnO samples were found to be 52 and 56 K, respectively. Our calculations indicates that the criterion for Mott VRH conduction, $R_{hop}/\ \xi > 1$, is not satisfied in both the cases. This clearly indicates that the charge transport in ZnO and Au- modified ZnO NWs is governed by thermal conduction and nearest neighbor hopping mechanism. The role of Au modification and the influence of the electrode (Schottky or Ohmic) contact needs to be investigated further (especially on single NWs) to get a complete understanding over the charge transport properties.

5.2.2 Gas sensing response and sensing mechanism

Fig.5.4 shows the room temperature (25°C) response curves for pure and Au modified ZnO NWs towards 1 and 5 ppm of H_2S, respectively. The sensor response of Au modified sample towards 1 and 5 ppm, were 38 and 79.4, respectively as compared to that of pure ZnO NWs for which the values were 2 and 5, respectively. Modification with Au also resulted in the improvement of the recovery time. It being 860 and 170 s for pure and Au modified samples towards 5 ppm H_2S, respectively.

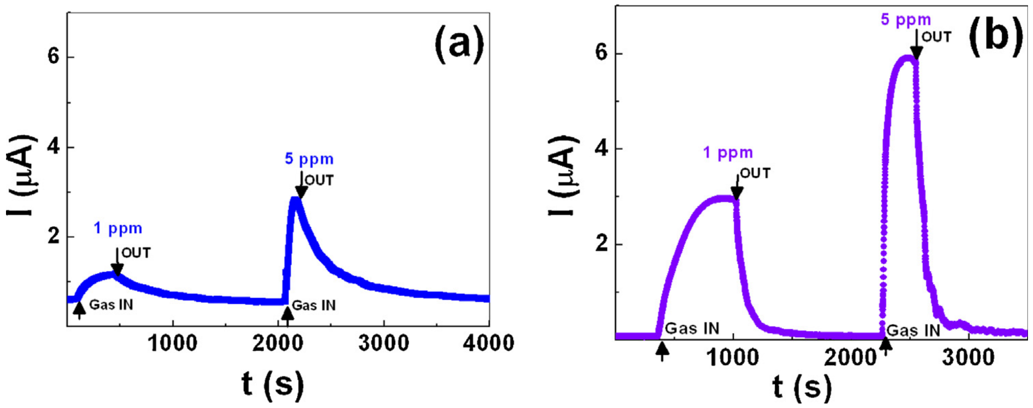

Fig.5.4 Response curves of (a) pure and (b) Au modified ZnO NWs (Au at%=1.2) towards 1 and 5 ppm H_2S, respectively at room temperature.

Selectivity histogram as shown in Fig.5.5 (a) clearly indicates that the Au modified samples are highly selective towards H_2S. Sensor films exhibited a negligible response towards all the other interfering gases. For commercial applications the stability of the gas sensing devices is also an important parameter. Fig.5.5 (b) shows the stability measurements performed over a period of 5 weeks for the Au modified ZnO NWs films towards 10 ppm of H_2S at room temperature.

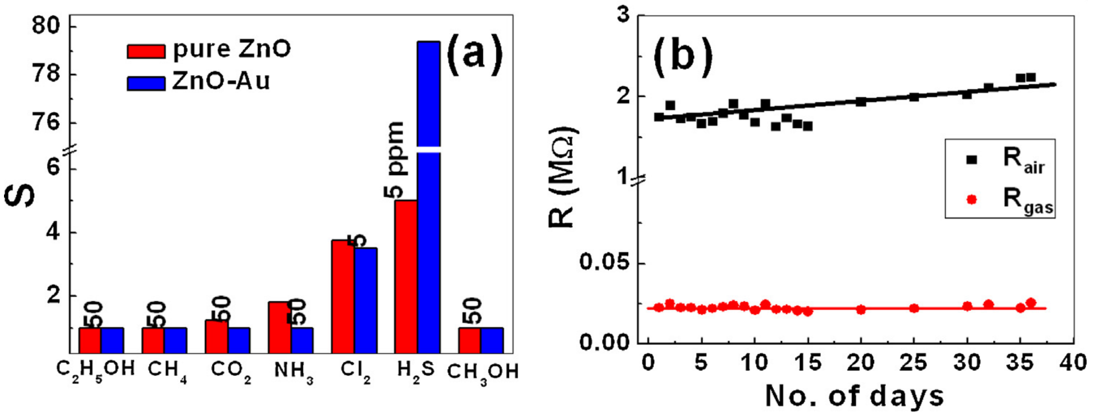

Fig.5.5. (a) Selectivity histogram of pure and Au (at%= 1.2%) modified ZnO NWs samples towards different gases, and (b) Long term stability measurement for Au modified ZnO NWs showing R_a and R_g recorded over a 15 day period at room temperature.

The resistance of the sensor film (R_a) was found to increase with time with a corresponding increase in the sensor response. Throughout the measurement period the sensor response was found to vary between from 75 to 95. The change in the resistance of the sensor film could be attributed to the surface poisoning, catalyst poisoning, migration and/or segregation of additives, degradation of contacts (diffusion), fluctuations of temperatures in the surrounding atmosphere and humidity related effects [191]. It has been shown that the adsorption of water is a dominant factor in the formation of surface characteristics, both with respect to the adsorption of other species and in surface catalysis. The electronic properties of ZnO NWs have been shown to be affected by the presence of water vapor [192,193]. More specifically, with increase in the relative humidity values the resistance is observed to decrease attributed to the chemisorbed hydroxyl groups (OH^{-}) onto the surface following the Grotthuss mechanism [194]. Further at constant humidity values the resistance variation was found to be 2% measured over a period of 3 months.

The contact provided to the ZnO NWs films is by Au layer which also results in a symmetrical Schottky-type barrier or the contact resistance. For the flow of electrons at the two electrodes there exist two junctions one at entering Au/ZnO interface and the other leaving the ZnO/Au interface. The room temperature resistance of pure and Au-modified ZnO NWs is 0.16 and 1.75 MΩ, respectively. The contribution of symmetrical contact resistance to the total resistance is minimum compared to its bulk value and can be neglected. The deposition of thin Au layer (10 nm) results in a discontinuous film or island formation that is randomly distributed along the length of NWs. This leads to the formation of nano-Schottky type barriers or junction between metallic Au and semiconducting ZnO. In other words, a continuum of gap states induced by the Au islands locally pins the ZnO Fermi level [195]. The Fermi levels are forced to coincide and electrons pass from the ZnO to Au. The result is an excess of negative charge on Au and the formation of a positive charge depletion zone in the ZnO near its surface. The gap between Au and ZnO vanishes and the electric field now corresponds to a gradient of the electron potential in the depletion region. The Schottky barrier height (SBH) at the interface is controlled by the interaction between the metal adatoms and the semiconductor dangling bonds. Also, metal lattices could introduce different interface geometries, associated with the various adsorption sites of the metal adatoms. The potential barrier thus formed would result in the electron depleted NWs surface. This is the reason why the resistance of Au modified NWs is higher than the pristine NWs. Now, the barrier properties can easily be altered by the adsorption or desorption of adsorbed species or target gas molecules. Besides, Au is also known to promote the catalytic dissociation of molecular oxygen species which is also known as spillover in catalysis. The resulting oxygen atoms migrate onto the sensor surface and forms oxygen ions (O_2^-at room temperature) by capturing the free electrons. Modification with Au significantly increases the quantity of oxygen ions on the surface (additional active sites) as shown in Fig.5.6. This is the reason why the sensor exhibits a lower current in air. Modification with Au nanoparticles imparts high response and response kinetics to the host material and is attributed to its dual role. More specifically, it acts as a catalyst for the dissociation of molecular oxygen species and secondly it forms nano-Schottky-type barrier junction with ZnO NWs.

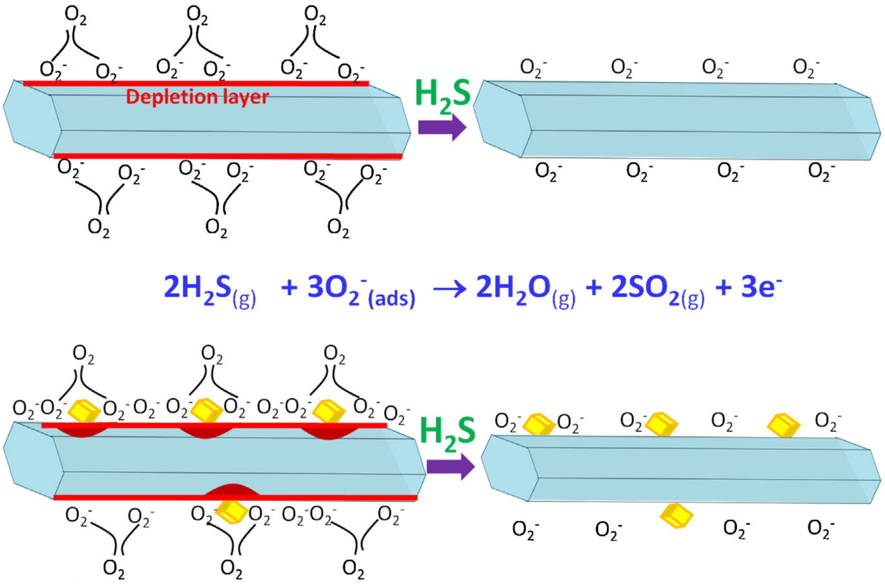

Fig.5.6. Schematic representation of the H_2S sensing mechanism in Au modified ZnO nanowires random networks.

Here the presence of Au nanoparticles on the surface facilitates the H_2S oxidation process by providing large number of adsorbed oxygen species. Thus, the dual role of Au coupled with the associated high surface area to volume ratio of NWs contributes towards an improved H_2S response kinetics. It is interesting to note that the gas response is mainly governed by the two factors. The first is the number of active sites available for the adsorption of oxygen and the test gases on the sensor surface. The amount of oxygen adsorbed on sensor surface depends on the particle size, specific surface area of the sensor and the operating temperature [196]. Second the reactivity of the test gas. In the case of H_2S, the bong energy of H-SH is 381 kJ/mol [197], so that it is easy to open the bond H-SH at lower temperature. Wang et al. have also observed the fast response kinetics towards H_2S at room temperature for CuO doped SnO_2 films [198]. In particular the sensor films exhibited a fast response (40 s) and recovery (15 s) times towards 50 ppm of H_2S at room temperature. The fast response kinetics has been attributed to the uniform distribution of CuO on the surface of the SnO_2, presence of the transitional layer at the CuO–SnO_2 interface due to interdiffusion processes as well as the n-SnO_2/p-CuO heterojunctions. We have also observed the similar response kinetics for CuO thin films wherein at low concentrations (<400 ppb) the response and recovery were observed to be very small (60s). In the present case, we anticipate that the dual role of Au coupled with the associated high surface area to volume ratio of NWs contributes towards an improved H_2S response kinetics at room temperature.

ZnO NWs deposited onto a conducting Au coated (Cr/Au: 10/120 nm) glass substrates were used for work function measurements. The difference between the work function of Au (5.1) and ZnO (5.3 eV) is ~0.2 eV. The barrier height thus formed will contribute at lower thickness of the material (ZnO). The ZnO nanowires grown over the surface of Au were having the length in the 1-2 µm range. At this length scale there is no contribution from the underlying Au layer for work function measurements. As shown in Fig.5.7 (a), Au modified ZnO NWs exhibited a higher work function of 5.39 eV as compared to that of pure NWs which exhibited ϕ of 5.09 eV. This higher value of ϕ can be attributed to the modulation of the Schottky barrier height at ZnO-Au interface. Fig.5.7 (b) demonstrates the changes in ϕ values for Au modified ZnO NWs upon exposure to different gases. As expected a maximum change is observed for the samples exposed to H_2S gas

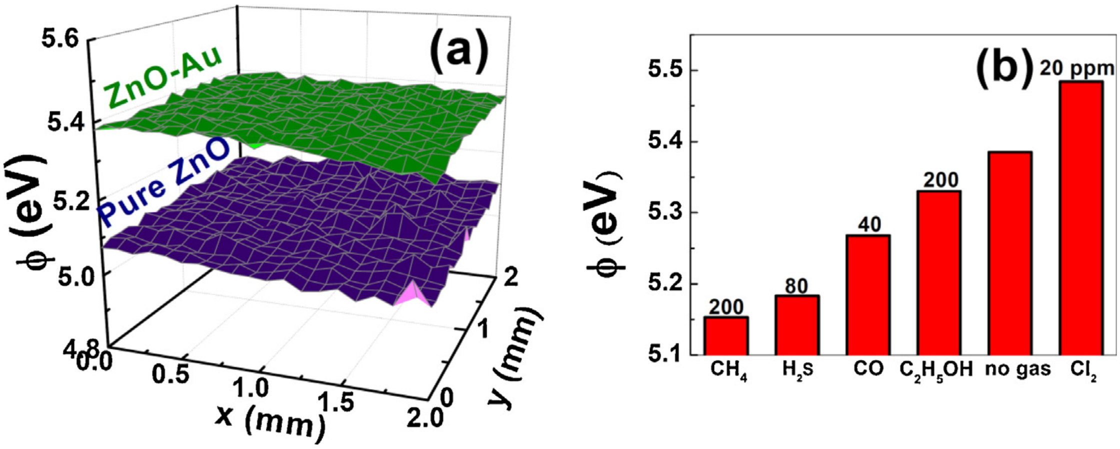

Fig.5.7. (a) Comparison in the ϕ value of pure and Au modified ZnO NWs and (b) Change in ϕ for Au modified sample upon exposure to various gases at room temperature.

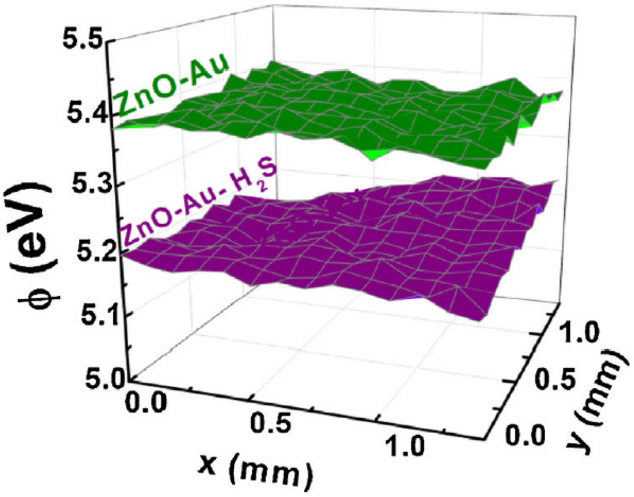

Fig.5.8.Change in ϕ upon exposure to H_2S at room temperature in Au: ZnO nanowires random networks.

Fig.5.8 shows the raster area scans for Au modified ZnO NWs upon exposure to reducing H_2S. The area scan map upon exposure exhibited a lowering trend attributed to the recovery of the sensor film during measurements. Herein the presence of Au nanoparticles on the surface facilitates the H_2S oxidation process by providing large number of adsorbed oxygen species. The donation of electrons by reducing gas at the sensor surface results in the shift of Fermi level (E_F) towards CB depicted as lower ϕ. In other words a drastic change in sensor resistance or higher current in H_2S environment is seen.

5.3 Au: WO_3 chemiresistive sensors

In this section, we show a systematic investigation of the gas sensing properties of pure and Au incorporated WO_3 sensor thin films towards H_2S. The sensor films have been realized using a simple method of vacuum deposition as discussed in section 2.2.2 (a) (i). We have investigated the effect of sensor operating temperature, Au loading, and gas concentration on sensing properties to determine the optimum conditions for the detection of H_2S gas. Additionally, Raman and work function measurements both with and without the test gases have been performed to elucidate the nature of interaction with the sensor film.

5.3.1 Structural and morphological characterization

The resultant W films after vacuum depositions are black in color, which when oxidized at an elevated temperature of 600°C in O_2 environment gets transformed into greenish yellow color corresponding to WO_3 phase formation. Fig.5.9 (a-e) shows the SEM images of the pure and Au incorporated WO_3 thin films. It is seen that pure film consists of large number of microparticles having an average grain size of ~5.4 μm containing microcracks and even cavities. Additionally, these particles are seemed to consist of large number of nanosized grains with size <100 nm. The sensor films color changes from greenish yellow to violet purple upon incorporation of Au. Besides it also causes elimination of microcracks. Additionally, grain size decreases (Fig.5.9 (f)) and porosity increases with Au incorporation.

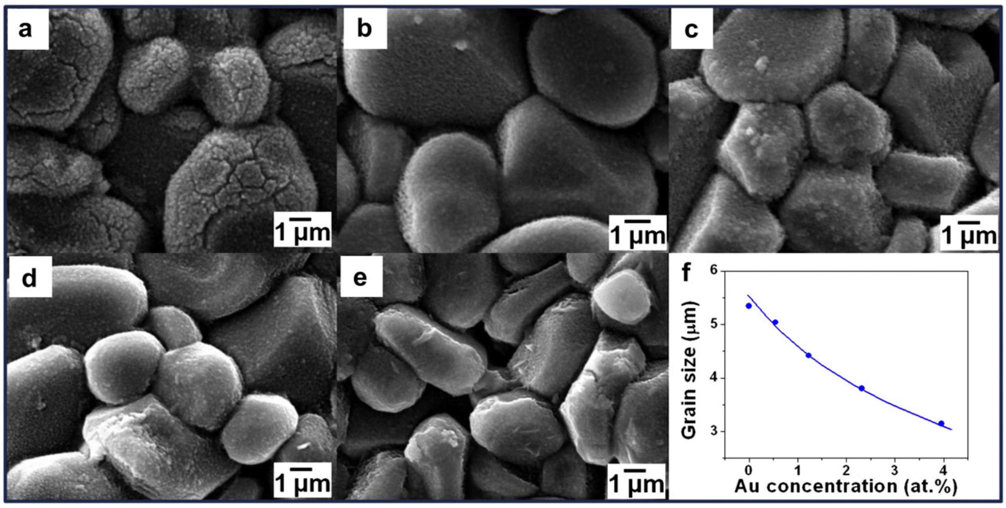

Fig.5.9. SEM images of (a) pure and Au incorporated WO_3 thin films containing (b) 0.55, (c) 1.23, (d) 2.32 and (e) 3.95 at.% Au, and (f) a plot of average grain size vs. Au content in WO_3 thin film

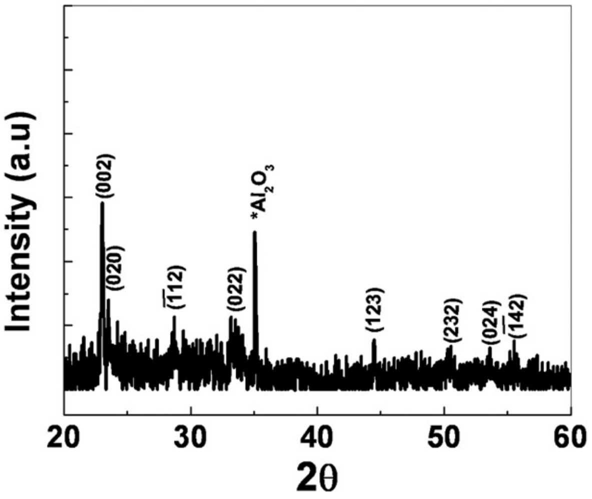

Fig.5.10. XRD profile of Au (2.32 at.%) incorporated WO_3 sensor thin film.

Fig.5.10 shows the XRD profile of Au incorporated (2.32 at.%) WO_3 thin film. The pattern matches with the monoclinic crystal structure of WO_3 having lattice parameters of a = 7.309, b = 7.545 and c = 7.689 Å, respectively.

5.3.2 Gas sensing properties of pure and Au modified WO_3 sensor films and sensing mechanism

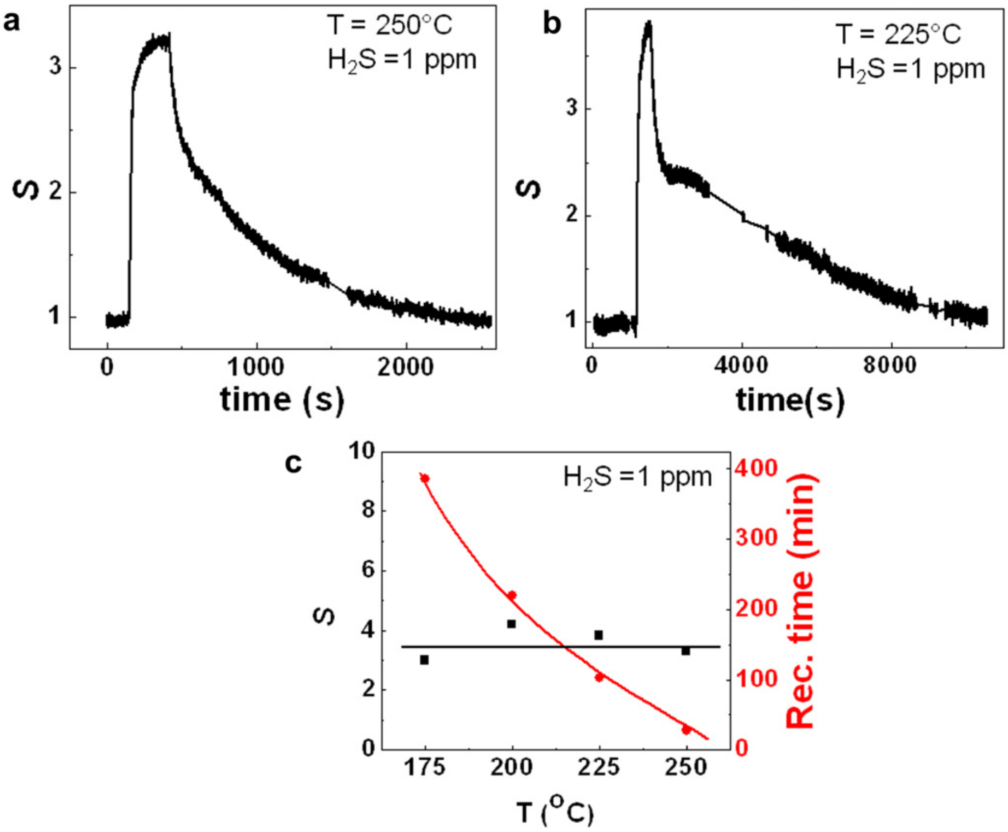

Fig.5.11 Sensors response curves at (a) 250, (b) 225°C and (c) the variation in sensitivity and recovery times as a function of an operating temperature for pure WO_3 thin films measured upon exposure to 1 ppm of H_2S

Fig.5.11 shows the sensing response curves recorded for pure WO_3 at an operating temperature of 250 and 225°C, respectively towards 1 ppm of H_2S. The sensitivity of sensor film towards H_2S is not affected much with the operating temperature however a strong variation in sensor films recovery time is seen. Recovery time is observed to decrease with increase in operating temperature. From Fig.5.11 (c) it is clear that the sensor responded with fairly good sensitivity and a reasonable recovery time at an operating temperature of 250°C and hence was chosen for all the further experiments.

To determine the optimum Au concentration in the host matrix a systematic investigation of Au loading and its effect on sensitivity towards H_2S have also been carried out. A typical bell shaped curveas shown in Fig.5.12 (a) with maxima for WO_3 thin films containing 2.32 at. % Au was observed. An overall trend of decrease in the air resistance (measured at fixed temperature of 250°C) with Au incorporation is seen. Fig.5.12 (b) shows the selectivity histogram of pure and Au incorporated (2.32 at. %) sensor film at an operating temperature of 250°C towards 1 ppm of different gases. Interestingly, both pure and Au incorporated samples exhibited a maximum sensitivity towards H_2S. However, upon Au incorporation the sensor became highly sensitive and thereby selective towards H_2S. A negligible response towards all the other interfering gases namely NH_3, Cl_2, CO, CH_4,CO_2 and NO_2 was observed.

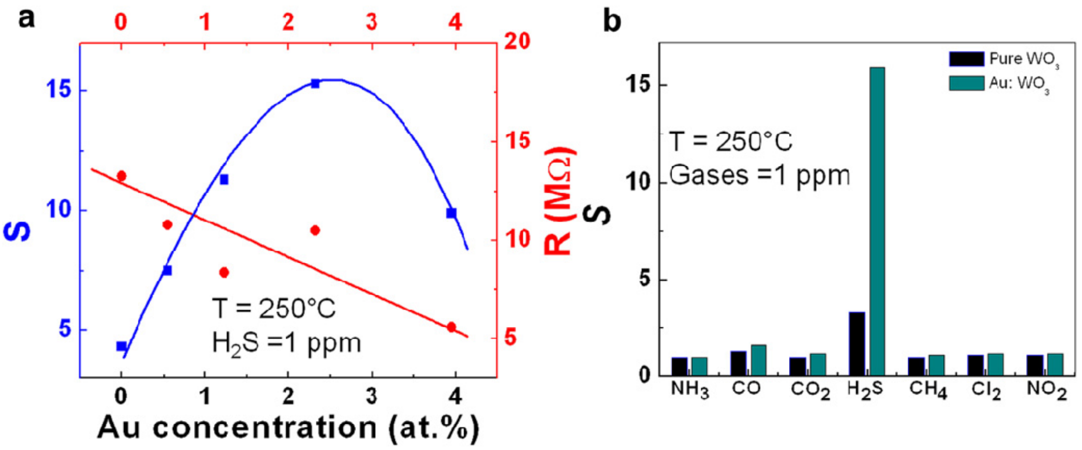

Fig.5.12 (a) Effect of Au loading on sensitivity and base (air) resistance on exposing to 1ppm H_2S (at an operating temperature of 250°C). (b) Selectivity histogram pure WO_3 and Au incorporated WO_3 thin film sensors towards different gases at an operating temperature of 250°C.

A systematic investigation of the effect of gas concentration was then performed at an operating temperature of 250°C. Fig.5.13 shows the response curves of pure and Au incorporated WO_3 sensor films recorded with the increasing concentration of test gas. As is evident from the figure sensitivity is found to increase with gas concentration. Au incorporated WO_3 films exhibited a better sensing performance in comparison with that of pure WO_3 sensor films. For example, towards 0.7 ppm of H_2S, pure WO_3 films showed a sensitivity of 2.9 with a response and recovery time of 106 s and 32 min, while Au incorporated sample (2.32 at. %) exhibited an increase in the sensitivity to 12 with a response and recovery times of 88 s and 18 min, respectively. Moreover, Au incorporated thin films were able to detect as low as 50 ppb of H_2S with a sensitivity value of 2.7.

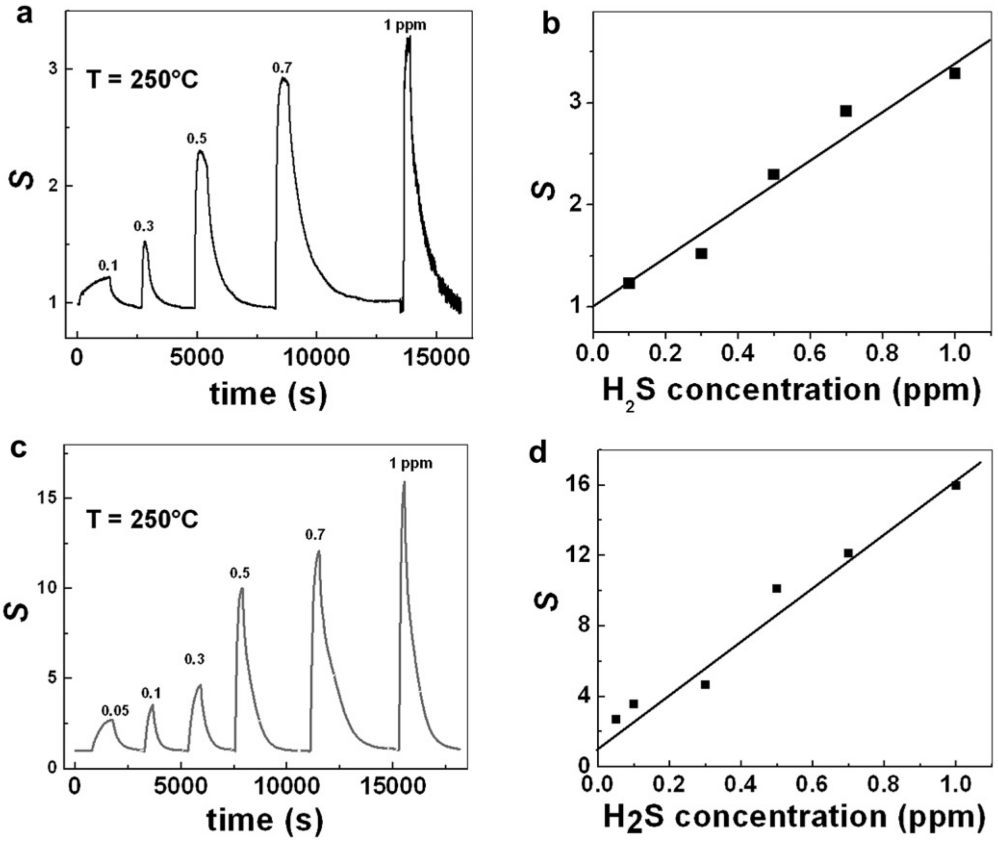

Fig.5.13 Response curves of (a) pure and (c) Au incorporated (2.32 wt.%) WO_3 thin films towards sub-ppm concentration of H_2S at an operating temperature of 250°C and corresponding variation in sensitivity with gas concentration (b) and (d).

Raman investigations of the sensor film before and after exposure to H_2S have also been performed as it is known to give the “fingerprint” of the material. Fig. 5.14 (a) shows the Raman spectra (recorded at room temperature) of a bare WO_3 film before and after exposure to 100 ppm of H_2S. All the spectra invariably exhibit a series of sharp peaks at wavenumbers lower than 250 cm^{-1} attributed to vibrational modes of the WO_3 lattice i.e. due to the relative translational and rotational motion of WO_6 octahedra in the same unit cell. They also exhibit peaks at intermediate frequency region (between 200-400cm^{-1}) assigned to the bending modes of O-W-O bridging bonds and at high frequency region (600-900cm^{-1}) attributed to the stretching modes of W-O bonds [199, 200]. By and large the Raman profile of the samples with peaks centered at approximately 40, 60, 73, 96, 136, 274, 328, 718 and 809 cm^{-1} resemble that of crystalline monoclinic phase of WO_3. Absence of 950 cm^{-1} peak in all the samples studied is indicative of their high crystalline nature [201].

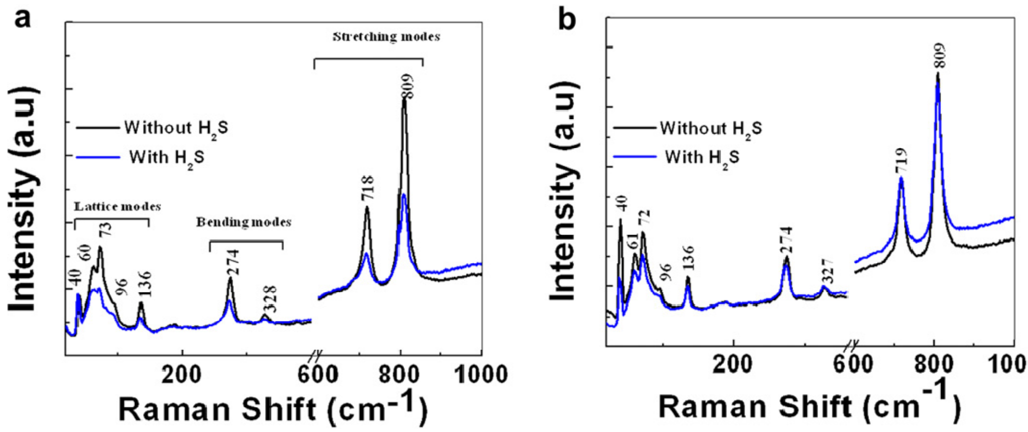

Fig.5.14 Raman spectra recorded for (a) pure WO_3 and (b) Au incorporated WO_3 sensor films before and after exposure to H_2S gas at room temperature

Upon exposure to gas, all the peaks reduced significantly in intensity however the peak positions were observed to remain almost unaltered. Raman spectra of Au incorporated WO_3as shown in Fig. 5.14 (b) are qualitatively similar to that of WO_3.

Interestingly, exposure to H_2S does not result in much variation in Raman peaks as compared to that of pure WO_3 sensor films. The peaks attributed to the lattice modes reduced in intensity marginally while there is no significant variation in the peaks attributed to the bending and stretching modes. This could be attributed to the faster reaction kinetics arising from the embedded Au in WO_3 matrix. Also, augmentation of signals due to the surface enhanced resonance Raman effects may also contribute towards the same.

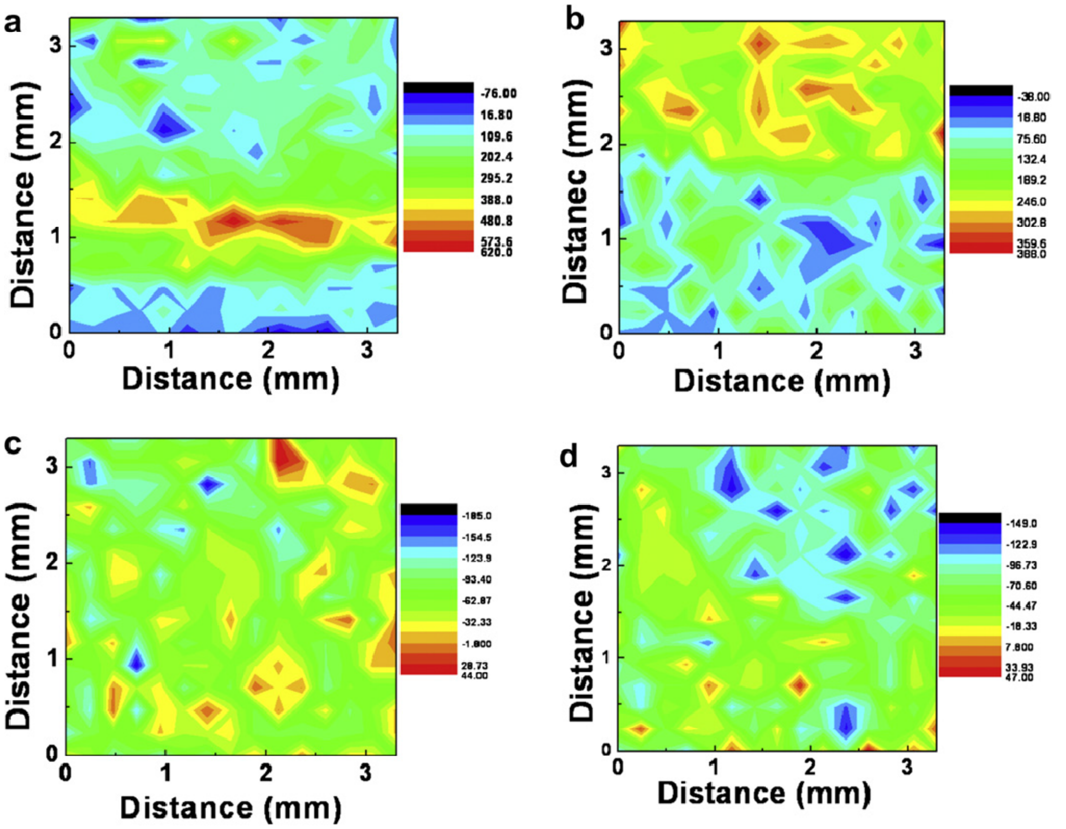

Fig.5.15 2-D work function map of pure WO_3sensor films (a) before and (b) after exposure to H_2S and Au incorporated WO_3 (c) before and (d) after exposure to H_2S

In order to support the findings of Raman investigations work function measurements were also carried out. Fig.5.15 shows the work function area scan as a contour plot recorded for 3.3 mm^2 of sensor samples before and after exposure to 10 ppm of H_2S. The x and y axis depicts the dimension of the sample across which the measurements were taken and different colors depict the contact potential difference between sample and the standard gold tip in mV. Table 5.2 illustrates the final work function values of the sensor samples. Incorporation of Au in the WO_3 matrix resulted in a decrease in work function by 0.25 eV. Exposure to H_2S resulted in the decrease in work function by 30 and 11 meV for pure and Au incorporated WO_3 samples, respectively. The small variation in the work function of Au incorporated sample is attributed to the faster reaction kinetics (recovery time). This result is in accordance with and corroborates further the findings of Raman investigations.

Table 5.2. Work function values recorded for sensor samples before and after exposure to H_2S.

Sample Name	**Φ, before exposure (eV)**	**Φ, after exposure (eV)**
Pure WO_3	5.221	5.191
Au: WO_3	4.973	4.962

It is established that interaction of H_2S with WO_3 leads to the generation of large number of oxygen vacancies. The interaction leads to the introduction of new energy levels in the mid gap states of WO_3. Besides, incorporation of doping elements in particular Au has been known to impart the sensitivity in the host material mainly via electronic sensitization mechanism. In this the additives enhances the rate of reaction by providing the additional active sites. The interaction with the test gas mainly occurs on the Au surface and the corresponding changes are transferred immediately to the host matrix reflected as a fast drop in the resistance of the sample. This is expected to contribute for improving both the response and the recovery times of the sensor films.

Further, the oxygen vacancies can easily be reoxidized upon exposure to fresh air thereby assuring complete recovery.

5.4 Conclusions

We have demonstrated Schottky barrier type sensors by modifying ZnO nanowires and WO_3 thin films with gold. Au formed randomly distributed island type film onto the sensor film. The formation of Schottky barriers at the Au: ZnO and Au: WO_3 interface depleted ZnO nanowires and WO_3 thin films of charge carriers. Observance of higher work function, a higher resistivity for Au modified samples and Raman spectroscopy further corroborated the findings. The catalytic property of Au in increasing the oxygen adsorption at the semiconductor surfaces of ZnO and WO_3 and depletion caused by Schottky barrier formation lead to enhanced sensor response upon Au modification. Our results clearly demonstrate that modification with metal nanoparticles could be effectively used to tailor the response of sensor. This could probably be extended to other similar systems to realize sensor with better response kinetics.

We were able to achieve room temperature H_2S sensing in case of Au: ZnO nanowires based sensors which showed enhanced sensitivity of 80 as against 5 for pure ZnO nanowires. The recovery times also improved in case of Au: ZnO as against their pure counterpart (170 s for Au: ZnO, 860 s for ZnO nanowires). Au modified WO_3 films showed a detection limit of 50 ppb and better sensitivity and response kinetics as compared to pure WO_3 thin films.

Chapter 6

Summary

The motivation of the thesis work was to investigate metals-oxides in the form of thin films and nanostructures for the selective detection of H_2S gas, which are needed for Indian Heavy Water Plants for monitoring its concentration in environment. The materials investigated in this thesis were: p-type CuO and n-type ZnO, SnO_2 and WO_3. In addition, we have investigated the sensing characteristics of films having p-n junctions and Schottky barriers.

The main results obtained on the sensing characteristics of metal-oxide thin films and nanostructures are summarized below.

- The 100-500 ppb range detection of H_2S has been obtained for the first time using CuO thin films at room temperature along with fast response (~60 s) and recovery (~90 s) times. The base line resistance stability of these films was found to be better than 5% over a prolonged period even after repeated exposure to H_2S. In air (before exposing to H_2S), the grains of CuO films absorb oxygen from air and form surface states. These surface states created by adsorbed oxygen species (O_2^-) allow electrons to be excited from valence band (VB) and induce holes in p-type CuO grains. When low concentrated H_2S gas reaches CuO grains, it reacts with O_2^- and the released electrons recombine with the holes in the VB and, thereby causing an increase in the film resistance. During recovery, the adsorption of oxygen species easily rejuvenates the CuO surface.
- CuO films are however unsuitable for the detection of high concentration of H_2S, as it reacts with CuO using almost an irreversible reaction: $H_2S_{(g)} + CuO_{(s)} \rightarrow CuS_{(s)} + H_2O_{(g)}$.
- Films of CuO nanowires, prepared by dispersing the CuO nanowires in methanol and spreading this solution between the two gold electrodes prefabricated on alumina substrate, exhibited response and recovery times (for 10 ppm H_2S)

respectively, ~4 and 16 minutes. These results are inferior as compared to that of CuO thin films, which is attributed to the lack of proper interconnections among CuO nanowires.

- Uncharacteristically, the sensors based on isolated CuO nanowires exhibited n-type behavior for H_2S, which is attributed to the surface states created by unintentional doping. Nevertheless, these sensors exhibited good sensitivity for H_2S (~200% for 10 ppm of H_2S gas) with very fast response (30 s) and recovery times (60 s), which is attributed to higher surface-to-volume ratio of nanowires. The flip side of the isolated nanowire sensors is the long term stability, as due to very reactive surfaces the chemisorptions of atmospheric gases modify the surface states and a drift in the base resistance occurs with time.
- The sensing characteristics of n-type SnO_2 thin films prepared using sputtering and RGTO methods revealed that sputtered films show better H_2S sensing characteristics (i.e. improved sensitivity and faster response/recovery kinetics), owing to uniformly distributed grains of relatively smaller in size and presence of bridging type oxygen vacancies that facilitated the charge transfer between the sensor surface and the H_2S molecules. Moreover, the optimum operating temperature of sputtered films was found to be quite lower (150°C) as compared to that of RGTO films (250°C).
- Films of ZnO-nanoparticles and ZnO-nanowires were investigated for H_2S sensing, which exhibited p-type and n-type behaviour, respectively. The n-type behavior of nanowires films is attributed to oxygen vacancies, whereas the p-type nature of nanoparticle films is attributed to the zinc vacancy. Nanowire films detected H_2S in ppm range with fast response and recovery times. Nanoparticles

based sensors were not found stable for periods > 2 weeks as nanoparticles got agglomerated with time.

Analyses of the results obtained on H_2S sensing characteristics of metal-oxides in different configurations namely, thin film, nanowire films and isolated nanowires show that each configuration has its own merits and demerits. Thin films based sensors are robust but are expensive as high cost equipments, such as, thermal evaporation system and sputtering techniques are needed. Moreover, in this case the sensitivity and response kinetics depend strongly upon the grain size, which in turn depend on the technique used (thermal evaporation, sputtering etc.), as well as on deposition and annealing conditions. Generally n-type metal-oxides are considered to suitable for H_2S sensors owing to their good stability, but our studies, for the first time, have shown that p-type CuO films are excellent H_2S sensors in sub-ppm range. On the other hand, sensors based on films of nanowires and isolated nanowires are cost effective as they are synthesized using chemical and/or thermal routes. These sensors are expected to exhibit superior characteristics, owing to be high surface-to-volume ratio. However, for sensors based on nanowires films, the sensing performance is found to be hampered by the inter-connectivity of the nanowires. In the case of sensors based on isolated nanowires, any unintentional doping of nanowires can create the surface states that can change the p-type to n-type and vice versa. This demands growth of nanowires under very stringent conditions so that any unintentional doping can be avoided.

In order to enhance the H_2S sensor characteristics, we have also investigated the chemiresistive sensors compromising of p-n junctions. The summary of main results is as follows:

- CuO:ZnO based p-n junction type chemiresistive sensors were obtained by depositing CuO onto ZnO-nanowires random networks grown on Si/SiO_2

substrates. The formation of p-n junction has been confirmed by quenching of near band edge emissions in photoluminescence spectra and Kelvin probe measurements. CuO:ZnO-nanowires random networks exhibited high selectivity and sensitivity towards H_2S as compared to ZnO random nanowires networks. The sensitivity of these sensors varies linearly in the concentration range of 0.5–10 ppm and their operating temperatures reduced to 200°C as compared to 300°C for pure ZnO random nanowires.

- A sensing mechanism based on the destruction of p–n junctions due to the formation of metallic CuS (product of chemical reaction between CuO and H_2S) has been proposed. H_2S-sensing mechanism has been further investigated using impedance and work function measurements. We successfully demonstrated that the gas sensing is predominantly a surface phenomenon wherein the bulk and the sample–electrode interface do not undergo any changes on interaction with the gas molecules. The major role is played by the resistive and capacitance contribution coming from the high-resistance depletion layers (interface between p-type CuO and n-type ZnO) between relatively conducting plates of bulk material, i.e., ZnO nanowires. A drastic variation in the resistance of the sample arises mainly due to the band bending. The extent of band bending depends upon the ambient oxygen and the interaction with the test gas. Temperature- and gas concentration-dependent studies clearly indicated that the CuS formation is the major cause for such bending. Work function measurements further corroborates the finding of impedance studies.
- We altered sputtered WO_3 thin films with CuO ultrathin films which also resulted in uniformly distributed p-n junctions throughout the WO_3 sensor film. Modification with CuO resulted in an enhanced response towards H_2S with

improved response kinetics. CuO modified sample containing 2.25 at.% of Cu in the WO_3 host matrix exhibited a sensor response of 534 towards 10 ppm of H_2S as compared to 21 exhibited by pure WO_3 at an operating temperature of 300 °C. The response and recovery times for pure and CuO: WO_3 were similar i.e. 5 & 7s and 30 and 24 minutes respectively. The enhanced response and the high specificity are attributed to the formation of random nano p–n junction between p-type CuO and n-type WO_3, and the unique interaction of H_2S with CuO forming metallic CuS. Increase in the resistance and work function of the sensor film with CuO modification further corroborates the findings.

- We also demonstrated the gas sensing properties of Fe_3O_4: SnO_2 based p-n junction type sensors. SnO_2 thin films deposited by rheotaxial grown and thermal oxidation method and the presence of Fe (deposited using e gun technique) as Fe_3O_4 over the sensor surface was confirmed using XPS studies. The operating temperatures for both the sensor films was same i.e. 225°C. SnO_2 films modified with 0.64 at.% Fe exhibited a better sensor response (S = 14.5 for 10 ppm H_2S)with faster response kinetics of 90 and 98 s and complete recovery as against partial recovery in case of pure SnO_2. An improved response has been attributed to the interaction of H_2S with adsorbed oxygen species and Fe (forming low band gap FeS). Increase in the base line resistance and work function values upon Fe modification further supports the findings.

In all three cases p-n junction type sensors exhibited improved gas sensing characteristics as compared to corresponding to individual p- or n-type chemiresistive sensors. Among CuO:ZnO, CuO:WO_3 and Fe_3O_4:SnO_2, the best sensitivity towards H_2S is exhibited by CuO: WO_3 which is 534 times for 10 ppm. But the operating temperature of these sensors is higher (300°C) as compared to that of CuO: ZnO (200°C) and

Fe_3O_4:SnO_2 (225°C) sensors. The fastest response kinetics is obtained for Fe_3O_4:SnO_2 based sensors. The utility of these sensors can be decided according to the priority of the sensing parameters. All three sensors are able to sense H_2S selectively with fairly high sensitivities, therefore choice can be made according to the requirement of technique of fabrication at hand, low operating temperature or high sensitivity.

We have also modified n-type chemiresistive sensors with gold which is well reported in literature to show catalytic effects in improving the gas sensing properties. Besides catalytic action, modification with gold results in the formation of Schottky barriers at the Au: metal-oxide interface which also proved advantageous in enhancing the gas sensing characteristics. ZnO random nanowires networks as well as WO_3 thin films were modified into Schottky barrier type sensors by altering them with Au. ZnO nanowires were modified by Au using RF sputtering. The formation of Schottky barriers between Au and ZnO or WO_3 interfaces was confirmed using Raman studies, resistivity and work function measurements. For both the sensors, Au: ZnO and Au: WO_3, higher work function and a higher resistivity was observed after Au modification. Modification of ZnO random nanowire networks resulted in room temperature H_2S sensor with a 16-fold increase in sensor response over pure ZnO NWs (5 ppm). Au loading of 2.32 at.% in WO_3 thin films resulted in sub ppm highly selective H_2S sensors. The better sensing characteristics were attributed not only to the formation of nano-Schottky barriers with Au but also to the catalytic properties of Au that leads to increase in atmospheric oxygen adsorption facilitating better response kinetics in the Au modified sensors. Our results clearly demonstrate that modification with metal nanoparticles could be effectively used to tailor the response of sensor. This could probably be extended to other similar systems to realize sensor with better response kinetics.

In summary, we have fabricated H_2S chemiresistive sensors based on n-type, p-type, p-n junction type and Schottky barrier type, and investigated their sensing mechanisms. Based on the results of this thesis work, H_2S sensors suitable for different concentration ranges are as follows:

- ***Sub ppm H_2S sensors: The chemiresistive sensor based on CuO thin films and Au:WO_3 Schottky barrier has the lowest detection limit of 100 and 50 ppb respectively.***
- ***1-50 ppm H_2S sensors: The chemiresistive sensors based on CuO:ZnO, CuO:WO_3 and Fe_3O_4:SnO_2 p-n junctions, sputtered SnO_2 thin films and Au:ZnO Schottky barriers were able to detect H_2S in the intermediate range with full recovery. Au: ZnO Schottky barrier based chemiresistive sensors could sense H_2S at room temperature. Also Fe_3O_4:SnO_2 p-n junctions type sensors showed the fastest response kinetics of 90 and 98 s respectively.***
- ***>50 ppm H_2S sensors: The chemiresistive sensors based on CuO islolated nanowires showed full recovery at high concentrations of H_2S but stability was a major issue due to poor electrical contacts to the individual nanowires.***

This thesis opens up following work in the future:

- Fabrication of robust electrical contacts to investigate the isolated nanowires sensors for high concentration (>50 ppm) H_2S.
- Testing of the sensors in actual plant conditions. In fact, initial testing of ZnO random nanowires based sensors at Heavy Water Plant, Manuguru, revealed that these sensor are quite stable for the measurements of 1-50 ppm concentration of H_2S. The stability has been observed for two months. All the other sensors will be deployed for such testing at Heavy Water Plant, Manuguru.

BIBLIOGRAPHY

---

[1] D.K. Aswal, S.K. Gupta (Eds.), Science and Technology of Chemiresistive Gas sensors, *Nova Science Publisher*, NY, U.S.A (2007).

[2] Giorgio Sberveglieri, Roberto Murri and Nicola Pinto *Sens. Actuat. B*, 23 (1995) 177-180

[3] M.Andersson,M.Holmberg, I.Lundstrom,A.Lloyd-Spetz,P.Martensson, Paolesse,R. Falconi, C. E.Proietti, C.D.Natale,A.D'Amica, *Sens. Actuat. B*, 77 (2001) 567-571.

[4] I. Lundstrom, S. Shivaraman, C. Svensson, L.Lundkvist, *Appl. Phys. Lett.* , 26 (1975) 55-57.

[5] S.-J. Jung, H.Yanagida, *Sens. Actuat. B*, 37 (1996) 55-60.

[6] S. Nakagomi, K. Okuda, Y.Kokubun, *Sens. Actuat. B*, 96 (2003) 364-371.

[7] U. Weimer, W. Gopel, *Sens. Actuat. B*,26-27 (2005) 13-18.

[8] T. Seiyama, A. Kato, K. Fujiishi, M.Nagatani, *Anal. Chem.*, 34 (1962) 1502-3.

[9] K. Ihokura, J. Watson, *The stannic oxide gas sensor*, CRC Press, Florida, Inc. © (1994).

[10] A.Kolmakov, D.O.Klenov, Y.Lilach, S.Stemmer, M.Moskovits, Nano *Lett.*, 5 (2005) 667–673.

[11] Noboru Yamazoe, Go Sakai, Kengo Shimanoe, *Catalysis Surveys from Asia*, 7 (2003) 63-75.

[12] V.E. Henrich, P.A. Cox, The Surface Science of Metal-oxides, *Cambridge University Press, Cambridge*, XIV (1994) 464.

[13] N. Barsan, A. Heilig, J. Kappler,U.Weimar,W. Gopel, *Proceedings of the 13th European Conference on Solid State Transducers, EUROSENSORS,* XIII (1999) 367–369.

[14] N. Barsan, U. Weimar, *J. Phys. Condes. Matter.*, 15 (2003) R1–R27.

[15] V. Golovanov, M.A. Maki-Jaskari, T.T. Rantala, G. Korotcenkov, V. Brinzari, A. Cornet, J. Morante, *Sens Actuat. B*, 106 (2005) 563–571.

[16] K.Batzill, J.M. Katsiev, U.Burst, A.M. Diebold, B. DelleyChaka, *Phys. Rev. B*, 72 (2005)1–20.

[17] M. Batzill, U. Diebold, *Prog. Surf. Sci.*, 79 (2005) 47–154.

[18] N. Yamazoe, *Sens. Actuat. B*, 108 (2005) 2–14.

[19] D.M. Wilson, S. Hoyt, J. Janata, K. Booksh, L. Obando, *IEEE Sens. J.*, 1 (2001) 4.

[20] P.T. Moseley, J.O.W. Norris, D.E.Williams (Eds.), Techniques and Mechanisms in Gas Sensing, *Adam Hilger, Bristol*, (1991).

[21] M.J. Madou, S.R. Morrison, Chemical Sensing with Solid State Devices, *Academic Press, Inc./Harcourt Brace Jovanovich Publ., Boston*, NY, (1987).

[22] G. Sberveglieri (Ed.), Gas Sensors—Principles Operation and Developmens, *Kluwer Academic Publishers, The Netherlands,* (1992).

[23] G. Korotcenkov, *Sens. Actuat. B*, 107 (2005) 209–232.

[24] L.Y. Kupriyanov (Ed.), Semiconductor Sensors in Physico-Chemical Studies, *Elsevier, Amsterdam*, (1996).

[25] V. Brinzari, G. Korotchenkov, S. Dmitriev, *J. Electr. Technol.*, 33 (2000) 225–235.

[26] D. Williams, *Sens. Actuat. B*, 57 (1999) 1–16.

[27] S.R. Morrison, *Sens. Actuat.*, 11 (1987) *283*–287.

[28] Vishal Balouria, Arvind Kumar, A. Singh, S. Samanta, A.K. Debnath, Aman Mahajan, R.K. Bedi, D.K. Aswal, S.K. Gupta, J.V. Yakhmi, *Sens. Actuat. B*, 157 (2011) 466-472.

[29] D.N. Suryawanshi, D.R. Patil, L.A. Patil, *Sens. Actuat. B*, 134 (2008) 579-584.

[30] Lili Wang, Jianan Deng, Zheng Lou, Tong Zhang, *Sens. Actuat. B*, 201 (2014) 1-6.

[31] Fengdong Qu, Juan Liu, Ying Wang, Shanpeng Wen, Yu Chen, Xu Li, Shengping Ruan, *Sens. Actuat. B*, 199 (2014) 346-353.

[32] D.P. Runthala, R.P. Gupta, P.D. Vyas, G. Eranna, R. Paris, D.Schipanski, *Ind. J. Engg. Mats. Sci.*, 7 (2000) 336- 339.

[33] J. Wöllenstein, M. Burgmair, G. Plescher, T. Sulima, J. Hildenbrand, H. Böttner, I.Eisele, *Sens. Actuat. B*, 93 (2003) 442-448.

[34] C. Cantalini, M. Post, D. Buso, M. Guglielmi,A. Martucci, *Sens. Actuat. B*, 108(2005) 184-192.

[35] Kun Li, Guoli Fan, Lan Yang, Feng Li, *Sens. Actuat. B*, 199 (2014) 175-182.

[36] Li Yang, Changsheng Xie, Guozhu Zhang, Jianwei Zhao, Xueli Yu, Dawen Zeng, Shunping Zhang, *Sens. Actuat. B*, 195 (2014) 500-508.

[37] Kwon-Il Choi, Hyo-Joong Kim, Yun Chan Kang, Jong-Heun Lee, *Sens. Actuat. B*, 194 (2014) 371-376.

[38] Tie-Shi Wang, Qing-Shan Wang, Chun-Ling Zhu, Qiu-Yun Ouyang, Li-Hong Qi, Chun-Yan Li, Gang Xiao, Peng Gao, Yu-Jin Chen, *Sens. Actuat. B*, 171-172 (2012) 256-262.

---

[39] V. Jayaraman, E. Prabhu, A. Sree Rama Murthy, P.C. Clinsha, K.I. Gnanasekar, T. Gnanasekaran, *Sens. Actuat. B,* 202 (2014) 9-13.

[40] Qing-Hong Xu, Dong-Mei Xu, Mei-Yu Guan, Ying Guo, Qi Qi, Guo-Dong Li, *Sens. Actuat. B*, 177 (2013) 1134-1141.

[41] B. Dong, T. Yang, M.K. Lei, *Sens. Actuat. B*, 123 (2007) 667-670.

[42] A. Ryzhikov,M. Labeau, A.Gaskov, *Sens. Actuat.B*, 109 (2005) 91-96.

[43] A. Cabot, A. Marsal, J. Arbiol, J.R. Morante, *Sens. Actuat. B*, 99 (2004) 74-89.

[44] A.A Tomchenko, *Sens. Actuat. B,* 68 (2004) 48-52.

[45] G.S. Devi, S.V. Manorama, V.J. Rao, *J. Electrochem. Soc.*, 145 (1998) 1039-1044.

[46] P. Althainz, L. Schuy, J. Goschnick,H. J. Ache, *Sens. Actuat. B*, 24-25 (1995) 448-459.

[47] G. Neri, A. Bonavita, G. Rizzo, S. Galvagno, S. Capone, P. Siciliano, *Sens. Actuat. B*, 114 (2006) 687-695.

[48] S.V. Ryabtsev, A.V. Shaposhnick, A. N. Lukin, E.P. Domashevskaya, *Sens. Actuat. B*, 59 (1999) 26-29.

[49] G. Neri, A.Bonavita, S. Galvagno, P. Siciliano, S.Capone, *Sens. Actuat. B*, 82 (2002) 40-47.

[50] Ch.Y. Wang, M. Ali, Th. Kups, C.-C. Röhlig, V. Cimalla, Th. Stauden, O. Ambacher, *Sens. Actuat. B*, 130 (2008) 589-593.

[51] Peng Song, Dan Han, Huihui Zhang, Jia Li, Zhongxi Yang, Qi Wang, *Sens. Actuat. B*, 196 (2014) 434-439.

[52] K. Inyawilert, A. Wisitsora-at, A. Tuantranont, P. Singjai, S. Phanichphant, C. Liewhiran, *Sens. Actuat. B*, 192 (2014) 745-754.

[53] Dianxing Ju, Hongyan Xu, Zhiwen Qiu, Jing Guo, Jun Zhang, Bingqiang Cao, *Sens. Actuat. B*, 200 (2014) 288-296.

[54] Xueli Yu, Changsheng Xie, Li Yang, Shunping Zhang, *Sens. Actuat. B*, 195 (2014) 439-445.

[55] M. Matsumiya, F. Qiu, W. Shin,N. Izu, N. Murayama,S. Kanzaki, *Thin Solid Films*, 419 (2002) 213-217.

[56] J. A. Dirksen, K. Duval, T. A. Ring, *Sens. Actuat. B*, 80 (2001) 106-115.

[57] I. Hotovy, J. Huran, P. Siciliano, S. Capone, L. Spiess, V. Rehacek, *Sens. Actuat. B*, 78 (2001) 126-132.

[58] I. Hotovy, V. Rehacek, P. Siciliano,S. Capone, L.Spiess, *Thin Solid Films*, 418 (2002) 9-15.

[59] Ai Hosoki, Michiko Nishiyama, Hirotaka Igawa, Atsushi Seki, Yongwoon Choi, Kazuhiro Watanabe, *Sens. Actuat. B,* 185 (2013) 53-58.

[60] M.Kimura, *Sens. Actuat. A*, 55 (1996) 7-11.

[61] J. Lančok, A. Santoni, M. Penza, S. Loreti, I. Menicucci, C. Minarini, M.Jelinek, *Surf Coatings Technology*, 200 (2005) 1057-1060.

[62] S.K. Song, J.S. Cho, W.K. Choi, H.J. Jung, D. Choi, J.Y. Lee, H.K. Baik, S.K. Koh, *Sens. Actuat. B*, 46 (1998) 42-49.

[63] J. Santos, P. Serrini, B. O’Beirn, L.Manes, *Sens. Actuat. B*, 43(1997) 154-160.

[64] R.K. Sharma, Z. Tang, P.C. H. Chan, J.K.O. Sin, I.M. Hsing, *Sens. Actuat. B*, 64 (2000) 49-53.

[65] G. Carbajal-Franco, A.T. Silver, J.M. Domínguez, A. Sánchez-Juárez, *Thin Solid Films*, 373 (2000) 141-144.

[66] T.Oyabu, *J. Appl. Phy.*, 53 (1982) 2785-2787.

[67] R.S. Niranjan, S.R. Sainker, K. Vijayamohanan, I.S. Mulla, *Sens. Actuat. B*, 82 (2002) 82-88.

[68] N. Yamazoe, J. Tamaki, N.Miura, *Mat. Sci. Engg. B*, 41 (1996) 178-181.

[69] A. Khanna, R. Kumar, S.S. Bhatti, *Appl. Phys. Letts.*, 82 (2003) 4388-4390.

[70] A. Chowdhuri, P. Sharma, V. Gupta, K. Sreenivas, K.V. Rao, *J. Appl. Phys.*, 92 (2002) 2172-2180.

[71] E. Comini, G. Faglia, G. Sberveglieri, D. Calestani, L. Zanotti, M.Zha, *Sens. Actuat. B*, 111-112 (2005) 2-6.

[72] E. Comini, G. Faglia, G. Sberveglieri, Z. Pan, Z. L. Wang, *Appl. Phys. Lett.* 81 (2002) 1869-1871.

[73] Jai S. Tawale, Gaurav Gupta, Anand Mohan, Ashavani Kumar, Avanish K. Srivastava, *Sens. Actuat. B*, 201(2014) 369-377.

[74] Jiangli Tian, Jing Wang, Yuwen Hao, Haiying Du, Xiaogan Li, *Sens. Actuat. B*, 202 (2014) 795-802.

[75] A. Stankova, X. Vilanova, E. Llobet, J. Calderer, C. Bittencourt, J.J. Pireaux, X. Coffeig, *Sens. Actuat.B*, 105 (2005) 271–277.

[76] Y.S. Kim, S.C. Ha, K. Kim, H. Yang, S.Y. Choi, Y.T. Kim, J.T. Park, C.H. Lee, J. Choi, J. Paek, K. Lee, *Appl. Phys. Lett*., 86 (2005) 213105–213107.

[77] Teng Xiao, Xiu-Yue Wang, Zhi-Hua Zhao, Liu Li, Lin Zhang, Hong-Chang Yao, Jian-She Wang, Zhong-Jun Li, *Sens. Actuat. B*, 199 (2014) 210-219.

[78] Young-Seok Shim, Lihua Zhang, Do Hong Kim, Yeon Hoo Kim, You Rim Choi, Seung Hoon Nahm, Chong-Yun Kang, Wooyoung Lee, Ho Won Jang, *Sens. Actuat. B*, 198 (2014) 294-30.

[79] Yanbai Shen, Baoqing Zhang, Xianmin Cao, *Sens. Actuat. B*, 193 (2014) 273-279.

[80] Vibha Srivastava, Kiran Jain, *Sens. Actuat. B*, 133 (2008) 46-52.

[81] M. Hjiri, L. El Mir, S.G. Leonardi, A. Pistone, L. Mavilia, G. Neri, *Sens. Actuat. B*, 196 (2014) 413-420.

[82] Mingshui Yao, Fei Ding, Yuebin Cao, Peng Hu, Junmei Fan, Chen Lu, Fangli Yuan, Changyong Shi, Yunfa Chen, *Sens. Actuat. B*, 201 (2014) 255-265.

[83] Minggang Zhao, Xinchang Wang, Lingling Ning, Jianfeng Jia, Xinjian Li, Liangliang Cao, *Sens. Actuat. B*, 156 (2011) 588-592.

[84] H. Gong, J.Q. Hu, J.H. Wang, C.H. Ong, F.R. Zhu, *Sens. Actuat. B*, 115 (2006) 247-251.

[85] Tonny-Roksana Rashid, Duy-Thach Phan, Gwiy-Sang Chung, *Sens. Actuat. B*, 193 (2014) 869-876.

[86] Jing Guo, Jun Zhang, Min Zhu, Dianxing Ju, Hongyan Xu, Bingqiang Cao, *Sens. Actuat. B*, 199 (2014) 339-345.

[87] Xin-jun Wang, Wei Wang, Yan-Li Liu, *Sens. Actuat. B*, 168 (2012) 39-45.

[88] Feng-Chao Chung, Zhen Zhu, Peng-Yi Luo, Ren-Jang Wu, Wei Li, *Sens. Actuat. B*, 199 (2014) 314-319.

[89] D.R. Patil, L.A. Patil, *Sens. Actuat. B*, 123 (2007) 546-553.

[90] Huixiang Tang, Mi Yan, Hui Zhang, Shenzhong Li, Xingfa Ma, Mang Wang, Deren Yang, *Sens. Actuat. B*, 114 (2006) 910-915.

[91] Sunghoon Park, Suyoung Park, Sangmin Lee, Hyoun Woo Kim, Chongmu Lee, *Sens. Actuat. B*, 202 (2014) 840-845.

[92] Sen Liu, Bo Yu, Hao Zhang, Teng Fei, Tong Zhang, *Sens. Actuat. B*, 202 (2014) 272-278.

[93] Shashwati Sen, V. Bhandarkar, K.P. Muthe, M. Roy, S.K. Deshpande, R.C. Aiyer, S.K. Gupta, J.V. Yakhmi, V.C.Sahani, *Sens. Actuat.B*, 115(2006) 270-275.

[94] Lei Guan, Shun Wang, Wen Gu, Jinxia Zhuang, Huile Jin, Weiming Zhang, Ting Zhang, Jichang Wang, *Sens. Actuat. B*, 196 (2014) 321-327.

[95] T. Siciliano, M. Di Giulio, M. Tepore, E. Filippo, G. Micocci, A. Tepore, *Sens. Actuat. B*, 138 (2009) 550-555.

[96] P. Fürjes, A. Kovács, Cs. Dücso, M. Ádám, B. Müller, U. Mescheder, *Sens. Actuat. B*, 95 (2003) 140-144.

[97] Yaqiao Wu, Ming Hu, Yuxiang Qin, Xiaoying Wei, Shuangyun Ma, Dali Yan, *Sens. Actuat. B*, 195 (2014) 181-188.

[98] P. Lauque, M. Bendahan, C. Jacolin, J.-L. Seguin, M. Pasquinelli, P. Knauth, *Sens. Actuat. B*, 59 (1999) 216-219.

[99] M. Bendahan, P. Lauque, C. Lambert-Mauriat, H. Carchano, J.-L. Seguin, *Sens. Actuat. B,* 84 (2002) 6-11.

[100] R. Benlikaya, P. Slobodian, P. Riha, R. Olejnik, *Sens. Actuat. B,* 201 (2014) 122-130.

[101] B. Ghaddab, J.B. Sanchez, C. Mavon, M. Paillet, R. Parret, A.A. Zahab, J.-L. Bantignies, V. Flaud, E. Beche, F. Berger, *Sens. Actuat. B*, 170 (2012) 67-74.

[102] M. Mittal, A. Kumar, *Sens. Actuat. B,* 203 (2014) 349-362.

[103] Purushottam Jha, Niranjan S. Ramgir, Preetam K. Sharma, N. Datta, S. Kailasaganapathi, M. Kaur,S.P. Koiry, V. Saxena, A.K. Chauhan, A.K. Debnath, Ajay Singh, D.K. Aswal, S.K. Gupta, *Mater. Chem. Phys*., 140 (2013) 300-306.

[104] Arvind Kumar, A.K. Debnath, S. Samanta, A. Singh, R. Prasad, P. Veerender, S. Singh, S. Basu, D.K. Aswal, S.K. Gupta, *Sens. Actuat. B*, 171-172 (2012) 423-430.

[105] Soumen Samanta, A. Kumar, A. Singh, A.K. Debnath, D.K. Aswal, S.K. Gupta, *Chem. Papers*, 66 (2012) 484-491.

[106] S. Iijima, T.Ichihashi, *Nature*, 363(1993) 603-605.

[107] C. K. Chiang, Y. W. Park, A. J. Heeger, H. Shirakawa, E. J. Louis, A.G.MacDiarmid, *J Chem. Phys.*, 69 (1978) 5098-5104.

[108] S.P. Patil, Vijaya Puri, *Europeon Journal of Scientific Research*, 1 (2012) 113-121.

[109] J. Szuber, J. Uljanow, T. Karczewska-Buczek, W. Jakubik, K. Waczynski, M. Kwoka, S. Konczak, *Thin Solid Films*, 490 (2005) 54- 58.

[110] W. Hellmich, Ch. Bosch-v. Braunmühl, G. Müller, G. Sberveglieri, M. Berti, C. Perego, *Thin Solid Films*, 263 (1995) 231–237.

[111] I. Platzman, R. Brener, H. Haick, R. Tannnenbaum, *J. Phys. Chem. C*, 112 (2008) 1101-1108.

[112] Ian M. Watt, *The Principles and practice of electron microscopy*, Cambridge University Press, (1985)

[113] B. D. Cullity, *Elements of X-ray Diffraction*, second edition, Addison-Wesley (1978).

[114] Skoog, Holler, Nieman, *Principles of instrumental analysis*, 5thed, Brooks Cole (1998).

[115] D. Briggs, M.P. Seah, *Practical surface analysis by Auger and x-ray photoelectron spectroscopy*, Wiley (1983).

[116] J. F. Moulder, W.F. Stickle, P.E. Sobol, K. D. Bomben, *Handbook of X-ray photoelectron spectroscopy*, Physical electronics, USA, (1995).

[117] Wilhelm Melitz, Jian Shen, Andrew C. Kummel, Sangyeob Lee, *Surf. Sci. Rep.*, 66(2011) 1-27.

[118] Ivan Pelant, Jan Valenta, *Luminescence spectroscopy of semiconductors*, Oxford University Press (2012).

[119] S. Asbrink, A. Waskowska, *J. Phys.: Condens. Matter*,3 (1991) 8173-8080.

[120] C.Wagner, *Z. Phys. Chem. B*,21 (1933) 25-41.

[121] B.J. Hansen, N. Kaoklin, G. Lu, I. Lin, J. Chen, X. Zhang, *J. Phys. Chem.* , 114 (2010) 2440-2447.

---

[122] J. Bardeen, W. H. Brattain and W. Shockley, *J. Chem. Phys.*, 14 (1946) 714.

[123] N. Yamazoe, K. Shimanoe, *Sens. Actuators B*, 154 (2010) 277-282.

[124] H. Liu, S.P. Gong, Y.X. Hu,b, J.Q. Liu, D.X. Zhou, *Sens. Actuators B*, 140 (2009) 190–195.

[125] C.C. Chusuei, M.A. Brookshier, D.W. Goodman, *Langmuir*, 15 (1999) 2806-2808.

[126] J.T. Chen, F. Zhang, J. Wang, G.A. Zhang, B.B. Miao, X.Y. Fan, D. Yan, P.X. Yan, *J. Alloys Compd.*, 454 (2008) 268-273.

[127] Ang Li, Huaihe Song, Jisheng Zhou, Xiaohong Chen, Siyuan Liu, *Cryst. Eng. Comm.*, 15 (2013) 8559-8564.

[128] H.-H. Lin, C.-Y. Wang, H.C. Shih, J.-M. Chen, C.-T. Hsieh, *J. Appl. Phys.*, 95 (2004) 5889.

[129] Lu Yuan, Yiqian Wang, Rediola Mema, Guangwen Zhou, *Acta Mater*., 59 (2011) 2491-2500.

[130] Mingji Chen, Yumei Yue, Yang Ju, *J. Appl. Phys.*, 111 (2012), 104305.

[131] Yoon-Sung Kim, In-Sung Hwang, Sung-Jung Kim, Choong-Yong Lee, Jong-Heun Lee, *Sens. Actuat. B*, 135 (2008) 298-303.

[132] Yuan Peng, Zhen Zhang, Thien Viet Pham, Yang Zhao, Ping Wu, Junling Wang, *J. Appl. Phys.*, 111 (2012) 103708.

[133] D. Briggs, M. P. Seah (Ed), *Practical surface analysis, 2nd Ed, vol 1, Auger and X-ray photoelectron spectroscopy*,Wiley, (1990).

[134] G. Faglia, P. Nelli, and G. Sberveglein, *Sens. Actuat. B*, 18-19 (1994) 497–499.

[135] A.W. C. Lin, N. R. Armstrong, T. Kuwana, *Anal. Chem.*,49 (1977) 1228–1235.

[136] A.R. Phani, S. Manorama, V.J. Rao, *J. Phys. Chem. Solids*, 61 (2000) 985-993.

[137] A.K. Debnath, N. Joshi, K.P. Muthe, J.C. Vyas, D.K. Aswal, S.K. Gupta, J.V. Yakhmi, *App. Surf. Sci.*, 243 (2005) 220–227.

[138] N.S. Ramgir, S. Kailasa Ganapathi, M. Kaur, N. Datta, K.P. Muthe, D.K. Aswal, S.K. Gupta, J.V. Yakhmi,*Sens. Actuat. B*, 151 (2010) 90-96.

[139] M.W. Ahn, K.S. Park, J.H. Heo, J.G. Park, D.W. Kim, K. J. Choi, J. H. Lee, S.H. Hong, *Appl. Phys. Lett.*, 93 (2008) 263103.

[140] D. S. Vlachos, C. A. Papadopoulos, and J. N. Avaritsiotis, *J. Appl. Phys.*, 80 (10), (1996) 6050–6054.

[141] D. F. Cox, T. B. Fryberger, S. Semancik, *Phys. Rev. B*, 38 (1988) 2072.

[142] Q. Dong, H. Su, J. Xu, D. Zhang, *Sens. Actuat. B*, 123 (2007) 420-428.

[143] L.Z. Liu, T.H. Li, X.L. Wu, J.C. Shen, P.K. Chu, *J. Raman Spec.*, 43(2012) 1423-1426.

[144] W. H. Baur, A. A. Khan, *Acta Cryst*., B27(1971) 2133-2139.

[145]M. Epifani, J. D. Prades, E. Comini, E. Pellicer, M. Avella, P. Siciliano, G. Faglia, A. Cirera, R. Scotti,F. Morazzoni, J. R. Morante, *J. Phys. Chem. C*, 112 (2008)19540–19546.

[146] J. Chen, K. Wang, L. Hartman, W. Zhou, *J. Phys. Chem. C*, 112 (2008) 16017–16021.

[147] B. Xiang, P. Wang, X. Zhang, S. A. Dayeh, D. P. R. Aplin, C. Soci, D. Yu, D. Wang, *Nano Lett.*, 7 (2007) 323-328.

[148] D.C. Look, G.C. Farlow, P. Reunchan, S. Limpijumnong, S.B. Zhang, K. Nordlund, *Phys. Rev. Lett.*, 95 (2005) 225502.

[149] S.T. Tan, B.J. Chen, X.W. Sun, M.B. Yu, X.H. Zhang, S.J. Chua, *J. Electron. Mater.*,34 (2005) 1172-1176.

[150] B. Wang, J. Min, Y. Zhao, W. Sang, C. Wang, *Appl. Phys. Lett.*, 94 (2009) 192101.

[151] Y.F. Hsu, Y.Y. Xi, K.H. Tam, A.B. Djurisˇic´, J. Luo, C.C. Ling, C.K. Cheung, A.M. Ching Ng, W.K. Chan, X. Deng, C.D. Beling, S. Fung, K.W. Cheah, P.W.K. Fong, C.C. Surya,*Adv. Funct. Mater.*, 18 (2008) 1020–1030.

[152] S.T. Tan, X.W. Sun, Z.G. Yu, P. Wu, G.Q. Lo, D.L. Kwong, *Appl. Phys. Lett.*, 91 (2007) 072101.

[153] S.K. Chaudhuri, M. Ghosh, D. Das, A.K. Raychaudhuri, *J. App. Phys.*, 108 (2010) 064319.

[154] M. Yin, C.-K. Wu, Y. Lou, C. Burda, J.T. Koberstein, Y. Zhu, S.O’Brien, *J. Am. Chem. Soc.*, 127 (2005) 9506.

[155] J.F.Moulder, W.F.Stickle, P.E.Sobol, K.D. Bombson, *Handbook of X-ray photoelectron spectroscopy*, Physical Electronics Inc., Minnesota, (1995).

[156] Z. Zhang, P.Wang, *J. Mater. Chem.*, 22 (2012) 2456-2464.

[157] R.A. Rosenberg, M.A. Haia, K. Vijayalakshmi, J. Zhou, S. Xu, Z.L. Wang, *Appl. Phys. Lett.* 95 (2009) 243101-03

[158] P. Yang, H. Yan, S. Mao, R. Russo, J. Johnson, R. Saykally, N. Morris, J. Pham, R. He, H. J. Choi, *Adv. Funct. Mater.*12 (2002) 323-331.

[159] Y.B. Soskovets, A.Y. Khairullina, V.A. Babenko, *J. Appl. Spect.*73 (2006) 576-582.

[160] W.Y. Cheng, Y. F. Lin, S.Y. Lu, Nanowires improved charge separation and light utilization in metal oxide solar cells, *Appl. Phys. Lett.* 99 (2011) 063107.

[161] N.S.Ramgir, K.Subannajui, Y.Yang, R.Grimm, R.Michiels, M.Zacharias, *J. Phys. Chem. C*, 114 (2010)10323–10329.

[162] S.Jung, S.Jeon, K.Yong, *Nanotechnology*, 22 (2011) 015606.

[163] N.Barsan, U.Weimar, *J. Phys. Condens. Matter*, 15 (2003) R813–R839.

[164] N.H. Al-Hardan, M.J.Abdullah, A.Abdul Aziz, *International J. Hydrogen Energy*, 35 (2010) 4428-4434.

[165] M.Seitz, F.Hampton, W. Richmond, M. F.Yan, A. H. Heuer, (Eds.), *Advances in Ceramics*, Ohio: The American Ceramic Society Inc. 7 (1983) 60-70.

[166] H.Ishii, K.Sugiyama, E.Ito, *Adv. Mater.*, 11 (1999) 605 - 625.

[167] J.Lahiri, M. Batzill, *J. Phys. Chem. C*, 112 (2008) 4304- 4307.

[168] R. B. Slimane, F. S. Lau, R. J. Dihu, M. Khinkis, *Proceedings of the U.S. DOE hydrogen program review*, NREL/CP-610-32405 (2002).

[169] A. Šetkus, *Sens. Actuat. B*, 87 (2002) 346–357.

[170] A. Šetkus, C. Baratto, E. Comini, G. Faglia, A. Galdikas, Ž. Kancleris, G. Sberveglieri, D. Senulien, *Sens. Actuat. B,* 103 (2004) 448-456.

[171] G. Korotcenkov, I. Boris, V. Brinzari, S.H. Han, B.K. Cho, *Sens. Actuat. B*, 182 (2013) 112-124.

[172] V.R. Katti, A.K. Debnath, K.P. Muthe, Manmeet Kaur, A.K. Dua, S.C. Gadkari, S.K. Gupta, V.C. Sahni, *Sens. Actuat. B*, 96 (2003) 245-252.

[173] L. Ottaviano, M. Kwoka, F. Bisti, P. Parisse, V. Grossi, S. Santucci, J. Szuber, *Thin Solid Films*, 517 (2009) 6161–6169.

[174] M.N. Rumyantseva, O.V. Safanova, M.N. Boulova, L.I. Ryabova, A.M. Gaskov, *Russ. Chem. Bull. (Int. Ed.)*, 52 (2003) 1217–1238.

[175] N.S. Ramgir, I.S. Mulla, K.P. Vijayamohanan, *Sens. Actuat. B,* 107 (2005) 708-715.

[176] R.S. Niranjan, K.R. Patil, S.R. Sainkar, I.S. Mulla, *Mater. Chem. Phys.*, 80 (2003) 250-256.

[177] V. Balouria, A. Kumar, S. Samanta, A. Singh, A.K. Debnath, Aman Mahajan, R.K. Bedi, D.K. Aswal, S.K. Gupta, *Sens. Actuat. B.*, 181 (2013) 471-478.

[178] F. Martín, E. Navarrete, J. Morales, C.Roldán, J. Ramón Ramos-Barrado, L. Sánchez, *J. Mater. Chem.*, 20 (2010) 2847-2852.

[179] T. Yamashita, P. Hayes, *Appl. Surf. Sci.*, 254 (2008) 2441–2449.

[180] Y. Li, R.A. van Santen, Th. Weber, *J. Solid State Chem.*, 181 (2008) 3151–3162.

[181] A.Davydov, K. T. Chuang, A. R. Sanger, *J. Phys. Chem. B*, 102 (1998) 4745-4752.

[182] L. Bergman, X.-B. Chen, J. Huso, J.L. Morrison, and H. Hoeck, *J. Appl. Phys.*, 98 (2005) 093507.

[183] L. Yang, J. Yang, D. Wang, Y. Zhang, Y. Wang, H. Liu, H. Fan, J. Lang, *Physica E,* 40 (2008) 920-923.

[184] A. C. Mofor, F. Reuss, A. El-Shaer, H. Ahlers, U. Siegner, A. Bakin, W. Limmer, J. Eisenmenger, Th. Mueller, P. Ziemann, and A. Waag, *Phys. Stat. Sol.*, C 3 (2006) 1104-1108.

[185] C. Bundesmann, N. Ashkenov, M. Schubert, D. Spemann, T. Butz, E.M. Kaidashev, M. Lorenz, M. Grundmann, *Appl. Phys. Lett.*, 83 (2003) 1974.

[186] R. Nagarajan, A. D. Draeseke, A. W.Sleight, J. Tate, *J. Appl. Phys.*, 89 (2001) 8022-8025.

[187] C. Lien, C. Wu, Z. Li, J. Line, *J. Appl. Phys.*, 110 (2011) 063706.

[188] N. F. Mott, *Phil. Mag.*, 19 (1969) 835-852.

[189] Y.-L. Huang, S.-P. Chiu, Z.-X. Zhu, Z.-Q. Li, J.-J. Lin, *J. Appl. Phys.*, 107 (2010) 063715.

[190] R. Plugaru, T. Sandu, N. Plugaru, *Results in Phys.*, 2 (2012) 190–197.

[191] G. Korotcenkov, B.K. Cho, *Sens. Actuat. B,* 156 (2011) 527-538.

[192] S.-P. Chang, S.-J. Chang, C.-Y. Lu, M.-J. Li, C.-L. Hsu, Y.-Z. Chiou, T.-J. Hsueh, I-C. Chen, *Superlatt. Microstructures*, 47 (2010) 772-778.

[193] N. Asar, A. Erol, S. Okur, M.C. Arikan, *Sens. Actuat. A*, 187 (2012) 37-42.

[194] N. Barsan, U. Weimar, *J. Electroceramics*, 7 (2001) 143–167.

[195] F. Flores, R. Miranda, *Adv. Mater.*, 6 (1994) 540–548.

[196] X.F. Chu, D.L. Jiang, Y. Guo, C.M. Zheng, *Sens. Actuat. B*, 120 (2006) 177–181.

[197] C. Wang, X. Chu, M. Wu, *Sens. Actuat. B*, 113 (2006) 320-323.

[198] S. Wang, Y. Xiao, D. Shi, H. K. Liu, S. X. Dou, *Mater. Chem. and Phys.*, 130 (2011) 1325-1328.

[199] T. Siciliano, A. Tepore, G. Micocci, A. Serra, D. Manno, E. Filippo, *Sens. Actuat. B*,133 (2008) 321.

[200] J. Gabrusenoks, A. Veispals, A. von Czarnowski, K.-H. Meiwes-Broer, *Electrochem. Acta*, 46 (2001) 2229.

[201] K. Nonaka, A. Takase, K. Miyakawa, *J. Mater. Sci.Lett.*, 12 (1993) 274.